

NOVEL MATERIALS AND OPTICAL FIBRE SENSORS TO REDUCE THE RISK OF INFECTION ASSOCIATED WITH ENDOTRACHEAL TUBES

Yasin Kurmoo, MPharm (Hons)

Thesis submitted to the University of Nottingham for the degree of Doctor of Philosophy

December 2017

Abstract

Bacterial attachment and subsequent biofilm formation on endotracheal tube (ETT) surfaces can cause the secondary pulmonary infection, Ventilator-Associated Pneumonia (VAP) in intubated patients. The severity of VAP is often exacerbated by the occurrence of antimicrobial resistance amongst pathogens, with mortality rates as high as 50%. These infections place significant strain and economic burden on healthcare services. Attempts to modify ETT surfaces to resist bacterial adhesion have so far lacked effectiveness and are expensive. In the first part of this thesis, a novel poly acrylate:methacrylate co-polymer is tested as a bacteria resistant coating for ETTs. It is found that the polymer coating, with a binary silane adhesion promoter, reduces bacterial attachment by up to 96% and 100% on device tubes and cuffs respectively, in RPMI-1640 medium. In Artificial Sputum Medium there is a 100% reduction in attachment across all coated samples, offering an inexpensive anti-attachment coating for ETTs. Differences in bacterial attachment between uncoated tubes and cuffs is found to be caused by phthalate plasticisers on cuffs, which is thought to have a bactericidal effect, reducing biofilm formation on cuffs. No correlation is observed between surface roughness and bacterial attachment.

There is currently no method to monitor bacterial attachment to ETTs in real time. This requires removal of the device for laboratory examination, causing tracheal wall damage and potentially facilitating VAP progression. In the second part of this thesis, the novel use of Long Period Grating optical fibre sensors (LPG OFS) to monitor biofilm formation in real time is examined. A linear increase in wavelength shift over time of immersion in bacteria culture media is observed for both uncoated and polymer coated (plus a silane primer) sensors, for both attenuation bands, indicating increased cell adsorption to sensor surfaces. R^2 values are no lower than 0.86, for all plots. The rate of change of wavelength shift is 21- and 15-fold lower for attenuation peaks 1 and 2 of the coated sensor respectively, indicating reduced adsorption of bacteria, further highlighting the effectiveness of the polymer. The spectral profiles are

the same when the sensors are incorporated into the lumens of ETTs, suggesting that attachment to LPG OFS surfaces, within the confines of the evanescent field, is responsible for the wavelength shift. An exponential function is fitted over the inverse biomass versus wavelength shift (of biofilms on ETT sections). This function can be used to quantify biomass using the wavelength shift alone. Incorporating the LPG OFS instrumentation into ETTs may allow for real time, *in situ* and label-free biofilm monitoring on device surfaces, with high repeatability and sensitivity.

With the emergence of antimicrobial resistance as a major global health issue, emphasis lies on rapid, non-invasive and label-free identification of pathogenic bacteria species to reduce the overuse of broad spectrum antibiotics. Identification of unknown bacteria species, in single and co-cultures, would be a powerful resource in both healthcare and research settings. In the final part of this thesis, materials that differentially bind three bacteria species (*Pseudomonas aeruginosa*, *Staphylococcus aureus* and Uropathogenic *Escherichia coli*) are combined with LPG OFS for label-free species identification. Principle component analysis is used to identify three materials that differentially bind the three pathogenic species. Three LPG OFS, each coated in one of these materials, are exposed to single cultures of the three species for 24 hours. The wavelength shifts of attenuation bands are linear, with differing rates of change for each coated LPG OFS in each species, due to the differential attachment of bacteria to the materials. The differential wavelength shifts can be used to identify the three species from the spectral responses in 12 hours. Two of these coated LPG OFS can also be used to identify *P. aeruginosa* (PA) and Uropathogenic *E. coli* (UPEC) from a mixed bacteria co-culture, using the ratios of wavelength shift gradients of the two coated sensors over 24 hours. These sensors also quantify the amount of each species in a mixed biofilm, which is found to be 88:12 for PA:UPEC. These coated LPG OFS can be used for fast, non-invasive bacteria species identification, with potential applications in infection diagnostics and research into microbe populations.

Acknowledgements

After three years of excitement, frustration, laughs and fury, I would like to thank the incredible people who have helped me down this long, winding path that is my Ph.D. This thesis is not a product of individual work, but a combination of outstanding contributions by many of my colleagues. Firstly, I would like to express my gratitude to my supervisors; Professor Morgan Alexander, Professor Steve Morgan, Dr Andrew Hook and Dr Serhiy Korposh. Their help, guidance and support through regular meetings allowed the development and growth of this project.

I am thankful to the post-doctoral researchers; Dr Jean Dubern, Dr Peter Magennis, Dr David Scurr, Dr Long Jiang, Dr Laurence Burroughs, Dr Ricardo Correia and Dr Jiri Hromadka. Their assistance was much appreciated when learning new laboratory instruments/protocols and analysing data.

Dr Dan Harvey has been a constant source of clinical knowledge and direction, allowing the research to be carried out with the clinical impact in mind. His expertise on intensive care and medical devices is kindly acknowledged.

The work of the technical and administrative staff in the Boots Science Building and Centre for Biomolecular Sciences is especially acknowledged, who allow the smooth running of operations and maintain the safety of everybody working in these buildings. Colin, Paul, Tom, Christy, Tammy, Esme, Karen, Gail, Maria and Julia are recognised.

Office D20 in Boots Science Building has been my 'base' during my Ph.D. project. Many wonderful students have come and gone during my time there, all of whom have been a source of banter and scientific discussion. I have made many lifelong friends in D20, including TJ, Sunny, Adam, Toba, Robert, Alessandro, Mike, Stephen and Akmal.

This year, I was given the opportunity to travel to Riva del Garda, Italy, for the 5th International Conference on Bio-Sensing Technology. I would like to thank the organisers of the conference for allowing me to attend and present a

poster. Funding for the conference was obtained from the University of Nottingham's Graduate School Travel Prize, to whom I am grateful.

Special thanks to the University of Nottingham and the Engineering and Physical Sciences Research Council for funding my research and paying my salary for the last three years.

Finally, I would not have made it to this point in life without the support of my family and friends. My mother has always been my source of comfort, advice and motivation. My sister is my role model, who has shown where hard work and dedication can take you. I am incredibly grateful to both. My friends have been a welcome distraction from work at times and allow me to keep in touch with reality. I owe them a great deal of thanks too.

"Impossible is just a big word thrown around by small men

who find it easier to live in the world they've been given

than to explore the power they have to change it.

Impossible is not a fact, it's an opinion.

Impossible is not a declaration, it's a dare.

Impossible is potential. Impossible is temporary.

Impossible is nothing."

- Muhammad Ali
(1942-2016)

Table of contents

Abstract……i

Acknowledgements……iii

Table of contents……vi

List of figures……xiv

List of tables……xx

List of abbreviations……xxi

1. Introduction……1
    1.1. Endotracheal tubes (ETTs) ……3
        1.1.1. Structure and function of endotracheal tubes……3
        1.1.2. Endotracheal tube materials and manufacture……5
    1.2. Biofilm formation and bacterial colonisation of endotracheal tubes……6
        1.2.1. Overview of biofilms……6
        1.2.2. Biofilm life cycle……7
        1.2.3. Development of antimicrobial resistance within biofilms……9
        1.2.4. Bacterial colonisation of endotracheal tubes……9
    1.3. Ventilator-Associated Pneumonia (VAP)……11
        1.3.1. Causes, risk factors and symptoms of VAP……11
        1.3.2. Prevalence and mortality of VAP……13
        1.3.3. Microbiology of VAP……13
        1.3.4. Diagnosis of VAP……14
        1.3.5. Treatment of VAP……15
        1.3.6. Economic impact of VAP……16
    1.4. Clinical and experimental methods for reducing the incidence of VAP……17
        1.4.1. Current clinical best practice for VAP prevention……17
        1.4.2. Endotracheal tube modifications for VAP prevention……18
        1.4.3. Surface modifications to resist biofilm formation……20
            1.4.3.1. Antibiotic coatings……20
            1.4.3.2. Poly-sulfobetaine (zwitterionic polymer)……21

1.4.3.3. Slippery liquid infused porous surfaces (SLIPS)……..22
1.4.3.4. Poly (ethylene glycol) (PEG) and poly (ethylene oxide) (PEO)……..23
1.4.3.5. Micropatterned, nano-patterned and rough surfaces..24
1.4.3.6. High throughput microarray screening to identify bacteria resistant polymers……25
1.5. Optical fibre sensors for the real time detection of bacterial attachment……..28
1.5.1. Overview of optical fibres……28
1.5.2. Optical fibre sensors (OFS) ……29
1.5.3. Long Period Grating optical fibre sensors (LPG OFS)……31
1.5.4. LPG OFS for the real time monitoring of bacterial attachment and biofilm formation……33
1.6. Materials with bacteria selective binding properties for species identification……..36
1.6.1. Materials with bacteria selective binding properties……..37
1.6.2. LPG OFS for species identification……39
1.7. Aims……..41
2. Materials and methods……..42
2.1. Materials……42
2.2. Polymerisation techniques……43
2.2.1. Catalytic chain transfer (CCT) using a cobalt catalyst……..43
2.2.2. UV photopolymerisation using DMPA……..46
2.3. Use of a binary silane adhesion promoter……..48
2.4. Time-of-Flight Secondary Ion Mass Spectrometry (ToF SIMS)……50
2.5. 3D optical profiling……..55
2.6. Confocal laser scanning microscopy (CLSM)……..57
2.7. Quantification of biomass and mean biofilm thickness using COMSTAT……..61
2.8. Long Period Grating optical fibre sensors (LPG OFS) for the real time detection of bacterial attachment……63
2.8.1. LPG OFS experimental set up……63

2.8.2. Processing optical spectra and wavelength shift calculations…65
3. Development of an endotracheal tube coating resistant to bacterial biofilm formation……..68
3.1. Introduction……68
3.2. Aims……70
3.3. Experimental……71
3.3.1. Synthesis of EGDPEA:DEGMA……71
3.3.2. Dip coating……71
3.3.3. Revolution-to-delamination (RTD) assay……72
3.3.4. Time-of-Flight Secondary Ion Mass Spectrometry (ToF SIMS)…73
3.3.5. 3D optical profiling……73
3.3.6. Biofilm assays……74
3.3.7. CLSM of biofilms grown on ETT tubes and cuffs……75
3.3.8. Quantification of biomass and mean biofilm thickness using COMSTAT……75
3.4. Results……77
3.4.1. Synthesis of EGDPEA:DEGMA……77
3.4.2. Dip coating and coating thickness……77
3.4.3. Revolution-to-delamination (RTD) assay……79
3.4.4. ToF-SIMS of ETT sections……80
3.4.5. 3D optical profiles and roughness quantification……82
3.4.6. CLSM images of *P. aeruginosa* biofilms on ETT sections and quantification of biomass and mean biofilm thickness……83
3.4.6.1. Biofilm assay in RPMI-1640……83
3.4.6.2. Biofilm assay in ASM……85
3.4.6.3. Comparison of cell culture media……90
3.4.6.4. Extended biofilm culture……91
3.5. Discussion……93
3.5.1. Synthesis of EGDPEA:DEGMA……93
3.5.2. Dip coating and coating thickness……94
3.5.3. Revolution-to-delamination (RTD) assay……96
3.5.4. Biofilm assay……96

3.5.4.1. Effect of the four surface modifications on bacterial attachment……96
3.5.4.2. Differences between cell culture media……98
3.5.4.3. Biofilm fate after 24 hours……99
3.5.4.4. Biomass and mean biofilm thickness……100
3.5.5. Ion intensities and chemical maps obtained from ToF-SIMS…100
3.5.6. 3D optical profiles and roughness quantification……101
3.6. Conclusions……103
4. Long Period Grating optical fibre sensors for the real time monitoring of bacterial attachment and biofilm formation……104
4.1. Introduction……104
4.2. Aims……106
4.3. Experimental……107
4.3.1. Fabrication of LPG OFS……107
4.3.2. Dip coating of LPG OFS and estimation of coating thickness…107
4.3.3. Calibration of LPG OFS using sodium chloride solutions……108
4.3.4. LPG OFS in bacterial culture media……109
4.3.4.1. Spectral response in *P. aeruginosa* culture medium….109
4.3.4.2. Quantifying biomass of *P. aeruginosa* biofilms grown on optical fibres and relating biomass to wavelength shift……110
4.3.4.3. Estimation of sensor sensitivity to biomass……110
4.3.5. LPG OFS instrumentation for ETTs……111
4.3.5.1. Spectral response from LPG OFS incorporated into ETTs……111
4.3.5.2. Quantifying biomass of *P. aeruginosa* biofilms grown on ETTs and relating biomass to wavelength shift……112
4.4. Results……113
4.4.1. Estimated coating thickness on optical fibres and LPG OFS…..113
4.4.2. Calibration of LPG OFS using sodium chloride solutions……113
4.4.3. LPG OFS in bacteria culture medium……115
4.4.3.1. Spectral response in bacteria culture medium……115

4.4.3.2. CLSM images and quantified biomass of *P. aeruginosa* biofilms grown on optical fibres……116
4.4.3.3. Relationship between biomass and wavelength shift.118
4.4.4. LPG OFS response in bacteria culture medium from 24 to 72 hours……119
4.4.5. Sensitivity of LPG OFS to biomass……121
4.4.6. LPG OFS incorporated into ETTs……121
4.4.6.1. Response in RPMI-1640……121
4.4.6.2. Response in ASM G……124
4.4.6.3. Response in ASM N……127
4.4.6.4. Comparison of wavelength shift between the three bacteria culture media……130
4.5. Discussion……132
4.5.1. Coating thickness on optical fibres……132
4.5.2. Calibration of LPG OFS using sodium chloride solutions……132
4.5.3. LPG OFS in *P. aeruginosa* culture medium……134
4.5.4. Spectral response from 24 to 72 hours……138
4.5.5. Sensitivity of LPG OFS to biomass……138
4.5.6. LPG OFS as sensing instrumentation for ETTs……139
4.5.6.1. Spectral response from LPG OFS incorporated into ETT sections……139
4.5.6.2. Biomass of *P. aeruginosa* biofilms n ETTs……140
4.5.6.3. Relationship between biomass and wavelength shift.140
4.5.6.4. Spectral response in different culture media……142
4.5.7. Designing an instrumented ETT……142
4.6. Conclusions……144
5. Development of a bacteria species identification LPG optical fibre sensor using polymers with differential bacterial attachment……146
5.1. Introduction……146
5.2. Aims……148
5.3. Experimental……149

5.3.1. Identification of selective binding materials from microarray fluorescent intensity data……149
5.3.2. Photopolymerisation of selective binding materials……149
5.3.3. Exposure of photopolymerised spots to bacteria culture media, CLSM imaging of biofilms and quantification of biomass……150
5.3.4. Principal component analysis to identify materials with the greatest differential attachment……150
5.3.5. Upscaling of selective binding materials and dip coating of LPG OFS……151
5.3.6. Calibration of LPG OFS in sodium chloride solutions……152
5.3.7. LPG OFS coated with selective binding materials exposed to single bacteria culture media……153
5.3.8. LPG OFS coated with selective binding materials exposed to mixed bacteria co-cultures……153
5.3.8.1. Spectra collection……153
5.3.8.2. CLSM imaging of co-culture biofilms and biomass quantification……153
5.3.8.3. Relationship between wavelength shift and biomass in bacteria co-cultures……154
5.4. Results……156
5.4.1. Identification of materials with differential bacterial attachment……156
5.4.2. Biomass quantification of three species on nine selective materials……157
5.4.3. Principal component analysis of biomass data……158
5.4.3.1. Separation of species using principal components of biomass……158
5.4.3.2. PCA to identify one material selective for each species……160
5.4.4. GPC and ^{1}H NMR spectroscopy analysis of three selective binding materials……163
5.4.5. Coating thickness of the three materials on optical fibres……164

5.4.6. Calibration of LPG OFS in sodium chloride solutions……165
5.4.7. LPG OFS coated with selective binding materials in bacteria single cultures……166
5.4.7.1. Wavelength shifts for each selective material……166
5.4.7.2. Wavelength shifts for each bacteria species……168
5.4.8. LPG OFS coated with selective binding materials in bacteria co-culture……170
5.4.8.1. Wavelength shifts in bacteria co-culture……170
5.4.8.2. Biomass of *P. aeruginosa* and Uropathogenic *E. coli* biofilms from co-culture media……171
5.4.8.3. Wavelength shift comparison between single and co-cultures……173
5.4.8.4. Relationship between wavelength shift and biomass ratios from co-cultures……175
5.5. Discussion……177
5.5.1. Nine materials identified from microarray data……177
5.5.2. Biomass of the three species on the selective materials……177
5.5.3. PCA for identification of selective binding materials……178
5.5.4. Synthesis of three polymers and coating of LPG OFS……179
5.5.5. Calibration of LPG OFS in sodium chloride solutions……180
5.5.6. Selective material-coated LPG OFS in single bacterial culture media……181
5.5.7. Selective material-coated LPG OFS in bacteria co-cultures……184
5.6. Conclusions……188
6. Summary and future work……190
6.1. Summary……190
6.2. Recommendations for future work……193
7. Appendices……196
7.1. Appendix A. Procedure of processing optical spectra and calculating wavelength shift in OriginPro 8.6……196
7.2. Appendix B. Method of producing Artificial Sputum Medium (ASM).197
7.3. Appendix C. ^{1}H NMR spectra of EGDPEA:DEGMA……200

7.4. Appendix D. Negative mass spectra of U, C, PC and P tubes and cuffs, from ToF-SIMS. Ion intensity maps of acrylate, methacrylate, silicate and phthalate anions obtained from ToF-SIMS……202
7.5. Appendix E. 2D CLSM images of *P. aeruginosa* (PA01-N, mCherry) biofilms on ETT tubes and cuffs at 24, 48 and 72 hours……214
7.6. Appendix F. Exponential relationship between the inverse biomass of *P. aeruginosa* biofilms and the wavelength shift of peak 2, from LPG OFS in the PTFE well and LPG OFS-ETT systems, in all three culture media……220
7.7. Appendix G. 2D CLSM images of *P. aeruginosa* (PA01-N) biofilms, labelled with mCherry, grown on U and PC ETT tubes and cuffs, in RPMI-1640, ASM G and ASM N……222
7.8. Appendix H. Wavelength shifts of peak 2 for U and PC LPG OFS-ETT systems in RPMI-1640, ASM G and ASM N……225
7.9. Appendix I. MATLAB 2016a script used to determine 95% confidence ellipses for triplicate repeats of *P. aeruginosa*, *S. aureus* and Uropathogenic *E. coli* biomass on the nine photocured selective materials in the principle component score plot……226
7.10. Appendix J. 2D CLSM images of *P. aeruginosa*, *S. aureus* and Uropathogenic *E. coli* on the nine photopolymerised materials with bacteria species selectivity……227
7.11. Appendix K. ^{1}H NMR spectra of the three materials with bacteria species selectivity……230
7.12. Appendix L. Wavelength shifts of peak 2 from LPG OFS coated with the three selective binding materials exposed to single cultures of the three bacteria species in RPMI-1640 medium……235
8. References……237

List of figures

Figure 1.1. An endotracheal tube, highlighting the main functional parts and the Murphy eye; an endotracheal tube in use……4

Figure 1.2. The biofilm life cycle……8

Figure 1.3. Hook *et al.*'s combinatorial methods for high throughput screening of polymer microarrays……27

Figure 1.4. Optical fibre principle and the difference between single and multi-mode optical fibres……29

Figure 1.5. LPG optical fibre sensor principle and an example of a transmission spectrum……32

Figure 1.6. Principle of using LPG optical fibre sensors for the detection of bacterial attachment……35

Figure 2.1. Heat generated AIBN decomposition……43

Figure 2.2. Propagation steps in acrylate free radical polymerisation……44

Figure 2.3. General CCT reaction using a cobalt(II) catalyst……44

Figure 2.4. Summary of CCT polymerisation using a cobalt catalyst……45

Figure 2.5. Cobalt mediated CCT polymerisation of EGDPEA and DEGMA……46

Figure 2.6. Acrylate photopolymerisation using DMPA……47

Figure 2.7. Chemical structures of tetra-*n*-propyl silicate and tetra (2-methoxyethoxy) silane……48

Figure 2.8. Hydrolysis, condensation and bonding steps when using a binary silane primer……49

Figure 2.9. Primary ion bombardment of a surface in ToF-SIMS……50

Figure 2.10. Scheme of ToF-SIMS instrumentation……52

Figure 2.11. Workings of an optical profilometer……55

Figure 2.12. The principle of fluorescence……57

Figure 2.13. Confocal laser scanning microscopy principle……58

Figure 2.14. General set up of sensor apparatus, principle of optical spectrometers and a recorded transmission spectrum……64

Figure 2.15. Example of a pre- and post-processed optical spectrum……67

Figure 3.1. 1 cm^2 sections of ETT tubes and cuffs, with the four surface modifications……78

Figure 3.2. RTD observed for ETT cross sections……80

Figure 3.3. Ion intensities of four secondary ions ejected from ETT surfaces measured by ToF-SIMS……81

Figure 3.4. Optical profiles of ETT sections and quantified mean square roughness……82

Figure 3.5. 2D CLSM images and quantified biomass/mean thickness of *P. aeruginosa* biofilms grown on ETT sections in RPMI-1640……..84

Figure 3.6. 2D CLSM images and quantified biomass/mean thickness of *P. aeruginosa* biofilms grown on ETT sections in ASM G……86

Figure 3.7. 2D CLSM images and quantified biomass/mean thickness of *P. aeruginosa* biofilms grown on ETT sections in ASM N……88

Figure 3.8. Comparison of biomass and mean biofilm thickness between RPMI-1640, ASM G and ASM N……90

Figure 3.9. *P. aeruginosa* biomass and mean biofilm thickness at 24, 48 and 72 hours, in RPMI-1640……..92

Figure 4.1. The PTFE well used for LPG OFS spectra collection……..109

Figure 4.2. LPG OFS fixed into the lumen of a section of ETT tube and cuff……112

Figure 4.3. Processed transmission spectra in water for the uncoated and primed and coated LPG OFS……..113

Figure 4.4. Wavelength shifts for attenuation peaks 1 and 2 with increasing concentration of sodium chloride in water……114

Figure 4.5. Wavelength shift change over time for both attenuation peaks of LPG OFS immersed in *P. aeruginosa* culture medium in RPMI-1640, for 24 hours……115

Figure 4.6. *Z*-stack CLSM images and quantified biomass of *P. aeruginosa* biofilms grown on uncoated and primed and coated optical fibres in RPMI-1640……..117

Figure 4.7. Exponential relationship between biomass and peak 1 wavelength shift, for *P. aeruginosa* grown on optical fibres in RPMI-1640……118

Figure 4.8. Wavelength shifts of both attenuation peaks from 24 to 72 hours, for LPG OFS immersed in *P. aeruginosa* culture in RPMI-1640……..119

Figure 4.9. *Z*-stack CLSM images and quantified biomass of *P. aeruginosa* biofilms grown on uncoated and pried and coated optical fibres in RPMI-1640 between 24 and 72 hours……120

Figure 4.10. Wavelength shifts for both attenuation peaks of LPG OFS incorporated into ETT tubes and onto cuffs, immersed in *P. aeruginosa* culture medium in RPMI-1640 for 24 hours……122

Figure 4.11. Biomass increase of *P. aeruginosa* biofilms grown on tubes and cuffs, in RPMI-1640……123

Figure 4.12. Exponential relationship between biomass and peak 1 wavelength shift, for *P. aeruginosa* grown on ETT tubes and cuffs in RPMI-1640……124

Figure 4.13. Wavelength shifts for both attenuation peaks of LPG OFS incorporated into ETT tubes and onto cuffs, immersed in *P. aeruginosa* culture medium in ASM G for 24 hours……125

Figure 4.14. Biomass increase of *P. aeruginosa* biofilms grown on tubes and cuffs, in ASM G……126

Figure 4.15. Exponential relationship between biomass and peak 1 wavelength shift, for *P. aeruginosa* grown on ETT tubes and cuffs in ASM G……127

Figure 4.16. Wavelength shifts for both attenuation peaks of LPG OFS incorporated into ETT tubes and onto cuffs, immersed in *P. aeruginosa* culture medium in ASM N for 24 hours……128

Figure 4.17. Biomass increase of *P. aeruginosa* biofilms grown on tubes and cuffs, in ASM N……129

Figure 4.18. Exponential relationship between biomass and peak 1 wavelength shift, for *P. aeruginosa* grown on ETT tubes and cuffs in ASM N……130

Figure 4.19. Wavelength shift profiles of attenuation peak 1 from LPG OFS-ETT systems exposed to *P. aeruginosa* culture in RPMI-1640, ASM G and ASM N for 24 hours……131

Figure 4.20. Schematic of LPG OFS instrumentation incorporated into an ETT lumen, working in reflection mode……143

Figure 5.1. Nine materials with bacteria species selectivity……157

Figure 5.2. Biomass of the three bacteria species' biofilms on the nine photopolymerised materials with selective binding properties……158

Figure 5.3. Score plot of PCs 1 and 2 for biomass of the three bacteria species on the nine photopolymerised materials, with 95% confidence ellipses……159

Figure 5.4. Biplot of principle component loadings for the nine selective materials laid over the principal component scores of the three bacteria species……160

Figure 5.5. Score plot of PCs 1 and 2 for biomass of the three bacteria species on the three selected materials with differential bacterial attachment, with 95% confidence ellipses……162

Figure 5.6. Processed transmission spectra from the uncoated and the three selective material coated LPG OFS in water……165

Figure 5.7. Wavelength shifts of both attenuation peaks from all four LPG OFS in sodium chloride solutions of increasing concentration……166

Figure 5.8. Wavelength shifts of peak 1 from each of the four modified LPG OFS immersed in single cultures of the three bacteria species in RPMI-1640 medium for 24 hours……..167

Figure 5.9. Wavelength shifts of peak 1 from the four modified LPG OFS exposed to single cultures of the three bacteria species in RPMI-1640 medium for 24 hours……..169

Figure 5.10. Wavelength shifts of both attenuation peaks from pPGMEA and EOEA coated LPG OFS exposed to a *P. aeruginosa* and Uropathogenic *E. coli* co-culture for 24 hours……170

Figure 5.11. *Z*-stack CLSM images and quantified biomass of PA and UPEC mixed biofilms grown on pPGMEA and EOEA coated optical fibres……172

Figure 5.12. Comparison of wavelength shifts of both attenuation peaks, from pPGMEA and EOEA coated LPG OFS, for PA and UPEC single cultures and the co-culture of the two species in RPMI-1640 medium……..174

Figure 7.1. Procedure of processing optical spectra and calculating wavelength shift in OriginPro 8.6……196

Figure 7.2. ^{1}H NMR spectrum of EGDPEA monomer……200

Figure 7.3. ^{1}H NMR spectrum of DEGMA monomer……200

Figure 7.4. ^{1}H NMR spectrum of EGDPEA:DEGMA crude mix (before precipitation)……201

Figure 7.5. ^{1}H NMR spectrum of EGDPEA:DEGMA polymer (after precipitation)……201

Figure 7.6. Negative mass spectra of uncoated ETT tubes, obtained from ToF-SIMS……202

Figure 7.7. Negative mass spectra of coated ETT tubes, obtained from ToF-SIMS……203

Figure 7.8. Negative mass spectra of primed and coated ETT tubes, obtained from ToF-SIMS……204

Figure 7.9. Negative mass spectra of primed only ETT tubes, obtained from ToF-SIMS……205

Figure 7.10. Negative mass spectra of uncoated ETT cuffs, obtained from ToF-SIMS……206

Figure 7.11. Negative mass spectra of coated ETT cuffs, obtained from ToF-SIMS……..207

Figure 7.12. Negative mass spectra of primed and coated ETT cuffs, obtained from ToF-SIMS……208

Figure 7.13. Negative mass spectra of primed only ETT cuffs, obtained from ToF-SIMS……209

Figure 7.14. 2D CLSM images of *P. aeruginosa* biofilms on uncoated, polymer coated, primed and coated and primed only ETT tubes, at 24, 48 and 72 hours, in RPMI-1640……..214

Figure 7.15. 2D CLSM images of *P. aeruginosa* biofilms on uncoated, polymer coated, primed and coated and primed only ETT cuffs, at 24, 48 and 72 hours, in RPMI-1640……..215

Figure 7.16. 2D CLSM images of *P. aeruginosa* biofilms on uncoated, polymer coated, primed and coated and primed only ETT tubes, at 24, 48 and 72 hours, in ASM G……216

Figure 7.17. 2D CLSM images of *P. aeruginosa* biofilms on uncoated, polymer coated, primed and coated and primed only ETT cuffs, at 24, 48 and 72 hours, in ASM G……217

Figure 7.18. 2D CLSM images of *P. aeruginosa* biofilms on uncoated, polymer coated, primed and coated and primed only ETT tubes, at 24, 48 and 72 hours, in ASM N……218

Figure 7.19. 2D CLSM images of *P. aeruginosa* biofilms on uncoated, polymer coated, primed and coated and primed only ETT cuffs, at 24, 48 and 72 hours, in ASM N……219

Figure 7.20. Exponential relationship between biomass and peak 2 wavelength shift, for *P. aeruginosa* grown on optical fibres in RPMI-1640……220

Figure 7.21. Exponential relationship between biomass and peak 2 wavelength shift, for *P. aeruginosa* grown on ETT tubes and cuffs in RPMI-1640……..220

Figure 7.22. Exponential relationship between biomass and peak 2 wavelength shift, for *P. aeruginosa* grown on ETT tubes and cuffs in ASM G……221

Figure 7.23. Exponential relationship between biomass and peak 2 wavelength shift, for *P. aeruginosa* grown on ETT tubes and cuffs in ASM N……221

Figure 7.24. 2D CLSM images of *P. aeruginosa* biofilms on U and PC ETT tubes and cuffs in RPMI-1640, taken at 6 hour intervals for 24 hours……222

Figure 7.25. 2D CLSM images of *P. aeruginosa* biofilms on U and PC ETT tubes and cuffs in ASM G, taken at 6 hour intervals for 24 hours……223

Figure 7.26. 2D CLSM images of *P. aeruginosa* biofilms on U and PC ETT tubes and cuffs in ASM N, taken at 6 hour intervals for 24 hours……224

Figure 7.27. Wavelength shift profiles of attenuation peak 2 from LPG OFS-ETT systems exposed to *P. aeruginosa* culture in RPMI-1640, ASM G and ASM N for 24 hours……225

Figure 7.28. 2D CLSM images of *P. aeruginosa* biofilms on the nine photocured polymer spots, after a 24 hour incubation……227

Figure 7.29. 2D CLSM images of *S. aureus* biofilms, labelled with mCherry, on the nine photocured polymer spots, after a 24 hour incubation……228

Figure 7.30. 2D CLSM images of Uropathogenic *E. coli*. biofilms, labelled with mCherry, on the nine photocured polymer spots, after a 24 hour incubation……229

Figure 7.31. ^{1}H NMR spectrum of pPGMEA monomer……230

Figure 7.32. ^{1}H NMR spectrum of pPGMEA crude mix (before precipitation).230

Figure 7.33. ^{1}H NMR spectrum of pPGMEA polymer (after precipitation)…….231

Figure 7.34. ^{1}H NMR spectrum of HEOdA monomer……231

Figure 7.35. ^{1}H NMR spectrum of HEOdA crude mix (before precipitation)….232

Figure 7.36. ^{1}H NMR spectrum of HEOdA polymer (after precipitation)…….232

Figure 7.37. ^{1}H NMR spectrum of EOEA monomer……233

Figure 7.38. ^{1}H NMR spectrum of EOEA crude mix (before precipitation)…….233

Figure 7.39. ^{1}H NMR spectrum of EOEA polymer (after precipitation)……234

Figure 7.40. Wavelength shifts of peak 2 from each of the four modified LPG OFS immersed in single cultures of the three bacteria species in RPMI-1640 medium for 24 hours……235

Figure 7.41. Wavelength shifts of peak 2 from each of the four modified LPG OFS immersed in single cultures of the three bacteria species in RPMI-1640 medium for 24 hours……236

List of tables

Table 1.1. Risk factors for VAP……12

Table 2.1. Details of plasmids, fluorophores/dyes, excitation wavelengths and emission wavelengths for the bacterial strains used in this thesis……60

Table 3.1. Yield by weight, molecular weight, polydispersity index, monomer conversion and feed monomer ratio of synthesised EGDPEA:DEGMA……77

Table 3.2. Average weight gain and coating thickness of EGDPEA:DEGMA coatings on ETT sections……79

Table 3.3. Mean percentage reduction in biomass and mean thickness on C and PC ETT tubes and cuffs, relative to U substrates, for *P. aeruginosa* (PA01-N) biofilms grown in RPMI-1640……..85

Table 3.4. Mean percentage reduction in biomass and mean thickness on C and PC ETT tubes and cuffs, relative to U substrates, for *P. aeruginosa* (PA01-N) biofilms grown in ASM G……87

Table 3.5. Mean percentage reduction in biomass and mean thickness on C and PC ETT tubes and cuffs, relative to U substrates, for *P. aeruginosa* (PA01-N) biofilms grown in ASM N……89

Table 5.1. Selective binding materials' species separation, based on the materials' component loadings……..161

Table 5.2. Yield by weight, molecular weights, polydispersity and monomer conversion of the three materials with bacteria species selectivity……..163

Table 5.3. Density of each selective material, the average weight gain of one hundred 3 cm lengths of coated optical fibres and the average coating thickness of each material on optical fibres……..164

Table 5.4. Ratios of wavelength shift gradients (rates of change) between pPGMEA and EOEA coated LPG OFS in single and co-cultures of PA and UPEC……175

Table 5.5. Ratios of 24 hour biomass between pPGMEA and EOEA photopolymerised spots in single and co-cultures of PA and UPEC……176

List of abbreviations

^{1}H NMR	Proton nuclear magnetic resonance (spectroscopy)
AIBN	2,2'-Azobis(2-methylpropionitrile)
ARDS	Acute Respiratory Distress Syndrome
ASM G	Artificial Sputum Medium with glucose
ASM N	Artificial Sputum Medium without glucose
AU	Airy Units
C (sample)	Coated (sample)
CCD	Charge-coupled device
CCT	Catalytic chain transfer
CDC	Centers for Disease Control
CFU	Colony forming units
CI	Confidence interval
CLSM	Confocal laser scanning microscopy
COPD	Chronic Obstructive Pulmonary Disease
CPIS	Clinical Pulmonary Infection Score
DCM	Dichloromethane
DEGMA	Di (ethylene glycol) methyl ether methacrylate
DEHP	Di-(ethylhexyl) phthalate
dMAmEA	Dimethylamino-ethyl acrylate
DMPA	2,2'-dimethoxy-2-phenylacetophenone
EGdA	Ethylene glycol diacrylate
EGDPEA	Ethylene glycol dicyclopentenyl ether acrylate
EOEA	Ethoxyethyl acrylate
EPS	Extra Polymeric Substances
ETT	Endotracheal tube
FBG	Fiber-Bragg Grating
GA	Glycidyl acrylate
GFP	Green Fluorescent Protein
GPC	Gel permeation chromatography
HEOdA	Hexanediol ethoxylate diacrylate
ICP	Intracranial pressure
ICU	Intensive Care Unit
iOA	Isooctyl acrylate
LB	Luria-Bertani
LPG	Long Period Grating
MOPS	3-(N-morpholino) propanesulfonic acid
MRSA	Methicillin Resistant *Staphylococcus aureus*
N	Experimental repeats from separate experiments on different days
n	Experimental repeats from a single experiment on the same day
NA	Numerical aperture
Ng:YAG	Neodymium-doped yttrium aluminium garnet
NIPPV	Non-invasive positive pressure ventilation
NNIS	National nosocomial infection surveillance
nPGPOdA	Neopentyl glycol propoxylate diacrylate

OD_{600}	Optical density at 600 nm
OFS	Optical fibre sensor
OR	Odds Ratio
P (sample)	Primed only (sample)
PA	*Pseudomonas aeruginosa*
PBP	Penicillin-binding protein
PBS	Phosphate-buffered saline
PC (sample)	Primed and coated (sample)
PC1	Principal component 1
PC2	Principal component 2
PCA	Principal component analysis
PDMS	Polydimethylsiloxane
PEG	Poly (ethylene glycol)
PEO	Poly (ethylene oxide)
pGA	Poly (glycidyl acrylate)
PhCobF	Bis[(difluoroboryl)diphenylglyoximato] cobalt(II)
PIA	Polysaccharide intercellular antigen
PMTP	Phase matching turning point
PolySB	Poly-sulfobetaine
pPGMEA	Poly (propylene glycol) methyl ether acrylate
PS	Polystyrene
PTFE	Polytetrafluoroethylene
PVC	Polyvinyl chloride
RIU	Refractive Index Unit
ROI	Region of interest
RR	Relative Risk
RTD	Revolution-to-delamination
SA	*Staphylococcus aureus*
SD	Standard deviation
SLIPS	Slippery liquid-infused porous surfaces
SMA	SubMiniature version A
ToF-SIMS	Time of Flight Secondary Ion Mass Spectrometry
ttriMSiOSiPMA	Tris(trimethylsilyloxy)-silyl propyl methacrylate
U (sample)	Uncoated (sample)
UPEC	Uropathogenic *Escherichia coli*
UTI	Urinary tract infection
VAP	Ventilator-Associated Pneumonia
WCA	Water contact angle
ZIF-8	Zeolitic imidazolate frameworks

1. Introduction

Ventilator-Associated Pneumonia (VAP) is the most common nosocomial infection associated with endotracheal tube (ETT) use [1]. It has a mortality rate of up to 50% [2], often due to antimicrobial resistance developing amongst the causative microorganisms. As a result, the resource and economic burden on healthcare services is immense. VAP is thought to arise from biofilm formation on ETT surfaces during use [3]. Unfortunately, current clinical best practice measures are inadequate for reducing biofilm formation on breathing tubes. The emergence of antimicrobial resistance requires research into prevention of bacterial attachment and biofilm formation on ETTs and other medical devices, in turn preventing secondary infections. Hence, this thesis begins with the investigation of a novel polymer (discovered during a high throughput microarray screening study) as a bacteria resistant coating for ETTs. Its effect is investigated on both device tubes and cuffs.

There is currently no method to measure biofilm formation on ETTs *in situ* and in real time. If bacterial contamination of a device is suspected, it is removed for microbiological examination. This is a time consuming process and can be damaging to the patient. Therefore, this thesis presents work looking into Long Period Grating optical fibre sensors (LPG OFS) as a novel tool for monitoring bacterial attachment and biofilm formation in real time. Optical fibres are primarily used for telecommunication purposes; modifying them to sense refractive index change of the surrounding medium allows them to sensitively detect analytes [4]. A biofilm forming on the surface of an optical fibre sensor provides its own refractive index source, which is measurable by using LPG OFS. Sensors are also incorporated into ETTs to investigate the possibility of *in situ*, real time and label-free monitoring of device biofouling, which allows the interception of ETT-centred infection.

The overuse of broad spectrum antibiotics has led to the rapid rise of antimicrobial resistant infections, causing significant morbidity and mortality in both the community and in hospital [5]. Accurate identification of pathogenic

bacteria species is key, as it enables tailored antibiotic regimens to be administered, reducing broad spectrum antibiotic use. To conclude this thesis, LPG OFS coupled with polymers that differentially bind different bacteria species are trialled for identification of those bacteria species. Using these polymers can modify sensors to give differential spectral responses based on the differential attachment of bacteria species, with the aim of identifying unknown cultures of pathogenic bacteria. The ability to identify individual species from a mixed bacteria co-culture is an exciting proposition, for both healthcare and research purposes, and may lead to the invention of an inexpensive and rapid diagnostic device.

1.1. Endotracheal tubes (ETTs)

1.1.1. Structure and function of endotracheal tubes

ETTs are medical devices used to mechanically ventilate patients who are unable to breathe unaided, such as those in cardiorespiratory arrest or those with severe head and neck trauma [6]. They are commonplace in intensive care units (ICUs) and on the scenes of medical emergencies, with approximately 136,000 patients mechanically ventilated in the UK in 2012 [7].

ETTs have two distinct functional parts; the tube (or main body) and the cuff. The tube allows air flow from the ventilator pump into the patient's lungs. The cuff is an inflatable sack, which provides a seal that prevents aspiration of gastric contents and reduced air leakage during positive pressure ventilation [8]. The cuff is filled with air from a syringe via a pilot tube, which at its end contains a pilot balloon with a one-way valve. The device is passed down the trachea, before the cuff is inflated (Figure 1.1). Once in place, the ETT is connected to the mechanical ventilator. At the end of the device inserted into the trachea, there is another orifice on the side of the tube, called the Murphy eye. This exists as an emergency orifice, allowing ventilation in case of a blockage occurring in the main exit [9].

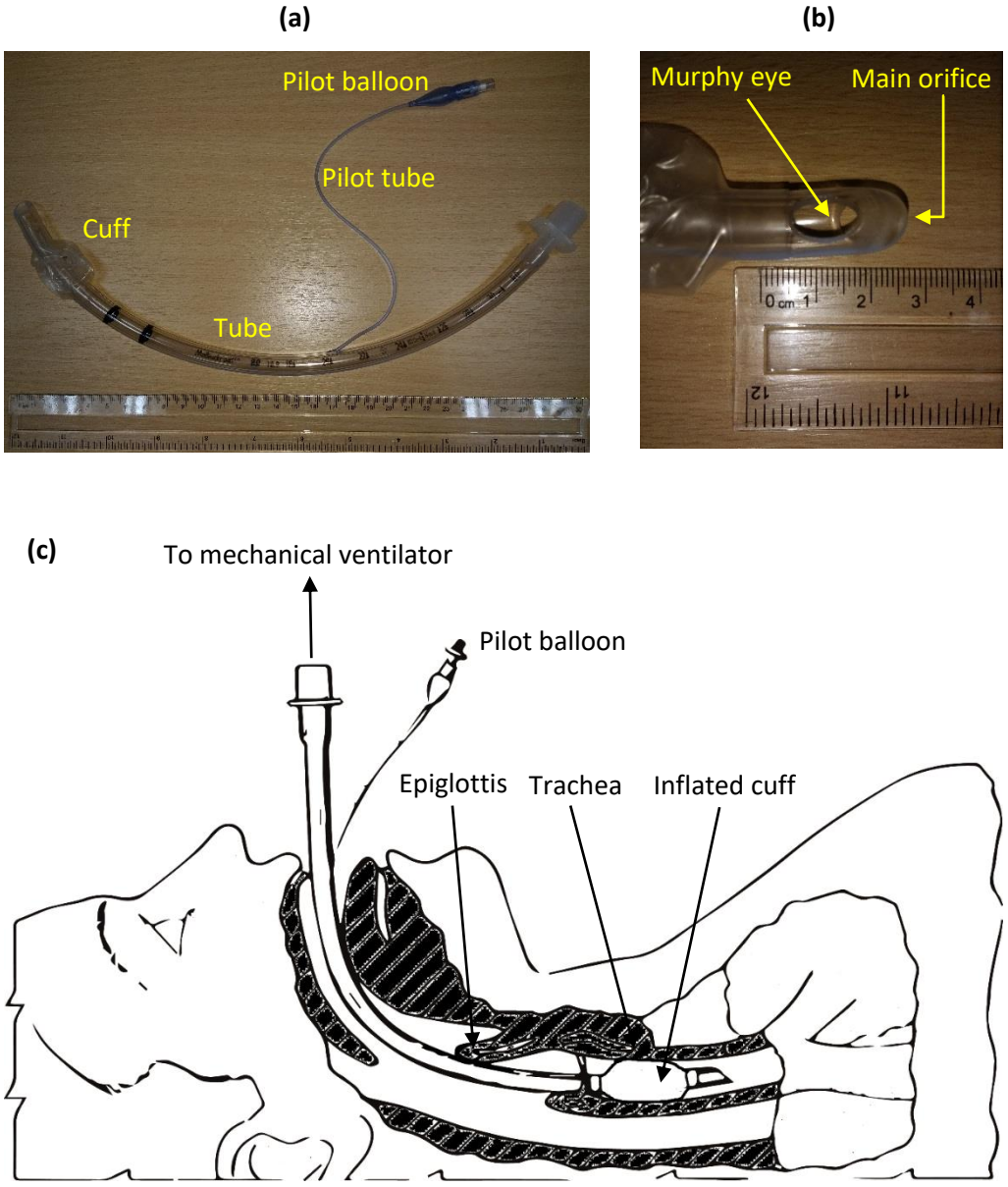


Figure 1.1. (a) An adult endotracheal tube, with the main functional parts highlighted. **(b)** The position of the Murphy eye in comparison to the main orifice. **(c)** An endotracheal tube in use, showing the inflated cuff in the trachea.

ETTs come in several sizes, with paediatric and veterinary devices available. The length of time that a patient is intubated for varies depending on the severity of their injury or the nature of the emergency. Patients can be ventilated from as little as a few hours to over ten days [10,11].

1.1.2. Endotracheal tube materials and manufacture

ETTs are largely made of polyvinyl chloride (PVC) [12,13]. This is due to its durability, thermoresponsive flexibility and chemical inertness. It has also been shown to not pose any toxicological threat to intubated patients. Both the tube and cuff are manufactured from PVC. The main body is most commonly fabricated using the hot melt extrusion process [14], whereby the material is subjected to high temperature and pressure in order to melt it, then forced through an orifice in a continuous process and cleaved once the desired length of tubing is achieved [15].

Manufacturing of the cuff is done separately, using a method known as cold parison blow moulding (Patent US 4130617 A, Method of making endotracheal tube cuffs, Dean R. Wallace, Published Dec 19 1978). The tube is placed in a vented hollow mould and one end stretched along the longitudinal axis whilst under high pressure. Heating that end of the tube softens it and allows it to expand into a cuff. In order for the cuff to maintain its elasticity, a plasticiser is added. The most common plasticiser used in ETTs is di-(2-ethylhexyl) phthalate (DEHP) [16,17]. The final product is vacuum wrapped to prevent contamination in transit.

1.2. Biofilm formation and bacterial colonisation of endotracheal tubes

Bacterial attachment and biofilm formation on ETT surfaces can cause Ventilator-Associated Pneumonia (VAP) [1,3], which is classed as a secondary, nosocomial pulmonary infection [3]. The interaction of bacterial cells with ETT surfaces is complex and cell-surface interactions are yet to be fully understood. Resisting attachment and subsequent biofilm formation to ETT surfaces is critical in reducing VAP risk.

1.2.1. Overview of biofilms

Biofilm formation is a survival tactic employed by microorganisms in response to adverse conditions. A biofilm can be described as an aggregation of microorganisms adhered to a surface, encased in a glycocalyx, also known as the Extracellular Polymeric Substances (EPS) layer [18,19]. This 'slimy' layer serves to protect the adhered microorganisms from environmental stressors and antimicrobials. Bacteria within biofilms are up to one thousand times more resistant to antimicrobials and the host's immune system than planktonic cells alone [20,21].

Within a bacterial biofilm, the EPS layer contains polysaccharides (such as alginate), proteins (such as albumin), DNA and other components [22]. These components allow the biofilm to remain hydrated, while simultaneously restricting access of external stressors. The exact content of the EPS layer varies from species to species; for example, biofilms of *Pseudomonas aeruginosa* contain at least three polysaccharides (alginate, Pel and Psl) in their EPS [23], whereas *Staphylococcus aureus* EPS layers contain teichoic acids and polysaccharide intercellular antigen (PIA), amongst other components [24]. Biofilms can form on numerous surfaces, where they can pose major problems in industry and healthcare. Such surfaces include living tissues, medical devices, foodstuffs and aquatic systems [19,25].

Biofilms are a significant healthcare problem, as they are known to facilitate bacterial infection [26]. Up to 80% of all infections are attributed to biofilms present in the body [27]. Examples of biofilm-related infections are otitis media, endocarditis and urinary tract infections (UTIs) [26]. Indwelling device-associated infections are caused by bacterial colonisation and biofilm formation on medical device surfaces [28,29]. For example, bacterial colonisation of central venous catheters and endotracheal tubes can lead to severe blood infections and VAP respectively, [1,30,31]. Device-associated infections can be difficult to treat, since bacteria within a biofilm population can develop antimicrobial resistance [32,33]. As a result, prevention of biofilm formation, particularly on medical devices, has been rigorously investigated to reduce infection incidence. In designing biofilm preventative techniques, the process of cell attachment and the biofilm life cycle must first be appreciated.

1.2.2. Biofilm life cycle

The general life cycle of bacterial biofilms is thought to be a five step process [34] (Figure 1.2); (i) reversible attachment, (ii) irreversible attachment, (iii) early maturation, (iv) late maturation and (v) dispersion. The first step involves bacteria reversibly adhering to a surface via weak electrostatic interactions, such as van der Waals forces, hydrogen bonding, or hydrophobic interactions [35,36]. These weak interactions are then converted to stronger, irreversible forces so that the cells are immobilised on the surface. To do so, bacteria use membrane bound structures, such as pili, which at their termini contain adhesion molecules, allowing for irreversible attachment [37]. Pili are hair-like extensions of varying dimensions (typically shorter than 5 μm and under 7 nm in diameter [38,39]). They are made of proteins of varying peptide chain length and amino acids. Different pili types have been identified and bacteria can selectively express certain types (amongst others), such as Type I pili on *E. coli* and Type IV pili on *P. aeruginosa* [39]. Pili can be specific to certain surfaces or host cell membrane proteins, due to their differing peptide makeup. For

example, the P pilus expressed by Uropathogenic *E. coli* (UPEC) allows attachment to GbO3, a protein found on human uroepithelial cells [39,40].

Once adhered, bacteria within the microcolony begin to excrete EPS, forming an EPS-encased microcolony, during the early maturation phase. If conditions continue to favour biofilm formation, i.e. the presence of antimicrobials or extremes of temperature/pH, further cell growth and EPS excretion occurs, resulting in a mature biofilm, termed late maturation. Further growth can lead to cells dispersing from the biofilm to the surrounding areas. Dispersion can occur by bacteria actively exiting the biofilm, or by shear stresses (caused by flow) acting on the biofilm exterior [19,41]. Cells released from the biofilm can go on to colonise other surfaces, repeating the biofilm life cycle, in turn spreading contamination and infection. The time taken to complete this life cycle depends on the microorganisms involved, the conditions and the surface, and can range from a few hours to several days [42].

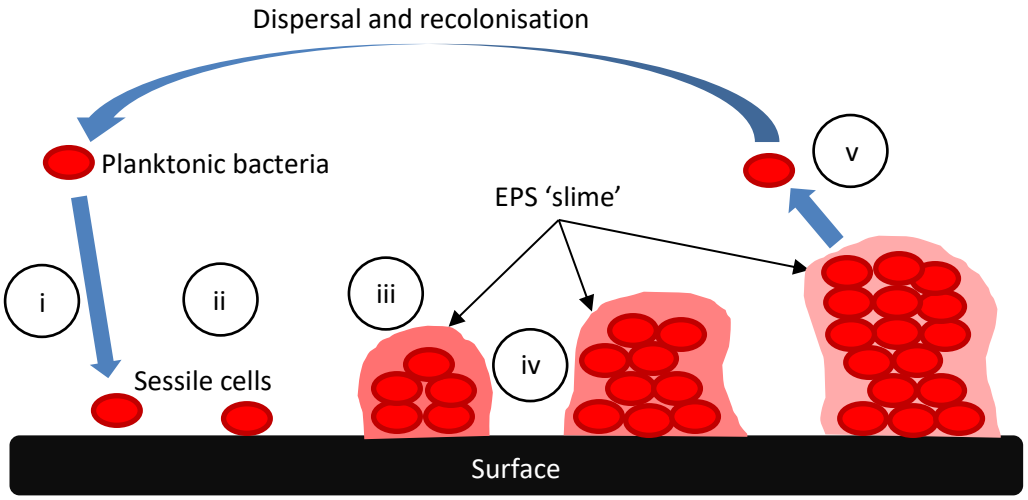


Figure 1.2. The biofilm life cycle, indicating the five stages of the cycle. (i) reversible attachment, (ii) irreversible attachment, (iii) early maturation, (iv) late maturation, (v) dispersion.

1.2.3. Development of antimicrobial resistance within biofilms

During maturation and growth, biofilms can facilitate the development of antimicrobial resistance within the bacteria population [33]. Cells in a biofilm have been shown to upregulate certain genes responsible for antibiotic resistance [43], caused by exposure to low doses of antimicrobials inducing a 'survival' or 'SOS' response in cells [44]. The high density of bacterial cells within a biofilm allows any genetic adaptation to be spread throughout the population [45]. Plasmids (extrachromosomal genetic material) are used as gene vectors, allowing antibiotic resistance genes to be passed on to other cells [46]. Plasmids are exchanged between gram-negative cells via sex (F) pili [47].

Pseudomonas aeruginosa has been shown to spread resistance via this method, using cell-to-cell signalling to spread a range of virulence factors and resistance genes, such as the LasR-*lasB* system [48]. Utilising this system can rapidly result in an antimicrobial resistant population. Infections caused by resistant bacteria are notoriously difficult to treat, such as those associated with cystic fibrosis sufferers [49,50].

1.2.4. Bacterial colonisation of endotracheal tubes

Bacteria can adhere to PVC and form biofilms [51]. Hence, bacterial colonisation on ETT surfaces is routinely observed in healthcare and laboratory settings [52]. One study reported at least 50 mg (dry weight) of biofilm present on 30 out of 40 ETTs used to intubate intensive care patients for between 2 hours and 10 days [53].

Bacteria that colonise ETTs are thought to originate from both the ventilator apparatus and connecting tubes [53] and/or the intubated patient's own microflora, particularly from gastro-oesophageal secretions [54]. Bacteria come into contact with ETT surfaces during use via microaspiration, resulting in the pooling of secretions on the device [55]. These secretions, in the form of small droplets, act as bacteria cell 'reservoirs', allowing bacteria to attach to

device surfaces and form biofilms. This process can occur on both tubes and cuffs [53,55], the latter of which can contain small folds in its wall, even when fully inflated [12], further enabling pooling of bacteria-containing fluids. Cells which disperse from biofilms on ETTs can fall into the lower airway, resulting in nosocomial pulmonary infections, such as VAP [56].

1.3. Ventilator-Associated Pneumonia (VAP)

1.3.1. Causes, risk factors and symptoms of VAP

VAP refers to the secondary pulmonary infection affecting patients who undergo tracheal intubation. VAP is caused by bacterial contamination and biofilm formation on ETTs [1,3]. Dispersion of microorganisms from biofilms leads to the spread of infection in the lower airways [56,57]. VAP is the second most common nosocomial infection in ICUs and the most common in mechanically ventilated patients [58].

VAP occurs 48 hours or more after intubation [59,60], with the risk being greatest within the first five days [2]. The length of intubation is a defining risk factor for VAP, with a 3% per day risk for the first 5-7 days, a 2% per day risk up to 10-14 days, which drops off to 1% per day thereafter [2,61].

Patient-related risk factors are numerous, with pre-existing pulmonary illness, coma and organ failure posing the highest risk. Antacid use [62] and enteral nutrition [63] are also known risk factors. Table 1.1 summarises the risk factors for VAP.

Risk factor class, type	OR (95% CI)
Nonmodifiable risk factors	
Patient-related risk factors	
COPD	1.9 (1.4 - 2.6)
	18.3 (3.8 - 89.8)
Organ System Failure Index of > 2	10.2 (4.5 - 23)
Age of > 60 years	5.1 (1.9 - 14.1)
Coma	40.3 (3.3 - 423.1)
ARDS	9.7 (1.6 - 59.2)
Head trauma	5.2 (0.9 - 30.3)
Male sex	2 (1.5 - 2.7)
Intervention-related risk factor	
Neurosurgery	10 (1.6 - 64.9)[a]
Thoracic surgery	2.16
ICP monitor	4.2 (1.7 - 10.5)
Transportation out of ICU	3.8 (2.8 - 5.5)
Reintubation	5.94 (1.27 - 22.71)
Modifiable risk factors	
Intervention-related risk factor	
Use of H_2-antagonist	2.5 (1.2 - 5)
	2.33
Use of antacids	20
Use of sucralfate	3.44
24h circuit changes, compared with 48h circuit changes	2.3 (1.2 – 4.7)
Use of antibiotics	3.1 (1.4 – 6.9)
	2.3
	0.1 (0.01 – 0.7)
Supine position	2.9 (1.3 – 6.6)
Receipt of enteral nutrition	31.2 (3.3 – 294.8)
Failed subglottic aspiration	5.3 (1.2 – 22.6)
Intracuff pressure < 20 cm H_2O	4.2 (1.1 – 15.9)
Tracheostomy	3.1 (2.2 – 4.5)
Aerosol treatment	1.9 (1.4 – 2.5)

Table 1.1. Risk factors for VAP. OR = odds ratio, CI = confidence interval, ARDS = acute respiratory distress syndrome, COPD = chronic obstructive pulmonary disease, ICP = intracranial pressure, ICU = intensive care unit. [a]Only associated with increased risk for VAP caused by *Acinetobacter baumanii* [60].

Symptoms of VAP are typical of the pneumonias, with extremes of body temperature (<36°C or >39°C), purulent bronchial secretions, leucocytosis/leukopenia, extreme fatigue, muscle pain and breathing difficulties commonly observed [2].

1.3.2. Prevalence and mortality of VAP

VAP affects 8-20% of ICU patients [64] and up to 27% of mechanically ventilated patients [1,2,64]. Between 50% [2] and 86% [1] of all hospital-acquired pneumonias are attributed to tracheal intubation. In the United States, 250,000 to 300,000 cases of VAP occur every year [1], which equates to incidence rates of 5 to 10 cases per 1000 hospital admissions. In England, Wales and Northern Ireland, 69,606 patients were mechanically ventilated in 2012 [65]. Applying the statistics to this figure gives 18,794 cases of VAP, which is 83 cases of VAP for every critical care unit.

Nosocomial infections have notoriously high mortality rates, due to the multiple patient risk factors, immunocompromised patients and microorganisms developing antibiotic resistance. The mortality rate associated with VAP varies depending on bacteria species and the patient's overall health [66] and has been recorded from 0-50% [67-69]. A 50% mortality rate equates to over 9500 deaths in England, Wales and Northern Ireland and over 40,000 deaths in the United States every year.

1.3.3. Microbiology of VAP

Numerous VAP-causing bacteria species have been identified. The frequency of VAP credited to each species is determined by geographic location, the nature of patients' microflora, hygiene protocols in critical care units and antibiotic use [70,71]. Multiple studies of bronchial secretions of VAP-infected patients (all age ranges), in critical care for at least 24 hours, across Europe and North America yields the following summary of VAP-causing species and their frequency (in parentheses) [3,64,72]:

- *Pseudomonas aeruginosa* (24.4%)
- *Staphylococcus aureus* (20.4%)
- Enterobacteriaceae (including *Klebisella* spp., *E. coli*, *Proteus* spp., *Enterobacter* spp., *Serratia* spp., *Citrobacter* spp.) (14.1%)

- *Streptococcus* spp. (12.1%)
- *Haemophilus* spp. (9.8%)
- *Acinetobacter* spp. (7.9%)
- *Neisseria* spp. (2.6%)
- *Stenotrophomonas maltophilia* (1.7%)
- Coagulase-negative *Staphylococcus* (1.4%)

One or more species can be present in a single VAP-infected patient. Identification of microorganisms is achieved via Gram staining, optical microscopy and metabolomics of cultures [2]. Pathogen identification is highly important in composing an effective treatment plan for the patient, since it allows antibiotics to be chosen that the bacteria are sensitive to, rather than broad spectrum agents, which may be ineffective and promote resistance among the pathogens [33,43,44].

1.3.4. Diagnosis of VAP

The symptoms of VAP are non-specific and often present as secondary to other illnesses [73], making clinical diagnosis of VAP difficult. Chest radiographs, combined with analysis of bronchial secretions are usually used to determine VAP status [73], although chest radiology is also limited by its non-specificity [74,75]. There is no gold standard for VAP diagnosis and the standard utilised is governed by local or national health service regulations.

In the United States, the Centers for Disease Control (CDC) developed the National Nosocomial Infection Surveillance (NNIS) system as a tool of diagnosing hospital-acquired infections in the 1970s. It involved analysis of bronchoalveolar fluid cultures (combined with chest radiographs). It displayed a sensitivity of 84% and a specificity of 69% [76]. Following that, Pugin *et al.* proposed the Clinical Pulmonary Infection Score (CPIS) [77], which uses six variables (fever, leucocytosis, tracheal aspirates, oxygenation, radiographic infiltrates and semi-quantitative cultures of tracheal aspirates with Gram

staining) in unison to diagnose VAP. This allowed a 93% sensitivity and 100% specificity to be achieved and so gives health services the closest technique to a gold standard. However, Pugin's methods take time to complete in clinical settings, often prompting health services to 'pick and choose' the most appropriate parameters to measure in a limited time frame. VAP diagnosis continues to be problematic and is sometimes missed altogether, due to the unspecific clinical indicators and multiple patient-related risk factors.

1.3.5. Treatment of VAP

VAP treatment combines antibiotic therapy with treatment of the accompanying symptoms [78]. Antibiotic therapy is different for early-onset (<4 days) and late-onset VAP (>4 days) [64]. Early-onset VAP can be treated with limited spectrum antibiotics, such as cephalosporin or fluoroquinolones [79], whereas late-onset VAP requires additional treatment with broad spectrum antibiotics, such as carbapenems, beta-lactams and aminoglycosides [79,80]. This is due to late-onset VAP posing a greater risk of antimicrobial resistance. Combination therapy is encouraged in all VAP cases, so to eliminate single-drug resistant bacteria without facilitating the development of multi-drug resistance [81]. Delays in initiation of antibiotic treatment can increase the mortality risk of VAP [64]. Antibiotic choice is also determined by bacteria species; *Acinetobacter* spp. respond best to carbapenems, whereas *Staphylococcus* spp. respond to beta lactams and fluoroquinolones [82,83]. VAP treatment is typically indicated for 8 days, although longer treatment periods may be required should multi-drug resistance arise [84].

Despite rapid initiation of antibiotic treatment and combination therapy, VAP-causing organisms still develop extensive antibiotic resistance [85], especially in late-onset VAP. It has been shown that *Pseudomonas aeruginosa* expresses antibiotic efflux pups and beta-lactamases; *Staphylococcus aureus* are often credited with the production of penicillin-binding protein (PBP), resulting in the evolution of methicillin resistance (MRSA). 50% of *S. aureus* present in VAP are

of the MRSA class. [3,72]. Antibiotic resistance further complicates VAP treatment and results in extended hospital stays, longer treatment times and increased mortality [86].

1.3.6. Economic impact of VAP

VAP places an immense economic burden on health services and the wider community. In the United States, VAP leads to increased mean ICU stay (11.5 days) and longer stays in hospital (13.1 days) [87]. The extra cost to treat VAP is almost US$40,000 per episode [87,88]. In the United Kingdom, VAP increases ICU stay by 28% and costs £6,000-£22,000 to treat per infection [89]. These costs arise from specialist care procedures, such as patient monitoring, antibiotic treatment and analytical tools. Additionally, working days are lost due to extended hospital stays, impacting the wider economic community.

Due to its economic and social impact, VAP prevention is at the forefront of critical care improvement discussions. Reducing incidences of VAP would relieve strain of healthcare services and reduce antibiotic use, treatment costs and mortality rates.

1.4. Clinical and experimental methods for reducing the incidence of VAP

1.4.1. Current clinical best practice for VAP prevention

Effectively reducing cases of VAP allows for reduced hospital stays for intubated patients, lesser antibiotic use and better overall patient health [3]. Hence, significant efforts are made in clinical settings for VAP prevention, as well as deterrence of other device-centred infections. However, there is currently no gold standard in clinical best practice to prevent VAP. Should a biofilm be suspected of forming on ETT surfaces, removal of the device is the only fully efficient method of preventing VAP [90]. However, there is evidence that removal of ETTs actually facilitates pulmonary infections [91]. This could be due to the inflated cuff preventing aspirated microorganisms falling into the lungs; deflation of the cuff removes this physical barrier, allowing VAP-causing bacteria to access the lower airways [92].

Since the length of intubation is an important risk factor for VAP, strategies to reduce the time of mechanical ventilation may decrease VAP risk [93]. Such strategies involve accelerated weaning off mechanical ventilation and by using non-invasive ventilation, known as non-invasive positive pressure ventilation (NIPPV), via a face mask [60]. Supine patient positioning can promote microaspiration and consequently, VAP development [60]; Torres *et al.* discovered greater cumulative numbers of endotracheal counts in completely supine (0°) patients compared to those in a semirecumbent (45°) position [94]. This was corroborated by Drakulovic *et al.*, who demonstrated a three-fold reduction in the incidence of VAP in semirecumbent patients compared to supine patients [95]. Therefore, raising the head of the intubated patient may reduce microaspiration and bacterial colonisation of ETTs.

The use of antacids and proton pump inhibitors can facilitate microaspiration, by increasing intragastric volume and decreasing intragastric acidity respectively [60]. Avoiding these medications may aid in the prevention of VAP.

In patients requiring gastro-oesophageal reflux relief, sucralfate has been postulated as an alternative, although double-blind, randomised controlled trials have failed to confirm these preventative effects [96,97].

Upper respiratory tract colonisation is thought to be a prerequisite for VAP [60]. Modulation of oropharyngeal colonisation can halt the development of VAP. This is achieved by antibiotics or chlorhexidine therapy [98-101]. Combined results of three studies of topical oropharyngeal antibiotics showed a relative risk reduction for VAP of 0.73 (95% confidence interval 0.50 – 0.96). ICUs tend to administer these medications as prophylaxis for many oral infections regardless, so VAP reduction is a welcome secondary benefit.

Other clinical preventative methods include correct hygiene procedures, such as proper hand washing and sterilisation protocols. Prophylactic probiotics and mechanical removal of biofilms (e.g. mucus shaver) are also implemented to reduce the incidence of VAP [78,80,102,103]. Choice of clinical VAP preventative methods is often made by individual ICUs, institutions or healthcare trusts, depending on the most common risk factors observed.

1.4.2. Endotracheal tube modifications for VAP prevention

Aside from clinical best practice measures in healthcare settings, modifying ETTs to resist bacterial adhesion and subsequent biofilm formation offers another method of preventing VAP in intubated patients [104]. Two modified ETTs have made it to market and are used in critical care settings for the prevention of VAP; the polyurethane-cuffed ETT and the silver hydrogel coated ETT. The former uses polyurethane cuffs, as opposed to the conventional PVC cuff. The latter is coated with a silver cation-impregnated hydrogel.

The polyurethane-cuffed ETT aims to reduce microaspiration pooling/fluid leakage on device cuffs [12]. It has been shown that PVC ETT cuffs can still contain folds and channels, even when fully inflated. Using ultrathin polyurethane cuffs reduces the prevalence of these folds, minimising

microaspiration pools. Poelaert *et al*. conducted a single-blind, randomised study on 134 surgical patients, half of which were intubated with polyurethane-cuffed ETTs and the other half intubated with standard PVC-cuffed ETTs [105]. It was found that the test group displayed lower incidence of early postoperative pneumonia and required fewer antibiotic prescriptions than the control group (23% v 42%, $p < 0.03$). However, mortality was not different between the groups, nor was length of ICU stay. Suhas *et al*. found a significant reduction in ICU stay with polyurethane-cuffed ETT use (median 6 days v 8 days), but no statistically significant reduction in the incidence of VAP [106]. Another study, comparing VAP rates in an ICU before and after the introduction of polyurethane-cuffed ETTs, found a significant reduction in VAP rates when using polyurethane cuffs (2.8 v 5.3 per 1000 ventilator days) [107].

The silver hydrogel coated ETT utilises the antibacterial property of silver cations [108,109], which are impregnated within the hydrogel coating. The silver cations are thought to prevent device colonisation, due to their broad spectrum antimicrobial properties [108-110], which have been widely reported, although the exact antimicrobial mechanism has not been fully established. Kollef *et al*. conducted a randomised, single-blind controlled study across 54 ICUs across North America, comparing silver hydrogel coated ETTs to conventional PVC ones. Rates of microbiologically confirmed VAP were reduced (4.8%; 95% confidence interval 3.4%-6.6%) in the silver hydrogel coated ETT intubated group compared to the PVC control group (7.5%; 95% confidence interval, 5.7%-9.7%) [111]. However, there was no statistically significant reductions in intubation duration, ICU stay or mortality with silver hydrogel coated ETT use. Li *et al*. reviewed two randomised controlled trials, comparing silver hydrogel coated and conventional ETTs in a total of 1630 participants. The relative risk (RR) of developing VAP was compared. It was found that the silver hydrogel coated ETT reduced the incidence of VAP (RR = 0.64; 95% confidence interval 0.43 to 0.96) [112]. There was no reduction in mortality.

It is difficult to establish whether these modified devices positively impact VAP rates in ICUs, since the resulting data is often inconclusive, or show no statistical significance between test and control groups. Although patients in test groups may display lower incidences of VAP, mortality and ICU stay often do not improve. These studies conclude that the evidence is limited and further rigorous examinations are required to determine the true effect of the modifications on VAP incidence. Furthermore, the silver hydrogel coated ETT is significantly more expensive than its PVC counterpart, prompting investigations into cheaper alternatives.

1.4.3. Surface modifications to resist biofilm formation

Resisting initial bacterial attachment to ETTs (and other medical devices) prevents biofilm formation and the rise of secondary infections [104]. Since the current surface-modified ETTs have problems, such as inconclusive trial data and high cost, research has been prompted into effective and inexpensive alternatives. Multiple laboratory investigations have been conducted into combatting bacterial adhesion by modifying surfaces, such as incorporating antibiotics into coatings, zwitterionic coatings and polyacrylate/methacrylate coatings etc., all of which provide potential routes for ETT modification.

1.4.3.1. Antibiotic coatings

Incorporating antibiotics into a device coating aims to localise the drug to the site of a potential infection. Bacteria that come into contact with the surface are killed [113], preventing attachment and biofilm formation. Saini *et al*. [113] impregnated silicone urinary catheters with azithromycin and ciprofloxacin, by immersing the catheter into antibacterial solutions (in solvent), then drying off the solvent. *In vitro* studies showed effective bactericidal activity against *Pseudomonas aeruginosa* for 30 days, whereby all cells that adhered within the first 24 hours were killed (concentration 3% w/v ciprofloxacin and 6% w/v azithromycin).

Shapur *et al*. [114] applied a sustained release varnish containing chlorhexidine to silicone urinary catheters and incubated with *P. aeruginosa* for 96 hours. The 1% chlorhexidine coating reduced biofilm growth by 94% ($p < 0.0001$) compared to the varnish coated catheter only. Fisher *et al*. [115], used the impregnation method previously described to impregnate three antibiotics into silicone urinary catheters (rifampicin, sparfloxacin and triclosan). Exposure to multiple bacteria species (*P. mirabilis*, *S. aureus* and *E. coli*) *in vitro*, under flow conditions, showed antibiofouling for up to 12 weeks (> 99.9% reduction).

There are several drawbacks with antibiotic coatings for medical devices; it is difficult to maintain sustained release of the drug throughout the duration of device use [116], with patients often receiving an initial bolus dose upon insertion of the device, and lower drug release later [117], rendering the coating ineffective in the later stages of device use. Also, should bacteria be killed by the drug, the possibility exists of cell debris collecting on device surfaces, forming a pacification layer [118]. This restricts drug release from coatings, negatively impacting the effectiveness of the antibiotic coating. Furthermore, there are a lack on *in vivo* and clinical data. Localising antibiotics to a particular area (e.g. urethra, trachea) may also lead to local side effects. Additionally, multi-drug resistance may hinder the advancement of this approach.

Loading surfaces with antimicrobials is not limited to antibiotics; other antimicrobial agents can be incorporated into device coatings, such as silver cations [111,112] and ammonium salts [119]. The latter has been shown to reduce Gram-negative biofilm formation by 50%, *in vitro*. However, as with antibiotic coatings, pacification, local side effects and the lack of clinical evidence have stalled the development of these surface modifications.

1.4.3.2. Poly-sulfobetaine (zwitterionic polymer)

Poly-sulfobetaine (PolySB) is a zwitterionic polymer that has been investigated for its antibiofouling effects [120]. It was shown to be effective against both Gram-positive and Gram-negative bacteria, with reduced attachment and

biofilm formation after 24 hours, compared with a negative control, *in vitro*. Since the polymer has both positive and negative charges, it is thought to interact with water molecules near its surface, via electrostatic interactions, creating a highly hydrophilic layer [121]. This makes it difficult for bacteria to access the surface, since they have to displace the superhydrophilic surface first.

Smith *et al*. [122] modified the surfaces of venous catheters with PolySB, using the redox polymerisation method, and showed reductions of up to 97% in biofilm formation of a broad spectrum of pathogenic bacteria species, compared to unmodified catheters, both *in vitro* and *in vivo*, after 24 hours. However, PolySB-modified surfaces have yet to be proven effective in clinical studies. Furthermore, the shortage of proof on safety currently limits its use.

1.4.3.3. Slippery liquid-infused porous surfaces (SLIPS)

The SLIPS approach utilises omniphobic liquid surfaces to prevent adhesion of bacteria. The method was inspired by the *Nepenthes* pitcher plant, which uses SLIPS on its leaves to prevent fungal, bacterial and insect attachment/growth [123]. The liquid on the surface creates a low friction layer, causing cells, insects etc. to slide off the surface. The liquid layer provides an omniphobic slippery barrier to attachment.

Leslie *et al*. [124], covalently bound a flexible molecular perfluorocarbon layer to PVC medical-grade tubing, followed by an approved liquid perfluorocarbon layer, forming a perfluorocarbon-based SLIPS on the tubing. *In vitro* exposure to *P. aeruginosa* showed an eight-fold reduction in bacterial adhesion for up to 6.5 weeks, compared to untreated PVC. There was no increase in attachment on SLIPS-modified PVC between 1.5 and 6.5 weeks. Although these modified devices are simple to manufacture (compared to antimicrobial coatings) and are already approved for use in medical devices, there currently is not enough clinical evidence supporting the antibiofouling effects of SLIPS.

1.4.3.4. Poly (ethylene glycol) (PEG) and Poly (ethylene oxide) (PEO)

Poly (ethylene glycol) and poly (ethylene oxide) are widely used for healthcare applications, due to their low toxicity and good water solubility [125]. They have also demonstrated good antibiofouling properties. Harris *et al*. [126] reported an 89%-93% reduction in *S. aureus* attachment to PEG treated titanium surfaces, compared to untreated surfaces. PEG was grafted onto titanium surfaces via poly (L-lysine), which electrostatically interacts with the negative titanium dioxide surface.

Kingshott *et al*. [127] showed that PEG, covalently immobilised onto poly (ethylene terephthalate) (PET) surfaces, reduced *P. aeruginosa* attachment by between 2 and 4 orders of magnitude for up to 5 hours, *in vitro*, compared to untreated PET surfaces. The grafting density of PEG chains was proportional to the degree of biofouling reduction, suggesting that a steric blocking effect may be the mechanism behind the anti-biofouling activity of PEG.

PEG can also be used to immobilise antibiotics to a surface. Du *et al*. [128] tested the antimicrobial effect of PEGylated tobramycin on *P. aeruginosa*. The PEGylated antimicrobial exhibited a 3.2-fold reduction in biofilm formation compared to tobramycin alone. Roosjen *et al*. [129], investigated the antibiofouling properties of PEO, which was covalently conjugated to a polyurethane substrate. Adhesion of *S. epidermidis*, *S. aureus*, *S. salivaris* and *E. coli* were reduced by at least 94%; adhesion of *P. aeruginosa* was reduced by 80%.

These coatings are known as polymer brush coatings, defined as polymer chains attached to a surface and stretching out into the surrounding medium [129], similar to teeth on a brush. Brush coating polymers are highly water soluble and mobile [130]. Their exact mechanism of bacteria repulsion is not fully understood but hypotheses include steric hindrance effects, hydrophilicity and electrostatic repulsion [131,132].

The major drawback of polymer brush coatings is degradation. PEO is known to oxidise [133]; reactions with oxidising agents, such as oxygen and hydrogen peroxide, generates hydroperoxides, which decompose via carbon-oxygen bond scission. Metal ions and UV light can also degrade PEO, by accelerating the decomposition of hydroperoxides [133]. Degradation of polymer brush coatings reduces their antibiofouling properties [133]. As with the methods mentioned in previous sections, there is a lack of clinical evidence for polymer brush coatings. Additionally, blood and salivary proteins have been shown to adhere to PEO coatings *in vivo* [131], reducing their antibiofouling ability.

1.4.3.5. Micropatterned, nano-patterned and rough surfaces

Applying antimicrobial/zwitterionic/polymer brush coatings to surfaces for antibiofouling purposes has issues with long term stability. Therefore, surface topographical modifications are increasingly studied for antibiofouling. Ivanova *et al*. [134] reviewed nanostructured bactericidal surfaces, whereby silicon-based surfaces were physically modified (using reactive ion etching) to create nano-structures, which resembled 'spikes' of 500 nm in height. These surfaces killed *P. aeruginosa* (Gram-negative) and *S. aureus* (Gram-positive) upon cell contact, with estimated average killing rates of 450,000 cells min^{-1} cm^{-2}. It was hypothesised that the 'spikes' punctured bacterial cell walls, causing cell lysis [134]. This approach is yet to be clinically trialled and requires further research.

The link between surface roughness and bacterial attachment has often been debated. Reddy *et al*. [135] demonstrated a 47% reduction in coverage of Uropathogenic *E. coli* on micropatterned silicone surfaces when compared to smooth surfaces. However, investigation of a nano-patterned titanium surface by Diaz *et al*. [136] showed an increase in *Pseudomonas fluorescens* and *Streptococci* spp. versus a smooth titanium surface. This difference could be due to the magnitude of the topography (micro versus nano-patterned surfaces). However, there is limited evidence to state outright whether bacteria prefer rough or smooth surfaces.

1.4.3.6. High throughput microarray screening to identify bacteria resistant polymers

The antibiofouling polymer coating trialled in this study was discovered using a high throughput microarray screen. Microarrays are a high throughput method of analysing multiple materials simultaneously. The technique was originally developed for genomics research, allowing gene expression to be analysed for an entire genome at once [137]. This was achieved by depositing tens of thousands of DNA sequences onto a glass slide, known as a 'chip'. Sequences were deposited in ordered rows and columns, allowing them to be easily located. The chip was then subjected to test conditions (e.g. complimentary mRNA assay) and DNA sequences analysed simultaneously [137]. Vaishampayan *et al*. [138] used the microarray process to investigate the bacterial diversity of the Phoenix spacecraft assembly clean room, by analysing complimentary 16S rRNA gene interaction with known DNA sequences printed onto microarray chips. This allowed the particular bacteria strains present in the clean room to be identified.

Anderson *et al*. [139] first developed polymer microarrays in 2004, in which DNA was replaced with a range of monomers. Deposition onto the chip was done using a contact printer. The printer held several pins in a robotic arm. Monomer solutions (mixed with a photoinitiator) were prepared in multi-well source plates; the printer was then set to dip the pins into the monomer solutions and deposit tiny droplets (400 µm) onto the chip. Hundreds of different monomers were printed in this manner. Once all monomers were deposited, the chip was exposed to UV light, which activated the photoinitiator and photopolymerised the monomers. The chip was then used for relevant experiments. Khan *et al*. [140] used polymer microarrays to screen 135 binary polymer blends for biocompatibility to human skeletal stem cells. Chips were exposed to stem cells and microscopic techniques (scanning electron and fluorescence) used to analyse which materials supported stem cell growth best. Several polymer blends were found that could be used as biocompatible scaffolds for stem cells.

The polyacrylate used in this thesis was identified using the high throughput polymer microarray screening technique. Hook *et al*. [141] investigated bacterial adhesion to hundreds of poly acrylates/methacrylates. Monomers were printed and photopolymerised onto poly (hydroxyethyl methacrylate) coated glass slides, before the chips were incubated with *P. aeruginosa*, *S. aureus* and *E. coli*. Several 'hit' materials were discovered, which were then scaled up for coating silicone catheter sections (Figure 1.3).

In vitro investigations included incubating coated catheter sections in cultures of the three bacteria species for 72 hours and analysing the fluorescence from surface-adhered cells, via confocal microscopy. One polymer had good antibiofouling activity against all three species, particularly *P. aeruginosa*, which had a 28-fold reduction in surface coverage compared to the uncoated catheter. This polymer was ethylene glycol dicyclopentenyl ether acrylate (EGDPEA). *In vivo* studies involved implanting EGDPEA-coated silicone catheter sections subcutaneously into mice. The animals were inoculated with *S. aureus* and the bioluminescence of bacteria measured daily for 4 days. There was a ten-fold reduction in bioluminescence on day 1, which persisted for the entire 4 days.

The exact mechanism by which EGDPEA resists bacterial attachment has not been fully established. Sanni *et* al. [142] linked a value combining *c*Log*P* and the number of rotatable bonds (*n*RotB) of poly(meth)acrylate hydrocarbon pendant groups to reduced *P. aeruginosa* attachment. EGDPEA appears to satisfy this value. Other possible mechanisms include steric blocking [143] and the introduction of opposing electrostatic forces [144], which interfere with stage (i) of the biofilm life cycle (Figure 1.2). Due to the efficacy of EGDPEA *in vitro* and *in vivo*, it forms the basis for the work conducted in this thesis. To improve the ductility of EGDPEA coatings, it was co-polymerised with di (ethylene glycol) methyl ether methacrylate (DEGMA) [145] in Hook *et al*.'s study, which will also be implemented in this report (Figure 1.3).

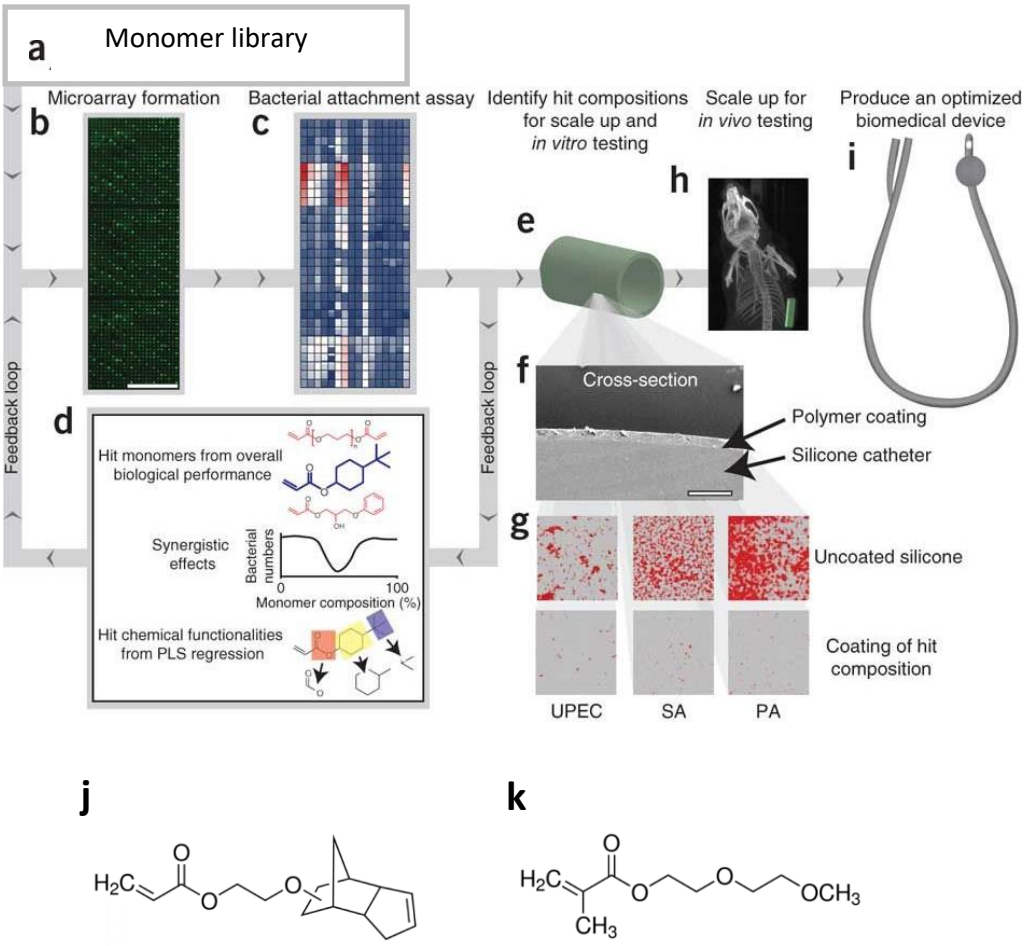


Figure 1.3. Hook *et al.*'s combinatorial methods for high throughput screening of polymer microarrays [141]. **(a)** Monomer selection is made from a library of compounds. **(b–f)** Outline of the strategy utilised for identifying hit material composition. **(b)** Fluorescence scanning image of the first-generation microarray after incubation with *P. aeruginosa* for 72 h. Three replicate arrays were present on each glass slide. Scale bar, 10 mm. **(c)** Intensity map of the bacterial data from the first-generation array. **(d)** The feedback loop used to select monomer compositions for a second-generation array. The biological performance of each monomer, the identification of hit material compositions that have synergistic effects and the results from the PLS regression of ToF-SIMS spectra and bacterial data were used to inform the composition of the second-generation array. **(e)** Schematic representation of the hit material composition scaled up. **(f)** An SEM image of the cross-section of a silicone catheter coated with a hit polymer (thickness, 20–25 µm). Scale bar, 100 µm. **(g)** Confocal images of SYTO17-stained biofilm for the three pathogens studied (*P. aeruginosa* (PA), *S. aureus* (SA), UPEC) from coated and uncoated silicone catheters. Each image is 160 × 160 µm. **(h)** Microcomputed tomography scan of a coated catheter implanted subcutaneously into a murine model. The catheter has been coloured green in this image. **(i)** A schematic representation of a catheter coated with the hit composition. **(j)** Chemical structure of EGDPEA. **(k)** Chemical structure of DEGMA.

1.5. Optical fibre sensors for the real time detection of bacterial attachment

Resisting bacterial adhesion to ETTs (and other indwelling medical devices) is an effective method of reducing the incidence of secondary nosocomial infections associated with biofilms [3). If it was also possible to monitor bacterial attachment and biofilm formation on device surfaces in real time and *in situ*, it would be possible to intercept device-centred infections. An early warning of biofilm formation would allow physicians to treat the patient immediately, by removal of the device and/or appropriate antimicrobial treatments. This would prevent the development of serious secondary infections.

Currently, in order to examine device contamination, the device is removed and sent for microbiological analysis. In the case of ETTs, repeated removal and reinsertion can harm the patient; it can facilitate VAP [91], and insertion of a new ETT can cause tracheal wall damage and inflammation [146]. Long Period Grating optical fibre sensors (LPG OFS) are a novel, simple and inexpensive method of monitoring bacterial attachment. By incorporating LPG OFS into ETTs, the real time assessment of biofilm formation can be made *in situ.*

1.5.1. Overview of optical fibres

Optical fibres have been used for telecommunication purposes since the 1980s. Their popularity arose because they allowed fast transfer of information across large distances with very little loss of signal [147]. Optical fibres were also cheaper, smaller and easier to manufacture than conventional coaxial cables [147]. Optical fibres are made of glass (silica) and comprise of two parts; the core and the surrounding cladding (Figure 1.4). The core has a higher refractive index than the cladding [147]; therefore, light input at one end of an optical fibre is totally internally reflected through the core, allowing large information transmission bandwidth [147,148].

There are two types of optical fibre; single mode and multi-mode (Figure 1.4). Single mode optical fibres have smaller core diameters (< 10 µm) and only transmit one light mode, resulting in higher bandwidth and lower attenuation (loss of transmission). Multi-mode fibres have larger core diameters (> 50 µm), allowing several light modes to propagate through the core, resulting in smaller bandwidth and larger attenuation [147-149]. Single mode optical fibres are therefore used for long distance telecommunication, whereas multi-mode optical fibres are used for shorter distance purposes. The diameter of the entire fibre (including the cladding) is usually 125 µm.

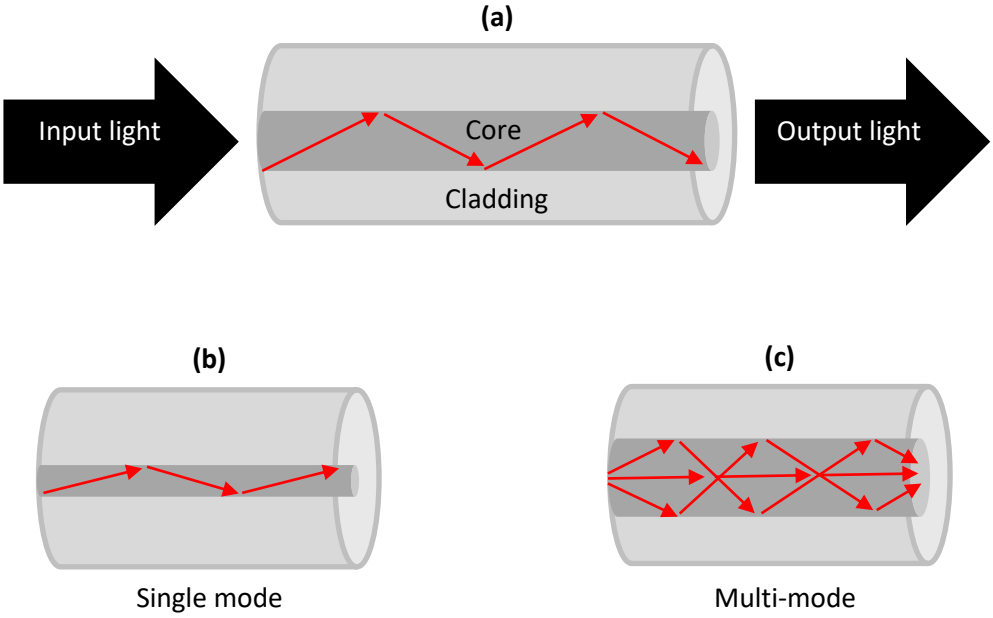


Figure 1.4. (a) Optical fibre principle, showing the core, cladding and total internal reflection of input light (red arrows). **(b,c)** Difference between single and multi-mode optical fibres. Single mode optical fibres allow one light mode to propagate through a small core diameter, whereas multi-mode optical fibres allow multiple modes to propagate through a core of larger diameter.

1.5.2. Optical fibre sensors (OFS)

Optical fibres are made into sensors by modulating the fibre and/or the associated signal transducer in some way [150]. This allows input light to undergo changes in its optical properties and be converted into an optical signal [151]. The optical properties of input light, and therefore the associated

signal, differs depending on the nature of the analyte being sensed. OFS can be classified as either extrinsic or intrinsic. In extrinsic OFS, the fibre is used to transmit light to and from an external signal transducer, where sensing occurs. The optical fibres act as a means of getting light to the sensing element and do not require modulation. In an intrinsic OFS, sensing occurs within the fibre itself. This requires modulation of the optical fibre, so that physical/chemical perturbations alter the optical properties of light propagating through the fibre [152].

Depending on the type of transducer or the nature of fibre modulation, the optical property that is measured can be selected; OFS can be classified as intensity, phase, frequency, polarisation or wavelength sensors [151]. Intensity-based sensors measure signal loss (or change in intensity), whereas wavelength-dependent OFS measure changes in wavelength of attenuations [151]. A certain type of OFS is often chosen for a given application, since they usually possess advantageous properties for that given application. For example, intensity-based sensors are used to measure physical pressure, since physical strain and bending of the fibre cause absolute intensity changes [153]. Wavelength-dependent sensors are used for chemical and temperature sensing [154], since they do not measure absolute intensity, but rather relative transmission loss at certain wavelengths [154]. Wavelength-dependent sensors can also be multiplexed, allowing for sensing of multiple analytes simultaneously [154]. Intensity-based OFS are cheaper to manufacturer but are more prone to signal interference and noise. Wavelength-dependent OFS are more robust and have multiplexing opportunities, but can cost more to manufacture. Examples of intensity and wavelength sensors are the microbend sensor and Fibre-Bragg gratings (FBGs) respectively [153,155].

OFS are versatile devices and can be used for a wide range of applications, such as measuring physical properties (strain, temperature etc.), chemical/pollutant concentrations and concrete ‘health’ in buildings [151]. One such study reported the use of an FBG for temperature sensing, with an operational range of 2-400 K and a temperature resolution better than 10 mK [156]. The FBG was

mounted onto a polytetrafluoroethylene (PTFE) coupon, which was immersed into a temperature-controlled cryo-chamber, which was gradually heated up to 400 K. A third-order polynomial was found when plotting FBG intensity peak position (at certain wavelengths) against temperature, which could be used to determine temperature to the nearest 10 mK, using the FBG signal. Another study used tapered OFS to detect hazardous and noxious pollutants in seawater [157], by immersing them in samples and measuring signal change. It was found that pollutants with a refractive index range of 1.329-1.501 could be sensed, with a limit of detection of 0.002 refractive index units (RIUs).

OFS hold several advantages over other types of sensor; they are inexpensive, easy to implement, can be extremely sensitive and have multiplexing opportunities. However, light propagating through OFS can be interfered with by unwanted external factors, such as mechanical stress. Another drawback is that reference readings often need to be made to eliminate false readings from relative optical measurements [158].

1.5.3. Long Period Grating optical fibre sensors (LPG OFS)

LPG OFS are a type of single mode, intrinsic, wavelength-dependent OFS commonly used for a range of physico-chemical sensing applications. LPG OFS are made by periodically modulating the refractive index of the core of an optical fibre (to form a grating), allowing the core mode to couple with co-propagating cladding modes [159]. This results in the appearance of attenuation bands (losses of transmission) centred at discrete wavelengths, with each attenuation band corresponding to coupling to a different cladding mode [160,161] (Figure 1.5). The grating is usually written into the core of the optical fibre using UV laser inscription [162] and have grating periods (distance between grating structures) of between 100 μm and 1 mm [159]. The wavelength(s) at which light couples from the core mode to the cladding modes is governed by equation 1 [163,164]:

$$\lambda_i = (\eta_{core} - \eta_{cladding(i)})\,\Lambda \quad (1)$$

Where λ_i is the wavelength at which light is coupled to the cladding mode (i = 1, 2, 3….), η_{core} is the refractive index of the core, $\eta_{cladding(i)}$ is the effective index of the i^{th} cladding mode and Λ is the grating period. Since the refractive index of the core is fixed, the wavelength(s) of light coupling to the cladding modes is dependent upon the effective refractive index of the cladding [163]. The refractive index of the cladding changes depending on the refractive index of the media it's placed in. Therefore, media with different refractive indexes will alter the $\eta_{cladding(i)}$ parameter, in turn shifting the wavelength of core-cladding mode coupling. This shift can be measured, allowing the LPG to be used as a sensor. Figure 1.5 summarises LPG OFS spectral response.

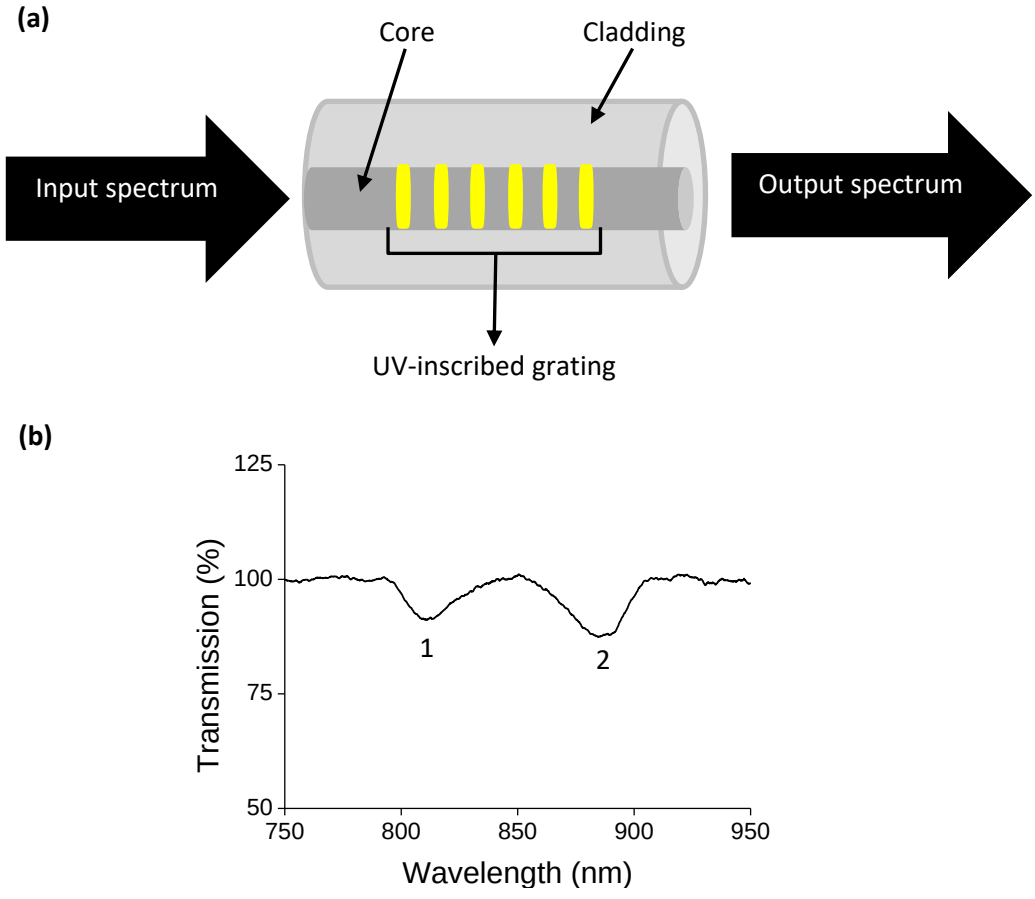


Figure 1.5. (a) LPG OFS schematic, indicating the UV-inscribed grating and the input and output optical spectra. **(b)** Transmission spectrum for an LPG of length 30 mm and grating period 109 µm in air; two attenuation bands (losses of transmission) are visible, labelled '1' and '2', indicating the wavelengths at which core-cladding mode coupling occurs.

The phase matching condition (or coupling condition, given by equation 1), contains a turning point, known as the phase matching turning point (PMTP) [165]. Coupling occurring near or at the PMTP gives rise to attenuations with highest sensitivity [166], resulting in a broad attenuation band in the optical spectrum. As the effective refractive index of the cladding increases (or $\eta_{core} - \eta_{cladding(i)}$ decreases), this attenuation band splits into two, due to coupling to the same cladding mode occurring at two different wavelengths [159,165,166], known as dual resonance. Further increases in cladding refractive index cause these two bands to shift apart from each other, in opposite directions in the output spectrum. The grating within LPG OFS is often inscribed near or on the PMTP, to give the sensor the highest possible sensitivity.

The advantages of LPG OFS over other grating types (such as Fibre-Bragg gratings) are low insertion loss and low-level back reflection, which result in maximum signal output with minimal signal loss [167]. LPG OFS surfaces can be modified to selectively sense an analyte of interest. Marques *et al*. [163] used LPG OFS modified with silica:gold nanoparticles and biotin to sense streptavidin, with a sensitivity of 6.88 nm / (nm/mm^2) and a limit of detection of 19 pg/mm^2. Hromadka *et al*. [168] modified LPG OFS surfaces with ZIF-8 (zeolitic imidazolate frameworks) in order to sense methanol, ethanol, 2-propanol and acetone vapours. Sensitivity was highest to methanol, with 1790 ppm detected. The sensitivity of LPG OFS (and detection limit) depends on how close to the PMTP coupling occurs, the thickness of any deposited layer and the porosity of such layer [169]. Due to the sensitivity, relative ease of fabrication (compared to other sensor types) and versatility of LPG OFS, this thesis investigated their potential use for monitoring biofilm formation in real time.

1.5.4. LPG OFS for real time monitoring of bacterial attachment and biofilm formation

LPG OFS can be used for the detection of bacterial attachment. Bacteria and their biofilms have their own refractive indexes, so adsorption of bacteria to

LPG OFS surfaces induces a change in $\eta_{cladding(i)}$, resulting in a shift in coupling wavelength. Smietana *et al.* [170] immobilised *E. coli* selective bacteriophages onto LPG surfaces and exposed the sensor to an *E. coli* culture. A wavelength shift of 1.3 nm was observed when bacteria were bound by the bacteriophages. Similarly, Tripathi *et al*. [171] covalently immobilised T4 bacteriophages onto LPG OFS and measured wavelength shift in *E. coli* culture medium. A wavelength shift of 2.1 nm was recorded, with a limit of detection of 10^3 CFU/mL. However, both these studies required the use of expensive biological agents to promote bacterial adhesion.

This thesis investigated LPG OFS as a novel, non-invasive, label-fee method for the real time detection of bacterial attachment and biofilm formation. Rather than promoting adhesion, biofilms were allowed to form on sensor surfaces naturally and the wavelength shift of attenuation bands monitored. Response was compared between unmodified and EGDPEA:DEGMA coated sensors. Should the coating effectively resist biofouling, lesser attachment would occur on the coated LPG OFS surface, resulting in a smaller change in cladding refractive index, and therefore smaller wavelength shifts (Figure 1.6).

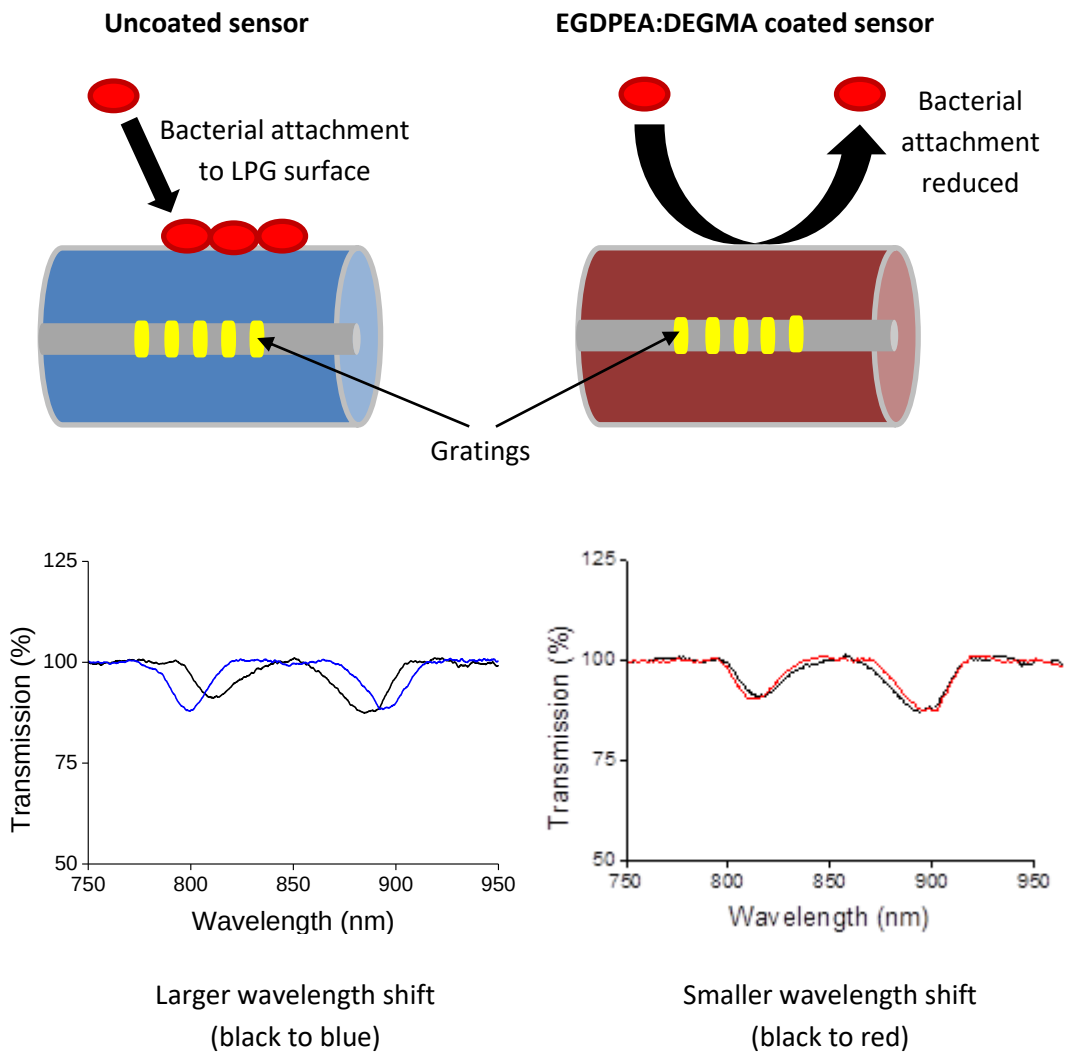


Figure 1.6. LPG OFS for the detection of bacterial attachment. The EGDPEA:DEGMA coating reduces bacterial adhesion, causing smaller wavelength shifts of attenuation bands in the output optical spectrum.

The protocol schemed in Figure 1.6 was also used as an alternative method for assessing the anti-attachment ability of EGDPEA:DEGMA.

For monitoring biofilm formation on ETT surfaces, sensors were incorporated into ETTs in the hope of developing an instrumented device capable of *in situ* measurements, providing physicians with instant feedback on bacterial colonisation of ETTs. LPG OFS can also be used in industries where biofouling is problematic, such as the food and marine industries [172,173].

1.6. Materials with bacteria selective binding properties for species identification

The ability to sense bacterial attachment and biofilm growth would provide healthcare professionals with a tool for predicting and intercepting device-centred infection. However, LPG OFS are not selective for bacteria species, hence cannot identify individual pathogens.

Current bacteria species identification (for diagnostic purposes) involves taking a sample from the patient, culturing the microorganism in a laboratory and using various staining and microscopic techniques, such as Gram staining [174]. This process is slow and can take several days [175], during which an infection can worsen. Furthermore, if an infection is suspected, patients may be treated with broad spectrum antibiotics while waiting for laboratory results [176]. These broad spectrum agents have been shown to facilitate antimicrobial resistance [5,177]. The non-specificity of these antibiotics means that they target cellular components that all (or most) pathogens possess [5,177]. However, some bacteria species can develop methods to protect these cellular targets [5,177], hence rendering the antimicrobial ineffective.

Antimicrobial resistance has been identified as a serious threat to global public health by the World Health Organisation. Without effective antibiotic therapies, simple infections can become fatal. Also, the success of major surgery and cancer chemotherapy would be compromised [178]. Should the spread of antimicrobial resistance continue, there will be 10 million deaths caused by resistant infections, costing the global economy £66 trillion by 2050 [179].

In order to curb the spread of antimicrobial resistance, the use of broad spectrum antibiotics needs to be reduced. Instead, species-specific antibiotics should be administered. These drugs target species-specific cellular components, which are sensitive to these agents. Using these medications, especially in combination, lessens the risk of pathogens developing resistance

to them [178,180]. The choice of specific antimicrobial depends on the bacteria species causing the infection.

Therefore, identification of pathogenic bacteria species is imperative and requires faster methods, to prevent the use of broad spectrum antimicrobials. Rapid species identification would allow for specific antimicrobials to be administered early, preventing the development of resistance and allowing for faster patient recovery, in turn reducing strain on healthcare services.

In this thesis, materials that differentially bind different bacteria species were identified and combined with LPG OFS to create a non-invasive, inexpensive, label-free tool for species identification. Since the sensors have potential to be used *in situ*, it may be possible to rapidly identify bacteria species at the bedside, allowing specific antibiotics to be administered sooner and restricting unnecessary overuse of broad spectrum antibiotics. A device capable of identification of bacteria species would also provide industry and research with a powerful tool for multiple applications.

1.6.1. Materials with bacteria selective binding properties

Bacteria selective binding refers to the ability of a material to differentially bind different bacteria species. Hence, on a given material, one species may attach more than others. The ratio of attachment between species on a selective material allows for species identification, providing the attachment profiles of species to the materials are known. The differential attachment rates may also allow these materials to be used for identifying species from multi-species bacteria mixtures [181].

Species selective identification has long been investigated. These studies use species-specific membrane-bound proteins, such as lectins [182], to identify bacteria species. During bacterial attachment, these membrane-bound proteins are used for irreversible attachment to specific cell targets (stage (ii) of the biofilm life cycle (Figure 1.2)). Functionalising a surface with the

complimentary target for these proteins allows for species-selective attachment. Richards *et al*. [182] investigated lectin-glycan interactions to identify lectin-selective sugars. Glycans were conjugated with labelled gold nanoparticles, exposed to bacterial lectins and absorbance measured between 450-700 nm. Discriminant analysis was used to separate the lectins based on their attachment to the glycans (degree of absorbance). It was found that the lectins could be identified based on their selective interaction with the glycans. Since some lectins are bacteria specific [182,183], the glycans can be thought of as species selective moieties.

Research into species selective polymers is a more recent approach. Magennis *et al*. [184] exploited bacterial redox systems to generate selective polymers *in situ*, via a copper-mediated radical polymerisation process. Bacteria were incubated with monomers and a copper catalyst. The bacteria-specific redox systems induced polymerisation of certain monomers, via reduction of the copper catalyst, termed bacteria-instructed synthesis. The resulting polymers could selectively bind the species that induced their reaction, since they were selective to the associated membrane redox machinery. The polymers were then separated from the cells and tagged with a fluorophore. Incubating the tagged polymers with unlabelled bacteria allowed selective binding to the species that synthesised them, allowing identification of the species from the fluorescence intensity.

Pernagallo *et al*. [185] used the microarray screening process to identify synthetic polymers that selectively bound the foodborne pathogens *Salmonella enterica* and *E. coli*. The authors concluded that selective binding was caused by differential interaction between chemical groups of the polymers and membrane-bound structures, such as pili. However, they were unable to establish a correlation between chemical group structure and attachment of each species. The authors stated that the selective polymers could have applications in identifying food contaminates and pathogenic bacteria in clinical settings.

Hook *et al*. [141,186] used the high throughput microarray process to screen hundreds of polymers for their resistance to the attachment of three pathogenic bacteria; *P. aeruginosa*, *S, aureus* and Uropathogenic *E. coli*. Since these species were tagged with fluorophores, a large dataset of fluorescence intensity was gathered, with high fluorescence representing greater bacterial attachment to a particular polymer spot on the microarray 'chip'. These data were analysed to find materials that possessed selectivity (or the greatest differential attachment) for these three species.

1.6.2. LPG OFS for species identification

OFS have previously been utilised for selective species identification; biological agents are often combined with OFS for this application. The works by Smietana *et al*. [170] and Tripathi *et al*. [171] are examples of *E. coli* selective OFS systems, using bacteriophages conjugated to LPG OFS for *E. coli* selective binding. Inzana [187] developed a nanoparticle-OFS system, consisting of an optical fibre with self-assembled nanoparticle film coatings bound to monoclonal antibodies and DNA specific to MRSA, *Brucella abortus* or *Histophilus somni*. Exposure to these bacteria allowed a change in output light transmission to be detected within an hour, for the selective species only, with a limit of detection for MRSA as low as 100 cells. Although these approaches are highly sensitive, selective and label-free, the expense to modify OFS with bacteriophages and antibodies can be extremely high. Furthermore, the stability of these systems can be compromised by the environment. It may also be difficult to incorporate these sensors into indwelling medical devices, since putting antibodies, phages and pathogenic DNA into patients can compromise their health.

If polymers could be found that differentially bind *P. aeruginosa*, *S. aureus* and Uropathogenic *E. coli*, it may be possible to combine them with LPG OFS for label-free bacteria species identification. Three identical LPG OFS could be coated in each of three selective polymers and exposed to each bacteria

species in culture media. Should the polymer coating differentially bind the species, the wavelength shifts of attenuation bands for each coated sensor will be different for different species. The principle is highlighted in Figure 1.6, where the uncoated sensor is replaced with a sensor coated in a selective material. This will allow quick identification of bacteria species using only optical spectra (wavelength shift), minimising time and resources in healthcare settings. Furthermore, the poly acrylates/methacrylates studied by Hook *et al*. [141,186] can be inexpensively mass produced, offering cheaper OFS modifications than current options.

Therefore, fluorescence data generated by Hook *et al*. [186], were analysed to find three materials with selectivity (or the largest variation in differential attachment) between the three aforementioned bacteria species. These materials were upscaled and used to coat three LPG OFS, which were subsequently exposed to single and co-cultures of the bacteria. The wavelength shifts were plotted and compared to note if species identification was possible based on the differential wavelength shifts from each sensor. Overall, LPG OFS combined with selective polymers may lead to an adaptable, self-contained, sensitive, label-free bacteria species identification tool with multiple applications in healthcare and research.

1.7. Aims

The aims of this thesis are:

1. Investigate the effect of EGDPEA:DEGMA polymer coatings on bacterial attachment and biofilm formation on endotracheal tube surfaces.
2. Compare surface properties of device tubes versus cuffs, and uncoated versus polymer coated substrates.
3. Explore Long Period Grating optical fibre sensors as a method of detecting bacterial attachment and biofilm formation in real time. Incorporate Long Period Grating optical fibre sensors into endotracheal tubes for the monitoring of attachment to devices.
4. Analyse fluorescence data from high throughput polymer microarrays to identify materials that selectively or differentially bind *Pseudomonas aeruginosa*, *Staphylococcus aureus* and Uropathogenic *Escherichia coli*.
5. Functionalise Long Period Grating optical fibre sensors with selective binding materials to design a tool for bacteria species identification. Observe spectral response of each sensor in single and co-cultures of each bacteria species.

2. Materials and methods

2.1. Materials

All monomers used in this project were obtained from Sigma Aldrich UK. All solvents were acquired from Fisher Scientific UK. Monomers and solvents were used as supplied. 2,2'-Azobis(2-methylpropionitrile) (AIBN, 98%) was obtained from Sigma Aldrich UK and purified by recrystallization with methanol. Bis[(difluoroboryl)diphenylglyoximato] cobalt(II) (PhCobF) was obtained from DuPont and used as received. 2,2'-dimethoxy-2-phenylacetophenone (DMPA, 99%) was bought from Sigma Aldrich UK and used as received. The binary silane primer (MED1-161) was supplied by NuSil Technology LLC UK.

The endotracheal tubes (ETTs) used in this project were Hi-Contour oral/nasal cuffed endotracheal tubes, supplied by Mallinckrodt™ (under the Covidien™ corporate umbrella). All tubes were adult sized, with an inner diameter of 8 mm, outer diameter of 10.9 mm and maximum cuff diameter of 30 mm.

The bacterial strains used were taken from Dr Jean Dubern and Dr Ewan Murray's lab collection (Centre for Biomolecular Sciences, University of Nottingham). RPMI-1640 medium (R0883) was obtained from Sigma Aldrich UK. Artificial Sputum Medium (ASM) was made up from Dr Freya Harrison's stock solutions (Centre for Biomolecular Sciences, University of Nottingham).

LPGs were fabricated in photosensitive boron-germanium co-doped optical fibres (Fibercore PS750), using custom made amplitude masks made of 1Cr18Ni9Ti steel alloy. LPGs were inscribed into a 3 cm length of the optical fibre using a frequency-quadrupled Nd:YAG laser, emitting at a wavelength of 266 nm (Continuum minilite I). Insensitive optical fibres were acquired from Thorlabs Ltd. (460HP, fibre ID: 10-C0157-20-4H-08). LPG OFS and insensitive optical fibres had core dimeters of 5 μm and fibre diameters of 125 μm, with the LPG OFS grating period of 109 μm. The HL-2000 halogen light source, HR-4000 optical spectrometer, SubMiniature version A (SMA) connectors and the SpectraSuite software were obtained from Ocean Optics UK.

2.2. Polymerisation techniques

2.2.1. Catalytic chain transfer (CCT) using a cobalt catalyst

EGDPEA:DEGMA and the three selective binding polymers were synthesised using a CCT technique. This was a free radical polymerisation, the speed of which was controlled by a cobalt catalyst [188]. Free radical polymerisations, without cobalt catalysts, are non-selective, meaning that chain transfer to monomers are random, leading to termination of polymer chains at varying lengths [189,190]. This results in polymers with increased polydispersities. By incorporating a cobalt catalyst into the reaction, the molecular weight of polymers can be controlled. Polymers synthesised by CCT have lower polydispersities [191].

In a CCT polymerisation, initiation requires a radical generation species. In this thesis, 2,2'-Azobis(2-methylpropionitrile) (AIBN) was used as the radical initiator. The first step in the reaction is generation of the 2-cyano-prop-2-yl radical by heating AIBN (Figure 2.1).

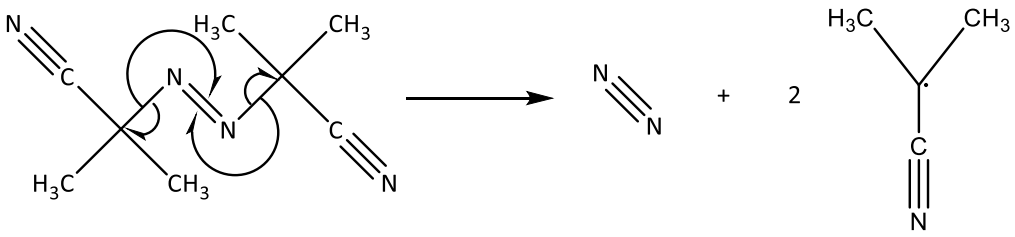


Figure 2.1. Heat generated AIBN decomposition, resulting in Nitrogen gas and two 2-cyano-prop-2-yl radicals.

Once the radical is generated, it reacts with the acrylate/methacrylate terminus to generate monomer radicals via terminal carbon-carbon double bond breakage. The monomer radicals then undergo propagation, leading to a growing polymer chain (Figure 2.2).

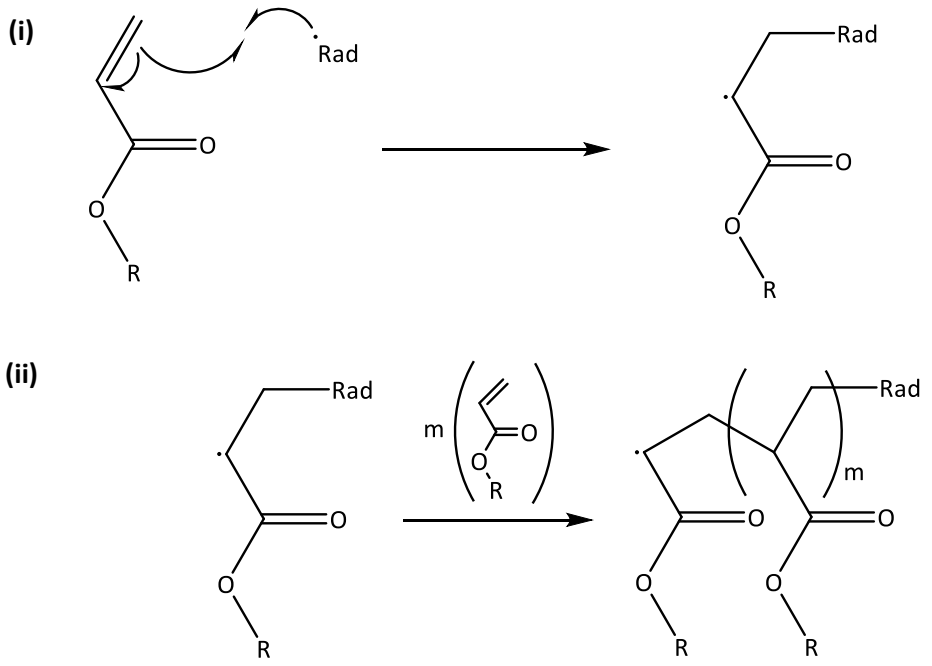


Figure 2.2. (i) Generation of a radical on an acrylate monomer terminus by the activated radical species (Rad), via terminal carbon-carbon double bond breakage. **(ii)** Propagation of the monomer radical, by addition of further acrylate monomers.

In a CCT reaction, the growing polymer chain encounters the cobalt catalyst (PhCobF), in the form of a Co(II) species, forming a 'dead', or unsaturated, transfer chain and a cobalt(III) hydride (Co(III)-H) [192]. The cobalt hydride can then go on to react with other unreacted monomers, producing a monomeric radical, which can then propagate to form another polymer chain (Figure 2.3).

(i) $P^{\bullet} + Co(II) \longrightarrow P + Co(III)\text{-}H$

(ii) $Co(III)\text{-}H + M \longrightarrow M^{\bullet} + Co(II)$

Figure 2.3. CCT reaction using a cobalt(II) catalyst. **(i)** The growing polymer chain ($P^{\bullet}$) reacts with the cobalt(II) species, forming a 'dead' transfer chain (P) and a cobalt(III) hydride. **(ii)** The cobalt(III) hydride reacts with unreacted monomer (M), forming a monomeric radical ($M^{\bullet}$) and recycles the cobalt(II) catalyst.

The ‘dead’ transfer chain can be thought of as terminated, although it is still possible for it to react with the cobalt hydride and continue propagating. However, since the monomers are more abundant than polymer chains, the cobalt hydride is more likely to react with monomers [192], hence the cobalt catalyst prevents the uncontrolled propagation of polymer chains, reducing the polydispersity. The general scheme of a CCT reaction is summarised in Figure 2.4.

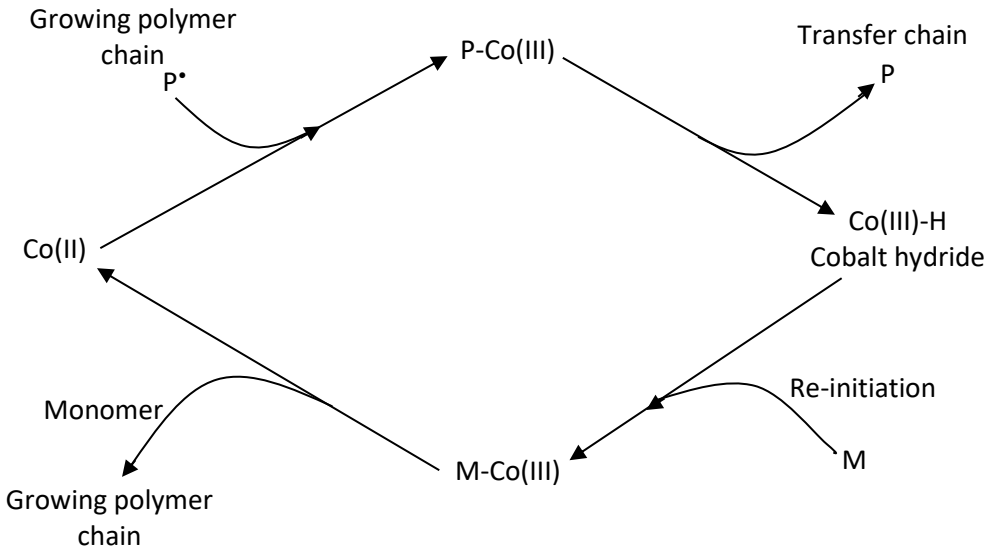


Figure 2.4. Summary of CCT polymerisation using a cobalt catalyst. The growing polymer chain (P•) reacts with the cobalt(II) catalyst, forming a polymer-cobalt(III) intermediate (P-Co(III)), which then undergoes hydrogen abstraction, resulting in a ‘dead’ transfer chain (P) and the cobalt(III) hydride. The cobalt(III) hydride re-initiates an unreacted monomer (M), forming a monomer-cobalt(III) intermediate (M-Co(III)). The monomer then propagates, via reaction with other monomers, recycling the cobalt(II) catalyst for further chain transfer.

CCT reactions allow control of polymer chain length and minimises polydispersity [193-197]. This comes at the cost of reaction speed; CCT reactions are slow, due to the cobalt radical species favourably ‘activating’ unreacted monomer. Nonetheless, control of molecular weights of EGDPEA:DEGMA and the selective binding polymers is invaluable, as it reduces batch to batch variation in molecular weight, polydispersity and therefore

mechanical properties. The CCT polymerisation of EGDPEA and DEGMA is summarised in Figure 2.5.

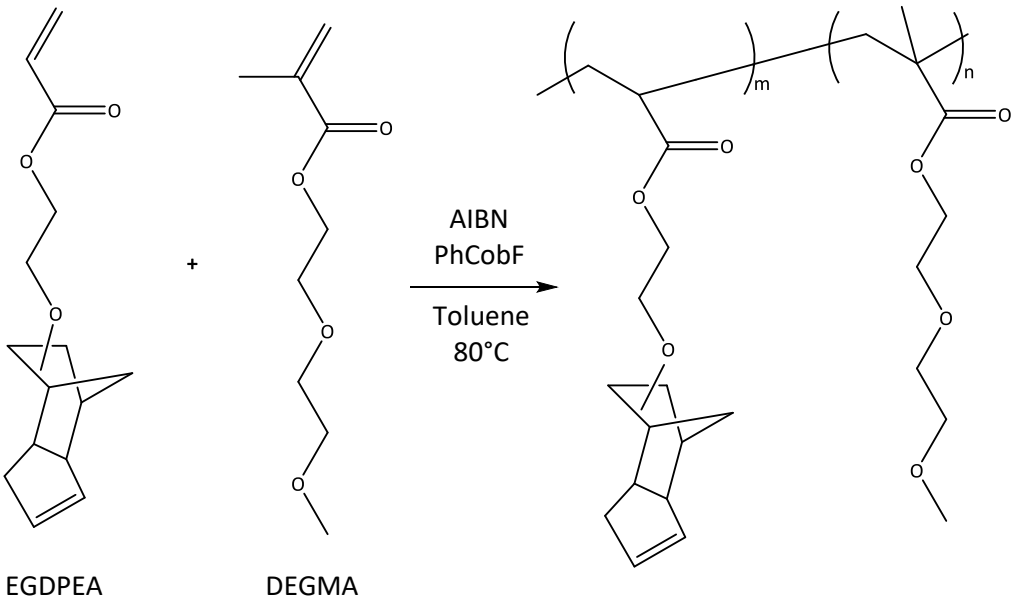


Figure 2.5. Cobalt mediated CCT polymerisation of EGDPEA and DEGMA.

2.2.2. UV photopolymerisation using DMPA

To test the selective binding properties of hit materials identified from polymer microarray fluorescence data, monomer spots were photopolymerised onto silanised glass slides. The photopolymerisation process undergoes the initiation-propagation-termination scheme as in free radical polymerisation [190]. The initiator used was 2,2'-dimethoxy-2-phenylacetophenone (DMPA), which can absorb ultraviolet or visible wavelengths and undergo fragmentation, leading to the formation of two radicals [198,199] (Figure 2.6). Both fragments can transfer their radical onto the monomers to initiate polymerisation (Figure 2.6). Propagation then occurs via acrylate terminal double bond scission, adding monomers onto the growing polymer chain (Figure 2.6). Termination occurs when two radicals (chain-chain or chain-initiator) combine, forming a final polymer chain (Figure 2.6). For this project, UV light was used to activate DMPA; the main advantage of UV

photopolymerisation is the speed of the reaction, with high polymerisation rates occurring in seconds or minutes [200].

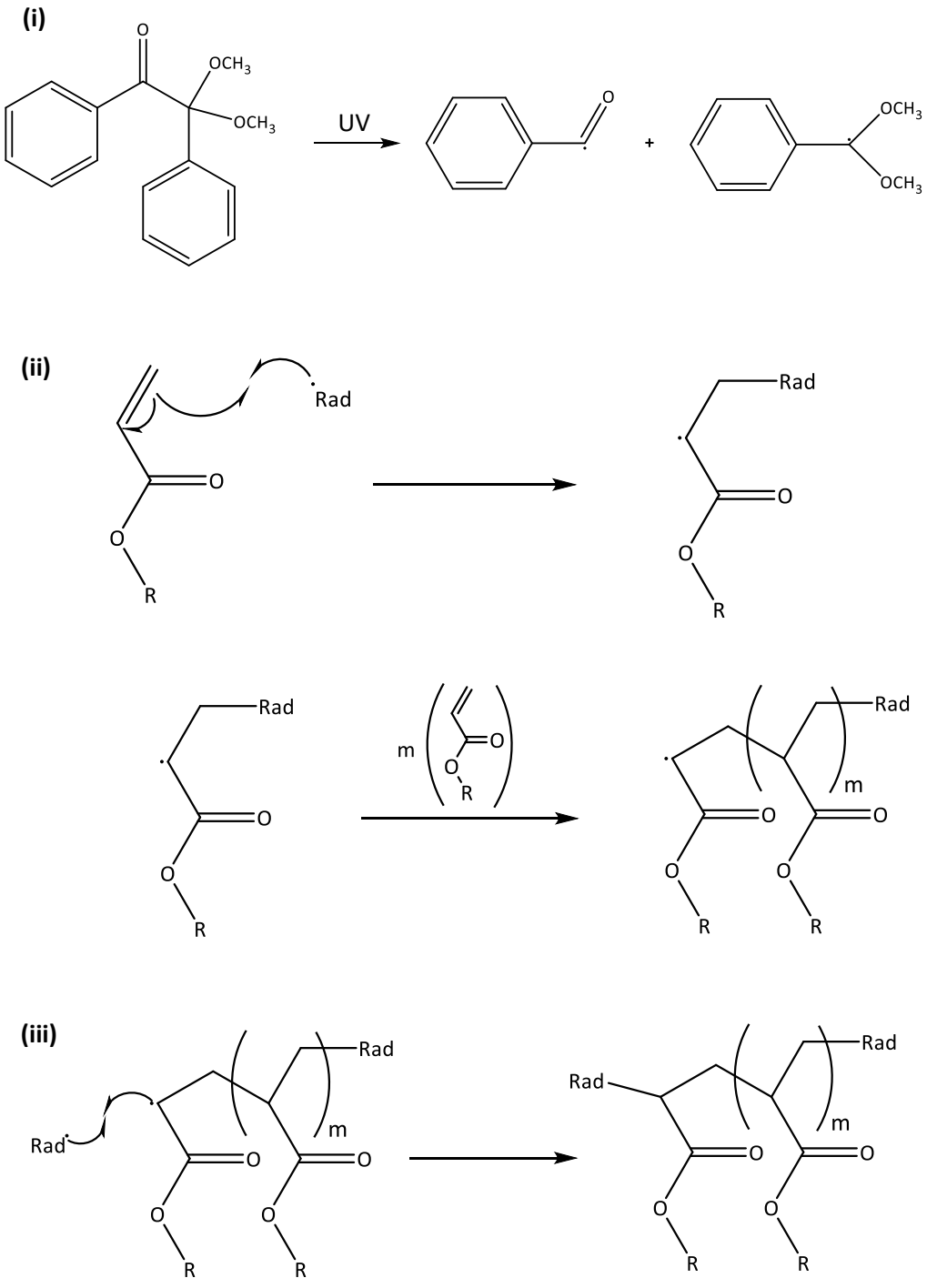


Figure 2.6. (i) Initiation of DMPA by UV light. DMPA fragments into benzoyl and acetal radicals. **(ii)** Propagation steps in acrylate photopolymerisation; radical species (Rad) reacts with a monomer, creating a monomer radical. Further monomers are then added onto the growing polymer chain via the radical terminus. **(iii)** Termination of free radical polymerisation; radical species forms a bond ('cap') with polymer chain terminus.

2.3. Use of a binary silane adhesion promoter

A binary silane adhesion promoter (or primer) was used to improve the adhesion of EGDPEA:DEGMA and the species-selective polymers to PVC and glass substrates. The primer contained two silanes, tetra-*n*-propyl silicate and tetra (2-methoxyethoxy) silane (Figure 2.7).

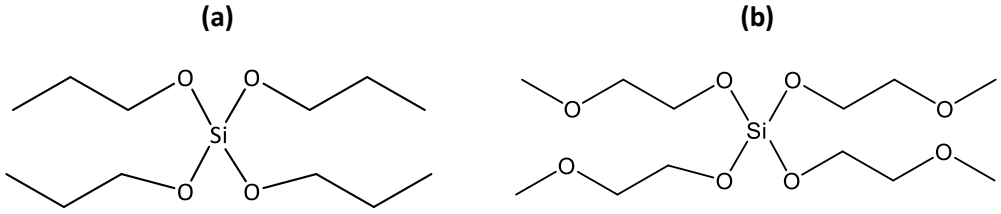
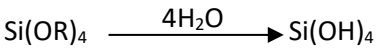


Figure 2.7. Chemical structures of **(a)** tetra-*n*-propyl silicate and **(b)** tetra (2-methoxyethoxy) silane.

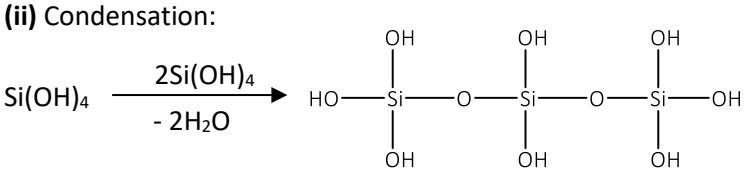
These compounds have substrate and polymer reactive functionalities, allowing improved adhesion between materials [201]. In solution, the alkoxysilanes are hydrolysed to form reactive silanols [202]. The formulation contained a condensation catalyst, which condenses the silanols together [202]. The condensed silanols then hydrogen bond with the substrate, and upon drying, form covalent bonds with the substrate (Figure 2.8). The surface can be thought of as 'reactive' after this step [202].

In the case of PVC, the silanols are unlikely to covalently bind to the substrate. It is more likely electrostatic interactions, such as hydrogen bonding, that are taking place. Nevertheless, the silanols still introduce a reactive layer on PVC substrates, allowing improved polymer-substrate adhesion.

(i) Hydrolysis:



(ii) Condensation:



(iii)

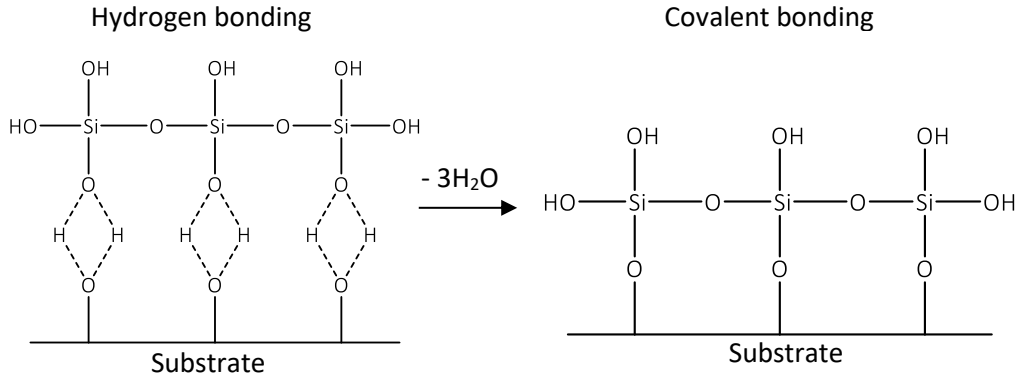


Figure 2.8. (i) Hydrolysis of silanes, forming reactive silanols. **(ii)** Condensation of three silanols to form a silanol trimer. **(iii)** Hydrogen bonding of silanols with substrate, which form stable covalent bonds after the elimination of water.

The polymer was then deposited onto the reactive substrate. The silanes can interact with the polymer via hydrogen bonding, hydrophobic interactions or covalent bonding [201,203]. In each case, the silane-polymer interaction is more resistant to stress than the substrate-polymer interaction, hence the silanes can be thought of as adhesion promoters, improving polymer deposition onto substrates [202]. This serves the purpose of preventing polymer film delamination, which would render an antibiofouling coating ineffective. The binary silane primer used in this thesis was MED1-161 (NuSil Technology LLC).

2.4. Time-of-Flight Secondary Ion Mass Spectrometry (ToF-SIMS)

ToF-SIMS is a surface sensitive technique used to analyse the chemistry of a material's surface, *in vacuo*. This is achieved by bombarding the surface with a focused, pulsed primary particle beam (Figure 2.9) of high energy (0.1 – 40 keV) [204], for a very short time. The ions commonly used in the primary beam are liquid metal ion sources (Ga^+, Bi_n^+; n = 1-7, CS^+), gas ion sources (Ar^+, O^+) or large clusters (C_{60}^+, Ar_{2000}^+) [205]. Bi_3^+ was the primary ion beam used in this thesis, since it offered better secondary ion yield than gallium sources [204]. The primary beam can be rastered over the sample surface, allowing the chemical profile of whole surfaces to be examined. The primary ions impact the surface, dislodging secondary particles from it (single atoms, molecules or ion fragments) at a depth of 1 – 2 nm [205,206]. The ejected secondary particles may be positively or negatively charged ions or unionised species, the latter of which is ejected more abundantly.

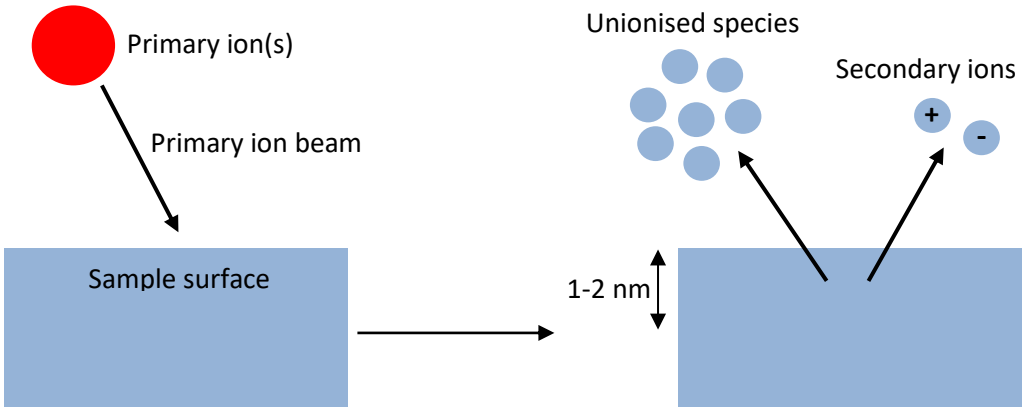


Figure 2.9. Primary ion bombardment of a surface in ToF-SIMS, ejecting secondary species. Most ejected particles are unionised or neutral. Charged secondary species pass into mass spectrometer for analysis.

Only the ionised secondary particles pass into the mass spectrometer for analysis. ToF-SIMS is a destructive process; molecular layers at the material's surface are physically removed. The primary ion dose is kept below 10^{13}

ions/cm^2 to minimise this [205]. Also, ToF-SIMS needs to be carried out in a high vacuum.

During bombardment, the ionisation of secondary species is strongly influenced by the chemical state of the material. Hence, the intensity of detected secondary ions, and the ion yield, is influenced by the surrounding matrix material, known as the matrix effect [207]. This complicates quantitative analysis in static ToF-SIMS and the technique is seen as semi-quantitative. ToF-SIMS can be operated in positive or negative modes, permitting mass spectra of both positive and negative secondary ions to be formed from a single sample.

Once ejected, secondary ions are accelerated over a voltage to impart the same kinetic energy to all ions, provided they have the same charge. This is important for the time-of-flight detection method employed by ToF-SIMS, which separates secondary ions based on the time taken to reach the detector. Since kinetic energy is the same, the time of flight of secondary ions depends on their velocity, which differs between ions of different mass. Ions with high velocity have low mass and short times of flight and vice versa. The time taken for an ion to reach the detector can be calculated using equation 2:

$$t - t_0 = L\left(\frac{m}{2E_K}\right)^{\frac{1}{2}} \quad (2)$$

Where t and t_0 are the arrival and start times of the ion's journey respectively, L is the flight path length, m is the mass of the ion and E_k is the ion's kinetic energy. The different times of flight allow the generation of a mass spectrum, which encompasses all ionised species across the full mass range. A scheme of the ToF-SIMS general operation is shown in Figure 2.10.

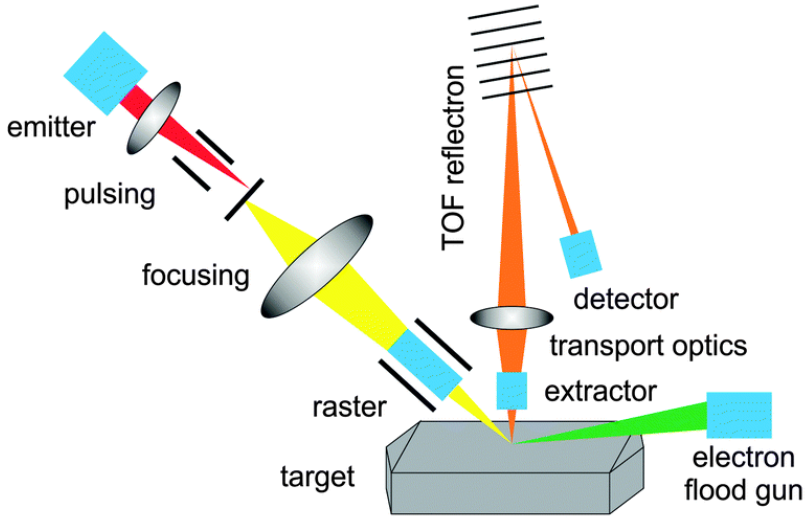


Figure 2.10. Scheme of ToF-SIMS instrumentation and general process of obtaining SIMS data. Image adapted from [208] (open access).

An electron flood gun is required when analysing insulating materials, such as polymers. Using a positively charged primary ion beam can result in the build-up of a net positive charge at the sample surface, which can deflect the primary ion beam (especially when low energy primary ions are used) away from the region of interest. Also, the emission of ions from the surface can be hindered. Surface potential variations affect the energy distribution of emitted secondary ions, which affects their transmission and detection by the mass spectrometer [208]. The electron gun floods the sample surface with low energy electrons to neutralise the surface potential, minimising this undesired collection of positive charge [208].

There is also a reflectron, or ion mirror (represented by the parallel lines in Figure 2.10), between the transport optics and the detector. It serves the function of preventing secondary ions of identical mass and velocity reaching the detector at different times [209]. Although considerable efforts (in instrument design) are made to maintain the same kinetic energies of secondary ions, there may still be slight variations. The reflectron extends the distance that higher energy ions have to travel to reach the detector. Therefore, ions of equal mass and velocity but slightly different kinetic energies

will reach the detector at the same time. They are perceived to have the same time of flight. This reduces false readings, caused by secondary ions of the same mass and charge giving additional peaks in the mass spectrum. These modifications allow the assembly of mass spectra across the full mass range using low primary ion doses [204,205,207].

ToF-SIMS offers a range of data types for analysis. Aside from mass spectra, the detected secondary ion intensities can be used to build a chemical/ion map of the rastered surface. This allows visual representation of the intensity of a desired ion across the sample; the distribution of atomic/molecular species of interest can be assessed. ToF-SIMS can also be used for depth profiling, where secondary ions from different depths of a sample are analysed. This is achieved by bombarding a point of the sample with a primary ablating beam, followed by a primary analysis beam [210]. The ablating beam 'sheds' particles from the surface. The analysis beam generates secondary ions at the depth created by the ablating beam, allowing mass spectra to be gathered for each 'layer' of the sample surface (depth profile). Furthermore, 3D ion maps can be obtained, providing useful visual data about molecular distribution in the *x, y* and *z* directions.

The advantages of ToF-SIMS are the multiple types of data that can be generated (mass spectra, ion map, 3D profiles) across a large mass range, surveying of all secondary ions simultaneously and high sensitivity to ejected secondary ions [204-206]. The acquired data is also chemically rich. ToF-SIMS analysis can be thought of as retrospective; all ion data (mass and point(s) of origin) is recorded, allowing the user to go back and generate spectra/maps of ions not previously investigated. The disadvantages are the destructive nature of the primary ion beam, the lack of quantitative data and the potential of unwanted charge collection on sample surfaces (although the electron flood gun generally abates this) [208].

In this thesis, ToF-SIMS was used to compare the chemical profiles of ETT tubes and cuffs, as well as uncoated and polymer coated surfaces. Ion maps (and ion

intensity data) were generated to compare spatial distribution of desired molecules between samples, in an attempt to relate chemical profiles of surfaces to bacterial attachment. The instrument used was a ToF-SIMS IV (ION TOF GmbH) and data was processed in the SurfaceLab 6 software.

2.5. 3D optical profiling

3D optical profiling is an optical microscopic technique used to analyse the topography of surfaces. Also known as interference microscopy, this system is commonly used to measure height variations at a sample's surface, allowing roughness measurements to be made. This is achieved by using the wave properties of light (constructive and destructive interference) to compare the optical path difference between the sample surface and a reference surface [211], which is a flat mirror. Within the instrument lies a beam splitter, which reflects half the light from the sample and the other half from the reference mirror (Figure 2.11). The distance from the beam splitter to the reference mirror is the same as the distance from the beam splitter to the focal plane(s) of the sample. When the split light from both sources is recombined, constructive and destructive interference occurs, depending on whether the split beams are in phase or out of phase. As the reference mirror is perfectly flat, the differences in optical paths between the split beams is due to height variances at the sample surface. Hence, the 'degree' of destructive interference is representative of height differences between the sample and the reference mirror. The combined beam reaches a digital camera, which portrays constructive interference as lighter areas and destructive interference as darker areas in the interference image (interferogram, Figure 2.11).

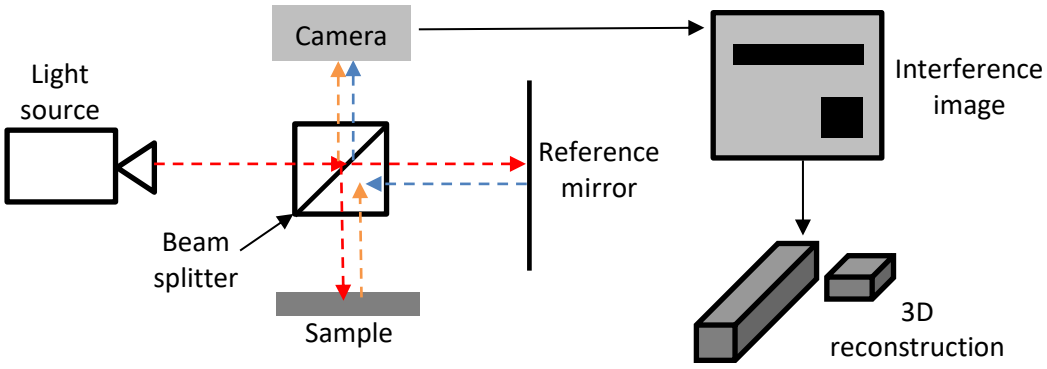


Figure 2.11. Workings of an optical profilometer. The beam splitter splits the light beam between the reference mirror and sample (red arrows), which recombine and constrictively/destructively interfere (blue and orange arrows), resulting in an interferogram. This can then be constructed into a 3D image of the surface. Image adapted from [212].

In the interference image, each transition, from light to dark, represents a height difference in the sample of half the wavelength (of input light – usually pre-selected). The interferogram can be used to generate a 3D image of the surface. Prior to image acquisition, the user selects the upper and lower *z* values (axial focal range of the sample surface), and the number of *z*-stacks within this axial range. An interferogram is generated for the entire *z* range and used to construct a 3D image. Therefore, it is possible to visualise and quantify height differences at the focal plane(s) of the sample surface and calculate mean surface roughness. Roughness is defined as the height difference at a given *x,y* point. The mean roughness is the height variation across the entire image. The 3D image can also be used to produce a 2D composite image, should the user require it. The resolution of the interference microscope depends on the objective used; the *x,y* resolution can get down to 60 nm, with a *z* resolution of 10 nm [213], although sub-nanometer resolution has been reported [211,214]. The optical profiler can also be used as a simple optical microscope, which has a spatial resolution in the sub-micron range [213].

The key advantages of optical profiling are that it is non-contact, so the sample is not damaged. Also, 3D measurements and images can be obtained, the resolution is high and data acquisition is not affected by the environmental conditions, hence samples do not require pre-treatment. Imaging can also be done quickly. However, samples with extremely high or low reflectivity can be challenging to image, as are samples with topographical variations in the tens or hundreds of microns [211,213,214].

In this thesis, a Zeta-20 optical profiler (Zeta Instruments) and associated Zeta3D software were used to image ETT tube and cuff surfaces, to obtain both 3D and 2D images. The mean roughness of all samples was calculated, allowing roughness comparison between device tubes and cuffs; and between uncoated and polymer coated surfaces. ToF-SIMS and optical profile data were used to relate chemical and physical surface properties respectively to bacterial adhesion.

2.6. Confocal laser scanning microscopy (CLSM)

In this thesis, CLSM, or simply 'confocal microscopy', was used to image fluorescent biofilms grown on sample surfaces. Fluorescence refers to the phenomenon undergone by some molecules, which absorb a certain wavelength of light and enter an 'excited' state. In returning to the 'unexcited' or 'ground' state, they emit light of lower energy (longer wavelength, Figure 2.12). In CLSM, only light emitted from the fluorescent object is detected, thus can be differentiated from its surroundings, allowing an image to be created from the emitted fluorescence [215].

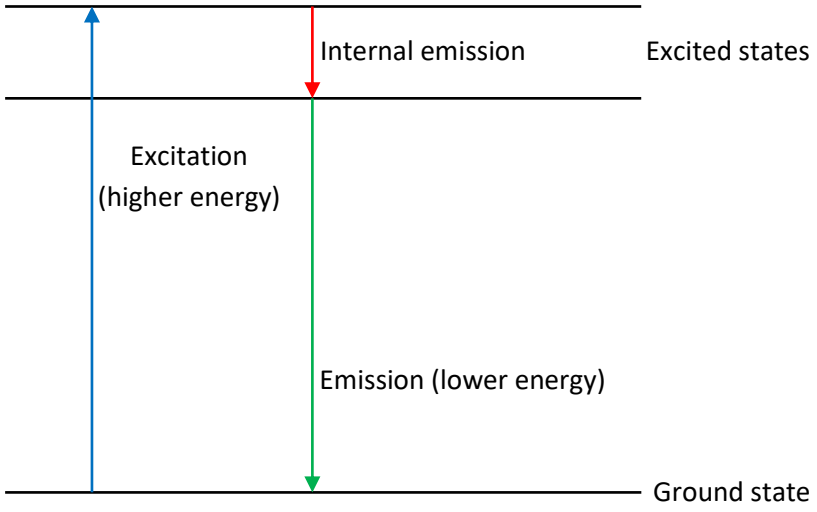


Figure 2.12. The principle of fluorescence. Light of high energy (e.g. blue) is absorbed, causing the molecule to enter an excited state. Some energy is lost internally (within the excited states), represented by the red arrow. On returning to the ground state, light of lower energy (e.g. green) is emitted.

In a confocal laser scanning microscope, the excitation light source is a laser, which is focused onto a dichromatic mirror. The dichromatic mirror reflects the laser light onto the focal plane(s) of the sample via the objective. Fluorophores within the sample then undergo fluorescence (Figure 2.12), emitting lower energy light, which passes through the dichromatic mirror, with a band-pass filter, onto the detector (often a photomultiplier detector) [216]. In a confocal

microscope, a screen with a small pinhole aperture is located between the objective lens and the detector. This pinhole only allows emitted light from the focal point of the objective to pass through to the detector (Figure 2.13 [217]). This removes out-of-focus rays and the subsequent haze often seen in widefield microscope images, which employ much wider detector apertures (allowing emitted light from all planes to reach the detector). Widefield microscopy therefore requires bright illumination sources, to differentiate between focal and non-focal emitted rays, whereas CLSM only requires a focused laser. The pinhole is conjugate to the focal point of the lens, hence the term 'confocal' microscopy.

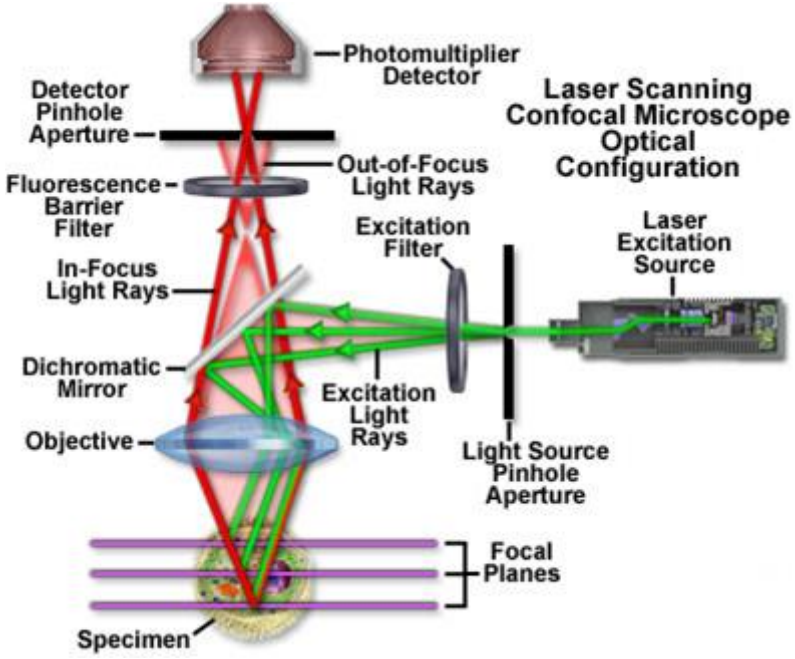


Figure 2.13. CLSM principle. Laser light is focused onto the sample, which emits light of lower energy (fluorescence). Emitted light from the focal plane(s) pass through the detector pinhole aperture onto the photomultiplier detector, whilst out-of-focus light rays do not pass through the detector pinhole. Image adapted from [217].

Due to the focused excitation light source, only small areas of the sample can be imaged at once. However, it is possible to image across the *x,y* plane of the sample by programming the sample stage to move, allowing the laser to scan the sample in a raster pattern. This allows collection of 2D images at multiple areas of the sample. The *x,y* (spatial) resolution of confocal microscopes is

dependent on the numerical aperture (NA) of the lens used and the detector pinhole size and can be as high as 0.2 µm [215,218].

CLSM can also be used for 3D imaging of samples. Since the focal plane covers an axial range (in the *z* direction), it is possible to obtain multiple 2D *z*-stack images within this axial range. The laser 'illuminates' the range of *z*-stacks (or slices), each of which fluoresces, is imaged and then combined to generate a 3D fluorescence image. The field of depth (*z* focal range) is dependent on the numerical aperture and the magnification [219]. The axial resolution (slice thickness), as with the spatial resolution, depends on numerical aperture and pinhole size. Axial resolution is not as high as spatial resolution, but 0.5 µm is achievable [218-220].

The key advantages of confocal microscopy (over widefield techniques) are the ability to control depth of field, elimination of background fluorescence from outside the focal plane and the ability to collect optical sections from thick samples [217,220]. A major advantage of fluorescence microscopy in general is the ability to image multiple biological components in the same environment. This is achieved by labelling each component with a different fluorophore and setting the laser to produce different excitation wavelengths. The main limitation of CLSM is speed; a focused laser beam only excites a small spatial area, so performing a raster scan or *z*-stack can take several minutes.

The ability to control the depth of *z* slices, image in 3D and the higher resolution (compared to widefield microscopy) means that CLSM is widely used for imaging biological samples. Biofilms are commonly imaged using CLSM, since biofilms and/or individual whole cells can be examined in 2D and 3D, with high resolution.

In order to obtain a CLSM image, the sample needs to be tagged with a fluorescent moiety. In the case of bacteria, they can either by dyed or transformed with a plasmid coding for a fluorescent protein. In this project, three pathogenic bacteria were investigated. Each were tagged with a different

fluorophore. Details of the plasmids, fluorophores, excitation and emission wavelengths are summarised in Table 2.1.

Bacteria strain	Plasmid details	Fluorophore/ dye	Excitation wavelength	Emission wavelength
P. aeruginosa (PA01-N)	Nottingham strain with pME6032lacl:: mCherry plasmid [221]	mCherry	587 nm	610 nm
S. aureus (SH1000)	Wild type with PBS10 mKat plasmid	SYTO64	599 nm	619 nm
Uropathogenic *E. coli* (UPEC-GFP)	Clinical isolate with 536 GFP plasmid	Green Fluorescent Protein (GFP)	395 nm (major) and 475 (minor)	509 nm

Table 2.1. Details of plasmids, fluorophores/dyes, excitation wavelengths and emission wavelengths for the bacterial strains used in this thesis [222-224].

2.7. Quantification of biomass and mean biofilm thickness using COMSTAT

CLSM allows excellent visual representation of biofilms and provides qualitative information on bacterial colonisation of a surface, but the ability to quantify biofilm parameters would prove invaluable in analysing biofilm formation on ETT surfaces over time. In this project, biofilms were quantified from their CLSM images using the ImageJ plugin, COMSTAT.

COMSTAT works by analysing each image pixel (for 2D images) or pixels in each *z*-stack (for 3D images), and assigning them an 'ON' (one) or 'OFF' (zero) status. 'ON' pixels are those which have high enough fluorescence to represent biofilm, whereas 'OFF' pixels do not fluoresce enough to be counted as biofilm. In order to decide the 'ON' or 'OFF' status, a user defined threshold value was assigned to the whole image. To determine this value, the threshold was initially set low, then gradually increased until the user was confident that only fluorescence arising from biofilm remained. This allowed removal of single pixels of low brightness, usually on the periphery of the image. Once set, the same threshold value was used for all proceeding images. Though highly subjective, applying the same method to all acquired images meant that false positive or negative selections were the same for all images. COMSTAT then allocated an 'ON' status to pixels that had values equal to or above the threshold and an 'OFF' status to pixels that had values below the threshold. The 'ON' pixels were then used to quantify the selected biofilm parameters.

COMSTAT was used in an attempt to quantify ten different parameters of *Pseudomonas* spp. biofilms by Heydorn *et al*. [225]. The authors concluded that COMSTAT could be used to quantify these ten biofilm parameters and successfully compare differences in biofilm formation between the *Pseudomonas* spp. In this thesis, two specific biofilm features were quantified from CLSM images [225]. Since *z*-stack images were generated, these parameters best permitted the volume of biofilms to be assessed in 3D.

(1) **Biomass** - defined as the number of 'ON' pixels in all images of a stack multiplied by the voxel size [(pixel size)*x* * (pixel size)*y* * (pixel size)*z*] and divided by the substratum area of the image stack. The resulting value was biomass volume divided by substratum area ($\mu m^3/\mu m^2$). Can also be referred to as bio-volume.

(2) **Average biofilm thickness** - this function located the highest point (μm) above each (*x,y*) pixel in the lowest *z*-stack containing biomass. Hence, thickness is defined as the maximum thickness over a given location, ignoring pores and voids inside the biofilm. The thicknesses above each pixel were averaged to calculate mean biofilm thickness (μm).

COMSTAT was used to quantify biofilms of two different bacteria species in a co-culture. This was achieved by setting thresholds for each mode of fluorescence (different channels in the confocal microscope) and quantifying each channel in COMSTAT. This was done simultaneously, by setting up COMSTAT to quantify each channel, using their respective thresholds. The version of COMSTAT used was COMSTAT v. 2.1, downloaded from comstat.dk.

2.8. Long Period Grating optical fibre sensors (LPG OFS) for the real time detection of bacterial attachment

2.8.1. LPG OFS experimental set up

LPG OFS were used to detect bacterial attachment and monitor biofilm formation in real time. LPGs are created by inscribing periodic modulations of refractive index into the core of silica optical fibres, causing the core mode of input light to couple into certain cladding modes [159]. This coupling results in the formation of attenuation bands in the output optical spectrum, with each band representing coupling to a different cladding mode at a certain wavelength [160,161]. Changing the refractive index of the surrounding medium results in a change in the optical properties of the cladding, causing a shift in the wavelength(s) coupling into cladding modes (equation 1). The shift in coupling wavelength could be measured in the associated software, hence the LPG OFS was used as a sensor.

The general set up of the sensor apparatus is shown in Figure 2.14. Light from the HL-2000 halogen light source was directed through the LPG OFS, which passed through the grating to the HR-4000 optical spectrometer. The spectrometer works by splitting light into its spectral components and measuring the signal as a function of wavelength [226]. The light enters the spectrometer through the LPG OFS, where it is focused onto a diffraction grating by a concave mirror. This diffraction grating disperses the spectral components (different wavelengths) of light at different angles. This is then focused by a second concave mirror onto a charge-coupled device (CCD) detector, which is able to convert photons to an electronic signal (Figure 2.14). The electric charge generated is proportional to the intensity of each wavelength of light illuminating the CCD pixels. The software plots the signal as a function of wavelength over a given range, since the light is linearly dispersed across the wavelength range by the diffraction grating [226,227]. Therefore the optical spectrum is a plot of wavelength (x) versus intensity (y) (Figure 2.14). The wavelength(s) of light coupling from core to cladding modes have lower

intensity, resulting in lower charge at the detector and attenuations at those wavelength(s) in the optical spectrum.

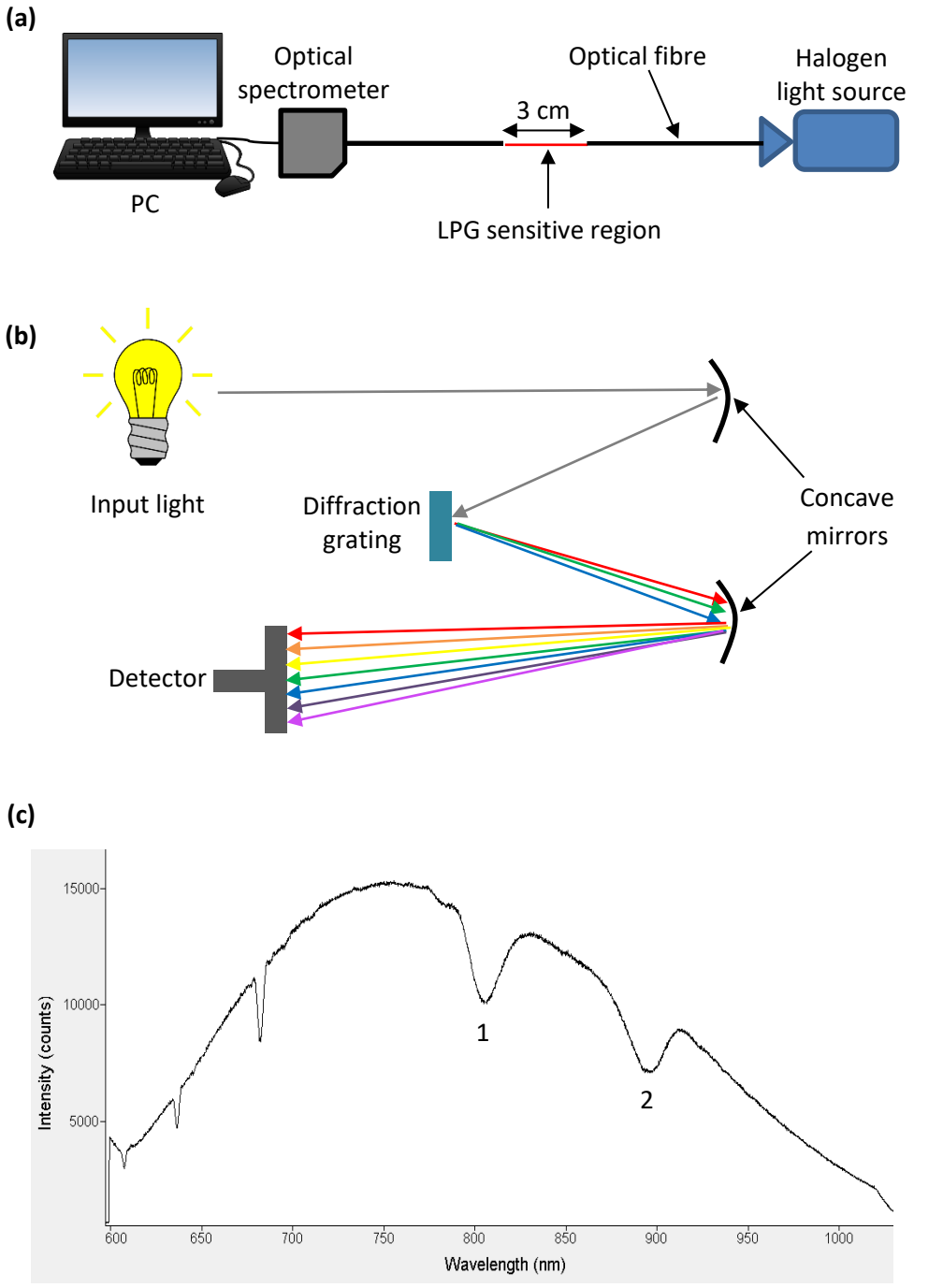


Figure 2.14. (a) Set up of LPG OFS apparatus for spectra collection. **(b)** Principle of optical spectrometers; the first mirror focuses light onto the grating, which separates light into its spectral components. A second mirror then focuses each wavelength onto the detector. **(c)** An example of an optical spectrum displayed in the SpectraSuite software; *x* = wavelength (nm) and *y* = intensity (counts). LPG grating period = 109 µm, in water. Two attenuation bands are present, labelled '1' and '2'.

The sensitive region of the OFS was a 3 cm length of fibre, where the protective jacket was removed and a grating inscribed into the core using a UV laser. This section was placed in the desired environment for sensing. In this project, the LPG was placed into a specially designed polytetrafluoroethylene (PTFE) well (7 x 1.9 x 1 cm, with a 4 cm long channel for the sensitive region of the OFS) for monitoring of biofilm formation; the bacteria culture medium was added into the channel and transmission spectra were collected to monitor changes in refractive index near to the sensor, caused by biofilm progression. In a separate experiment, to monitor biofilm growth on ETT surfaces, the sensitive region was fixed into the lumen of an ETT and onto a section of cuff. For the selective binding experiments, three LPG OFS (each coated with a different polymer) were fixed into the bottom of a petri dish, allowing for simultaneous spectra collection in a bacteria culture medium.

2.8.2. Processing optical spectra and wavelength shift calculations

The SpectraSuite software displays optical spectra as a wavelength versus intensity plot (Figure 2.14). This plot allows the intensity of output light to be established at wavelengths across the optical spectrum. However, it is difficult to measure transmission loss from this plot, since the intensity differs at different wavelengths. It was also difficult to accurately determine the wavelength(s) of attenuation bands.

Therefore, the output spectra were processed, to show wavelength versus transmission percentage. This allowed the transmission loss to be quantified, allowing attenuation (core-cladding mode coupling) efficiency to be observed. In the processed spectra, areas where core-cladding mode coupling did not occur (therefore there was no attenuation band) were displayed at 100% transmission. Attenuation band(s) were represented by ‘peaks’ (losses of transmission, or transmission troughs) at each coupling wavelength. The processed spectra also allowed the wavelengths of attenuations, and subsequently the wavelength shift, to be ascertained.

Processing of optical spectra was performed in OriginPro 8.6 (OriginLab®). Firstly, a baseline was created along the entire spectrum. The baseline was overlaid onto the spectrum, except the attenuations were omitted. The spectrum was then divided by the baseline, resulting in the aforementioned wavelength versus transmission plot. Within OriginPro, the "peak finder" function was used to find the *x* values (wavelengths), at which the minimum *y* values (transmission) of the attenuation bands were located. This was done on all collected spectra and wavelength shift calculated using equation 3.

$$\Delta\lambda = \lambda_{t/c} - \lambda_0 \quad (3)$$

Where $\Delta\lambda$ is the wavelength shift, $\lambda_{t/c}$ is the wavelength of the attenuation band at time *t* or concentration *c* and λ_0 is the wavelength of the attenuation band at time/concentration 0. Wavelength shift was then plotted as a function of time (of bacterial culture media immersion) or concentration (of calibrating solutions).

Figure 2.15 demonstrates a pre- and post-processed optical spectra. The full process of spectra processing is presented in Appendix A.

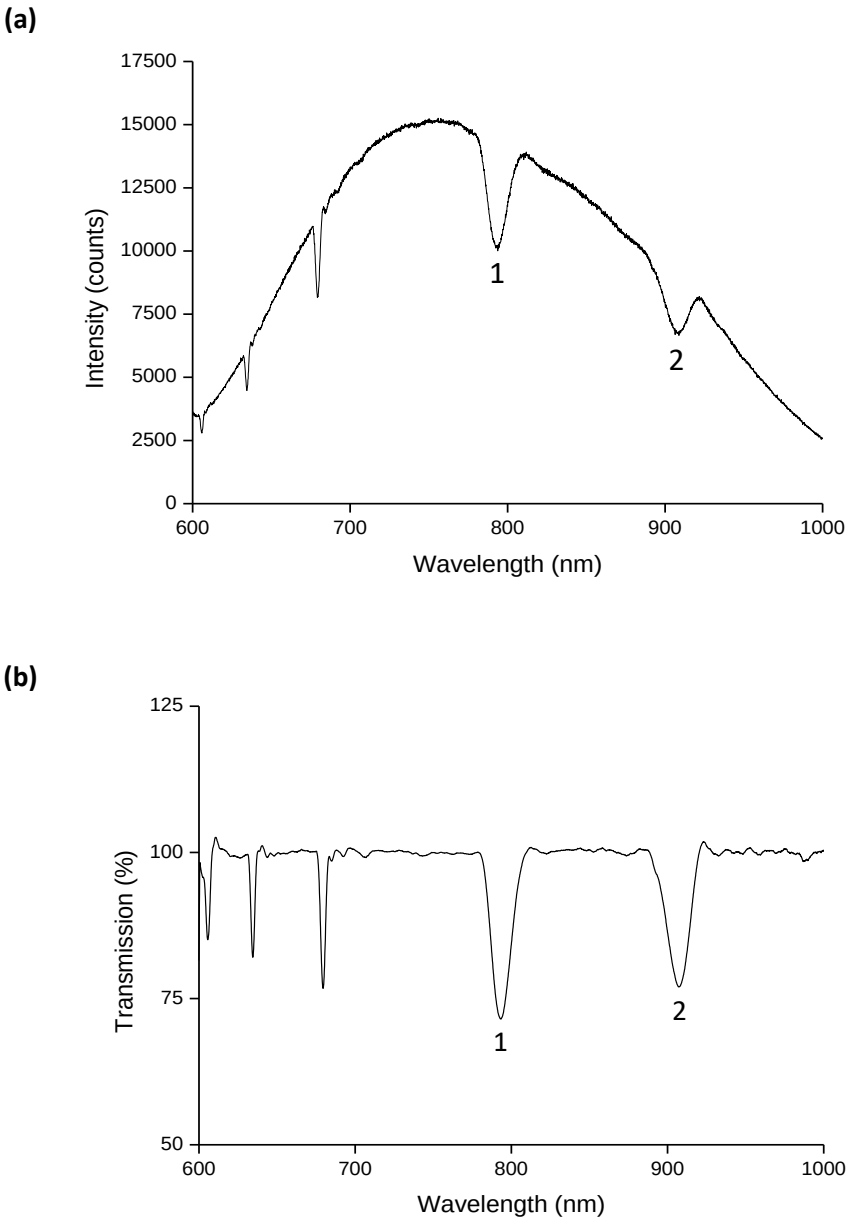


Figure 2.15. (a) Optical spectra before processing; attenuation bands (peaks) are labelled '1' and '2'. **(b)** Same spectra after processing. Note the change in the *y*-axis from intensity to transmission. The baseline is at 100% transmission and the same attenuations (1 and 2) are represented as transmission losses.

3. Development of an endotracheal tube coating resistant to bacterial biofilm formation

3.1. Introduction

Biofilm formation on ETT surfaces can result in the development of VAP in intubated patients [1], which can be fatal in up to 50% of cases [2]. Due to the rise of antimicrobial resistance, these infections are increasingly difficult to treat [49,50]; hence, emphasis lies on infection prevention. Modifying ETT surfaces to resist bacterial attachment may reduce biofilm formation and prevent VAP, reducing the need for antibiotic therapy and lowering mortality among ventilated patients.

Silver hydrogel coatings and polyurethane cuffs are such ETT surface modifications that are currently available [12,111]. Although both have been shown to reduce VAP rates (by 36% and 45% respectively), the clinical evidence is thus far limited [105,111]. Furthermore, these modified devices have not been shown to reduce intubation time, ICU stay or mortality [106,107,111,112]. The silver hydrogel coated ETT is also significantly more expensive than the equivalent PVC device. Antibiotic-impregnated devices [113], poly (ethylene glycol) (PEG) coatings [127] and zwitterionic coatings [122] have also been researched. However, these approaches are hampered by the lack of clinical evidence, interaction with mucus/proteins and potential safety concerns.

This chapter explored the efficacy of a novel polymer, ethylene glycol dicyclopentenyl ether acrylate (EGDPEA) as a bacteria-resistant coating for ETTs. EGDPEA belongs to a group of anti-biofilm polymers, characterised as having rigid hydrophobic side groups [186]. It was discovered by Hook *et al*. using a high throughput polymer microarray screening process [141]. It was shown to reduce bacterial adhesion to silicone catheters, both *in vitro* (by 96.7%) and *in vivo* (99.5% reduction in bacteria bioluminescence). It has also passed industry safety and toxicity tests and has been licensed to coat urinary

catheters for human use. The ductility of EGDPEA coatings was improved by co-polymerising it with di (ethylene glycol) methyl ether methacrylate (DEGMA) [186], in a 75:25 molar ratio.

The effect of a binary silane primer on the coating's adhesion and bacteria-resistant properties was also investigated. The primer consisted of two silanes, tetra-*n*-propyl silicate and tetra (2-methoxyethoxy) silane and has been used to improve the adhesion of polymers to a range of substrates, such as silica, plastics and ceramics [201]. Silane primers have previously been shown to improve the adhesion of EGDPEA:DEGMA to polydimethylsiloxane (PDMS) substrates [228]. Applying the primer to ETT surfaces before EGDPEA:DEGMA coating may improve the adhesion of the polymer, which could enhance the bacteria-resistant properties of the surface. In this study, polymer adhesion, coating thickness and anti-attachment activity with and without primer treatment was examined.

RPMI-1640 was the minimal medium used for biofilm assays. It contained the minimal necessities for cell growth and therefore accelerated biofilm formation [229]. Bacterial attachment in Artificial Sputum Medium (ASM) was also investigated. ASM contained all the amino acids and several salts and was intended to imitate human bronchial and lung secretions. It has been used in biofilm assays to model lung infections, such as in cystic fibrosis investigations [230], since sputum from live volunteers can have variations in sugar and protein content [231]. Bacterial attachment in ASM with and without glucose was investigated, on uncoated and coated ETT surfaces.

3.2. Aims

The aims of this experimental chapter were:

1. Synthesise EGDPEA:DEGMA and ascertain polydispersity and monomer conversion.
2. Coat ETT main bodies and cuffs in EGDPEA:DEGMA and investigate the attachment of *Pseudomonas aeruginosa* to uncoated and coated substrates, in RPMI-1640 and ASM.
3. Explore the usefulness of a binary silane primer as an adhesion promoter for EDGPEA:DEGMA coatings.
4. Compare surface chemical and physical profiles of device tubes and cuffs, and uncoated and coated surfaces, using ToF-SIMS and optical profiling respectively.

3.3. Experimental

3.3.1. Synthesis of EGDPEA:DEGMA

240 mg AIBN, 100 mg PhCobF, 75.2 mL EGDPEA, 20.8 mL DEGMA and 200 mL toluene were combined and degassed with argon for 30 minutes, before heating at 80°C for 24 hours with stirring. Argon gas was flushed into the headspace of the reaction vessel throughout, to prevent early termination by oxygen. The polymer was then precipitated twice, by adding dropwise to cold hexane. Excess hexane was decanted and the remainder removed by vacuum drying the polymer at 0.11 Torr for 4 hours.

An aliquot of the final polymer product was analysed by gel permeation chromatography (GPC), using a PL-GPC 50 plus instrument (Agilent-Varian Inc., USA). The column used was a Polymer Labs PLgel guard column (50 x 7.5 mm, 8 µm), followed by a pair of PLgel Mixed-D columns (300 x 7.5 mm, 8 µm). Polystyrene (PS) was the standard used, with chloroform as the eluent. GPC allowed the polydispersity and molecular weight of the polymer to be assessed. ^{1}H nuclear magnetic resonance (NMR) spectroscopy was also performed on EGDPEA and DEGMA monomers, the polymer crude mix and the purified polymer, in deuterated chloroform, using a Bruker AV400 spectrometer, operating at a frequency of 400.3 MHz. The ^{1}H NMR spectra allowed monomer conversion and feed ratio to be established.

3.3.2. Dip coating

1 cm^{2} sections of ETT tube and cuff were cut, cleaned by immersing in acetone and left to dry. A 30% w/v polymer solution was made by dissolving 7.5 g polymer in 25 mL dichloromethane (DCM). ETT sections were dipped into the polymer solution using a Holmarc HO-TH-01 dip coating unit (India); the mechanical arm of the unit was set to withdraw samples from the polymer solution at 1 mm/s. Coated samples were dried under ambient conditions for 24 hours, then under vacuum (0.11 Torr) for a further 24 hours. When using

the binary silane primer (MED1-161), samples were dip coated into the primer and withdrawn at 2 mm/s. They were left to dry under ambient conditions for 30 minutes before being dipped into the polymer solution. Four different ETT modifications were investigated; uncoated (U), polymer coated (C), primed and coated (PC) and primed only (P).

To calculate coating thickness, samples were weighed before and after coating (Mettler-Toledo AB265-S/FACT weighing balance, Switzerland). Since the density of EGDPEA:DEGMA was measured to be 1.61 g/mL (by weighing 1 mL of the polymer) and the *x,y* dimensions of the ETT sections were 1cm^2, the volume of the coating, and subsequently the coating thickness, was calculated using equation 4.

$$t = m/(2\rho) \quad (4)$$

Where t is the coating thickness (in cm), m is the average weight gain per sample (in g) and ρ is the measured polymer density (in g/cm^3 or g/mL).

3.3.3. Revolution-to-delamination (RTD) assay

The RTD assay was used to assess the stability (or resistance to stress) of the interface between EGDPEA:DEGMA and PVC ETTs. The RTD of the polymer coating alone was compared to the binary silane primer plus the polymer coating, to assess the utility of the primer. The RTD test subjects samples to a rolling compression, which puts interfacial stresses upon the interfaces [228]. The output revolution-to-delamination (RTD) value can be compared to interfacial stability. For ETT tubes, an entire circular cross section was used for the test. Samples were dip coated in polymer, or in primer followed by polymer (section 3.3.2). Coated and dried samples were placed between two glass slides and a 1 kg weight placed on top. The bottom slide was fixed and the top slide was moved back and forth, causing the sample to roll between the two slides. For device tubes, the sample was rolled until a full revolution was completed,

then the direction of rolling was reversed. This process was continued until polymer delamination was observed or 1000 rotations was completed.

3.3.4. Time-of-Flight Secondary Ion Mass Spectrometry (ToF-SIMS)

Samples were loaded into the vacuum chamber of the ToF-SIMS IV (ION TOF GmbH) instrument. A primary Bi_3^+ ion beam, at 25 keV and 0.3 pA, was randomly rastered over a 500 µm x 500 µm area patch of the sample surface. The raster size was 256 x 256 pixels, with 1 shot/pixel acquired. 20 scans were performed on each sample. The primary ion dose was kept below 1 x 10^{12} ions/cm^2, maintaining static SIMS conditions. A charge compensation device was employed, so to reduce the build-up of positive charge (originating from the primary ion beam) at the sample surface [208]. Both positive and negative ions were collected for analysis. Secondary ion masses were determined by the high resolution ToF analyser.

Secondary ion data were analysed in the SurfaceLab 6 software (ION TOF GmbH). Ion intensities were normalised to the total ion count and ion intensity 'maps' (chemical images) generated, allowing visualisation of the intensity of ions associated with the acrylate from EGDPEA ($C_3H_3O_2^-$, m/z = 71.01) [232], the methacrylate from DEGMA ($C_4H_5O_2^-$, m/z = 85.03) [233], silanes from the primer (SiO_4^{4-}, m/z = 22.99) [234] and the phthalate originating from the diethylhexyl phthalate (DEHP) plasticiser ($C_8H_4O_4^{2-}$, m/z = 82.01) [235]. On the whole ion chemical images, three 70.3 μm^2 regions of interest (ROIs) were randomly selected and a mass spectrum collected for each ROI. These mass spectra were used to calculate the average ion intensity for the desired secondary ions, after calibration using the C^- ion (m/z = 12.01).

3.3.5. 3D optical profiling

Samples were placed onto the stage of the instrument (Zeta-20 Optical Profiler). The upper and lower *z* limits of the surface were set by finding the axial focal range (i.e. the *z* range within which the sample was in focus). 400 steps (*z* slices) were profiled within the axial range of each sample. The spatial field of view was set at 1169 µm x 876 µm, using a 20x objective (NA = 0.45). 3D images and the associated 2D reconstructions were obtained, with the latter used to quantify mean square roughness. This was achieved by selecting three random 250 μm^2 areas of the 2D image. The Zeta3D software quantified surface roughness by recording height differences within the axial range (inside a 250 μm^2 area), based on the light and dark contrasts in the interferogram [211]. These height differences were used to calculate an average height difference between the sample and the reference mirror (Figure 2.11). The resulting datum was the mean square roughness of one 250 μm^2 area. This was done on all three selected squares, to ascertain the average roughness across the random areas of the sample surface. Optical profiles were acquired and mean square roughness quantified for U, C, PC and P tubes and cuffs.

3.3.6. Biofilm assays

The *Pseudomonas aeruginosa* strain (PA01-N) was streaked onto a pre-prepared LB (Luria-Bertani) agar plate and left to grow at 37°C for 24 hours, after which a single colony was taken using a sterile plastic loop and added to a 50 mL centrifuge tube (Falcon) containing 5 mL RPMI-1640 medium. This centrifuge tube was incubated at 37°C overnight, with shaking (200 rpm). The optical density at 600 nm (OD_{600}) was measured for the overnight culture and diluted with more RPMI-1640 to achieve a final OD_{600} of 0.05. ETT samples (U, C, PC and P) were placed into single well chamber slides (Nunc® Lab-Tek® II, Sigma Aldrich UK) and the bacteria culture medium added. The lids were placed onto chamber slides and samples incubated at 37°C, with 60 rpm shaking, for 24 hours. Samples then underwent three 10 minute wash cycles; twice with

phosphate-buffered saline (PBS, pH = 7.4) and once with deionised water, to remove any unattached cells.

Two types of Artificial Sputum Medium (ASM) were investigated; ASM containing glucose (ASM G) and without glucose (ASM N). The method of producing ASM was adapted from Palmer *et al*. [236] and is presented in Appendix B. The biofilm assay in both ASM types followed the same directive as in RPMI-1640, except the RPMI-1640 was substituted with the desired ASM for the overnight and diluted cultures. The wash cycles were also done twice with PBS (pH = 7.4) and once with water, as with RPMI-1640.

The fate of any biofilms beyond 24 hours was also investigated, with biofilms allowed to grow until the 72 hour time point, in all three media, on all modified surfaces. CLSM images were acquired at 48 and 72 hours (after three wash cycles) and biomass/mean thickness quantified using COMSTAT.

3.3.7. CLSM of biofilms grown on ETT tubes and cuffs

Biofilms were imaged using a Zeiss LSM 700 confocal microscope (Carl Zeiss, Germany). Washed samples were placed under a 10x objective (NA = 0.3) and the wavelength of the Ar/Kr laser set at 555 nm, to excite mCherry (excitation = 587 nm and emission = 610 nm) [222]. The power of the laser was set at 1.5 mW and the detector gain was kept between 800 and 900. *Z*-stack images were taken for each sample; the upper and lower slices were set by cycling through the axial range, in both directions, until no fluorescence was observed (or the image was out of focus). The slice at which no fluorescence was seen was set as the upper/lower stack. An average of 40 *z* slices were taken for each image, with an average step height of 6.10 µm. The detector pinhole was optimised to 1 AU, which gave a pinhole size of 34.1 µm. Images were acquired and processed in the ZEN 2009 software. 2D and 3D images were taken, for display and biomass/thickness quantification respectively.

3.3.8. Quantification of biomass and mean biofilm thickness using COMSTAT

All CLSM images were imported into the ImageJ plugin, COMSTAT, for quantification of biomass and mean biofilm thickness. A user-defined threshold was established for the first image in the queue, by setting the threshold to its minimum and increasing it until only fluorescence associated with biomass was observed (i.e. bright pixels clustered together). The threshold value was kept the same for the remaining images in the queue. This ensured that any background fluorescence or low brightness pixels associated with noise were minimised and any background contributions were the same for all images. The threshold was inputted into the COMSTAT menu and biomass and average thickness selected for quantification. The resulting data was copied into Microsoft Excel 2013 for analysis and presentation.

3.4. Results

3.4.1. GPC and ^{1}H NMR analysis of EGDPEA:DEGMA

GPC was used to quantify the molecular weight and the polydispersity index of the EGDPEA:DEGMA polymer. Proton nuclear magnetic resonance (^{1}H NMR) spectroscopy was used to calculate the conversion of monomers to polymer, as well as the feed monomer ratio. Table 3.1 summarises the data from both techniques, as well as the yield by weight (measured using a Mettler-Toledo AB265-S/FACT weighing balance, Switzerland). ^{1}H NMR spectra are presented in Appendix C.

Yield by weight	58%
Molecular weight (g/mol ± % 0.95 CI)	1.841×10^{4} (± 6.2335%)
Polydispersity index (± % 0.95 CI)	1.637 (± 8.815%)
EGDPEA conversion	57%
DEGMA conversion	>99%
Feed monomer ratio	1.3:1

Table 3.1. Yield by weight, molecular weight (from GPC), polydispersity index (from GPC), monomer conversion (from ^{1}H NMR) and feed monomer ratio (from ^{1}H NMR) for synthesised EGDPEA:DEGMA. CI = confidence interval.

3.4.2. Coating thickness on ETT tubes and cuffs

After dip coating and drying ETT sections, a visible 'sheen' was seen on C substrates (Figure 3.1) and a translucent silane layer was seen on the P samples. The weight difference per ETT sample before and after polymer coating was calculated, and the density of the polymer was measured, by weighing 1 mL of EGDPEA:DEGMA. The weight gained and density were used to calculate polymer coating volume, which was subsequently used to estimate coating thickness, since the *x,y* dimensions of the ETT samples were known (1 cm^{2}). Equation 4 was used to calculate coating thickness.

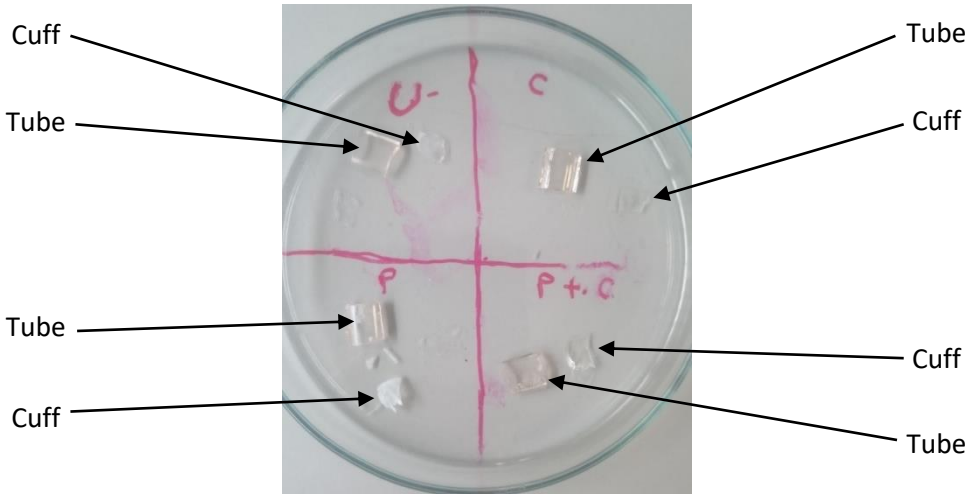


Figure 3.1. 1 cm^2 sections of ETT tubes and cuffs, with the four surface modifications. U = uncoated, C = EGDPEA:DEGMA coating, P = silane primer only, P+C = silane primer plus EGDPEA:DEGMA coating. A visible sheen is seen on polymer coated substrates and a translucent white layer seen on the primed only samples.

The sheen was visible on both C and PC samples, such that they were visually indistinguishable from each other. The polymer coating thicknesses were calculated using the density of EGDPEA:DEGMA, which was measured to be 1.61 g/mL.

Since the sensitivity of the weighing scales was insufficient to accurately determine weight gain per sample, ten tube sections and ten cuff sections were weighed together and the average weight gain per tube/cuff calculated. The volume of the coating and therefore the average coating thickness was established using equation 4 (n = 3; 3 repeats of 10 samples, total 30 samples). The average weight gain and calculated coating thicknesses are shown in Table 3.2, for C and PC tubes and cuffs.

ETT section	Surface modification	Average weight gain (mg) (± SD, n = 10)	Average coating thickness (nm) (± SD, n = 3)
Tube	Coated	0.180 ± 0.010	559 ± 32
	Primed and coated	0.202 ± 0.007	627 ± 22
Cuff	Coated	0.157 ± 0.008	487 ± 25
	Primed and coated	0.177 ± 0.009	549 ± 29

Table 3.2. Average weight gain and coating thickness of EGDPEA:DEGMA coatings on ETT sections. Polymer coated (C) and silane primed plus polymer coated (PC) samples are displayed. Weight gain per sample was the average of ten samples weighed together. The coating thickness was the average of three repeats of ten samples (total 30 individual samples).

The coating thickness varied between 480 and 630 nm for all samples. The thickest coating of 627 ± 22 nm was on PC tubes, which was higher than without the primer. This was also the case on cuffs. Furthermore, the coating thickness on ETT tubes was higher than on cuffs, for C and for PC surfaces. Samples which were primed only did not gain any weight, although a silane layer was seen on sample surfaces.

3.4.3. Revolution-to-delamination (RTD) assay

The RTD test was performed to establish the resistance to stress of the polymer-PVC (or polymer-primer) interface. Delamination was confirmed when any polymer residue was observed on the bottom glass slide, which was examined after each revolution. There was a significant increase (no error bar overlap) in RTD on PC ETT tubes than on C ETT tubes (mean 505 versus 11), highlighting the adhesion promoting effects of the binary silane primer (Figure 3.2).

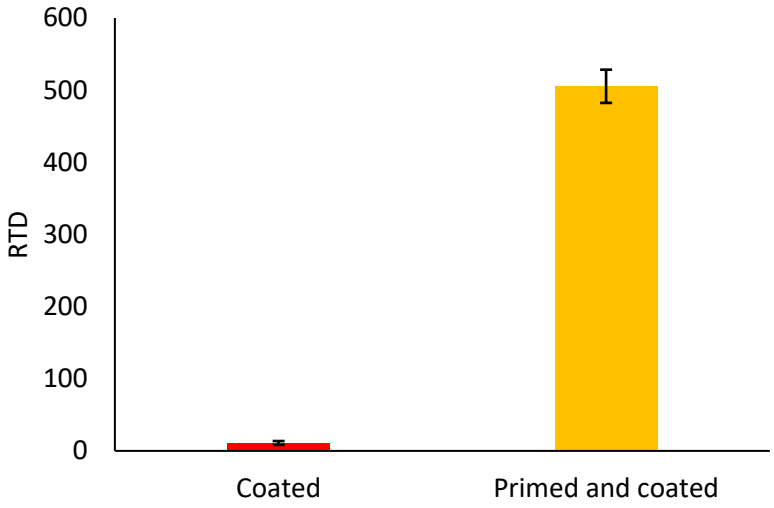


Figure 3.2. RTD observed for ETT cross sections dip coated in EGDPEA:DEGMA polymer only, and silane primer with the EGDPEA:DEGMA coating. Error bars are ± SD, n = 3.

3.4.4. ToF-SIMS of ETT sections

The surface chemistry of the four different surfaces were assessed by ToF-SIMS. Ion intensity maps were generated for four secondary ions of interest; the acrylate anion ($C_3H_3O_2^-$), the methacrylate anion ($C_4H_5O_2^-$), the silicate anion (SiO_4^{4-}) and the phthalate anion ($C_8H_4O_4^{2-}$). Chemical images were generated for both tubes and cuffs and comparisons made between the four surface modifications, where relevant. The normalised ion intensity for each ion was also plotted. Figure 3.3 shows the ion intensities for the secondary ions quoted above. The negative mass spectra and chemical images are presented in Appendix D.

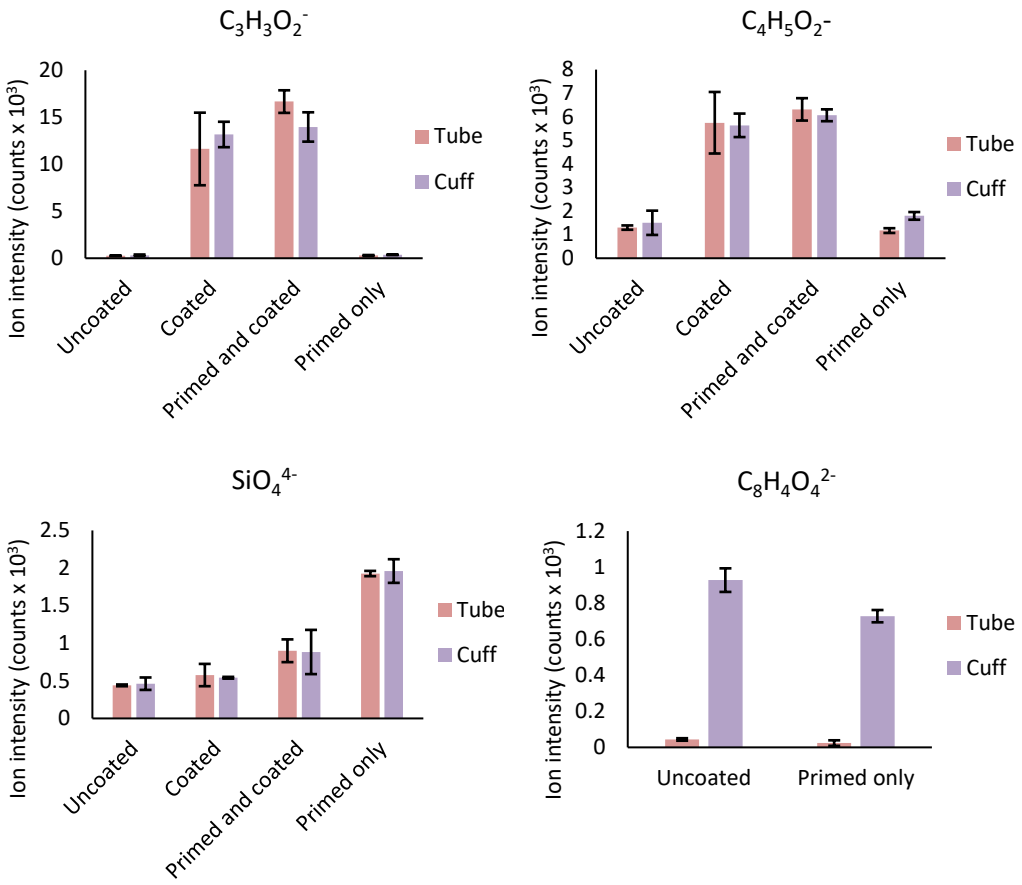


Figure 3.3. Ion intensities of four secondary ions ejected from ETT surfaces measured by ToF-SIMS; the acrylate anion ($C_3H_3O_2^-$), the methacrylate anion ($C_4H_5O_2$-), the silicate anion (SiO_4^{4-}) and the phthalate anion ($C_8H_4O_4^{2-}$). Ion intensities are expressed as counts x 10^3. Error bars are ± SD, n = 3 ROIs.

For the acrylate, methacrylate and silicate anions, there was no difference between tubes and cuffs. However, there was a 21- and 36- fold increase in phthalate ion intensity on U and P cuffs respectively, compared to tubes, which was a significant increase (no error bar overlap). This indicates a higher phthalate content on those surfaces. There were no phthalate ions detected on C or PC substrates. For the acrylate and methacrylate anion intensities, C and PC substrates were higher than U and P substrates and there was no difference between either pair. The P substrates were higher than the other three surfaces when comparing silicate ion intensity, with no difference between the other three surface modifications (error bar overlap).

3.4.5. 3D optical profiles and roughness quantification

Surface optical profiles were obtained for all ETT samples, with all four surface modifications. They were imaged under a 20x objective (NA = 0.45) and *z*-stack (3D) and 2D reconstructions were obtained. The 2D reconstructions were used to quantify mean square roughness (in µm) across three randomly selected 250 μm^2 areas. Figure 3.4 shows the 2D images acquired from optical profiling and the quantified mean square roughness of ETT samples.

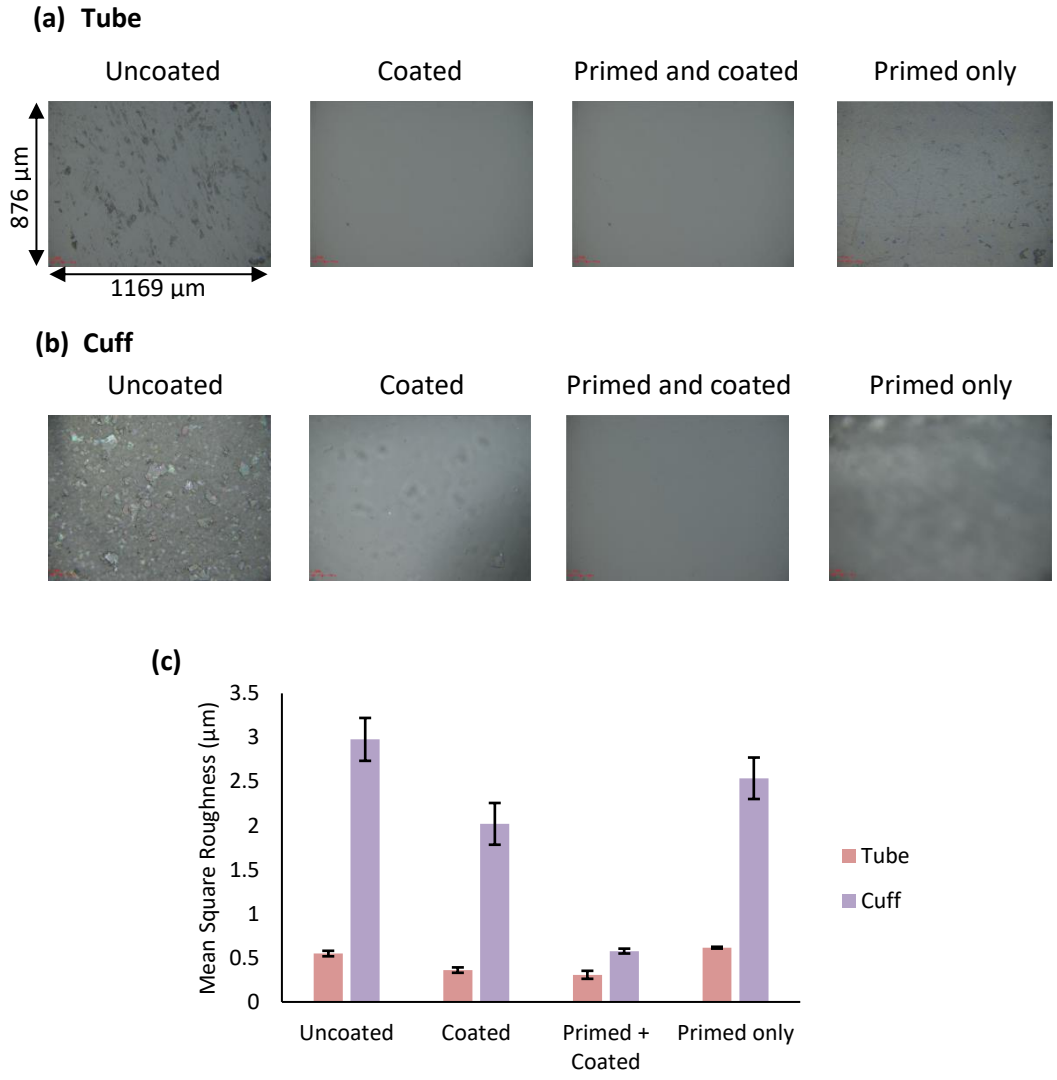


Figure 3.4. Optical profiles of ETT sections and quantified mean square roughness. **(a)** 2D reconstruction of tube surfaces. **(b)** 2D reconstruction of cuff surfaces. U, C, PC and P substrates are shown. 2D image dimensions are 1169 µm x 876 µm and are applicable to all images. **(c)** Quantified mean square roughness of ETT tubes and cuffs, with the four surface modifications. Error bars are ± SD, n = 3.

For each of the four surface modifications, the roughness of tube surfaces was between 0.3 and 0.7 µm and were significantly lower than their cuff counterparts (no error bar overlap). On both tubes and cuffs, the application of the EGDPEA:DEGMA coating reduced the mean surface roughness compared to the U substrates. This was also the case on PC tubes and cuffs, compared to the U versions. Furthermore, PC surfaces had lower surface roughness than C surfaces, for both tubes and cuffs. However, the surface roughness between tubes and cuffs were more comparable on PC substrates than the other three surface modifications. There was no difference in surface roughness between U and P substrates.

3.4.6. CLSM images of *P. aeruginosa* biofilms on ETT sections and quantification of biomass and mean biofilm thickness

U, C, PC and P tube and cuff sections were incubated in a *P. aeruginosa* (PA01-N) culture in RPMI-1640, ASM G and ASM N for 24 hours. After the three wash cycles, they were imaged under a Zeiss LSM 700 confocal microscope, with *z*-stack and 2D images acquired. The *z*-stack images were used for biomass and biofilm thickness quantification in COMSTAT.

3.4.6.1. Biofilm assay in RPMI-1640

Figure 3.5 shows the 2D images of *P. aeruginosa* biofilms, labelled with mCherry, on tubes and cuffs, with the four surface modifications, in RPMI-1640. The corresponding biomass and average thickness data from COMSTAT are also presented.

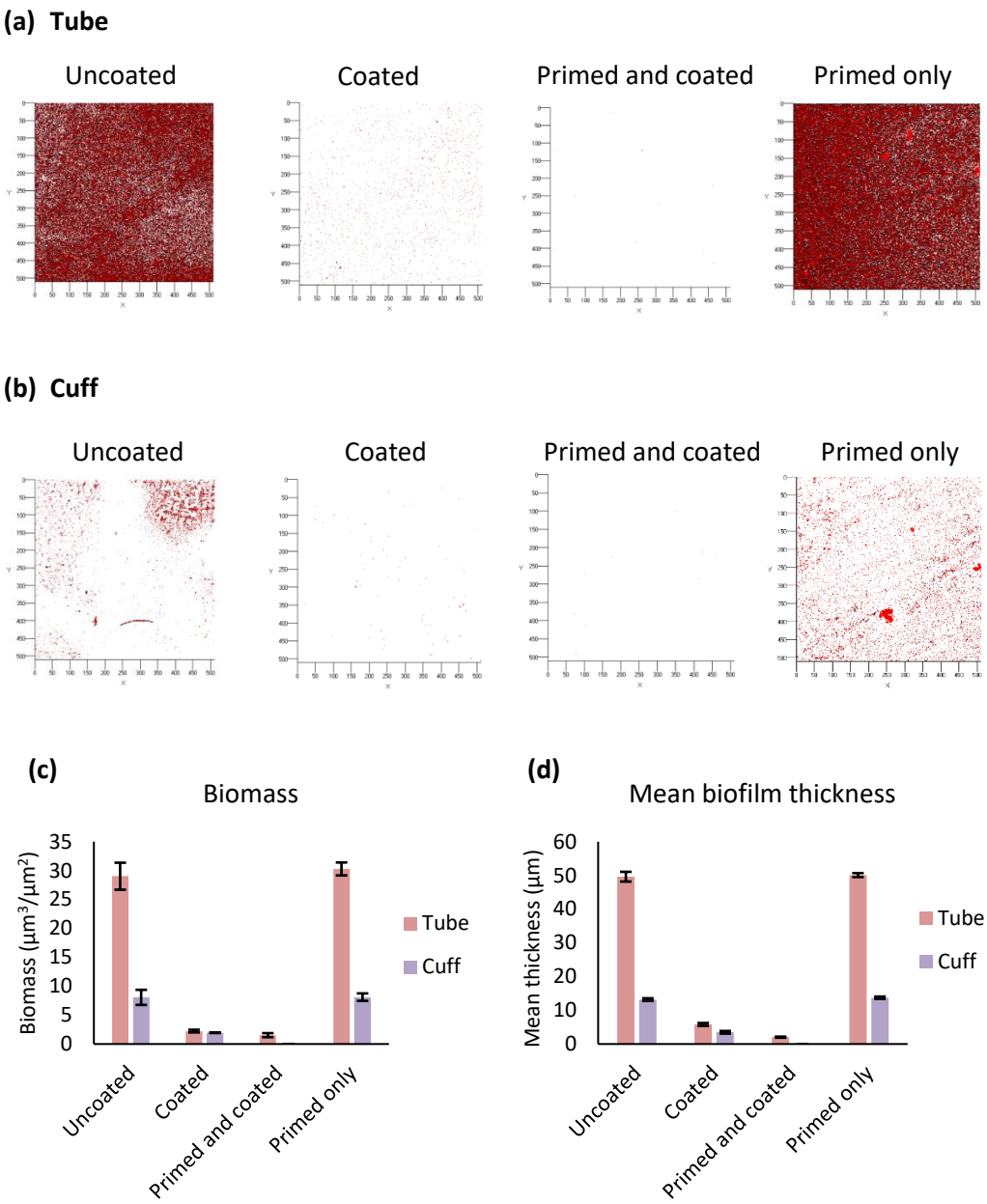


Figure 3.5. 2D CLSM images of *P. aeruginosa* (PA01-N) biofilms, labelled with mCherry, grown on **(a)** ETT tubes and **(b)** cuffs in RPMI-1640, for 24 hours, with the four surface modifications (U, C, PC and P). The red areas indicate biofilm. Scale bars are 500 µm x 500 µm. **(c)** Quantified biomass of images (a) and (b), using a COMSTAT threshold of 60. Error bars are ± SD, N = 3. **(d)** Quantified mean biofilm thickness of images (a) and (b), using a COMSTAT threshold of 60. Error bars are ± SD, N = 3.

On U, PC and P substrates, biomass and thickness on device tubes were significantly higher than on cuffs (no error bar overlap for both parameters). There was no difference in biofilm parameters between tubes and cuffs for C substrates. The EGDPEA:DEGMA coating, with and without the primer,

significantly reduced attachment to both tubes and cuffs, compared to the U ETTs (no error bar overlap for both parameters, on all substrates). The PC tubes had lower biofilm thickness compared to C tubes, but there was no difference in biomass. Furthermore, biomass and thickness were significantly reduced on PC cuffs (no error bar overlap) than on C cuffs. There was no biofilm present on the PC cuff after 24 hours. Biomass and thickness on P samples were no different to the corresponding U samples.

The mean percentage reduction in biomass and mean thickness on C and PC tubes and cuffs are summarised in Table 3.3.

	Tube		Cuff	
	B	T	B	T
Coated	92%	88%	76%	74%
Primed and coated	95%	96%	100%	100%

Table 3.3. Mean percentage reduction in biomass (B) and mean thickness (T) on C and PC ETT tubes and cuffs, relative to U substrates, for *P. aeruginosa* (PA01-N) biofilms grown in RPMI-1640.

3.4.6.2. Biofilm assay in ASM

The same biofilm assay was performed in ASM G and ASM N. The same method was applied as with RPMI-1640, with CLSM images obtained for tubes and cuffs, with the same four surface modifications. Figures 3.6 and 3.7 show the CLSM images and the corresponding biomass/thickness data obtained from COMSTAT for *P. aeruginosa* (PA01-N) biofilms grown on ETT sections in ASM G and ASM N respectively.

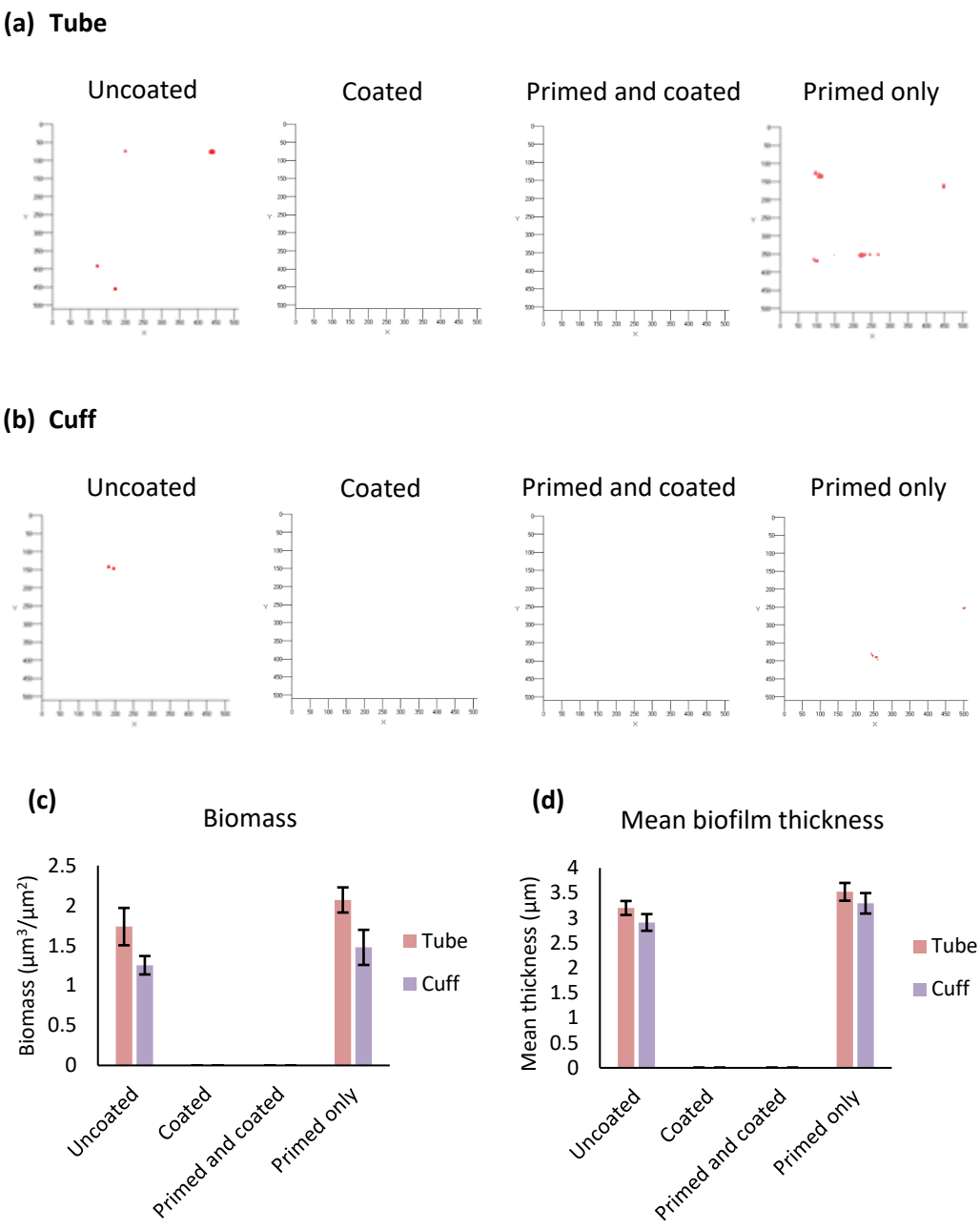


Figure 3.6. 2D CLSM images of *P. aeruginosa* (PA01-N) biofilms, labelled with mCherry, grown on **(a)** ETT tubes and **(b)** cuffs in ASM G, for 24 hours, with the four surface modifications (U, C, PC and P). The red areas indicate biofilm. Scale bars are 500 µm x 500 µm. **(c)** Quantified biomass of images (a) and (b), using a COMSTAT threshold of 60. Error bars are ± SD, N = 3. **(d)** Quantified mean biofilm thickness of images (a) and (b), using a COMSTAT threshold of 60. Error bars are ± SD, N = 3.

In ASM G (Figure 3.6), unlike in RPMI-1640, there was no difference in biomass or thickness between tubes and cuffs (error bar overlap), although the mean values were lower on device cuffs for U and P surfaces. Also, there was no

difference in biofilm formation between U and P surfaces. In ASM G, no cell attachment and biofilm formation was observed on C and PC tubes and cuffs. Biomass and mean thickness was significantly reduced on these surfaces, compared to the U substrates (no error bar overlap); but there were no differences between these two modifications.

The mean percentage reduction in biomass and mean thickness on C and PC tubes and cuffs are summarised in Table 3.4.

	Tube		Cuff	
	B	T	B	T
Coated	100%	100%	100%	100%
Primed and coated	100%	100%	100%	100%

Table 3.4. Mean percentage reduction in biomass (B) and mean thickness (T) on C and PC ETT tubes and cuffs, relative to U substrates, for *P. aeruginosa* (PA01-N) biofilms grown in ASM G.

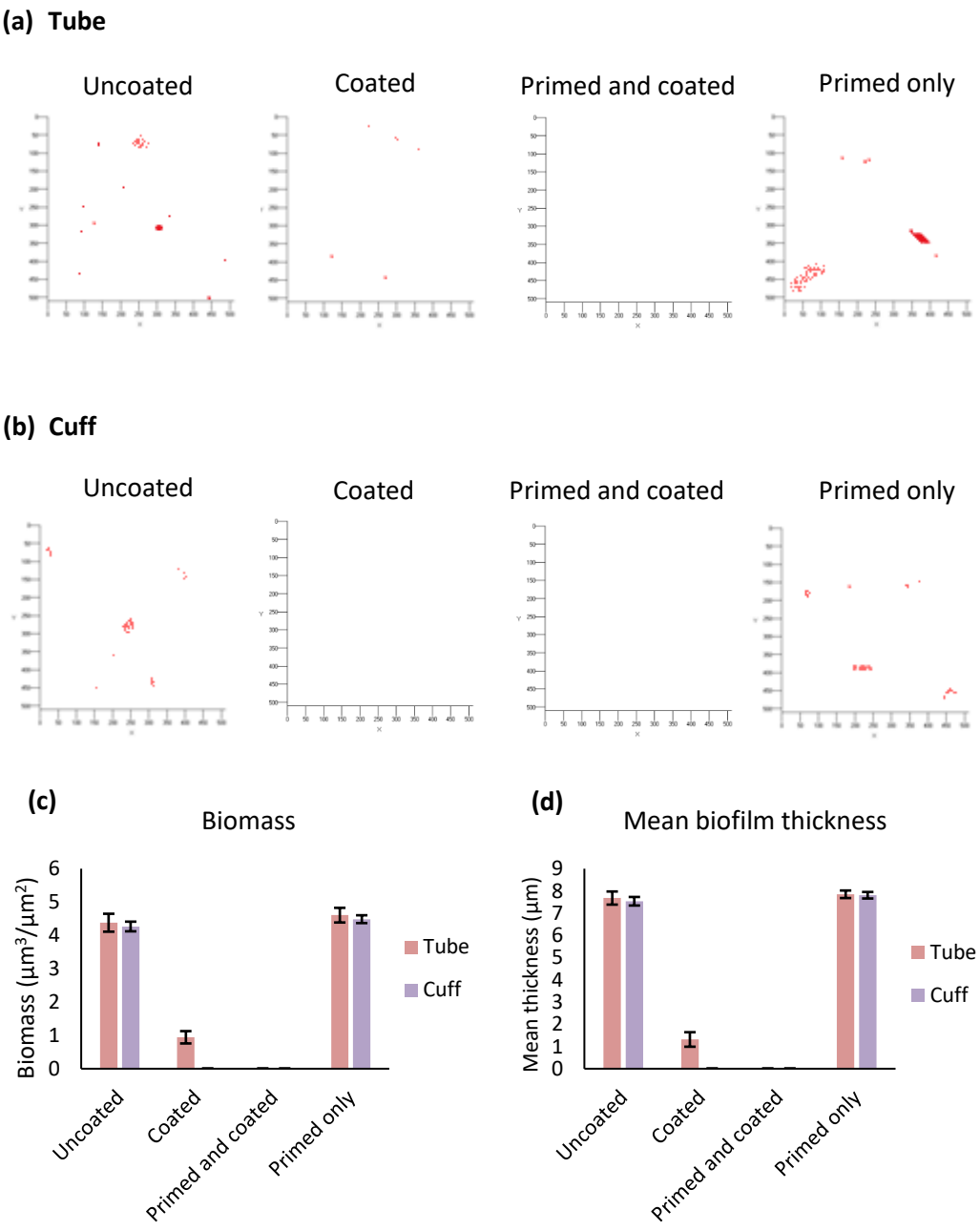


Figure 3.7. 2D CLSM images of *P. aeruginosa* (PA01-N) biofilms, labelled with mCherry, grown on **(a)** ETT tubes and **(b)** cuffs in ASM N, for 24 hours, with the four surface modifications (U, C, PC and P). The red areas indicate biofilm. Scale bars are 500 µm x 500 µm. **(c)** Quantified biomass of images (a) and (b), using a COMSTAT threshold of 60. Error bars are ± SD, N = 3. **(d)** Quantified mean biofilm thickness of images (a) and (b), using a COMSTAT threshold of 60. Error bars are ± SD, N = 3.

In ASM N (Figure 3.7), as with ASM G, there was no difference between tubes and cuffs for U, PC and P substrates. However, there was observable bacteria that had adhered to C tubes, hence there were significant differences between C tubes and cuffs (no error bar overlap for both biomass and mean thickness).

As with the previous two media, biofilm formation on U and P substrates were the same. EGDPEA:DEGMA coatings, with and without the primer, reduced biomass and mean thickness on tubes and cuffs, compared to U substrates. There was no observed biofilm on C cuffs, nor on PC surfaces (tubes and cuffs). Hence, on device tubes, the PC surface resisted bacterial attachment significantly more than on the C tube (no error bar overlap for biomass and mean thickness).

The mean percentage reduction in biomass and mean thickness on C and PC tubes and cuffs are summarised in Table 3.5.

	Tube		Cuff	
	B	T	B	T
Coated	79%	83%	100%	100%
Primed and coated	100%	100%	100%	100%

Table 3.5. Mean percentage reduction in biomass (B) and mean thickness (T) on C and PC ETT tubes and cuffs, relative to U substrates, for *P. aeruginosa* (PA01-N) biofilms grown in ASM N.

Overall, the smallest reduction in biomass/mean thickness was on C cuffs in RPMI-1640 (Table 3.3). In RPMI-1640, the primer plus coating prevented any attachment to device cuffs, and showed a 95% and 96% reduction in biomass and thickness on device tubes respectively. No difference in bacterial coverage was observed on coated samples, with and without the primer, in ASM G (Table 3.4), whereby all surfaces completely inhibited bacterial attachment and biofilm formation. This was also the case in ASM N (Table 3.5), except for the C tube, which showed biomass and mean thickness reductions of 70% and 83% respectively.

3.4.6.3. Comparison of cell culture media

Three different culture media were used for biofilm assays. RPMI-1640 was the minimal medium used to accelerate biofilm formation, whereas the two types of ASM were used to imitate bronchial/lung secretions, hence mimicking the environment in which ETTs would be exposed to during mechanical ventilation. Figure 3.8 compares biomass/mean thickness on both tubes and cuffs, with the four different surface modifications, between these three media, adapting the data presented in Figures 3.5, 3.6 and 3.7.

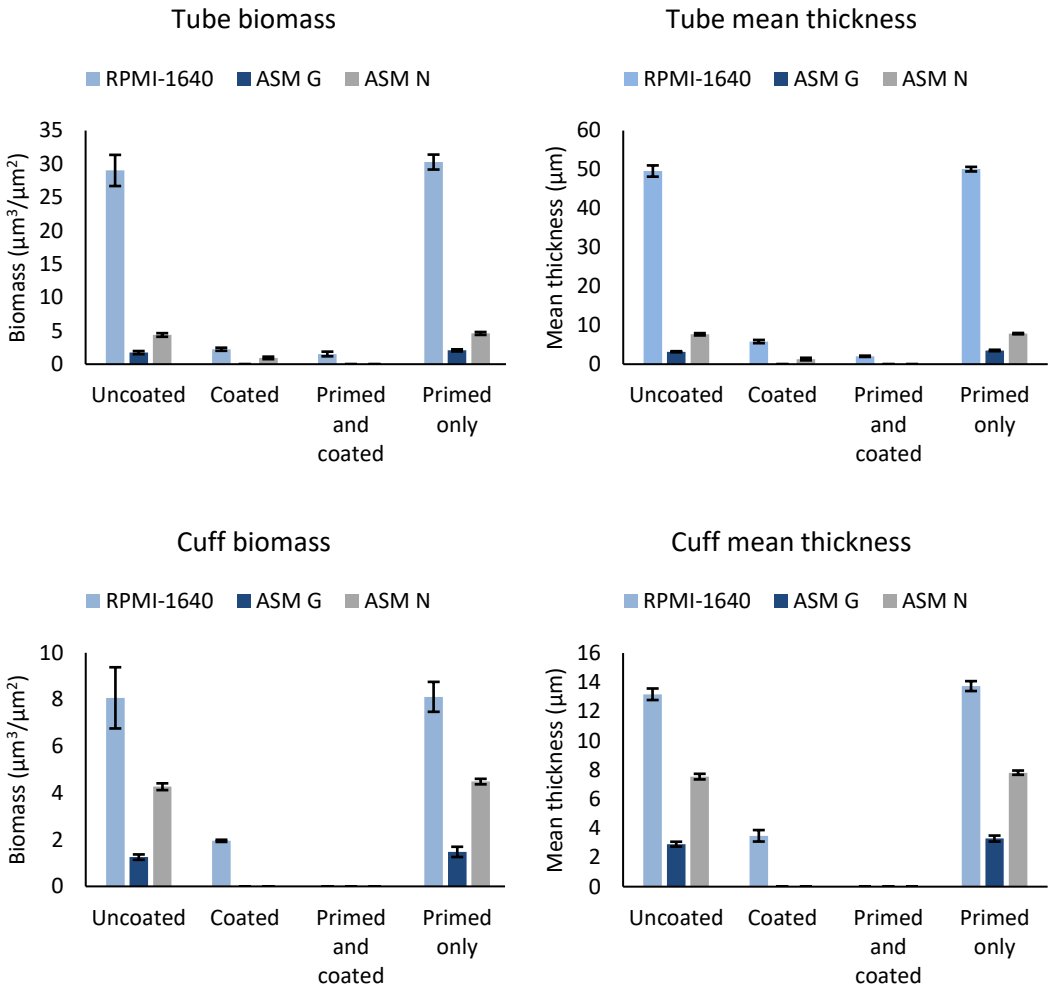


Figure 3.8. Comparison of biomass and mean biofilm thickness between RPMI-1640, ASM G and ASM N. Data for tubes and cuffs are shown, for all four surface modifications. All images had COMSTAT threshold values of 60 prior to biomass and mean thickness quantification. Error bars are ± SD, N = 3.

On U substrates, biofilms grown in RPMI-1640 had higher biomasses and thicknesses than in ASM G and ASM N. For example, on U tubes, the biomasses were 29.02, 1.74 and 4.38 $\mu m^3/\mu m^2$, in RPMI-1640, ASM G and ASM N respectively. The corresponding mean thicknesses in these media, on U tubes, were 49.61, 3.20 and 7.68 μm respectively. ASM N promoted biofilm formation more than ASM G. These differences were also observed on C tubes. No biofilm was observed in either ASM type on PC surfaces. No biofilm was observed on PC cuffs for any of the three media. Therefore, on U, C and P substrates, the rank of the media, in terms of promoting biofilm formation, was ASM G < ASM N < RPMI-1640.

3.4.6.4. Extended biofilm culture

CLSM images and quantification of biomass/mean thickness were performed on *P. aeruginosa* biofilms at 48 and 72 hours, to examine biofilm development beyond the initial 24 hour experiment. This was done on device tubes and cuffs, with the four surface modifications, in RPMI-1640, ASM G and ASM N. The biomass/mean thickness data in RPMI-1640 are presented in Figure 3.9. The corresponding CLSM images are shown in Appendix E.

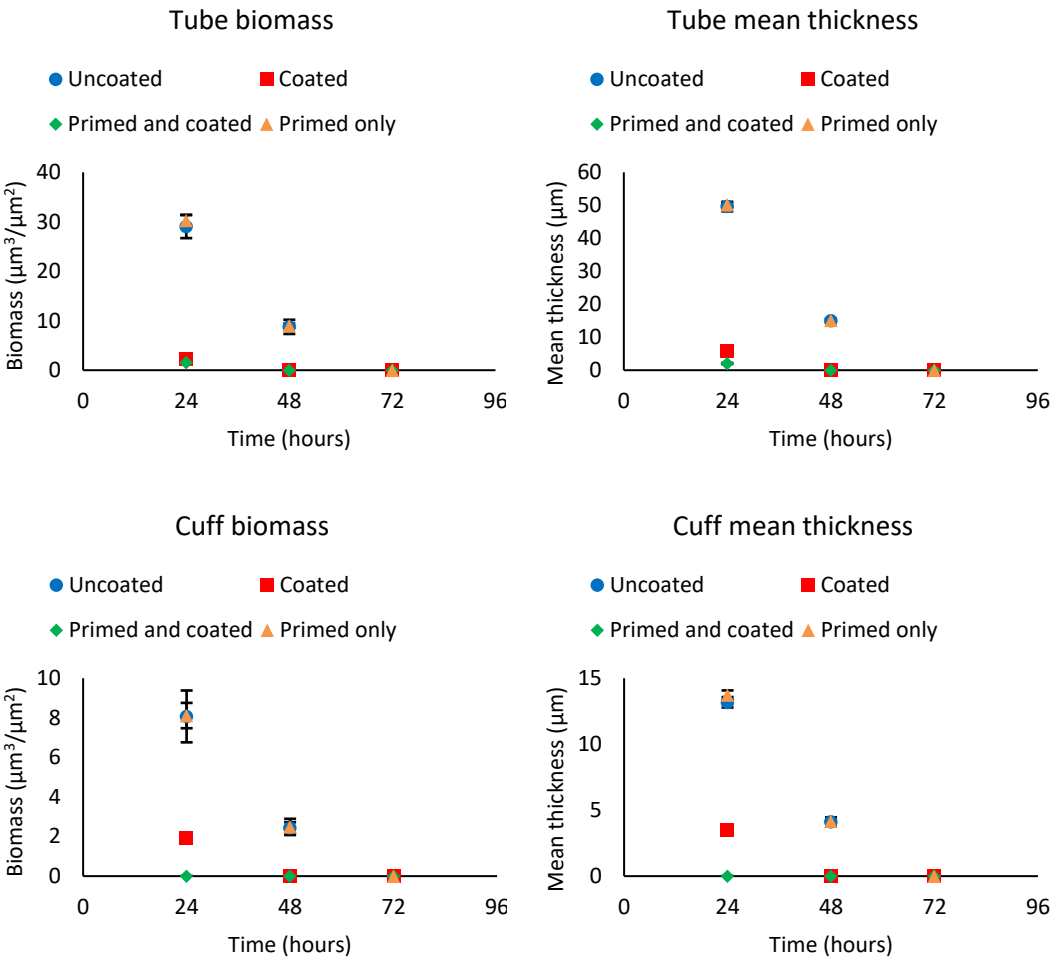


Figure 3.9. *P. aeruginosa* biomass and mean biofilm thickness plots at 24, 48 and 72 hours, in RPMI-1640, for tubes and cuffs with the four surface modifications. Image thresholds were set to 57 prior to biomass/mean thickness quantification. Error bars are ± SD, N = 3.

In RPMI-1640, on U and P substrates, the biomass/mean thickness of biofilms at 48 hours was below one-third of the 24 hour value. On C and PC substrates, there was no biofilm observed at 48 hours. There was no biofilm observed on any substrate at 72 hours. In both types of ASM, no biofilm was seen on any substrate at 48 or 72 hours.

3.5. Discussion

3.5.1. Synthesis of EGDPEA:DEGMA

GPC analysis (Table 3.1) indicated that the polydispersity index of EGDPEA:DEGMA polymer was 1.637. Previous EGDPEA:DEGMA synthesis, without the cobalt catalyst, yielded a polydispersity index of 3.493, highlighting the ability of the cobalt species to reduce the 'distribution' of molecular weights throughout the polymer chain population [195]. The molecular weight was 1.841 x 10^4 g/mol, which correlates with previous syntheses of EGDPEA:DEGMA [186].

^{1}H NMR spectroscopy showed an EGDPEA conversion of 57%, which was estimated by comparing the integral of peaks associated with acrylates (~6 ppm shift) between spectra for EGDPEA monomer and for the EGDPEA:DEGMA crude mix. Since there were no peaks associated with the methacrylate of DEGMA observed in the spectra for the crude mix, it can be concluded that all the DEGMA was polymerised. The ^{1}H NMR spectra of the final polymer product showed a feed EGDPEA:DEGMA ratio of 1.3:1, estimated by comparing the integrals of peaks associated with the terminal methyl group of DEGMA (~3.4 ppm) and the alkene peak from the ring structure of EGDPEA (~5.6 ppm). A feed ratio of 3:1 was expected when using the reported polymerisation protocol [186].

It therefore appears that EGDPEA underreacted, or didn't fully polymerise, possibly due to the presence of residual oxygen in the reaction mixture and/or exhaustion of the AIBN radical initiator. Monomers exist in a normal distribution of energy [237]. EGDPEA is more reactive than DEGMA, due to the formation of the unstable secondary acrylate radical, compared to the more stable tertiary methacrylate radical [238]. Upon initiation, EGDPEA monomers of high energy would have formed radicals first. However, any oxygen present in the reaction mixture would have terminated the high energy EGDPEA. The medium energy EGDPEA were then available for propagation with DEGMA, the latter of which was less abundant, causing all available DEGMA to polymerise.

The lower energy EGDPEA would also have not reacted, since it was likely that the AIBN initiator had been exhausted by that time. It appears that only 57% of the EGDPEA reacted, resulting in the conversion and feed ratio observed.

The polymerisation protocol therefore requires further optimisation, to minimise oxygen presence and allow more initiated EGDPEA to undergo propagation. Nevertheless, EGDPEA:DEGMA polymer was present and could be used for sample coating and assessment of biofilm formation.

3.5.2. Dip coating and coating thickness

Using the Holmarc dip coating unit allowed full control of dipping parameters. Samples were completely immobilised during the dipping process, reducing the risk of delamination during coating. Two factors influence the coating thickness; the concentration of the polymer solution [239] and the speed of withdrawal from polymer solution [240]. Higher polymer solution concentrations and faster withdrawal speed result in thicker coatings, and vice versa. The increased viscosity of a higher polymer concentration solution results in slower drainage of the polymer solution associated with the ETT into the polymer solution reservoir [240], resulting in greater deposition of polymer onto the surface. Faster withdrawal speeds reduce the drainage time, hence also decrease the amount of polymer solution that can drain off the ETT after dipping, producing thicker deposits [241].

In this study, polymer solutions greater than 30% w/v in dichloromethane could not be achieved. When using concentrations of 5-25% w/v, the coatings on ETT substrates appeared to be ‘patchy’, with small areas of the surface left uncoated. Withdrawal speeds quicker than 1 mm/s resulted in polymer ‘clumps’ being deposited onto substrates. Hence, a 30% w/v polymer concentration, with a 1 mm/s withdrawal speed was chosen, as it allowed a thin coating to be applied to the entire substrate surface. Producing a complete

and thin coating is also beneficial when coating optical fibre sensors, allowing refractive index sensing without loss of signal, as demonstrated in chapter 4.

The results in Table 3.2 indicate that coatings on device tubes were thicker than on cuffs. The DEHP plasticiser used in the manufacture of cuffs may introduce a hydrated or waxy layer on cuff surfaces [242]. It has been shown that polymer film thickness on hydrated surfaces is thinner than on dry surfaces [243]. The interaction of the polymer (or DCM) with tube and cuff surfaces requires further investigation; it may be useful to compare the hydrophilicity/hydrophobicity of substrate surfaces using water contact angle (WCA) measurements. Differences in WCA would give a better understanding of the interactions between polymer/solvent with tubes and cuffs, in turn allowing a clearer explanation of the coating thickness differences in Table 3.2.

When the binary silane primer was used alone, there was no measurable weight gain, although a translucent silane layer was seen on sample surfaces. This corroborates the primer manufacturer's literature, which states that a slow withdrawal speed (2 mm/s) deposits an even molecular silane layer on surfaces. Using the primer before dipping in polymer resulted in a thicker polymer coating than on coated substrates alone (Table 3.2). This demonstrated the adhesion promoting effect of the primer, the mechanism of which is described in Figure 2.8. Reactive silanols interacted with both the PVC substrate and the polymer, with stronger silanol-polymer interactions than PVC-polymer interactions [202].

WCA measurements could also be made on unprimed and primed surfaces, to examine the hydrophilicity/hydrophobicity differences between the two. This would allow the nature of the primer-polymer interaction to be established (i.e. hydrophobic interactions). If the hydrophobicity of primed surfaces was higher than unprimed surfaces, it could be thought that stronger hydrophobic interactions were occurring between the primer and the polymer, resulting in greater deposition. Furthermore, the hydrophilicity/hydrophobicity of surfaces

could be linked with DCM drainage; slower DCM drainage results in greater polymer deposition and thicker coatings.

3.5.3. Revolution-to-delamination (RTD) assay

A significant increase in RTD was observed when the primer was used before polymer coating (Figure 3.2). There was a 45-fold increase in RTD, suggesting that the primer increased the resistance (to stress) of the interface between the surface and the polymer by 45 times. The primer increased the reactivity of the ETT surfaces, by introducing reactive silanols at substrate surfaces [202], which are thought to interact via stronger covalent bonds with the polymer than via weaker hydrogen bonds to PVC tubes alone [202]. Therefore, greater stresses were required to remove the polymer from the ETT tubes. Tyler *et al*. [228] noted that primed surfaces had significantly higher RTD than unprimed surfaces, due to the ingress of water between the polymer and unprimed silicone substrate, forming a hydrated layer on the substrate. In this study, the primer possibly reduced this ingress of water, resisting its hydrating effects.

No delamination was seen on either C or PC ETTs in cell culture media during biofilm assays, indicating sufficient resistance to stress of the interface between ETT surfaces and EGDPEA:DEGMA, with and without the primer.

3.5.4. Biofilm assays

3.5.4.1. Effect of the four surface modifications on bacterial attachment

In all three media investigated, EGDPEA:DEGMA coatings significantly reduced bacterial attachment and biofilm formation on ETT sections, evidenced by the reduced biomass/mean thickness of biofilms on these surfaces (Figures 3.5-3.7, Tables 3.3-3.5). This highlights the anti-attachment properties of the polymer, as previously demonstrated [141]. Depending on the growth media, the substrate (tube or cuff) or the use of the binary silane primer, the biomass

reduction was 76-100% and mean thickness reduction was 74-100%. When the primer was used, the smallest reduction in either parameter was 95%. Hook *et al*. noted a 96.7% reduction in bacterial coverage to EGDPEA:DEGMA coated silicone substrates *in vitro*, offering some correlation between the studies. The PC ETT in this study outperformed the currently available polyurethane-cuffed and silver hydrogel-coated ETT, hence offers an inexpensive alternative for VAP prevention.

It is known that the polymer does not have a bactericidal effect, only a repellent one [141,186]. The exact mechanism of attachment prevention is yet to be established, although it is thought that the polymer opposes the initial weak reversible interactions between bacteria cell membranes and the surface, such as van der Waals forces and hydrogen bonding [144,145]. The polymer may also resist attachment via a steric effect, with polymer chains preventing bacteria accessing the surface to induce attachment. Additionally, it has been found that a value combining *c*Log*P* and the number of rotatable bonds (*n*RotB) of poly(meth)acrylate hydrocarbon pendant groups correlates to reduced bacterial attachment [142], suggesting that the combined properties of molecular rigidity and hydrophobicity disrupt bacterial attachment and biofilm formation at the surface.

In some circumstances, PC surfaces outperformed C surfaces, in terms of attachment prevention. In RPMI-1640, this was observed on device tubes (when measuring biofilm thickness) and cuffs. In ASM N, it was seen on device tubes. This improved performance could be attributed to the improved adhesion/stability between the polymer and primed surfaces. Stronger adhesion forces are less likely to be disrupted by water in the media [202,243]. Although no delamination was seen in culture media, coating-PVC interfaces could have still been disturbed during the incubation. Furthermore, the coatings were subjected to physical stresses during the assay; samples were shaken at 60 rpm, which could have further damaged the coating-PVC interface, resulting is pores forming in the coating, allowing access of bacteria to the surface. Due to the improved RTD and bacteria resistance (on some

substrates), using the primer before applying the polymer will be the main modification focused on in the proceeding chapters.

The primer and coating reduced bacterial attachment by 100% on cuffs in RPMI-1640 and on tubes in ASM N. A 100% reduction in biomass/mean thickness was also seen on both C and PC surfaces in ASM G. This offers exciting opportunities for the development of a next generation ETT, which can be coated with primer and the coating for effective prevention of bacterial attachment *in situ*. Both the polymer and the primer are safe for human use, with the coating method CE mark approved, which has subsequently led to a licensed EGDPEA:DEGMA coated urinary catheter being manufactured. Prevention of initial reversible attachment should prevent the biofilm undergoing the full life cycle shown in Figure 1.2, in turn reducing VAP risk in intubated patients.

Biomass/mean thicknesses on P surfaces were not different from U surfaces. The differences between P and PC surfaces can therefore be attributed to the EGDPEA:DEGMA coating, with the primer acting as an adhesion promoter only.

3.5.4.2. Differences between cell culture media

ASM was used to mimic the tracheal environment and to assess biofilm formation on ETTs in contact with sputum. In general, biofilms formed more readily in RPMI-1640 than in either type of ASM. This was most likely due to ASM containing more nutrients to facilitate cell survival [244], hence bacteria were less likely to enter 'survival mode' and initiate surface attachment [245]. In contrast, RPMI-1640 is a minimal medium, with limited nutrients, which stressed bacteria, causing them to form biofilms more readily.

Biomass/mean thickness in ASM G were lower than in ASM N, in general (Figure 3.8). The glucose present in ASM G acts as a carbon source for *P. aeruginosa*. Bacteria exposed to glucose, up to a certain concentration, grow and multiply at a higher rate than in the absence of glucose [246]. Therefore, bacteria are less inclined to form biofilms when the conditions are favourable. Bacteria

causing lung infections have been observed to multiply and spread at a higher rate in the presence of glucose [247]. In ASM N, there isn't the extra carbon source but there are still amino acids, salts and iron, all of which promotes cell growth, resulting in greater biofilm formation than in ASM G, but less than in the minimal medium.

Lung sputum glucose content varies between subjects. Van Sambeek *et al*. [248] found a mean sputum glucose concentration of 4.75 mM in cystic fibrosis patients. Brennan *et al*. [247] noted increased airway glucose concentration in healthy volunteers with blood glucose levels of ≥ 8 mmol L^{-1}. There may therefore be a link between the fed/fasted state of the subject and airway glucose concentration. This justifies the use of ASM with and without glucose; to cover a range of patients' airway glucose content. The glucose concentration in ASM G was 3 mM.

3.5.4.3. Biofilm fate after 24 hours

Figure 3.9 indicates that *P. aeruginosa* biofilms reached their maximum biomass/thickness at 24 hours, then began to lose their structure. The time taken for *P. aeruginosa* to form fully mature biofilms is highly dependent on the growth conditions and has been reported to be between 2 hours and 7 days [249]. It is thought that *P. aeruginosa* produces enzymes that break down the EPS layer. One such enzyme is alginate lyase, which degrades alginate, causing the biofilm to lose its structural integrity [250]. This process allows cells to escape the biofilm to colonise other surfaces. However, if the media cannot support cell growth, cells may die [250], resulting in no further attachment to surfaces.

In RPMI-1640, on U and P surfaces, the biomass/mean thickness fell to below one-third from 24 to 48 hours, signifying the biofilm degradation process occurring rapidly in that 24 hour period. In both ASM types, as well as on C and PC surfaces in RPMI-1640, there was no biofilm detected on ETT surfaces at 48 hours; since biofilms weren't as thick in ASM compared to RPMI-1640, there was less biomass to be degraded. ASM supports cell survival more than RPMI-

1640; cell death after degradation may have been slower. Nevertheless, there was no recorded biofilm at 72 hours.

This study allowed the general biofilm life cycle timeline in each media to be established over 72 hours. Although VAP is diagnosed after 48 hours of intubation, it is not known when in the first 48 hours of intubation the initial attachment of pathogens to ETTs occur. EGDPEA:DEGMA does resist bacterial attachment, by preventing initial attachment, offering effective VAP prevention.

3.5.4.4. Biomass and mean biofilm thickness

Biomass and mean thickness were quantified in order to better understand the structural nature of *P. aeruginosa* biofilms. Although these parameters are independent of each other, they were decreased by similar rates on C and PC substrates, compared to U substrates (Tables 3.3-3.5). The key difference between the two measurements is that biomass ($\mu m^3/\mu m^2$) is a measurement of biovolume per μm^2, whereas mean thickness (μm) measured the average biofilm thickness over the entire imaged substratum. Nevertheless, both measurements allowed biofilm structure to be compared on different substrates and either can be used to assess bacterial colonisation. In proceeding chapters, biomass is the main biofilm parameter quantified.

3.5.5. Ion intensities and chemical maps obtained from ToF-SIMS

ToF-SIMS is generally regarded as non-quantitative, due to known matrix effects [207]. However, comparing relative ion intensities allowed a semi-quantitative approach to surface chemical analysis. Generating ion maps for secondary ions of interest (Appendix D) allowed the visualisation of relative ion intensities. For the acrylate and methacrylate anions, greater ion intensities were seen on C and PC surfaces, indicating the presence of the polymer. Since ToF-SIMS analyses secondary ions generated from the top 1-2 nm of the surface [205,206], the ion intensities were no different between C and PC

surfaces on both tubes and cuffs, as the coating thickness exceeded 400nm. ToF-SIMS also detected the presence of the silane primer, through measurement of the silicate ion, which was significantly higher on P surfaces compared to the other three surface modifications (no error bar overlap, 3 ROIs). The silicate ion was not detected after polymer coating.

ToF-SIMS also enabled the assessment of differences between tubes and cuffs. The most significant secondary ion analysed in this regard was the phthalate ion, which originated from the diethylhexyl phthalate (DEHP) plasticiser used in ETT cuffs [16,251]. The phthalate ion intensity was significantly higher on U and P cuffs than on tubes (no error bar overlap, 3 ROIs). This may explain the difference in bacterial attachment between U/P ETT components, where biomass and mean thickness on tubes were at least 3.5x higher than on cuffs. DEHP has been shown to exhibit bactericidal and/or cytotoxic activity [252-254]. The DEHP could therefore have prevented attachment and biofilm formation on device cuffs. This effect was more pronounced in RPMI-1640 medium, which stressed the cells, forcing them to adhere and form biofilms more rapidly, readily contacting phthalate-containing cuffs. Phthalates were not detected on C and PC substrates, due to the coverage of the coating, thus would have contributed less to the bacterial response on these samples. The phthalate ion was however, detected on P surfaces, indicating a nanometer-order silane layer, beyond which the primary ion beam could still generate secondary ions. Overall, ToF-SIMS allowed polymer, silane and phthalate presence to be detected.

3.5.6. 3D optical profiles and roughness quantification

The link between surface roughness and bacterial adhesion is poorly understood. Micro- and nano-patterned surfaces have been linked to decreased and increased bacterial adhesion respectively [135,136]. The measured mean square roughness of ETT substrates (Figure 3.4) appears to have contradicting observations; cuffs had higher mean square roughness than

tubes, for all surface modifications and had lower bacterial attachment (Figures 3.5-3.7). However, C and PC surfaces had lower surface roughness than U surfaces, yet biomass/mean thickness was reduced.

Cuffs contain small folds and plasticiser particles in their walls, possibly causing the increased surface roughness observed. When the polymer coating was applied, there was a reduction in surface roughness. It is thought that the polymer fills voids in surfaces and 'blankets' the topography, effectively evening out the surface [255]. This effect may be enhanced when using the primer, as polymer adhesion was improved. On P surfaces, roughness was no different to uncoated substrates, suggesting that the silane layer did not contribute to the reduction in surface roughness.

Of the chemical (ToF-SIMS) and physical (optical profiling) analyses of ETT surfaces, the secondary ion maps and relative ion intensities from ToF-SIMS appear to offer the best explanation for the differing bacterial adhesion on tubes and cuffs, and on U, C and PC substrates. ToF-SIMS allowed the presence of polymer to be confirmed, as well as the phthalate plasticiser, which seems to have the greatest effect of bacterial attachment to cuffs. Bacterial adhesion, in general, is influenced by the combined chemical and physical profile of a surface. However, no correlation was made between surface roughness and bacterial attachment, hence the chemistry of the surface possibly overwhelms the influence of roughness in attachment.

3.6. Conclusions

In this study, a novel poly acrylate:methacrylate (EGDPEA:DEGMA) was synthesised and used to coat PVC ETTs. The coating's effect on bacterial attachment to ETTs was then investigated. EGDPEA:DEGMA was successfully synthesised using a cobalt mediated CCT method. It had a polydispersity of 1.637 and a molecular weight of 1.841×10^4. Since only a 57% EGDPEA conversion and a 1.3:1 feed monomer ratio was observed, the polymerisation protocol may require further optimisation.

Sections of tube and cuff were dip coated in polymer, resulting in mean coating thicknesses of 559 nm 487 nm respectively. The MED1-161 binary silane primer increased the polymer coating thicknesses to 627 nm and 549 nm respectively, due to the improved adhesion between the polymer and substrate.

EGDPEA:DEGMA coatings on ETTs reduced biomass and mean biofilm thickness of *P. aeruginosa* biofilms by between 74% and 100%. The binary silane primer plus the polymer coating reduced bacterial attachment more than the polymer coating alone, particularly in RPMI-1640 medium, indicating greater resistance to stress of polymer-substrate interactions when using the primer. A lower biomass and mean thickness was observed in ASM compared to RPMI-1640, likely due to the higher concentration of a carbon source within this media, leading to less nutrient stress and a concomitant reduction in biofilm formation. Biofilm biomass and mean thickness increased up to 24 hours but then degraded in all growth media, with no biofilm present after 72 hours.

At least a 3.5-fold increase in biomass and mean thickness was observed on uncoated tubes compared to uncoated cuffs. This was likely due to phthalate plasticiser presence in cuffs, identified using ToF-SIMS. Surface roughness, measured using optical profiling, was higher on cuffs than on tubes. Roughness decreased on polymer coated and primed plus coated substrates. However, there was no correlation between surface roughness and bacterial adhesion for the materials studied. It is likely that the surface chemistry overwhelmed the topography and had a greater effect on bacterial attachment.

4. Long Period Grating optical fibre sensors for the real time monitoring of bacterial attachment and biofilm formation

4.1. Introduction

Mechanically ventilated patients are closely monitored for signs of VAP and other infection [256]. However, the signs often do not become apparent until after the infection has developed [256]. The assessment of bacterial colonisation of ETTs provides a good indicator of VAP risk. Currently, bacterial adhesion to ETTs is assessed by the removal and inspection of the device, which can cause tracheal wall damage and facilitate VAP development [91,146]. Ideally, physicians would be provided with live feedback on bacterial colonisation of ETTs *in situ*, so they can evaluate the patient's VAP risk in real time and intercept ETT-centred infection.

In this chapter, Long Period Grating optical fibre sensors (LPG OFS) were, for the first time, explored as a method of monitoring bacterial attachment to ETTs in real time. LPG OFS have a UV-inscribed grating in the core of the optical fibre, which allows the core mode to couple into the cladding modes, resulting in the appearance of attenuation bands (losses of transmission) in the optical spectrum, centred at discrete wavelengths [160,161]. LPG OFS are refractive index sensors; a change in the refractive index at the cladding-medium interface results in a change of the optical properties of the cladding, causing core-cladding mode coupling to occur at different wavelengths, in turn shifting the wavelength of attenuation bands (governed by equation 1) [163,164]. Bacterial attachment and subsequent biofilm formation on LPG OFS surfaces will change the local refractive index, causing a measurable shift in the wavelength of attenuation bands, which has the potential to enable the real time monitoring of attachment and biofilm formation.

In this study, LPG OFS was used as a stand-alone unit for general bacterial attachment detection, by immersing it in *P. aeruginosa* culture in RPMI-1640

and observing wavelength shift of attenuation bands over time. LPG OFS were also incorporated into ETT tube lumens and onto cuffs for real time monitoring of surface adhesion, in RPMI-1640, ASM G and ASM N, the latter two of which enabled sensor assessment in conditions mimicking a patient's airway. This also involved measuring attenuation band wavelength shift over time of sensor immersion in *P. aeruginosa* culture, in the three different growth media. This would provide physicians with live, *in situ* feedback of device colonisation.

LPG OFS were left uncoated or coated in EGDPEA:DEGMA (with a binary silane primer) to compare spectral changes with differing degrees of bacterial attachment. LPG OFS in this sense could also be used to validate the anti-attachment properties of EGDPEA:DEGMA.

The biomass of biofilms grown on ETTs was quantified over time, using confocal microscopy and COMSTAT, and the relationship between wavelength shift of attenuation bands and biomass explored. The sensitivity of LPG OFS to biomass was also studied. Relating wavelength shift to distinct biomass values would allow the biomass to be quantified from the spectral response alone, allowing the severity of device biofouling and therefore the patient's VAP risk to be immediately identified and preventative action taken. LPG OFS may offer a simple, inexpensive and sensitive sensing instrumentation for ETTs.

4.2. Aims

The aims of this experimental chapter were:

1. Explore the novel use of Long Period Grating optical fibre sensors (LPG OFS) for the real time monitoring of *P. aeruginosa* attachment and biofilm formation.
2. Establish the sensitivity of LPG OFS to biomass.
3. Incorporate LPG OFS into ETT lumens and onto cuffs for the real time monitoring of bacterial attachment to device surfaces.
4. Note the relationship (if any) between optical spectral response and the biomass of biofilms grown on ETTs.

4.3. Experimental

4.3.1. Fabrication of LPG OFS

LPGs with grating periods of 109 µm and lengths of 30 mm were fabricated in boron-germanium co-doped optical fibres (Fibercore PS750), with a cut-off wavelength of 670 nm, in a point-by point fashion, via custom made amplitude masks made of 1Cr18Ni9Ti steel alloy, allowing for reproducibility of the grating across multiple LPGs. The optical fibre was side-illuminated by the output from a frequency-quadrupled Nd:YAG laser, emitting at a wavelength of 266 nm (Continuum minilite I).

The transmission spectrum of the optical fibre was recorded by coupling the output from a tungsten-halogen lamp (HL-2000) into the fibre and analysing the transmitted light using a fibre-coupled CCD spectrometer (HR-4000). The grating period was selected such that the LPG operated at or near the phase matching turning point (PMTP), which, for coupling to a particular cladding mode, ensured optimum sensitivity [166].

4.3.2. Dip coating of LPG OFS and estimation of coating thickness

LPG OFS were left uncoated, or dip coated in a binary silane primer (MED1-161, withdrawal speed 2 mm/s) followed by a 30% w/v EGDPEA:DEGMA solution in DCM (withdrawal speed 1 mm/s). The Holmarc HO-TH-01 dip coating unit was used for dip coating, with the robotic arm set to withdraw samples from the desired solutions at the speeds quoted. After dipping into the primer, LPG OFS were left to dry under ambient conditions for 30 minutes before dip coating in the polymer solution. They were then left to dry under ambient conditions for 24 hours, followed by a further 24 hours under vacuum (0.11 Torr).

To calculate coating thickness, 3 cm lengths of insensitive optical fibre (Thorlabs Ltd., 460HP, fibre ID: 10-C0157-20-4H-08) were dip coated in parallel, and the average weight gain per optical fibre measured after polymer coating

(weight difference between P optical fibres and PC optical fibres, (Mettler-Toledo AB265-S/FACT weighing balance, Switzerland)). The dimensions of these optical fibre sections were known; the diameter was 125 µm and the length was 3 cm, to imitate the sensitive region of LPG OFS. The density of EGDPEA:DEGMA was measured to be 1.61 g/mL (by weighing 1 mL of EGDPEA:DEGMA), so the coating thickness on optical fibres could be calculated, using equation 5.

$$t = m/\pi dl\rho \quad (5)$$

Where t is the coating thickness (in cm), m is the average weight gain per optical fibre section (in g), d and l are the diameter and length of the optical fibre respectively (in cm) and ρ is the measured density of EGDPEA:DEGMA.

4.3.3. Calibration of LPG OFS using sodium chloride solutions

LPG OFS were calibrated using sodium chloride solutions in water. This was to ensure that they were sensitive to refractive index change, to note the presence of attenuation bands in the optical spectrum and to confirm that there were no spectral differences between U and PC sensors in solutions of the same refractive index.

U and PC LPG OFS were set up as shown in Figure 2.14, with one end connected to the halogen light source (HL-2000) and the other connected to the optical spectrometer (HR-4000), via SubMiniature version A (SMA) connectors. The 3 cm sensitive region of the OFS was placed into a specially designed polytetrafluoroethylene (PTFE) well (Figure 4.1), which had dimensions of 7 x 1.9 x 1 cm, with a 4 cm long channel. Sodium chloride solutions, ranging from 0 to 25% w/v (in 5% w/v increments) were made up by serial dilution from a 25% w/v stock in water. Each solution was pipetted into the PTFE well separately, which held approximately 1.5 mL of liquid, and the transmission spectra recorded in the SpectraSuite software. This was done with both U and PC LPG OFS.

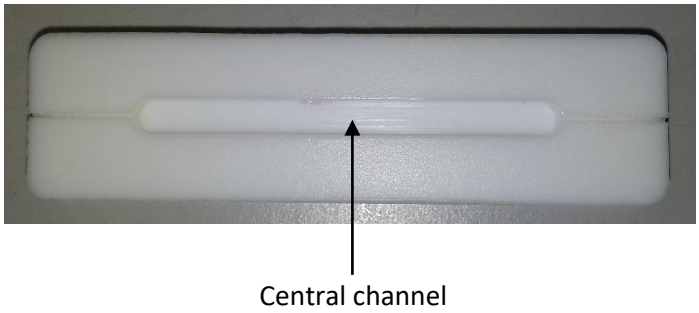


Figure 4.1. The PTFE well used for LPG OFS spectra collection. The 3 cm sensitive region of LPG OFS were placed into the 4 cm central channel and fixed either side of the well using adhesive tape.

Once all transmission spectra were collected, they were processed in OriginPro 8.6 (OriginLab®), using the method described in Appendix A. The wavelengths of attenuation bands (minimum transmission % - apex of attenuation peaks) were found using the "peak finder" function within OriginPro 8.6. The wavelength shifts of attenuation bands were calculated using equation 3, where λ_c was the wavelength of the attenuation band at concentration c, and λ_0 was the wavelength of the attenuation band in water. Wavelength shift was then plotted against concentration, allowing observation of LPG OFS spectral response in increasing sodium chloride concentration (and increasing refractive index), for both U and PC sensors.

4.3.4. LPG OFS in bacterial culture media

4.3.4.1. Spectral response in *P. aeruginosa* culture medium

U and PC LPG OFS were set up as illustrated in Figure 2.14, with the 3 cm sensitive region positioned in the PTFE well (Figure 4.1). The well was placed into a petri dish of water, to prevent medium evaporation. A culture of *P. aeruginosa* (PA01-N) was prepared as described in section 3.3.6, in RPMI-1640 medium, with OD_{600} = 0.05, and 1.5 mL pipetted into the PTFE well. A 0 hour transmission spectrum was recorded and the system was left to record

transmission spectra every 6 hours for a 24 hour period of immersion in culture medium. Transmission spectra were also recorded at 48 and 72 hours. The experiment was conducted at 20°C. Spectra were then processed in OriginPro 8.6 (Appendix A) and the wavelength shift of attenuation bands (calculated using equation 3) plotted against time of immersion in bacteria culture medium, for both U and PC LPG OFS.

4.3.4.2. Quantifying biomass of *P. aeruginosa* biofilms grown on optical fibres and relating biomass to wavelength shift

Lengths of 7.5 cm of insensitive optical fibre (Thorlabs Ltd., 460HP, fibre ID: 10-C0157-20-4H-08), U and PC, were inserted into a 3-channel flow cell (IBI Scientific). 1.5 mL of the same *P. aeruginosa* (PA01-N) culture medium was pipetted into the cell and a glass slide fixed on top. The system was placed into a petri dish of water, to prevent medium evaporation. Biofilms were left to grow on the optical fibres at 20°C for 72 hours. At 6 hour intervals, from 0 to 24 hours, and at 48 and 72 hours, the flow cell, containing the optical fibres immersed in bacteria culture medium, was imaged using CLSM (LSM 700, Carl Zeiss, Germany), using the same protocol described in section 3.3.7. *Z*-stack CLSM images were obtained and processed in ZEN 2009.

Images were then imported into COMSTAT, which was used to quantify the biomass of *P. aeruginosa* biofilms grown on optical fibres, under the same directive presented in section 3.3.8. Biomass was plotted against time, giving an indication of biofilm development on U and PC optical fibres over 24 hours.

The relationship between biomass and wavelength shift was established and used to derive a mathematical association between the two sets of data. This association could be used to quantify biomass from the wavelength shift alone, removing the need for microscopic analysis.

4.3.4.3. Estimation of sensor sensitivity to biomass

The U LPG OFS, set up as shown in Figure 2.14, was exposed to the same *P. aeruginosa* (PA01-N) culture medium in the aforementioned PTFE well (Figure

4.1). Transmission spectra were recorded every 5 minutes and the earliest time point at which a measurable attenuation band wavelength shift occurred was noted. Simultaneously, 7.5 cm sections of U insensitive optical fibre were immersed in the same *P. aeruginosa* culture medium in the 3-channel flow cell. Both trials were conducted at 20°C. When a measurable wavelength shift was observed, Z-stack CLSM images were acquired of biofilms on the optical fibres, using the previously described protocol (section 3.3.7). Images were imported into COMSTAT and the biomass at that particular time point quantified (section 3.3.8). This allowed the sensitivity of the system to be reported as a wavelength shift per unit biomass.

4.3.5. LPG OFS instrumentation for ETTs

4.3.5.1. Spectral response from LPG OFS incorporated into ETTs

Incorporating LPG OFS into an ETT allows the response of the sensors to be examined when in contact with the device and permits the *in situ* simulation of an instrumented ETT. LPG OFS were fixed (using autoclave tape) into the lumen of a 5 cm length of tube and onto a 3 cm^2 section of cuff, which had been removed from the main body of the device (Figure 4.2). The combined LPG OFS-ETT systems were either left uncoated or silane primed and EGDPEA:DEGMA coated as described in section 4.3.2. Each system was then immersed in *P. aeruginosa* (PA01-N) culture in RPMI-1640, ASM G and ASM N, with OD_{600} = 0.05 (section 3.3.6.), at 20°C, in a petri dish. 0 hour transmission spectra were recorded and the system left immersed in bacteria culture media for 24 hours, with transmission spectra recorded at 6 hour intervals. Transmission spectra were processed and wavelengths of attenuation bands established in OriginPro 8.6 (Appendix A). Wavelength shift was plotted against time for both tubes and cuffs, U and PC and for the three culture media.

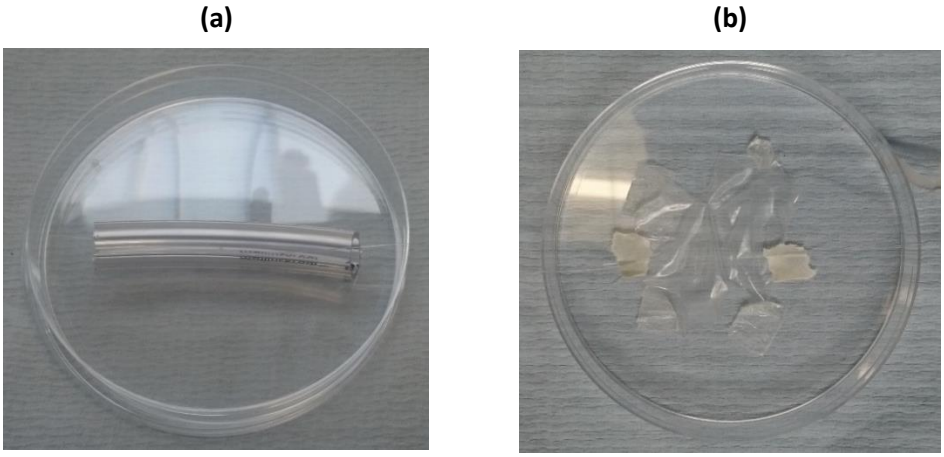


Figure 4.2. (a) LPG OFS fixed into the lumen of a section of ETT tube. **(b)** LPG OFS fixed onto a section of ETT cuff.

4.3.5.2. Quantifying biomass of *P. aeruginosa* biofilms grown on ETTs and relating biomass to wavelength shift

1 cm^2 sections of U and PC tubes and cuffs were immersed in the same *P. aeruginosa* culture, in RPMI-1640, ASM G and ASM N, at 20°C. The experiment was conducted in single well chamber slides (Nunc® Lab-Tek® II, Sigma Aldrich UK). At 6 hour intervals, from 0 to 24 hours, 2D and *z*-stack CLSM images were acquired, using the method described in section 3.3.7. Z-stack images were imported into COMSTAT for biomass quantification (section 3.3.8). Biomass was plotted against time, for U and PC tubes and cuffs, and for the three growth media. The relationship between biomass and wavelength shift (from LPG OFS-ETT systems) was noted. The relationship may allow biomass on ETTs to be quantified based on the wavelength shift alone.

4.4. Results

4.4.1. Estimated coating thickness on optical fibres and LPG OFS

3 cm lengths of optical fibre were dip coated in a binary silane primer, followed by a 30% w/v EGDPEA:DEGMA solution in DCM. There was no measurable weight gain after priming, although a translucent silane layer was observed on optical fibres, an observation previously made on sections of ETT. After polymer deposition, an average weight gain of 9.7 µg was calculated per 3 cm length of optical fibre (total 100 fibres). The density of EGDPEA:DEGMA was measured to be 1.61 g/mL. Since the diameter of the optical fibres was known to be 125 µm, the average coating thickness per fibre was calculated to be 511 nm, using equation 5.

4.4.2. Calibration of LPG OFS using sodium chloride solutions

U and PC LPG OFS were exposed to sodium chloride solutions in water, of concentration 5-25% w/v, in 5% w/v increments. Two attenuation bands were observed in the optical spectrum for water for each surface modification (Figure 4.3).

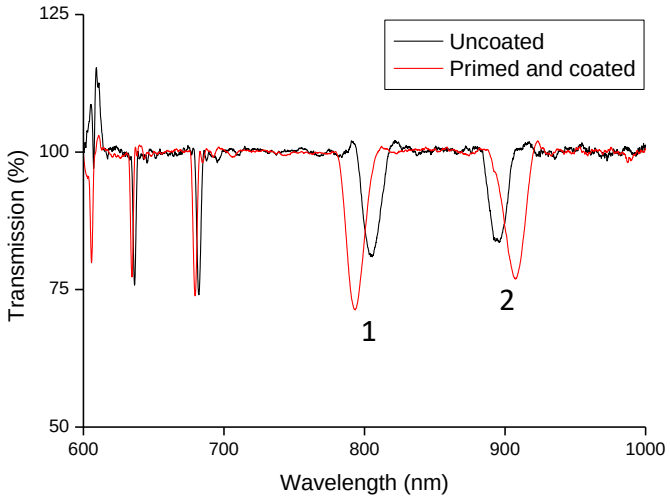


Figure 4.3. Processed transmission spectra in water for the uncoated (black) and primed and coated (red) LPG OFS, with a grating period of 109 µm. Two attenuation bands (peaks) were observed, labelled '1' and '2'.

The application of the primer and the polymer coating caused both attenuation bands to become deeper (greater transmission loss); peak 1 displayed a 10% transmission loss and peak 2 displayed a 7% transmission loss. Also, peaks 1 and 2 shifted to the left and right respectively. Peak 1 shifted down the *x* axis by 11.83 nm and peak 2 shifted up the *x* axis by 12.25 nm.

Transmission spectra were collected for each concentration of sodium chloride in solution. The wavelengths of attenuation bands were noted and the wavelength shift calculated using equation 3. Figure 4.4 shows the plots of wavelength shift against sodium chloride concentration, for both the attenuation 'peaks' and for U and PC LPG OFS.

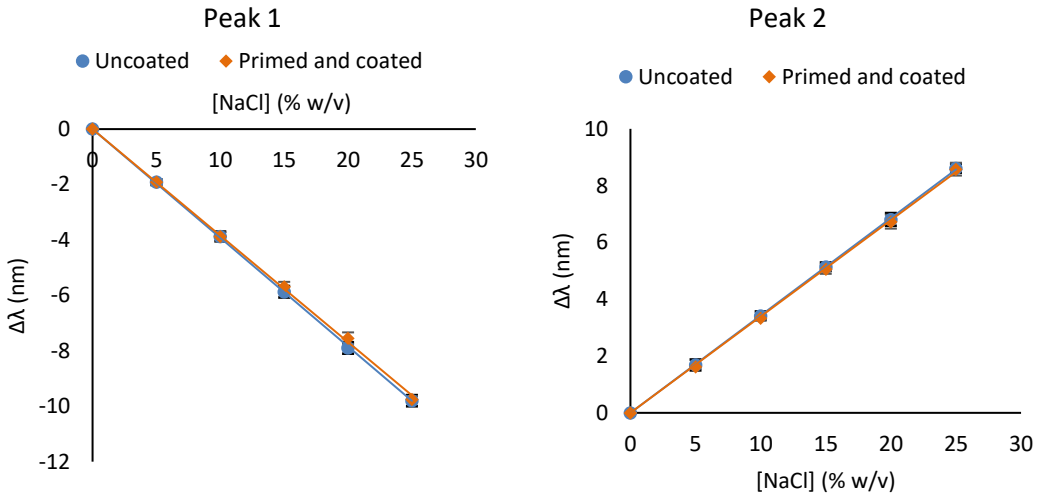


Figure 4.4. Wavelength shift (Δλ) plots for attenuation peaks 1 and 2 with increasing concentration of sodium chloride in water, for both U and PC LPG OFS. Error bars are ± SD, N = 3.

The wavelength shift was linear ($R^2 \geq 0.99$) for both peaks and for both U and PC LPG OFS. Wavelength shift increased with increasing sodium chloride concentration and increasing refractive index [257]. Peak 1 had a greater rate of change of wavelength shift; at 25% w/v of sodium chloride in water, peak 1 had a shift of -9.8 nm and peak 2 had a shift of 8.6 nm. The peaks shifted in opposite directions with increasing sodium chloride concentration. There was no difference in the wavelength shift profiles between U and PC LPG OFS.

4.4.3. LPG OFS in bacteria culture medium

4.4.3.1. Spectral response in bacteria culture medium

The calibration showed that there were two attenuation bands in the transmission spectrum, both of which shifted linearly with increasing refractive index. Also, there was no difference in wavelength shift between U and PC LPG OFS. This meant that any differences in wavelength shift in bacteria culture medium would be due to differing bacterial attachment rates. Hence, after calibration, LPG OFS were immersed in *P. aeruginosa* (PA01-N) culture medium, in RPMI-1640 and the wavelength shift of attenuation bands measured with increased time of immersion. Figure 4.5 are the wavelength shift plots for U and PC LPG OFS in *P. aeruginosa* culture medium for 24 hours.

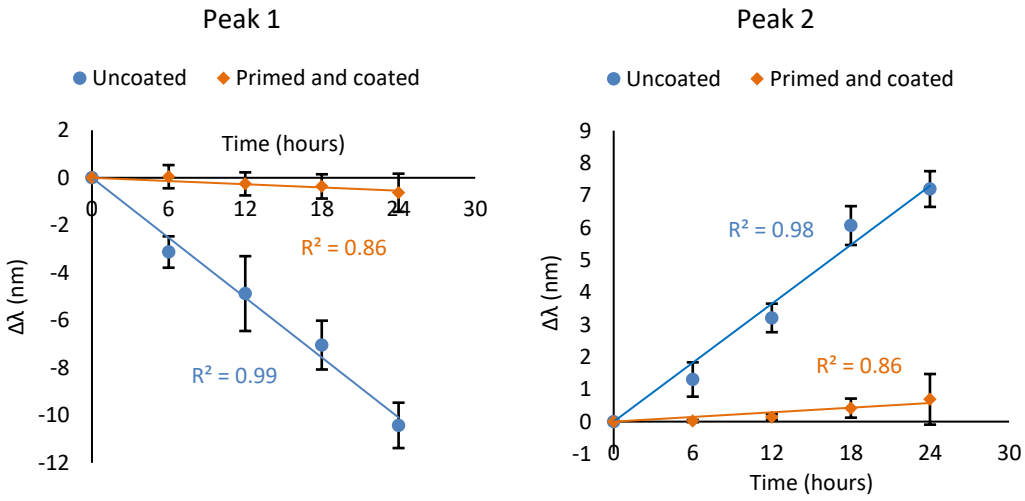


Figure 4.5. Wavelength shift change over time for both attenuation peaks of LPG OFS immersed in *P. aeruginosa* culture medium in RPMI-1640, for 24 hours. U and PC sensors are shown, with the R^2 displayed in labels of corresponding colours. Error bars are ± SD, N = 8.

Both attenuation peaks shifted linearly with increased time of immersion in bacteria culture medium. At 24 hours, the peak 1 shifts were -10.4 and -0.6 nm, for U and PC LPG OFS respectively. The corresponding peak 2 shifts were 7.2 and 0.7 nm. The rates of change for the U LPG OFS were 21- and 15-fold higher than for the PC LPG OFS, for peaks 1 and 2 respectively. At all time points after

0 hours, the wavelength shifts corresponding to the U LPG OFS were significantly higher ($p < 0.05$) than the PC wavelength shifts. Attenuation peaks shifted in opposite directions over time of immersion.

LPG OFS were also immersed in RPMI-1640 medium with no bacteria culture and the wavelength shift of attenuation bands measured for 24 hours. There was no measurable wavelength shift in the medium only, for both U and PC LPG OFS.

4.4.3.2. CLSM images and quantified biomass of *P. aeruginosa* biofilms grown on optical fibres

7.5 cm lengths of insensitive optical fibre (U and PC) were exposed to the *P. aeruginosa* (PA01-N) culture in RPMI-1640 medium and *z*-stack CLSM images acquired at 6 hour intervals for 24 hours. Images were processed and biomass quantified at each time point using COMSTAT. Figure 4.6 are the CLSM images and corresponding biomasses for *P. aeruginosa* biofilms grown on optical fibres.

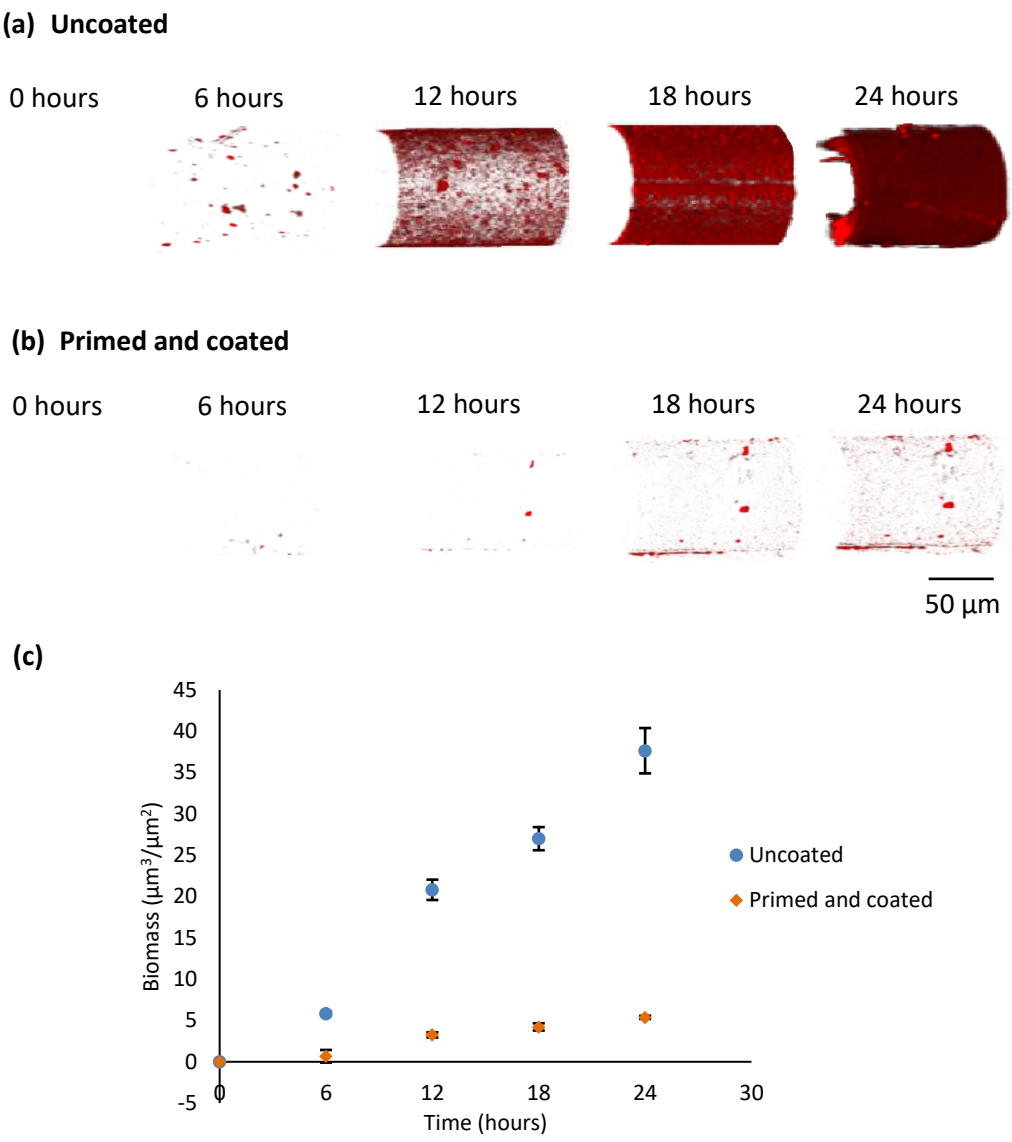


Figure 4.6. (a) *Z*-stack CLSM images of *P. aeruginosa* biofilms, labelled with mCherry, on U optical fibres, at 6 hour intervals for 24 hours. The red masses represent biofilm. **(b)** *Z*-stack CLSM images of *P. aeruginosa* biofilms, labelled with mCherry, on PC optical fibres, at 6 hour intervals for 24 hours. The red masses represent biofilm. The scale bar is 50 µm and is applicable to all images. **(c)** Quantified biomass for all images in (a) and (b), using a COMSTAT threshold of 56. Error bars are ± SD, N = 3.

CLSM images show a progression in biofilm development on the U fibre. Bacterial microcolonies were observed at 6 hours and full biofilm structures were observed by 18 hours. On the PC fibre, no fully formed biofilm was present after 24 hours. Attachment was not completely prevented, as some adhered cells and microcolonies were observed from 6 to 24 hours. This was

reflected after quantification of biomass; the increase in biomass was greater over time on the U fibre than the PC fibre. At all time points after 0 hours, the biomass was significantly higher (no error bar overlap) on U fibres than their PC counterparts. After 24 hours, the biomass of *P.* aeruginosa biofilms on U and PC optical fibres were 37.65 and 5.38 $\mu m^3/\mu m^2$ respectively.

4.4.3.3. Relationship between biomass and wavelength shift

The relationship between biomass and wavelength shift would allow the biomass of a biofilm to be quantified using the wavelength shift alone, removing the need for microscopic analysis and separate biomass quantification. The evanescent field decay from the cladding surface of optical fibres is governed by mathematical formulas derived from Maxwell equations. The strength of the evanescent field decays exponentially [258,259] and is dependent on the refractive index of the cladding and the surrounding film [259]. However, the cladding and biofilm refractive indexes were not known. Furthermore, the refractive index of the biofilms would be different depending on the rate of cell attachment and the nature of the growth media. Hence, the biomass (Figure 4.6) was used as an indicator of refractive index. An exponential function was applied to the inverse biomass versus wavelength shift. Figure 4.7 shows the plots for peak 1, for U and PC LPG OFS. Data for peak 2 are presented in Appendix F.

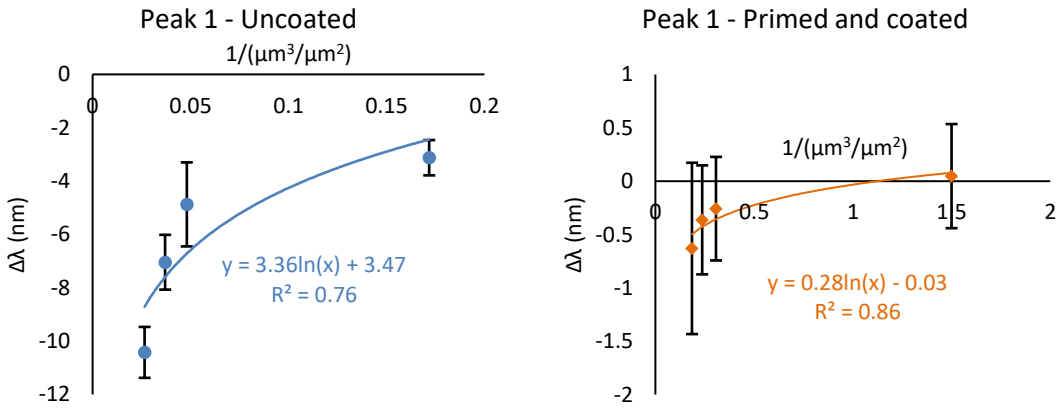


Figure 4.7. Exponential relationship between the inverse biomass of *P. aeruginosa* biofilms on U and PC optical fibres and the wavelength shift of peak 1 from U and PC LPG OFS exposed to *P. aeruginosa* culture medium in RPMI-1640, for 24 hours. Error bars are ± SD of wavelength shift, N = 8. Line equations and R^2 are also displayed.

The lowest R^2 was 0.66 for any of the LPG OFS (peak 2, PC LPG OFS; Appendix F). Differing relationships were observed for U and PC LPG OFS, due to the differing biomasses of biofilms on U and PC optical fibres (Figure 4.6).

4.4.4. LPG OFS response in bacteria culture medium from 24 to 72 hours

After spectra collection for 24 hours (Figure 4.5), U and PC LPG OFS were kept immersed in *P. aeruginosa* culture medium, in RPMI-1640, for a further 48 hours. Transmission spectra were collected at the 48 and 72 hour time points. Figure 4.8 shows the wavelength shifts (from the 0 hour peak wavelengths) of both attenuation bands, from 24 to 72 hours.

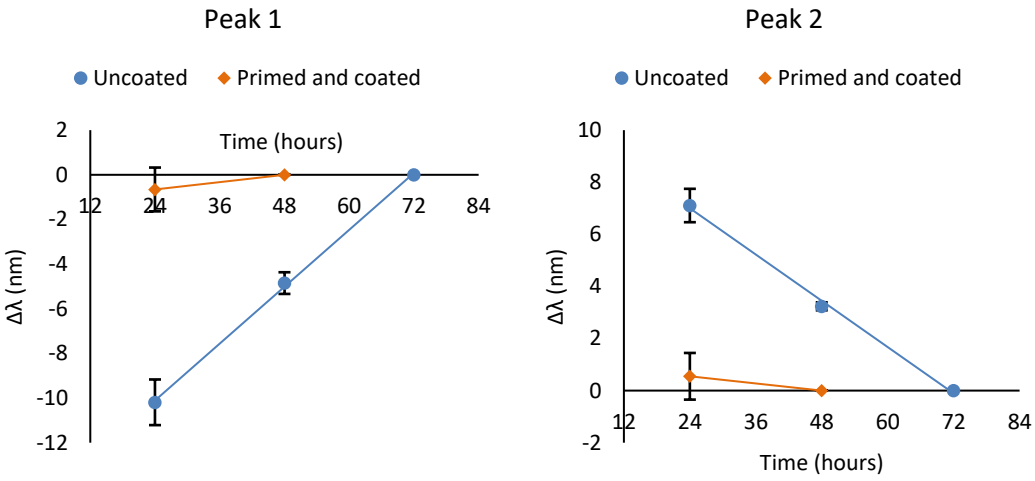


Figure 4.8. Wavelength shifts of both attenuation peaks in the optical spectrum, from 24 to 72 hours, for U and PC LPG OFS immersed in *P. aeruginosa* culture in RPMI-1640 medium. Error bars are ± SD, N = 5.

All attenuation peaks shifted linearly ($R^2 \geq 0.99$). For the U sensor, the wavelength shift of peak 1 fell from -10.19 nm to -4.85 nm between 24 and 48 hours. The wavelength shift for peak 2 fell from 7.11 nm to 3.24 nm between 24 and 48 hours. Both peaks then fell to zero at 72 hours. For the PC sensor, the wavelength shift of both peaks fell to zero at 48 hours. There was no further shift after this. At 24 and 48 hours, the wavelength shifts for both peaks of the U LPG OFS were statistically higher ($p < 0.01$) than the PC LPG OFS.

P. aeruginosa biofilms growing on insensitive optical fibres, in RPMI-1640, were imaged at 48 and 72 hours. *Z*-stack images were acquired and the biomass quantified using COMSTAT. Figure 4.9 shows the CLSM images and quantified biomass of biofilms at 24, 48 and 72 hours.

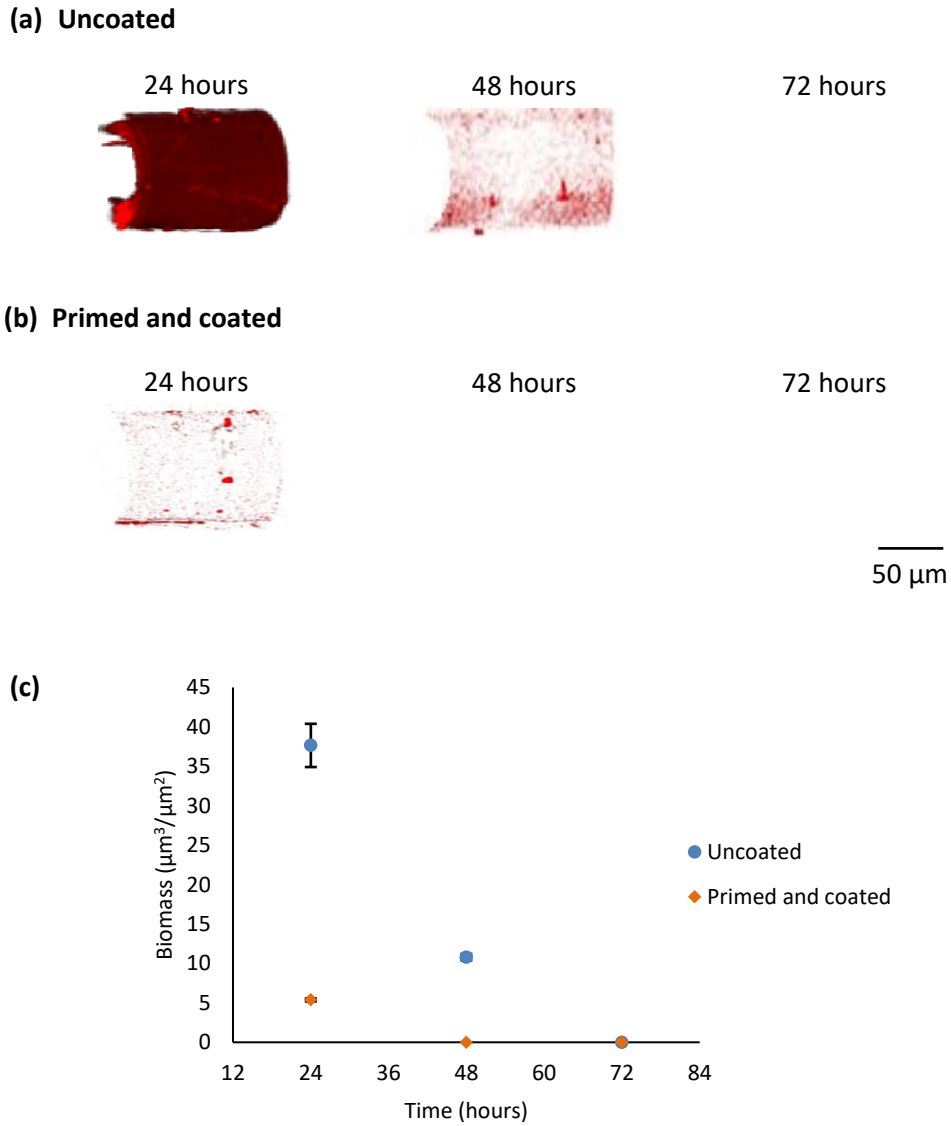


Figure 4.9. (a) *Z*-stack CLSM images of *P. aeruginosa* biofilms, labelled with mCherry, on U optical fibres, at 24, 48 and 72 hours. The red masses represent biofilm. **(b)** *Z*-stack CLSM images of *P. aeruginosa* biofilms, labelled with mCherry, on PC optical fibres, at 24, 48 and 72 hours. The red masses represent biofilm. The scale bar is 50 µm and is applicable to all images. **(c)** Quantified biomass for images in (a) and (b), using a COMSTAT threshold of 56. Error bars are ± SD, N = 3.

CLSM images show a progressive degradation of the biofilm from 24 to 48 and 72 hours, on PC and U substrates respectively. On the U fibre, the biomass fell from 37.65 $\mu m^3/\mu m^2$ to 10.80 $\mu m^3/\mu m^2$ between 24 and 48 hours, then to zero at 72 hours. On the PC fibre, the biomass fell from 5.38 $\mu m^3/\mu m^2$ to zero between 24 and 48 hours. No biomass was recorded at 72 hours. At 24 and 48 hours, the biomass on the U fibre was significantly higher (no error bar overlap) than on the PC fibre.

4.4.5. Sensitivity of LPG OFS to biomass

U LPG OFS were exposed to *P. aeruginosa* (PA01-N) culture in RPMI-1640 medium and transmission spectra collected every 5 minutes until a wavelength shift could be measured. This occurred after 1 hour; the wavelength shifts of attenuation peaks 1 and 2 at this time were -0.52 nm and 0.17 nm respectively. Simultaneously, *P. aeruginosa* biofilms were grown on U insensitive optical fibres. *Z*-stack CLSM images were obtained at 1 hour and the biomass quantified in COMSTAT, using a user-defined COMSTAT fluorescence threshold of 57. The biomass after 1 hour was 0.81 $\mu m^3/\mu m^2$. Therefore, the maximum sensitivity of LPG OFS to biomass can be expressed as the smallest wavelength shift per biomass unit, which is 0.21 nm per biomass unit ($\mu m^3/\mu m^2$).

4.4.6. LPG OFS incorporated into ETTs

4.4.6.1. Response in RPMI-1640

To simulate an LPG OFS-instrumented ETT, LPG OFS were fixed into lumens of 5 cm long sections of tube and onto 3 cm^2 sections of cuff (Figure 4.2). The combined LPG OFS-ETT systems (U and PC) were immersed in *P. aeruginosa* (PA01-N) culture medium, in RPMI-1640 and the wavelength shifts of attenuation bands plotted against time of immersion, over 24 hours. Figure

4.10 are the wavelength shift plots for both attenuation peaks and for U and PC systems. Wavelength shift profiles for tube and cuff systems are displayed.

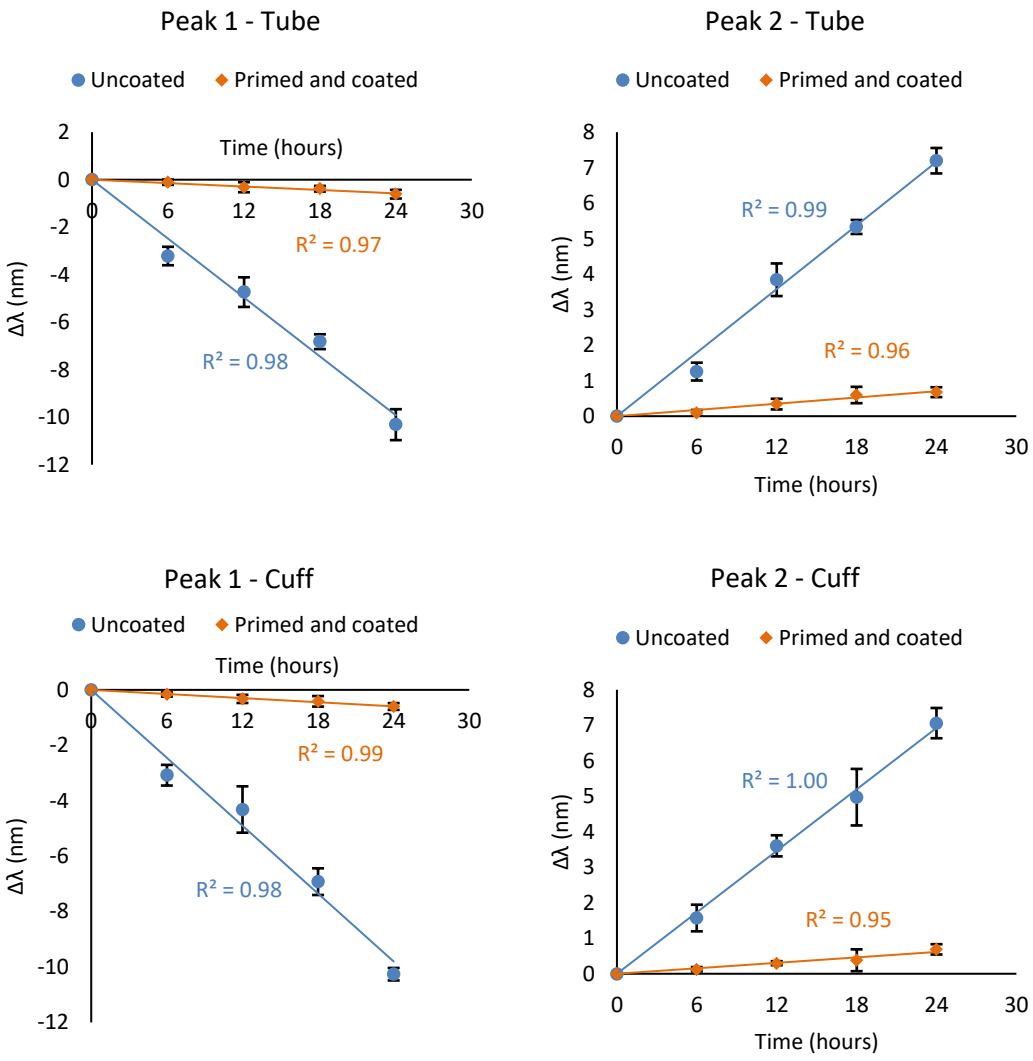


Figure 4.10. Wavelength shift against time for both attenuation peaks of U and PC LPG OFS incorporated into ETT tubes and onto cuffs, immersed in *P. aeruginosa* culture medium in RPMI-1640, for 24 hours. R^2 are displayed in labels of corresponding colours. Error bars are ± SD, N = 3.

In all cases, wavelength shift was linear with increased time of immersion in bacteria culture medium. Peaks 1 and 2 shifted in opposite directions. The PC LPG OFS-ETT systems displayed significantly lower wavelength shifts (no error bar overlap) than the U systems, at all time points after 0 hours. There was also no difference in wavelength shift, at any time point after 6 hours, between tube and cuff systems, for the equivalent peak and surface modification. There was

also no difference between wavelength shifts between LPG OFS incorporated into ETTs and LPG OFS in the PTFE well (Figure 4.5), for the equivalent peak and surface modification.

1 cm^2 sections of tube and cuff, U and PC, were exposed to *P. aeruginosa* culture medium, in RPMI-1640. 2D and Z-stack CLSM images were acquired and biomass quantified from the latter using COMSTAT. The quantified biomass is shown in Figure 4.11. The associated 2D CLSM images are displayed in Appendix G.

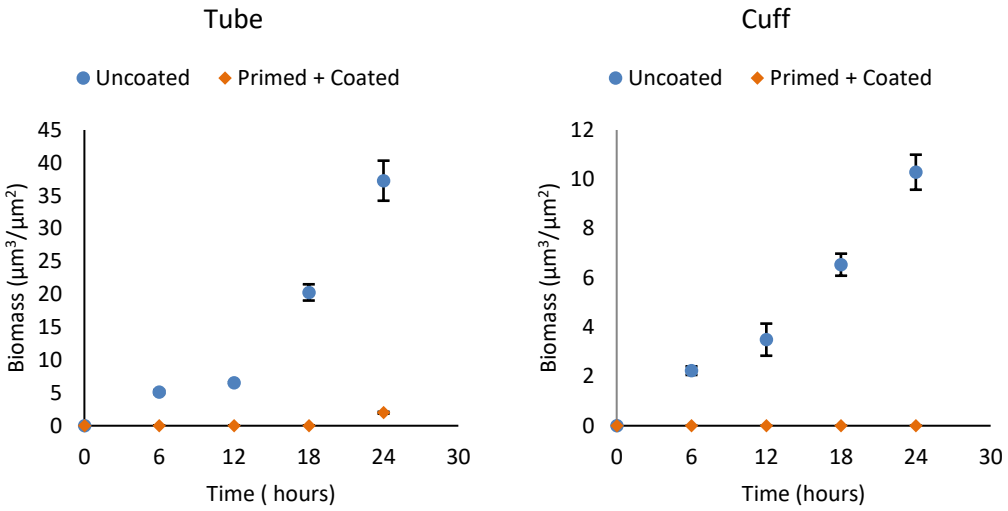


Figure 4.11. Biomass increase over time of *P. aeruginosa* biofilms grown on U and PC tubes and cuffs, in RPMI-1640 medium. The COMSTAT threshold was 60. Error bars are ± SD, N = 3.

On U tubes and cuffs, biomass increased to 37.29 and 10.29 $\mu m^3/\mu m^2$ respectively, over 24 hours. On PC tubes, no biomass was measured up to 18 hours; at 24 hours, a biomass of 1.98 $\mu m^3/\mu m^2$ was recorded. On PC cuffs, no biofilm was observed over 24 hours. At all time points after 0 hours, the U tubes and cuffs had biofilms with higher biomasses than the equivalent PC substrates. Biofilms on U tubes were higher than on U cuffs, after 0 hours. PC substrates had no biofilm present until 24 hours, where the tube biomass was significantly higher (no error bar overlap) than cuff biomass.

As with the LPG OFS in the PTFE well, the inverse biomass (of *P. aeruginosa* biofilms on tubes and cuffs) was plotted against wavelength shift and an exponential function fitted to the data. The peak 1 plots, for U tubes and cuffs are shown in Figure 4.12. Peak 2 data is presented in Appendix F. The function could only be applied to the U data, since no biomass was detected on the PC substrates (apart from on tubes at 24 hours).

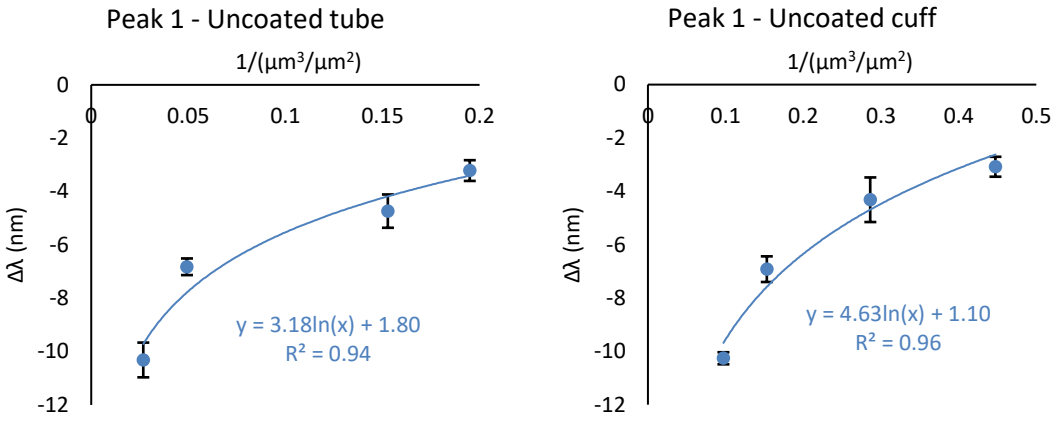


Figure 4.12. Exponential relationship between the inverse biomass of *P. aeruginosa* biofilms on U ETT tubes and cuffs and the wavelength shift of peak 1 from U LPG OFS-ETT systems immersed in *P. aeruginosa* culture medium in RPMI-1640, for 24 hours. Error bars are ± SD of wavelength shift, N = 3. Line equations and R^2 are also displayed.

Since the biomass was different on tubes and cuffs in RPMI-1640 (Figure 4.11), the relationship between biomass and wavelength shift was different for tube and cuff systems. The lowest R^2 was 0.89 (peak 2, tube; Appendix F).

4.4.6.2. Response in ASM G

The protocol of immersing LPG OFS-ETT systems, U and PC, in a *P. aeruginosa* (PA01-N) culture (section 4.4.6.1), was repeated in ASM G. Figure 4.13 are the wavelength shift profiles of both attenuation bands over time of immersion in bacteria culture medium, for both tube and cuff systems, for 24 hours.

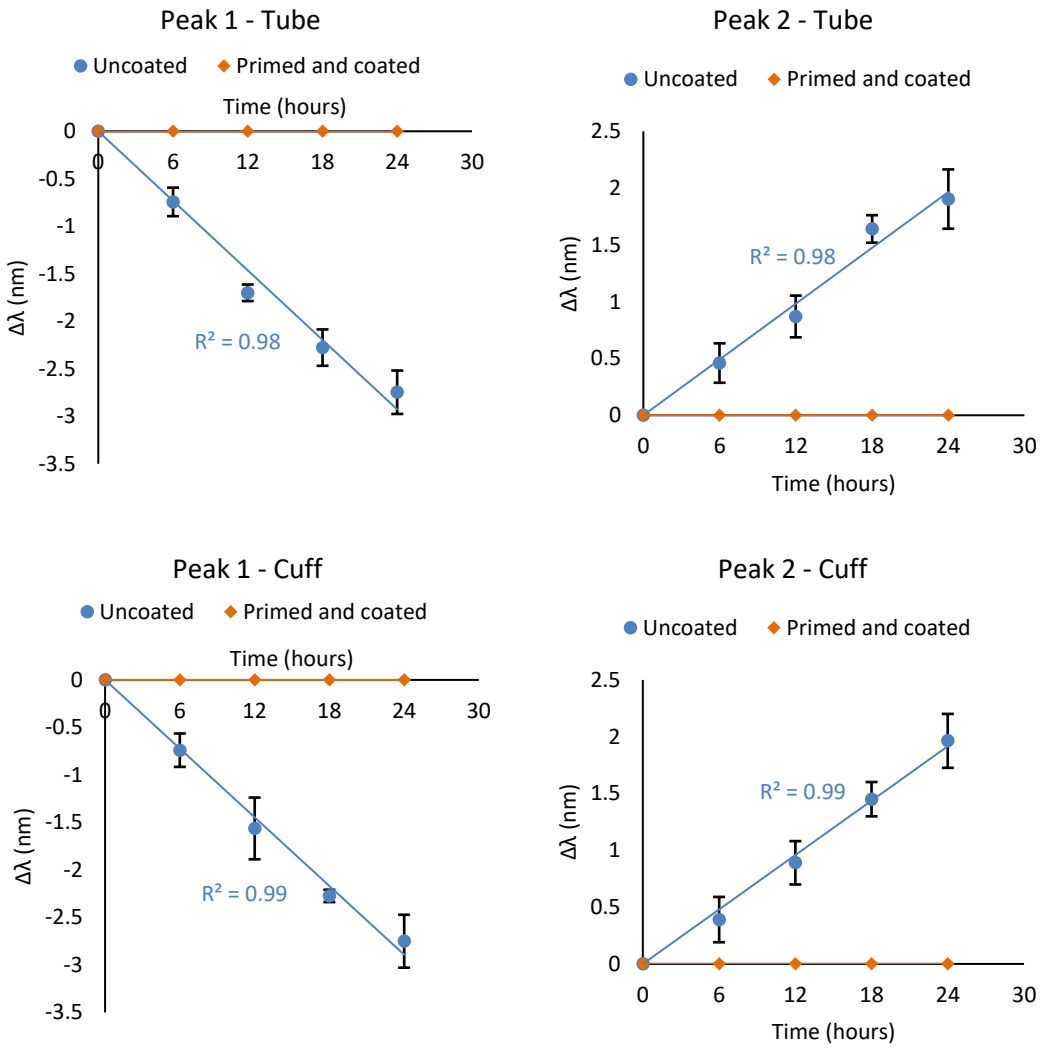


Figure 4.13. Wavelength shift against time for both attenuation peaks of U and PC LPG OFS incorporated into ETT tubes and onto cuffs, immersed in *P. aeruginosa* culture medium in ASM G, for 24 hours. R^2 are displayed in labels of corresponding colours. Error bars are ± SD, N = 3.

Both attenuation peaks shifted linearly over time and shifted in opposite directions. There was no wavelength shift observed for PC LPG OFS-ETT systems, therefore the PC LPG OFS-ETT systems displayed significantly lower wavelength shifts (no error bar overlap) than the U systems, at all time points after 0 hours. There was also no difference in wavelength shift, at any time point after 6 hours, between tube and cuff systems, for the equivalent peak and surface modification.

1 cm^2 sections of tube and cuff, U and PC, were exposed to *P. aeruginosa* culture medium, in ASM G. 2D and Z-stack CLSM images were acquired and biomass quantified from the latter using COMSTAT. The quantified biomass is shown in Figure 4.14. The associated 2D CLSM images are displayed in Appendix G.

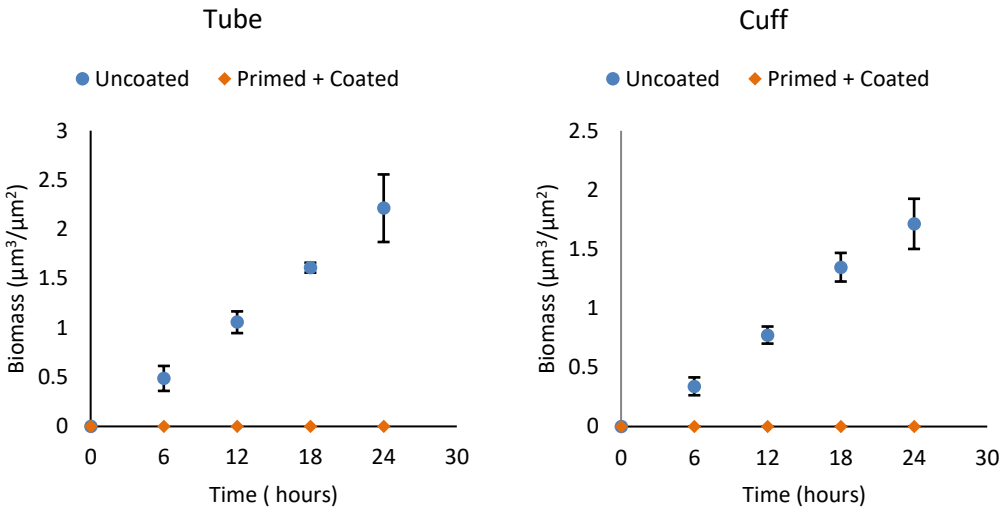


Figure 4.14. Biomass increase over time of *P. aeruginosa* biofilms grown on U and PC tubes and cuffs, in ASM G. The COMSTAT fluorescence threshold was 60. Error bars are ± SD, N = 3.

On U tubes and cuffs, biomass increased to 2.21 and 1.71 $\mu m^3/\mu m^2$ respectively, over 24 hours. On PC tubes and cuffs, no biomass was measured over 24 hours. At all time points after 0 hours, the U tubes and cuffs had biofilms with higher biomasses than the equivalent PC substrates. There was no difference between biomass on U tubes and cuffs, at any time point.

As with the LPG OFS in the PTFE well, the inverse biomass (of *P. aeruginosa* biofilms on tubes and cuffs) was plotted against wavelength shift and an exponential function fitted to the data. The peak 1 plots, for U tubes and cuffs are shown in Figure 4.15. Peak 2 data is presented in Appendix F. The function could only be applied to the U data, since no biomass was detected on the PC substrates (Figure 4.14).

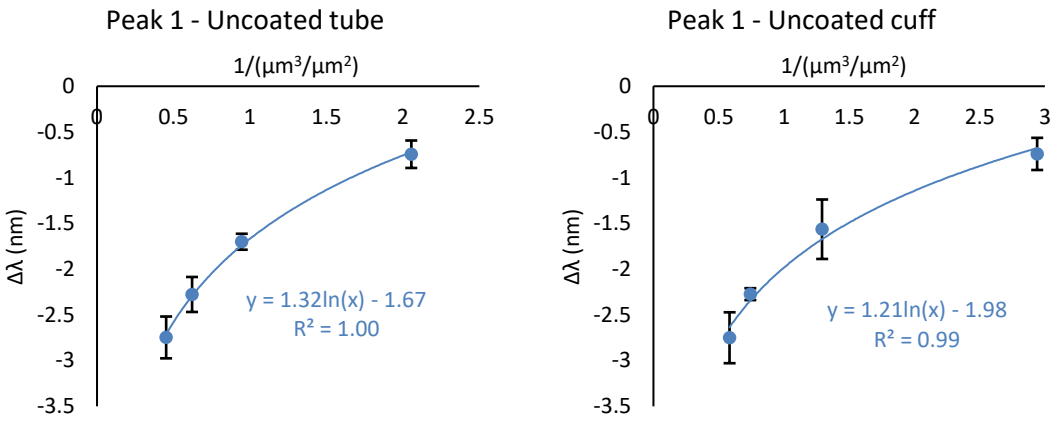


Figure 4.15. Exponential relationship between the inverse biomass of *P. aeruginosa* biofilms on U ETT tubes and cuffs and the wavelength shift of peak 1 from U LPG OFS-ETT systems exposed to *P. aeruginosa* culture medium in ASM G, for 24 hours. Error bars are ± SD of wavelength shift, N = 3. Line equations and R^2 are also displayed.

The differing functions between U tubes and cuff systems were a result of differing mean biomass of *P. aeruginosa* biofilms in ASM G (Figure 4.14). The lowest R^2 was 0.94 (peak 2, tube and cuff; Appendix F).

4.4.6.3. Response in ASM N

The protocol of immersing LPG OFS-ETT systems, U and PC, in a *P. aeruginosa* (PA01-N) culture (section 4.4.6.1), was repeated in ASM N. Figure 4.16 are the wavelength shift profiles of both attenuation bands over time of immersion in bacteria culture medium, for both tube and cuff systems, for 24 hours.

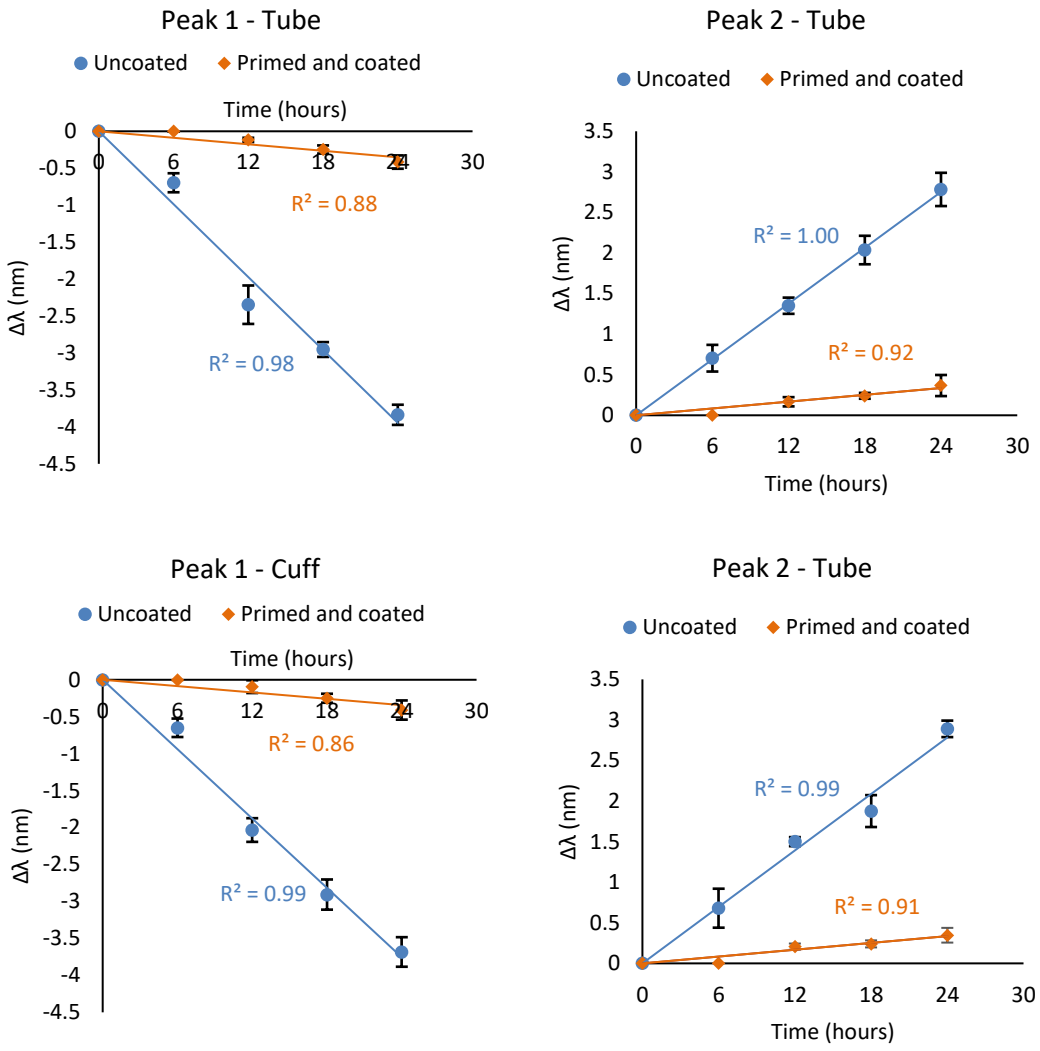


Figure 4.16. Wavelength shift against time for both attenuation peaks of U and PC LPG OFS incorporated into ETT tubes and onto cuffs, immersed in *P. aeruginosa* culture medium in ASM N, for 24 hours. R^2 are displayed in labels of corresponding colours. Error bars are ± SD, N = 3.

Both attenuation peaks shifted linearly over time and shifted in opposite directions. The PC LPG OFS-ETT systems displayed significantly lower wavelength shifts (no error bar overlap) than the U systems, at all time points after 0 hours. On PC tubes and cuffs, there was no wavelength shift observed at 6 hours, after which the wavelength shift increased between 12 and 24 hours. There was also no difference in wavelength shift, at any time point after 6 hours, between tube and cuff systems, for the equivalent peak and surface modification.

1 cm^2 sections of tube and cuff, U and PC, were exposed to *P. aeruginosa* culture medium, in ASM N. 2D and Z-stack CLSM images were acquired and biomass quantified from the latter using COMSTAT. The quantified biomass is shown in Figure 4.17. The associated 2D CLSM images are displayed in Appendix G.

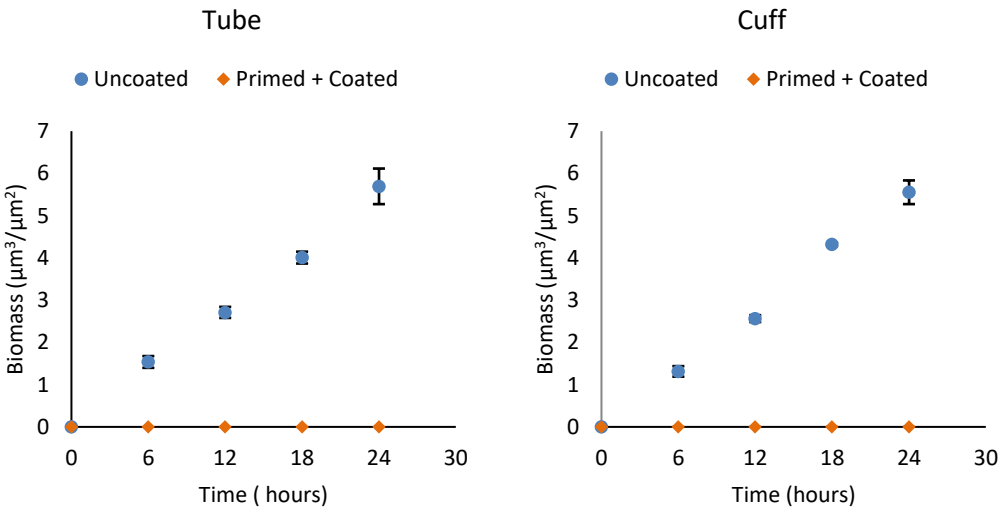


Figure 4.17. Biomass increase over time of *P. aeruginosa* biofilms grown on U and PC tubes and cuffs, in ASM N. The COMSTAT fluorescence threshold was 60. Error bars are ± SD, N = 3.

On U tubes and cuffs, biomass increased to 5.69 and 5.55 $\mu m^3/\mu m^2$ respectively, over 24 hours. On PC tubes and cuffs, no biomass was measured over 24 hours. At all time points after 0 hours, the U tubes and cuffs had biofilms with higher biomasses (no error bar overlap) then the PC substrates. There was no difference between biomass on U tubes and cuffs, at any time point.

As with the LPG OFS in the PTFE well, the inverse biomass (of *P. aeruginosa* biofilms on tubes and cuffs) was plotted against wavelength shift and an exponential function fitted to the data. The peak 1 plots, for U tubes and cuffs are shown in Figure 4.18. Peak 2 data is presented in Appendix F. The function could only be applied to the uncoated data, since no biomass was detected on the primed and coated substrates (Figure 4.17).

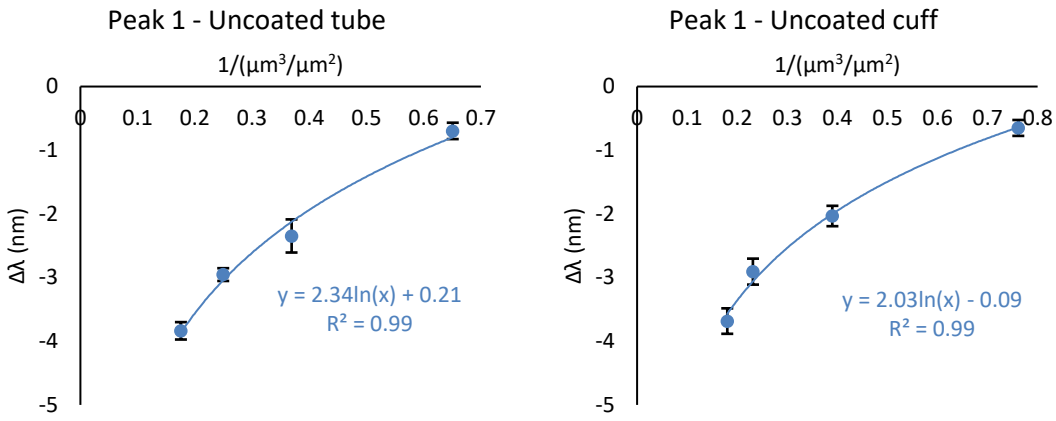


Figure 4.18. Exponential relationship between the inverse biomass of *P. aeruginosa* biofilms on U ETT tubes and cuffs and the wavelength shift of peak 1 from U LPG OFS-ETT systems exposed to *P. aeruginosa* culture medium in ASM N, for 24 hours. Error bars are ± SD of wavelength shift, N = 3. Line equations and R^2 are also displayed.

The differing functions between U tubes and cuff systems were a result of differing mean biomass of *P. aeruginosa* biofilms in ASM N (Figure 4.17). The lowest R^2 was 0.91 (peak 2, cuff; Appendix F).

4.4.6.4. Comparison of wavelength shift between the three bacteria culture media

Figure 4.19 are the wavelength shifts of peak 1 for U and PC LPG OFS-ETT systems in the three culture media used, obtained from Figures 4.10, 4.13 and 4.16. Data for peak 2 is shown in Appendix H.

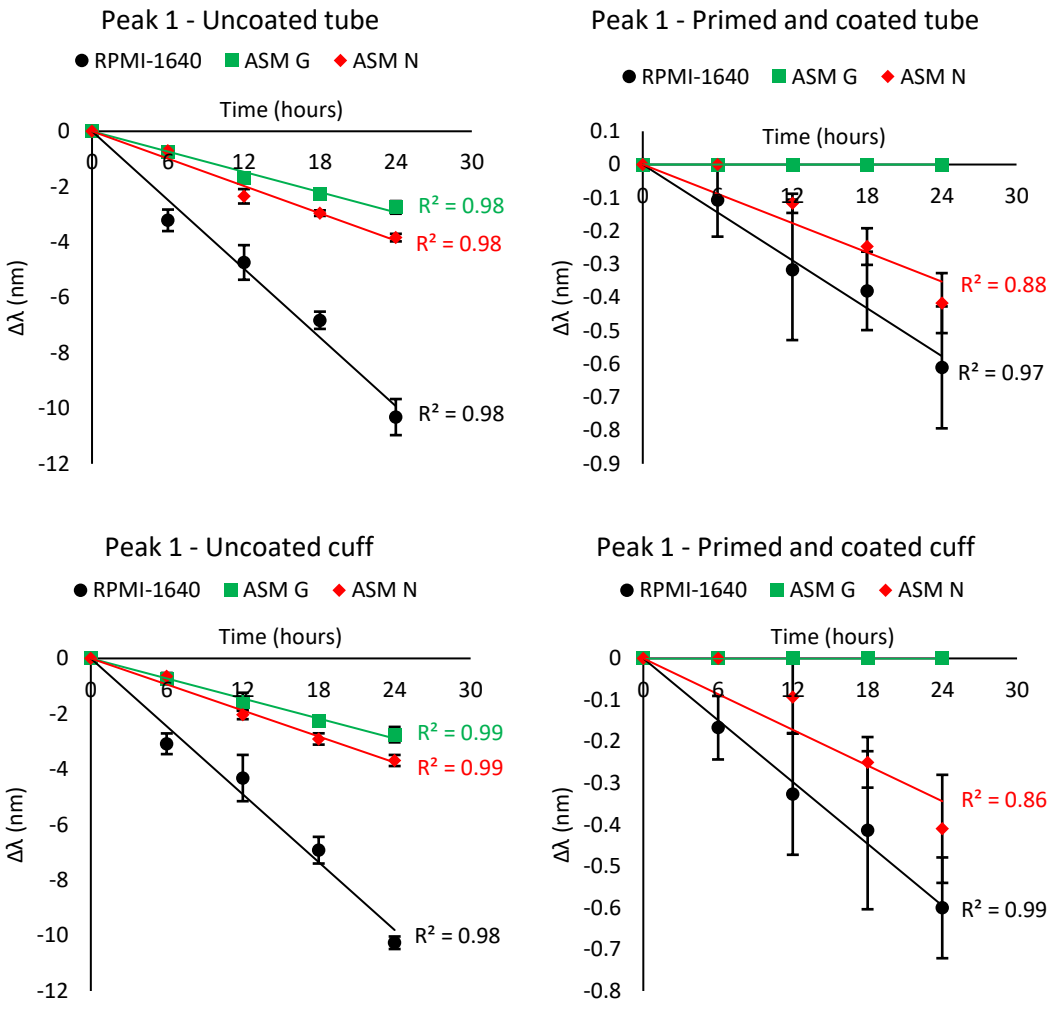


Figure 4.19. Wavelength shift profiles of attenuation peak 1 from U and PC LPG OFS-ETT systems exposed to *P. aeruginosa* culture in RPMI-1640, ASM G and ASM N for 24 hours. R^2 are displayed in labels of corresponding colours. Error bars are ± SD, N = 3.

Wavelength shifts were linear in all media, for both tube and cuff systems. For U systems, the wavelength shifts in RPMI-1640 were significantly higher (no error bar overlap) than the two types of ASM, at time points after 0 hours. ASM N had greater wavelength shifts than ASM G (no error bar overlap) at 18 and 24 hours. For PC systems, there was no difference between RPMI-1640 and ASM N, at any time point (apart from 6 hours on the PC cuff). The wavelength shifts between ASM G and ASM N differed at 12, 18 and 24 hours (no error bar overlap) on device tubes; but only at 18 and 24 hours on device cuffs. Wavelength shifts in RPMI-1640 were higher than ASM G (no error bar overlap) at time points after 0 hours, apart from at 6 hours on PC tubes.

4.5. Discussion

4.5.1. Coating thickness on optical fibres

The mean coating thickness on optical fibres, after priming, was 511 nm, which was lower than the coating thickness on ETT tubes (627 nm) and cuffs (549 nm). The binary silane primer, in principle, forms stable covalent bonds with the silica substrate [202] (Figure 2.8), compared to weaker hydrogen bonds with PVC substrates. This should therefore have increased the stability and/or resistance to stress of the interactions between the polymer and the fibre, resulting in greater polymer deposition.

The lower mean coating thickness on optical fibres, therefore, was more likely influenced by the surface roughness and shape of the substrate [260]. Smoother silica fibres could have allowed quicker drainage of polymer from the substrate into the polymer reservoir, reducing polymer deposition compared to rougher ETT substrates [260]. Furthermore, the cylindrical shape of the fibres, combined with the lower surface area, may have led to lower polymer deposition [261], via reduced retention of polymer on optical fibre surfaces. This would have resulted in lower coating thicknesses, compared to ETT tubes and cuffs, which were flatter cuboids with larger surface area. However, the effect of surface roughness and shape on polymer film thickness is yet to be established.

4.5.2. Calibration of LPG OFS using sodium chloride solutions

The purpose of the calibration was to establish the position of attenuation bands, to note the sensor response with increasing refractive index and to ensure that there were no differences in wavelength shift between U and PC sensors in sodium chloride solutions of the same concentration. Two attenuation bands (or peaks) were present in the transmission spectrum in water, located at roughly 800 and 900 nm (Figure 4.3). Using the amplitude masks for creating the grating (section 4.3.1) meant that these attenuation

bands were in the same position for all LPG OFS used (when immersed in the same medium). These two peaks arose due to coupling near or at the phase matching turning point (PMTP), which typically results in a single broad attenuation band [165,166], which splits into two as refractive index increases, because of coupling to a single cladding mode at two different wavelengths. The presence of two peaks suggests the attenuation band at the PMTP had already split, meaning coupling was occurring at the PMTP [166]. LPG OFS with this property have the highest sensitivity [166].

The application of the primer and polymer coating caused the attenuation peaks to lose transmission and to shift in opposite directions from the U attenuations. The loss of transmission represented more efficient core-cladding mode coupling [166], caused by the application of a film of higher refractive index (than air) on the LPG OFS cladding surface, which changed the effective index of the cladding modes. Peaks shifted in opposite directions due to differing cladding mode effective indexes, also caused by the increased surrounding refractive index [165,166]. This caused coupling centred at different wavelengths to the U LPG OFS (governed by equation 1).

A linear wavelength shift of both attenuation bands was observed with increasing sodium chloride concentration (and higher refractive index, Figure 4.4). As sodium chloride concentration increased, the effective index of cladding modes changed (governed by equation 1), resulting in the central wavelengths of attenuation bands shifting in opposite directions [166,167]. The shift was linear due to a linear increase in medium refractive index causing a step-wise change in cladding index. Peak 1 had a greater wavelength shift than peak 2 (Figure 4.4). This was likely caused by the turning point resonant wavelength being closer to the peak 1 than the peak 2 wavelength [167].

Although the application of the primer and coating lead to a positional change of the attenuation bands in water, there was no difference in the wavelength shift profiles between U and PC LPG OFS. This suggests that the primer and coating did not affect the sensitivity of the LPG OFS, nor did they change core-

cladding mode coupling behaviour with increasing refractive index. Coupling did occur at different wavelengths but the change in cladding mode effective index occurred at the same rate for both LPG OFS surface modifications.

The LPG OFS was able to sense refractive index changes with a 511 nm polymer coating over the cladding. The sensing 'radius' around the cladding is determined by the size of the evanescent field around the cladding [262]. The grating period, mechanical strain and the refractive index of any deposited layer can influence the size of the evanescent field [262]. The radius of detection from the cladding has been reported to be as little as 50 nm [263] and higher than 800 nm [264,265]. The LPG OFS used in this study appears to have an evanescent field greater than 511 nm. Since the wavelength shifts in sodium chloride solutions were the same for U and PC sensors, spectral differences in bacteria culture medium could be attributed to differing bacterial attachment on sensor surfaces.

4.5.3. LPG OFS in *P. aeruginosa* culture medium

A linear change in wavelength shift of both attenuation bands was observed over time of immersion in bacteria culture medium (Figure 4.5). The wavelength shift change is evidence of bacterial adhesion to the LPG OFS surface; bacterial cells and EPS are their own source of refractive index [266]. Biofilm formation linearly changed the local refractive index and thus linearly changed the effective index of the corresponding cladding modes. This caused core-cladding mode coupling to occur at different wavelengths, shifting away from the attenuation bands present at 0 hours. A linear attenuation band wavelength shift, in the order of 1.3 nm, was also observed by Smietana *et al*. [170] upon *E. coli* attachment to phage-functionalised LPG OFS.

The rate of change of wavelength shift was significantly higher ($p < 0.05$) on U sensors than their PC counterparts. This verified the anti-attachment properties of EGDPEA:DEGMA; reduced bacterial adhesion resulted in smaller

cladding mode index change and therefore lesser wavelength shifts (Figure 1.6). This offers exciting opportunities for testing the anti-attachment properties of other materials. Since spectral response is indicative of attachment, coating sensors in different materials and measuring wavelength shift in bacteria culture media may allow comparisons to be made between attachment to uncoated surfaces and attachment to surfaces functionalised with a test material.

CLSM images (Figure 4.6) allowed visualisation of *P. aeruginosa* biofilms on LPG OFS surfaces. On U optical fibres, microcolonies formed at 6 hours and quickly spread across the entire imaged surface over the next 6 hours, before forming biofilms after 18 hours. Referring to the five stage biofilm life cycle (Figure 1.2), it appears that stages (i), (ii) and (iii) all occurred within 6 hours. Late maturation (stage iv) then occurred over the next 18 hours. It was difficult to establish whether dispersion (stage v) was occurring, since biofilms on other parts of the optical fibre could have originated from the bulk culture and/or dispersed cells from other biofilms. *P. aeruginosa* biofilm formation has been described by Heydorn *et al*. [225], who stated that *P. aeruginosa* "colonized the entire substratum very rapidly" before forming "flat and uniform biofilm structures" (all within the first 24 hours). This process was prevented by the polymer coating. Some microcolonies were observed at 18 and 24 hours but a fully formed biofilm was not present. This supports the reduced rate of change of wavelength shift observed on PC LPG OFS.

The biomass plot shows a slow progression in biomass up to 6 hours on U surfaces, as planktonic cells adhered, formed microcolonies and began maturing (Figure 4.6). A rapid growth of the biofilm was then observed up to 12 hours, possibly caused by the RPMI-1640 minimal medium inducing rapid growth of biofilm structures from microcolonies [245]. Biomass then gradually increased to 18 hours, before an 'acceleration' up to 24 hours. This acceleration may be due to cells preparing to exit the biofilm and recolonise other surfaces [41]. On PC optical fibres, biomass slightly increased between 0 and 6 hours, but no significant increases in biomass occurred over the next 18 hours.

After 24 hours, the wavelength shifts for PC LPG OFS were 94% and 90% less than the U LPG OFS, for peaks 1 and 2 respectively. However, the biomass reduction after 24 hours was 86% on PC optical fibres. Also, despite linear changes in wavelength shift, biomass did not increase linearly over time (Figure 4.6). The extra polymeric substances (EPS) excreted by sessile bacteria may be the cause of these differing responses. EPS also provided a source of changing refractive index and therefore contributed to the wavelength shift [166,167,266]. However, EPS did not contain fluorescent markers, hence was not imaged using CLSM and was not quantified in COMSTAT. Both the EPS layer and the bacterial cells were sensed by the LPG OFS, and it is likely that the combination of cells and EPS increased in refractive index linearly, causing the linear wavelength shifts. However, only the cells were imaged and quantified, hence the biomass increases was not linear. The primer and coating resisted attachment and therefore prevented EPS excretion, so the wavelength shift reduction appears to be greater than the biomass reduction after 24 hours on PC substrates. It may be useful to measure the refractive index of *P. aeruginosa* over time, which would allow the relationship between biomass, biofilm refractive index and wavelength shift to be established.

The LPG OFS can sense refractive index changes at distances in the order of hundreds of nanometres from the cladding [217,218], depending on the size of the evanescent field. However, the biofilm growing on the surface of the fibre was in the order of tens of micrometres thick. It can be assumed that the LPG OFS was not sensing refractive index change of the entire biofilm but rather at areas at the cladding-biofilm interface, at a distance limited by the loss of the evanescent field. This may also explain the differing wavelength shift and biomass trends; biomass increases beyond the evanescent field would not be detected by the sensor but would be imaged by the confocal microscope.

When linking biomass to wavelength shift, the evanescent field decay from optical fibre surfaces was explored. The evanescent field decays exponentially with distance from the cladding surface [258,259], based on formulas derived from Maxwell equations [259]. The exact relationship between field decay and

distance from the cladding is dependent upon the refractive indexes of the cladding and the surrounding media [259], neither of which were known in this study. Furthermore, the refractive index of *P. aeruginosa* biofilms would be different depending on the surface and the growth medium. Differing rates of attachment result in differing extents of EPS excretion [267]. It has also been shown that the content of EPS may vary between different growth media [268]. Hence, the biofilm refractive index is highly variable.

In determining a general relationship between biomass and wavelength shift, the biomass was used as an indicator of refractive index and an exponential function was applied to the inverse biomass versus wavelength shift (Figure 4.7). The formulas derived from the plots in Figure 4.7 allow estimation of biomass based on the wavelength shift, which will be applied to LPG OFS-ETT systems in the proceeding experiments. The accuracy of the trendlines in Figure 4.7 is lower than in the experiments where LPG OFS were fixed onto ETT sections (Figures 4.12, 4.15 and 4.18). This could be improved by obtaining biomass data of *P. aeruginosa* biofilms at time points between 6 and 12 hours (where there was a large gap between data points). This would ensure that the exponential function indeed follows the trend as expressed in Figure 4.7, as well as improving the trendline accuracy.

Since biomass was different on U and PC LPG OFS, the exponential function was different between surface modifications. Therefore, for a given surface or material, a training set of data would first need to be acquired; the wavelength shift from LPG OFS and biomass on that material would first need to be measured and the exponential function established. The resultant equation could subsequently be applied to that material, in *P. aeruginosa* culture medium, allowing biomass to be quantified based on wavelength shift.

Since an exponential function was applied to the biomass versus wavelength shift plot, an asymptote exists, which represents the limit of detection of LPG OFS. Hence, beyond a certain biomass, there would be no further change in wavelength shift. This corroborates the evanescent field decay theory for

optical fibre sensors; beyond a certain level of decay, changes in surrounding refractive index can no longer be detected. Also, beyond a certain refractive index, no further wavelength shift would occur. This limit of detection (of refractive index) could be estimated by measuring the refractive index of biofilms over time, until no further change in wavelength shift occurs.

4.5.4. Spectral response from 24 to 72 hours

On U LPG OFS, the wavelength shifts fell to just below half of the 24 hour values between 24 and 48 hours, then fell to zero at 72 hours (Figure 4.8). On the PC LPG OFS, the wavelengths of attenuation bands returned to the 0 hour wavelengths at 48 hours and wavelength shift remained at zero at 72 hours. This is indicative of cell detachment and decreasing biomass on the optical fibres. The peak biomass occurred at 24 hours; on U optical fibres, biomass fell to below one-third at 48 hours and fell to zero at 72 hours. No biomass was recorded at 48 or 72 hours on PC substrates. The minimal RPMI-1640 medium did not allow dispersed cells (if any) to survive and recolonise other surfaces and so biofilms disintegrated after 24 hours [245]. Disintegrating biofilms on LPG OFS surfaces lowered the local refractive index and reversed the changes in the cladding mode effective index and so the wavelength shift returned back to zero. The LPG OFS could therefore detect both cell attachment and detachment. As with biofilm formation in the first 24 hours, the wavelength shifts decreased linearly but the biomass did not. This could also be due to the EPS disintegration and the effective radius of detection around the cladding of the LPG OFS.

4.5.5. Sensitivity of LPG OFS to biomass

The maximum sensitivity of the LPG OFS used in this study was 0.21 nm per biomass unit ($\mu m^3/\mu m^2$), with a limit of detection of 0.81 $\mu m^3/\mu m^2$. Smietana *et al*. [170] and Tripathi *et al*. [171] recorded minimum wavelength shifts of 1.3

and 2.1 nm respectively upon bacterial attachment to *E. coli* phage-functionalised LPG OFS. The minimum wavelength shift recorded in this study was 0.17 nm (peak 2, 1 hour after immersion in bacteria culture medium). Therefore, the LPG OFS used in this study, without surface modification, was more sensitive (higher wavelength resolution) than the ones used in previous reports. This may be due to the grating being inscribed at the PMTP, giving rise to two attenuation bands of highest sensitivity to refractive index [166]. It would also be beneficial to measure the refractive index of the biofilm after 1 hour, to ascertain the sensitivity to refractive index units (RIUs) and the RUI limit of detection. Nevertheless, due to the high sensitivity to biomass, LPG OFS could be a suitable instrumentation for ETTs to provide live, accurate feedback on device colonisation.

4.5.6. LPG OFS as sensing instrumentation for ETTs

4.5.6.1. Spectral response from LPG OFS incorporated into ETT sections

In all three culture media and on tubes and cuffs, attenuation peaks shifted linearly with increased time of exposure to bacteria, signifying linear changes in biofilm refractive index. U LPG OFS-ETT systems displayed higher wavelength shifts than the PC systems from 6-24 hours, indicating greater bacterial attachment to U systems. This further reinforces the anti-attachment property of EGDPEA:DEGMA.

There was no difference in wavelength shifts between tube and cuff systems, for the same peak, in the same medium. Furthermore, there was no difference in spectral response between LPG OFS fixed onto tubes/cuffs and the LPG OFS placed into the PTFE well, in RPMI-1640 medium. This was despite differing biomass of *P. aeruginosa* on tubes and cuffs (Figure 4.11). No biomass was recorded on PC surfaces, aside from tubes in RPMI-1640, even though wavelength shifts was recorded on PC systems in RPMI-1640 and ASM N (Figures 4.10 and 4.16). This suggests that spectral response is not influenced

by attachment to the substrate that the LPG OFS is incorporated onto, but rather attachment to the sensor cladding itself, within the reaches of the evanescent field. Therefore, the wavelength shifts observed from these systems are associated with changing refractive index at the cladding surface, not at the substrate surface.

4.5.6.2. Biomass of *P. aeruginosa* biofilms on ETTs

Different rates of bacterial attachment were observed when comparing tubes and cuffs, with the same surface modification, in RPMI-1640 (Figure 4.11). This was previously demonstrated; ToF-SIMS analysis of tube and cuff surfaces (Figure 3.3) suggested that DEHP plasticisers in cuffs may have a bactericidal effect [252-254], preventing biofilm formation. There were also differences in biomass on U ETT sections between the culture media. This was also previously demonstrated (Figure 3.8) and was thought to be associated with the nutrient composition of the three media. Biofilms had the highest biomass in RPMI-1640, then in ASM N, followed by ASM G, which is the reverse order of nutrient content. ASM G contains all the amino acids, salts, iron and glucose, which supported cell growth and thus prevented biofilm formation [244,245]. The difference between tubes and cuffs were not apparent in either ASM type, possibly due to the media supporting cell growth enough to prevent significant attachment/biofilm formation on any substrate. PC surfaces completely resisted bacterial attachment, aside from on device tubes in RPMI-1640, at 24 hours (Figure 4.11). Although some attachment occurred at this point, no microcolonies or biofilm structures were observed.

4.5.6.3. Relationship between biomass and wavelength shift

For U LPG OFS-ETT systems, the relationship between biomass on tubes and cuffs and wavelength shift was established, in all three culture media (Figures 4.12, 4.15 and 4.18). Even though the wavelength shift was caused by bacterial attachment to LPG OFS cladding, not the ETT, this relationship would still allow estimation of biomass on ETTs from the spectral response, since they were both exposed to the same culture medium, in the same environment. Since

there was no biomass on PC ETT substrates, there was no relationship between biomass and wavelength shift. Nevertheless, since the primer and the EGDPEA:DEGMA coating effectively reduced bacterial attachment on ETT surfaces, the need for sensing instrumentation would not be required.

Figures 4.12, 4.15 and 4.18 were the exponential functions of the inverse biomass versus wavelength shift in the three culture media. The lowest R^2 observed for any peak was 0.89, indicating good correlation between the biomass and wavelength shift using the exponential function. Differing biomass between tubes and cuffs and between culture media led to different exponential functions, each of which could be used as training data; the mathematical formulas presented on each plot in Figures 4.12, 4.15 and 4.18 could be used to estimate biomass from wavelength shift, on tubes and cuffs, in either culture medium. For example, for a biofilm on ETT tubes, grown in ASM G, a peak 1 wavelength shift of -2 nm would represent a biomass of 1.28 $\mu m^3/\mu m^2$, calculated by rearranging the formula displayed in Figure 4.15 to give equation 6.

$$x = e^{-(\frac{y+1.67}{1.32})} \quad (6)$$

Where *x* is biomass and *y* is the wavelength shift (of a given peak). For incorporation of LPG OFS into ETTs for the clinical use, the biomass beyond which infection occurs would first need to be established (i.e. an infection threshold). Should the wavelength shift represent a biomass at or beyond the threshold, the physician could then act appropriately, by either removal of the device and/or treating the patient with relevant antibiotics. LPG OFS, in this case, provides an early warning of infection, reducing the time required for examining contaminated devices and allowing interception of ETT-centred infection.

LPG OFS in these systems were not selective for *P. aeruginosa*, but the exponential functions applied to Figures 4.12, 4.15 and 4.18 were specific for *P. aeruginosa* biofilms. However, measuring the wavelength shift and

quantifying biomass for other bacteria species on U ETTs may allow for mathematical functions to be derived for many species, allowing biomass quantification from spectral response for multiple pathogens.

4.5.6.4. Spectral response in different culture media

The differing wavelength shifts in Figure 4.19 and Appendix H can be related to differing levels of bacterial attachment to the LPG OFS surface. U LPG OFS-ETT systems showed greater wavelength shifts in RPMI-1640, then ASM N, then ASM G (significance beginning from 12 hours and 18 hours on tubes and cuffs respectively). This represented greater attachment and biofilm formation to cladding surfaces in RPMI-1640 and the least attachment in ASM G. However, for PC LPG OFS-ETT systems, no differences were observed between RPMI-1640 and ASM N. This suggests that the primer and coating resisted attachment significantly enough to outweigh the effect of the media, compared to U systems. No wavelength shift was observed for PC systems in ASM G, indicating zero attachment. Overall, the LPG OFS-ETT systems were able to monitor biofilm formation in real time, in all three media. Since ASM was used to mimic the conditions of a patient's airway, the relationship between biomass and wavelength shift (Figures 4.15 and 4.18) may allow biomass of *P. aeruginosa* biofilms on ETT surfaces to be quantified from wavelength shift *in situ*, for patients with differing sputum glucose content.

4.5.7. Designing an instrumented ETT

The LPG OFS could easily be incorporated into the lumen of ETTs, by using safe, approved adhesives, such as the cyanoacrylates [269]. The LPG OFS would have to be manufactured to work in reflection mode, whereby the sensing region is at the optical fibre terminus (rather than in the middle) and the transmitted light is reflected back up the optical fibre by a mirror at the fibre terminus [270]. This would allow the light source and spectrometer to be positioned at the same end of the ETT, outside the body. Figure 4.20 schemes the designed

prototype of the instrumented ETT, which could be trialled in an animal model or live patients. Incorporating the LPG OFS onto device cuffs provides an additional challenge; inflation of the cuff and tracheal contact may cause damage to the sensor apparatus. Further research into the influence of cuff-trachea contact pressure on spectral response is required.

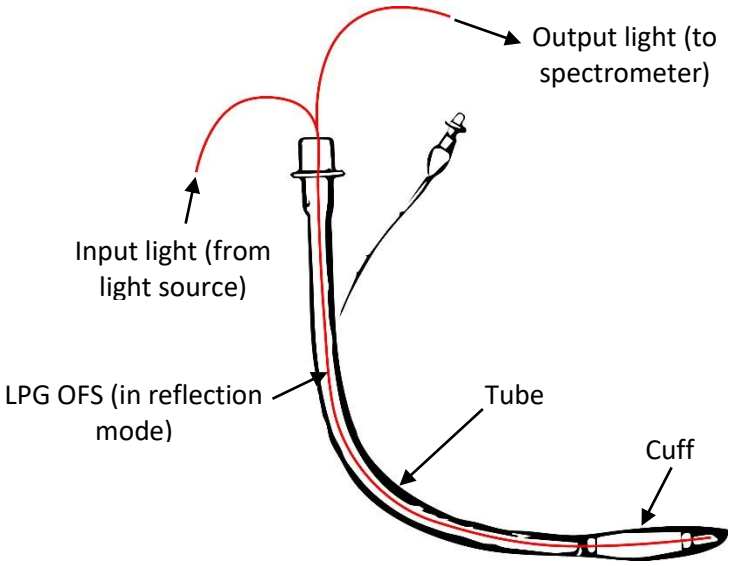


Figure 4.20. Schematic of LPG OFS instrumentation incorporated into an ETT lumen, working in reflection mode, with both ends of the LPG OFS exiting the end of the device outside the body.

4.6. Conclusions

This study examined the novel use of LPG OFS to monitor bacterial attachment and biofilm formation on ETTs in real time. Upon calibration of LPG OFS in solutions of increasing sodium chloride concentration, linear wavelength shifts occurred for both attenuation bands, with identical rates of change for U and PC LPG OFS. This was caused by linear increases in concentration (and refractive index) causing linear cladding mode effective index change.

When LPG OFS were immersed in *P. aeruginosa* culture medium in RPMI-1640, linear wavelength shifts were observed over time of immersion, for both U and PC LPG OFS, signifying increased bacterial adsorption and a linear change in biofilm refractive index. The wavelength shifts of the two attenuation peaks from PC LPG OFS, after 24 hours, were 94% and 90% less than the U LPG OFS, indicating that EGDPEA:DEGMA reduced bacterial adhesion to sensor surfaces.

P. aeruginosa biofilms were grown on U and PC insensitive optical fibres and the biomass quantified over 24 hours using COMSTAT. Biomass on PC optical fibres after 24 hours were significantly less than on U optical fibres, further highlighting the anti-attachment capability of EGDPEA:DEGMA and supporting the reduced wavelength shifts observed from PC LPG OFS. Unlike wavelength shift, biomass did not increase linearly. The differing trends in wavelength shift and biomass were possibly caused by EPS excretion by sessile cells, which would have contributed to the wavelength shifts, since EPS has its own refractive index. However, EPS could not be imaged or quantified, so it is likely that the combination of bacterial cells and EPS changed the cladding mode effective index linearly. The decay of the evanescent field with increased distance from the cladding is governed by an exponential function. Biomass was therefore related to the wavelength shift via an exponential function.

The sensitivity of the LPG OFS used was 0.21 nm per biomass unit ($\mu m^3/\mu m^2$), with a limit of detection of 0.81 $\mu m^3/\mu m^2$. This demonstrated a higher sensitivity compared to previous reports of *E. coli* sensing using LPG OFS. LPG OFS also allowed cell detachment and biofilm degradation to be sensed, with

linear decreases in wavelength shift observed between 24 and 72 hours, on U and PC LPG OFS. Biomass also decreased over this time, on both substrates.

Incorporation of LPG OFS into ETT tubes and cuffs and subsequent exposure to *P. aeruginosa* cultures in RPMI-1640, ASM G and ASM N also displayed linear wavelength shifts over time, in all three media. Differing rates of change of wavelength shift between media for U LPG OFS-ETT systems allowed the media's effect on biofilm formation to be assessed. RPMI-1640 appeared to stress the bacteria the most, with greater rates of change of wavelength shift from LPG OFS-ETT systems immersed in bacteria culture in RPMI-1640, representing a greater rate of biofilm formation. There was no difference in wavelength shifts between LPG OFS incorporated into ETTs and the equivalent LPG OFS placed into a PTFE well, demonstrating that biofilm formation on the optical fibre surface contributed to the wavelength shift, within the reaches of the evanescent field.

P. aeruginosa biofilms were grown on ETT tubes and cuffs, in all three growth media and the biomass quantified using COMSTAT. Exponential relationships were also observed when plotting the inverse biomass on U substrates against U wavelength shift, in each media. Even though the biomass on ETT sections did not directly contribute to the wavelength shift, the exponential functions could be used to quantify *P. aeruginosa* biomass on U ETTs from the wavelength shift alone, which could give an early warning of ETT biofouling and allow interception of VAP. LPG OFS could therefore, for the first time, be used as a sensing instrumentation for ETTs, allowing real time feedback on biofilm formation on device surfaces, with high sensitivity. Designing an instrumented device offers the possibility of *in situ* biofilm detection.

5. Development of a bacteria species identification LPG optical fibre sensor using polymers with differential bacterial attachment

5.1. Introduction

Antimicrobial resistance is a huge global health issue; it can cause ordinarily treatable infections to become fatal [178], as well as compromising surgical procedures and chemotherapy treatments [178]. Antimicrobial resistance is partly compounded by the overuse of broad spectrum antibiotics. [177]. Hence, identification of bacteria species is paramount, so that appropriate antibiotic regimens can be chosen. Choosing antibiotics that bacteria are sensitive to prevents the overuse of broad spectrum agents, which can limit the spread of resistance. Currently, identification of pathogenic bacteria involves taking samples from the patient, culturing the infectious organism and then using various microscopic and staining techniques to identify the organism [174]. This process can take several days, during which an infection can worsen and spread [256].

A more rapid, non-invasive and sensitive method of identifying bacteria species is required, to curb the spread of antimicrobial resistance and to allow treatment to be quickly administered to patients before infections cause serious harm. Moreover, real time bacterial species identification would be a powerful research tool for studying bacterial co-cultures. This is relevant for being able to study complex multi-species infections and environments, such as cystic fibrosis or the impact of antibiotic treatment on the gut biome [49,271].

In this chapter, materials with bacteria selective binding abilities were identified, synthesised and used as coatings for LPG OFS to generate a tool that can identify known bacteria species. Selective binding is defined as the property of a material to differentially bind different bacteria species [181]. Selective, or differential, binding of bacteria has previously been demonstrated

by investigating the interaction of bacterial lectins to various polysaccharides [182]. It is possible that species-specific membrane-bound proteins, such as lectins, may differentially interact with polymer pendant groups, resulting in the discovery of species-selective polymers [142]. In the case of LPG OFS, differential bacterial attachment to a species selective material coating would result in differential wavelength shifts, allowing species identification based on spectral response alone.

The materials were identified from a large data set generated by Hook *et al*. [186]. A range of acrylate and methacrylate polymers were printed onto microarray slides, incubated with *P. aeruginosa*, *S. aureus* and Uropathogenic *E. coli* culture media and the fluorescence associated with each species quantified on each polymer spot. The fluorescence intensity was proportional to attachment of that species to that particular material. Fluorescence data for the three species on 128 materials were analysed to identify materials with selectivity for the three pathogenic species.

Three LPG OFS coated with a material selective for each of the three species were exposed to single cultures of each bacteria and the wavelength shifts of attenuation bands plotted over time of exposure. The differential attachment of the bacterial species to the different polymer coatings was utilised to allow bacterial species identification.

Two of these coated LPG OFS were also exposed to *P. aeruginosa* and Uropathogenic *E. coli* co-cultures in an attempt to identify individual pathogenic species from a 'mixture' of species. This may prove beneficial in clinical settings, where infections are often caused by multiple bacteria species [272]. These LPG OFS can also be incorporated into medical devices, for sensing and identification of pathogenic bacteria that colonise device surfaces. Identification of multiple species in a mixed co-culture using LPG OFS would also provide research and industry with a powerful instrument.

5.2. Aims

The aims of this experimental chapter were:

1. Identify materials with selective binding properties from fluorescent intensity data, generated from a high throughput screen of three pathogenic bacteria species with a library of polymers expressed as a polymer microarray.
2. Use the biomass of the three bacteria species on the selected materials to identify three polymers that allow each species to be distinguished.
3. Scale up each material using the CCT polymerisation technique and coat LPG OFS with each polymer.
4. Identify which of the three materials could be used in combination with LPG OFS to design a bacteria species identification tool.
5. Determine whether the LPG OFS with varied coatings is able to accurately identify the amount of different bacteria species within a mixed co-culture.

5.3. Experimental

5.3.1. Identification of selective binding materials from microarray fluorescent intensity data

Data from a previous study [186], whereby bacterial attachment to a polymer microarray containing 128 polyacrylate/methacrylate homopolymers was quantified, was used to select potential selective binding polymers. Briefly, polymer microarrays were incubated with three pathogenic bacteria (*P. aeruginosa* (PA), *S. aureus* (SA) and Uropathogenic *E. coli* (UPEC)), each tagged with a green fluorescent protein (GFP) fluorophore. The fluorescence intensity from each bacterium was quantified on each polymer spot; this dataset was gathered by Hook *et al*. [186]. The data was normalised to the maximum fluorescence value for each species. A threshold value was then set to identify materials with selective binding properties; any material for which the normalised fluorescence for one species was above the threshold and the other two were below it was selected as a potential selective binding polymer. The threshold was set by gradually and concurrently increasing for all three bacteria species until nine materials with the strongest affinity for one species were identified.

5.3.2. Photopolymerisation of selective binding materials

1 mL of each of the nine monomers was added to 10 mg of the photoinitiator 2,2'-dimethoxy-2-phenylacetophenone (DMPA). 5 µL spots of each monomer solution were pipetted onto glass slides which had been dip coated in a binary silane primer (MED1-161), with a withdrawal speed of 2 mm/s and 30 minutes of drying at ambient conditions. Slides were then exposed to UV light under the flow of argon gas for 10 minutes, allowing the DMPA to photopolymerise the monomer spots. Slides were then vacuum dried (0.11 Torr) for 24 hours, to remove any unreacted monomer. Typical spot dimeters were 5 mm, with a 500 µm spot height.

5.3.3. Exposure of photopolymerised spots to bacteria culture media, CLSM imaging of biofilms and quantification of biomass

Each of the three bacteria species were cultured in RPMI-1640, using the method described in section 3.3.6, to achieve a final OD_{600} of 0.05 for each species. Slides with photopolymerised spots were immersed in each bacteria culture in RPMI-1640, and biofilms left to form on the polymer spots for 24 hours, at 20°C. The slides then underwent three 10 minute wash cycles; twice with phosphate-buffered saline (PBS, pH = 7.4) and once with deionised water.

All spots were imaged using CLSM (LSM 700, Carl Zeiss, Germany); PA (PA01-N) expressed mCherry (excitation = 587 nm and emission = 610 nm), so a 555 nm laser was used for imaging [222]. UPEC (UPEC-GFP) expressed GFP (excitation = 395/475 nm and emission = 509 nm), so was excited using a 488 nm laser [224]. SA (SH1000) was stained using a 1 in 250 solution of SYTO64 in water (Thermo Fisher Scientific, excitation = 599 nm and emission = 619 nm) [223]; after the wash cycles, the SYTO64 stain was pipetted over the spots and left for 30 minutes. Slides were then rinsed with water to remove any unbound stain. A 555 nm laser was used for imaging in the CLSM [223].

CLSM followed the same directive as described in section 3.3.7. When imaging UPEC (labelled with GFP), the detector pinhole was also optimised to 1 AU, which resulted in a pinhole size of 30.4 µm. Both 2D and *z*-stack images were acquired, the latter of which was used for biomass quantification of all biofilms in COMSTAT, as described in section 3.3.8. The user-defined threshold was separately determined for each species' fluorescence and kept the same for all images of the same species.

5.3.4. Principal component analysis to identify materials with the greatest differential attachment

Principal component analysis (PCA) is a mathematical algorithm that reduces the dimensionality of a dataset, whilst retaining the variance [273]. It does this

by identifying vectors, called principal components, along which the maximum variation in the data is located. These principal components allow the variation in the data to be represented by few, rather than many, variables [273]. PCA was used to analyse the bacterial attachment of the three species to the nine potential selective binding polymers.

The biomass data was normalised to the control (silanised glass) for each bacteria species and PCA used to find the principal components (up to the fourth principal component) that expressed the largest variance in the normalised biomass, using OriginPro 8.6. 95% confidence interval ellipses were calculated for replicate samples. The ellipses were determined in MATLAB R2016a using a script written by Dr Andrew Hook (School of Pharmacy, University of Nottingham, Appendix I). The PCA score plot(s) for the species and the associated confidence ellipses were used to determine if the three species could be separated based on their attachment to the nine materials.

PCA was then used on the normalised biomass data to identify three materials with species selectivity. The materials' loading plot (generated by PCA on normalised biomass) was overlaid onto the species' principal component plot, generating a biplot. This allowed the materials' association with the species to be visualised (contribution of materials' loadings to each principle component), hence one material associated with each species could be selected for upscaling and LPG OFS coating.

5.3.5. Upscaling of selective binding materials and dip coating of LPG OFS

Three polymers were chosen to be upscaled based on the PCA. Polymers were prepared using cobalt-mediated CCT polymerisation (section 2.2.1). 7.5 mL of monomer was added to 24 mg AIBN and 10 mg PhCobF. 40 mL of toluene was added and the solution degassed with argon for 30 minutes. The monomer was left to polymerise at 80°C for 24 hours, under argon flow, after which the polymer was precipitated drop wise in cold hexane twice. The hexane was then

decanted and the polymer vacuum dried for 4 hours at 0.11 Torr. For the diacrylate polymer, the reaction was terminated after one hour, as crosslinking (and subsequent gelation of the polymer reaction mixture) occurred in diacrylates reacted for longer times. Precipitation was done twice in cold methanol. The molecular weight, polydispersity and monomer conversion were established for each polymer using GPC and ^{1}H NMR spectroscopy, using the same protocols described in section 3.3.1.

Each polymer was dissolved in DCM at 30% w/v. LPG OFS, with a grating period of 109 µm, were fabricated using the method described in section 4.3.1 [134]. LPG OFS were dip coated, using the robotic arm of the Holmarc HO-TH-01 unit, in the silane primer (withdrawal speed 2 mm/s), left to dry for 30 minutes under ambient conditions, and then dipped in polymer solution (withdrawal speed 1 mm/s). The coating thicknesses of each polymer were established by measuring the density of each polymer (by weighing 1 mL of each polymer) and weighing 7.5 cm lengths of insensitive optical fibre (Thorlabs Ltd., 460HP, fibre ID: 10-C0157-20-4H-08) before and after polymer coating (Mettler-Toledo AB265-S/FACT weighing balance, Switzerland), then using equation 5. This lead to LPG OFS with four different surface modifications; uncoated (silane primed only) and three polymer coatings (after priming).

5.3.6. Calibration of LPG OFS in sodium chloride solutions

The four LPG OFS (uncoated and the three polymer coatings) were set up as illustrated in Figure 2.14, with the 3 cm sensitive regions placed into the PTFE well (Figure 4.1). Solutions of sodium chloride in water, ranging from 0 to 25% w/v, in 5% w/v increments, were pipetted into the PTFE well, which held approximately 1.5 mL of liquid. Transmission spectra were recorded for all solutions, for the four LPG OFS. Spectra were processed in OriginPro 8.6 and the wavelength shift calculated for all attenuation bands using equation 3. Wavelength shifts from each sensor were plotted against sodium chloride concentration.

5.3.7. LPG OFS coated with selective binding materials exposed to single bacteria culture media

The four functionalised LPG OFS were fixed into the bottom of a petri dish. Cultures of PA (PA01), SA (SH1000) and UPEC (UPEC-GFP) were prepared in RPMI-1640 from overnight cultures in RPMI-1640, OD_{600} = 0.05 (section 3.3.6). Each bacteria culture was added to the petri dish separately and 0 hour transmission spectra recorded. The four sensors were left immersed in each bacteria culture media for 24 hours at 20°C and transmission spectra from each LPG OFS obtained at 6 hour intervals. All spectra were processed in OriginPro 8.6 and the wavelength shifts plotted over time for each sensor, in each bacteria culture, using equation 3.

5.3.8. LPG OFS coated with selective binding materials exposed to mixed bacteria co-cultures

5.3.8.1. Spectra collection

LPG OFS coated with the materials selective for PA and UPEC were fixed into the bottom of a petri dish. Cultures of the two species were prepared in RPMI-1640 from overnight cultures in RPMI-1640, OD_{600} = 0.1 (section 3.3.6) and added to the petri dish at 50:50 volumes, resulting in final OD_{600} of 0.05 for each species' culture medium. A 0 hour transmission spectra was recorded for each sensor and the system left for 24 hours at 20°C. Transmission spectra were recorded for each sensor at 6 hour intervals. All spectra were processed in OriginPro 8.6 and the wavelength shifts plotted over time for each sensor in the bacteria co-culture.

5.3.8.2. CLSM imaging of co-culture biofilms and biomass quantification

3 cm lengths of insensitive optical fibre (Thorlabs Ltd., 460HP, fibre ID: 10-C0157-20-4H-08) were cleaned by immersion in acetone, dipped in the silane primer (withdrawal speed 2 mm/s) and then two polymer solutions (polymers

selective for PA and UPEC, 30% w/v in DCM, withdrawal speed 1 mm/s). Each coated fibre was immersed in a co-culture of the two species in RPMI-1640 medium, in single well chamber slides (Nunc® Lab-Tek® II, Sigma Aldrich UK) at 20°C (section 5.3.8.1). At 6 hour intervals, for 24 hours, the 'mixed' biofilms on each optical fibre were imaged using CLSM, using the protocol described in sections 3.3.7 and 5.3.3. Two channels were used for imaging co-cultures; a mCherry channel at 555 nm [222] (for PA) and a GFP channel at 488 nm [224] (for UPEC). *Z*-stack images were obtained on each fibre. The biomass from each channel (each species) was quantified using COMSTAT (sections 3.3.8 and 5.3.3 and the biomass plotted against time, for each species on each material, in the co-culture biofilm.

5.3.8.3. Relationship between wavelength shift and biomass in bacteria co-cultures

The ratio of the gradients (rates of change) of wavelength shifts over 24 hours, between the pPGMEA and EOEA coated LPG OFS, were measured for single cultures of PA and UPEC (section 5.3.7). These ratios were used to indicate a 0-100% scale of each species, based on the ratios in each species' single culture. The ratio of wavelength shift gradient between pPGMEA and EOEA was also calculated for the co-culture. This was used to calculate the percentage of each species causing the wavelength shift in a mixed co-culture, using equation 7:

$$x = \frac{r\Delta\lambda_{CC} - r\Delta\lambda_{UPEC}}{r\Delta\lambda_{PA} - r\Delta\lambda_{UPEC}} \quad (7)$$

where *x* is the ratio of the two species in a co-culture that caused the co-culture wavelength shift, $r\Delta\lambda_{CC}$ is the ratio of wavelength shift gradient of pPGMEA:EOEA coated LPG OFS in the co-culture, $r\Delta\lambda_{UPEC}$ is the ratio of wavelength shift gradients in the UPEC single culture and $r\Delta\lambda_{PA}$ is the ratio of wavelength shift gradients in the PA single culture.

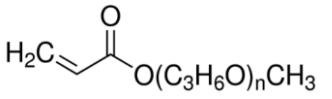
The process was repeated with biomass data at 24 hours; the single culture ratios were calculated for PA and UPEC on pPGMEA:EOEA to establish the 0-100% biomass ratio scale for each species, using the biomass data generated

from section 5.3.3. The co-culture biomass ratio was also calculated (data from section 5.3.8.2) and used to find where on the 0-100% scale it lay, using equation 7 (substituting wavelength shift ratios for biomass ratios at 24 hours), allowing the percentage of each species in a co-culture biofilm to be determined.

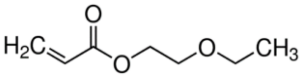
5.4. Results

5.4.1. Identification of materials with differential bacterial attachment

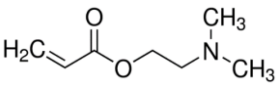
The initial step for the development of a sensor able to identify bacterial pathogens was the inclusion of a coating able to differentially bind different bacteria species. Synthetic polyacrylates can be fabricated inexpensively on an industrial scale, and were therefore explored as sensor coatings. To select suitable polymers, the fluorescence intensity data from the three species' attachment to 128 materials, using the high throughput microarray screening method, was analysed and yielded nine materials with species selectivity. The chemical structures of the nine materials are shown in Figure 5.1, along with the polymer full names and abbreviations.



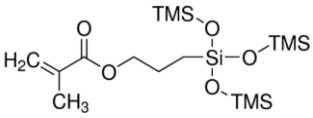
Poly(propylene glycol) methyl ether acrylate (pPGMEA)



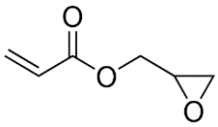
Ethoxyethyl acrylate (EOEA)



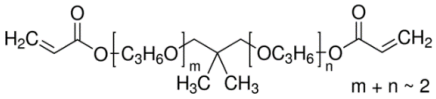
Dimethylamino-ethyl acrylate (dMAmEA)



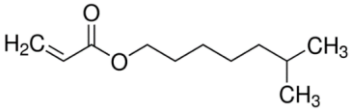
Tris(trimethylsilyloxy)-silyl propyl methacrylate (ttriMSiOSiPMA)



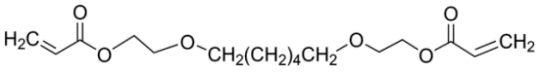
Glycidyl acrylate (GA)



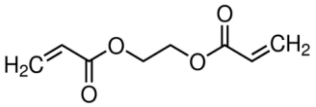
Neopentyl glycol propoxylate diacrylate (nPGPOdA)



Isooctyl acrylate (iOA)



Hexanediol ethoxylate diacrylate (HEOdA)



Ethylene glycol diacrylate (EGdA)

Figure 5.1. Nine materials with bacteria species selectivity, identified from fluorescence intensity data generated from microarray screening process. The polymer abbreviations are shown in parentheses.

5.4.2. Biomass quantification of three species on nine selective materials

The nine monomers were photopolymerised onto silane primed glass slides in triplicate and exposed to cultures of PA, SA and UPEC for 24 hours, after which 2D and *Z*-stack CLSM images were acquired for each species on all materials and biomass quantified in COMSTAT. The biomass of all three species on the nine materials are displayed in Figure 5.2. CLSM images of all biofilms are shown in Appendix J.

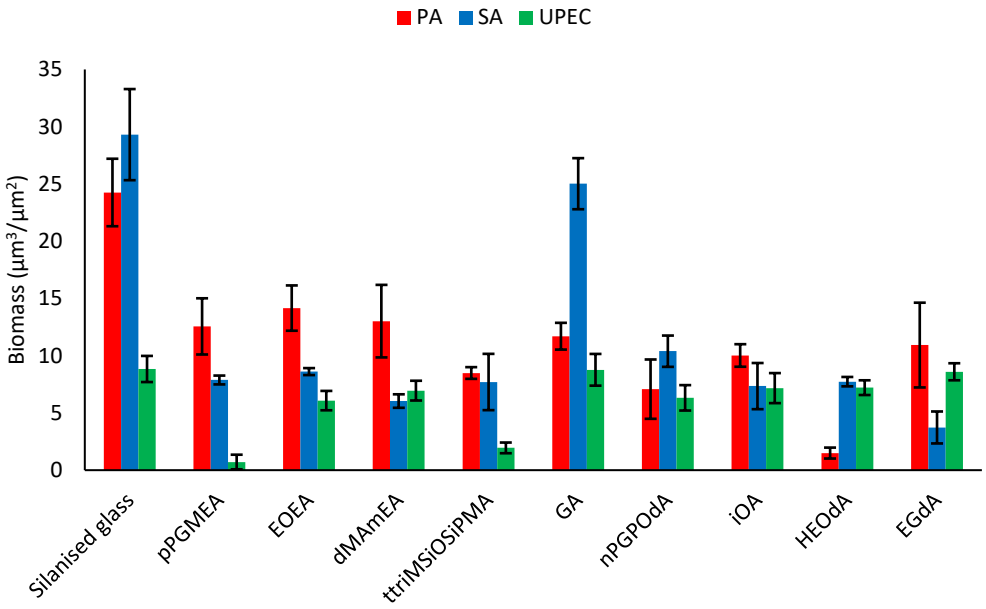


Figure 5.2. Biomass of the three bacteria species' biofilms on the nine photopolymerised materials with selective binding properties. PA = *P. aeruginosa* (mCherry, COMSTAT threshold = 56), SA = *S. aureus* (SYTO64, COMSTAT threshold = 56), UPEC = Uropathogenic *E. coli* (GFP, COMSTAT threshold = 60). Error bars are ± SD, n = 3.

For PA, biomass on silanised glass was significantly higher than any of the nine materials (no error bar overlap). This was also the case for SA, except for poly (glycidyl acrylate) (pGA), which was no different to silanised glass. For UPEC, biomass on silanised glass was only significantly higher than on pPGMEA and ttriMSiOSiPMA (no error bar overlap). There was no difference between UPEC biomass on silanised glass and the other seven materials. The lowest biomass for PA, SA and UPEC was on HEOdA, EGdA and pPGMEA respectively.

5.4.3. Principal component analysis of biomass data

5.4.3.1. Separation of species using principal components of biomass

The biomass of each species on the nine materials possessed high dimensionality (i.e. many random variables). As a result, it was difficult to choose materials with the greatest differential attachment between the three species, based on the biomass (Figure 5.2). Therefore, PCA was performed on

the biomass data to reduce the dimensionality and allow the maximum variance in biomass to be established.

The biomasses of each species on the nine materials were normalised to the biomass on silanised glass. This prevented the PCA from being biased towards bacteria species that form larger biofilms. PCA was performed on the normalised biomass to establish the principal components (PCs) that captured the largest variance in the data. Principal components 1 and 2 were found to capture 60% and 26% of the variance respectively and so were used to compare the three species. PC1 and PC2 were plotted against each other for each species, in triplicate (three biomass values for each species on each material). 95% confidence ellipses were drawn around the triplicate data points in the PCA plot. Figure 5.3 is the PCA plot for the three species, with the 95% confidence ellipses.

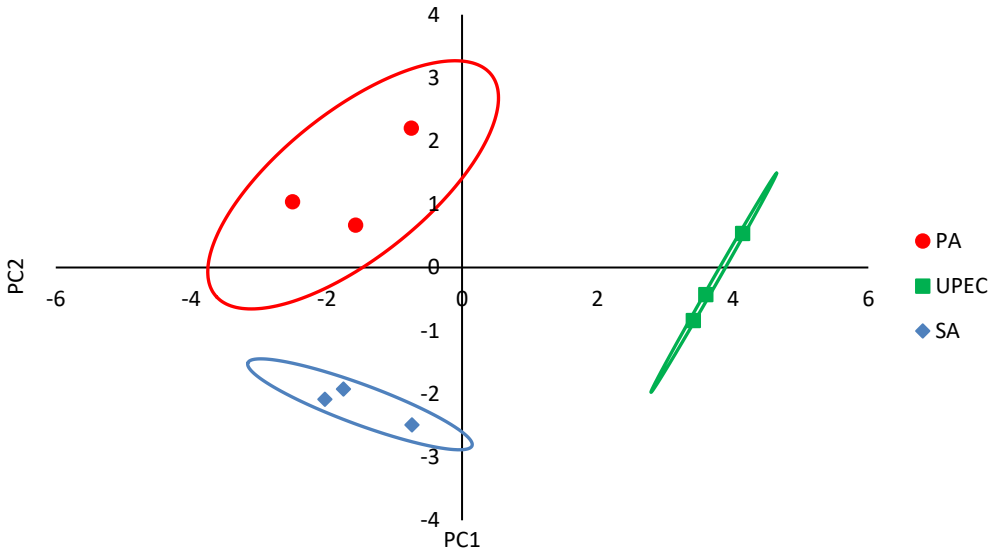


Figure 5.3. Score plot of PCs 1 and 2 for biomass of the three bacteria species on the nine photopolymerised materials. 95% confidence ellipses are drawn around the triplicate data points. PA = *P. aeruginosa*, SA = *S. aureus*, UPEC = Uropathogenic *E. coli*.

The three species could be separated by PCs 1 and 2. PA was located in the upper left quadrant and SA in the lower left quadrant of the plot. Therefore, these two species were separated by PC2. UPEC was located on the right hand

side of the plot, hence was separated from the other two species by PC1. The 95% confidence ellipses showed clear separations of the PC scores for each species in triplicate.

5.4.3.2. PCA to identify one material selective for each species

The principal component loadings are coefficients that allowed the correlation between materials and species to be established. The loadings of the materials showed how each material contributed to PCs 1 and 2. Material loadings were overlaid onto the principal component plot, generating a biplot (Figure 5.4) for principal components 1 and 2.

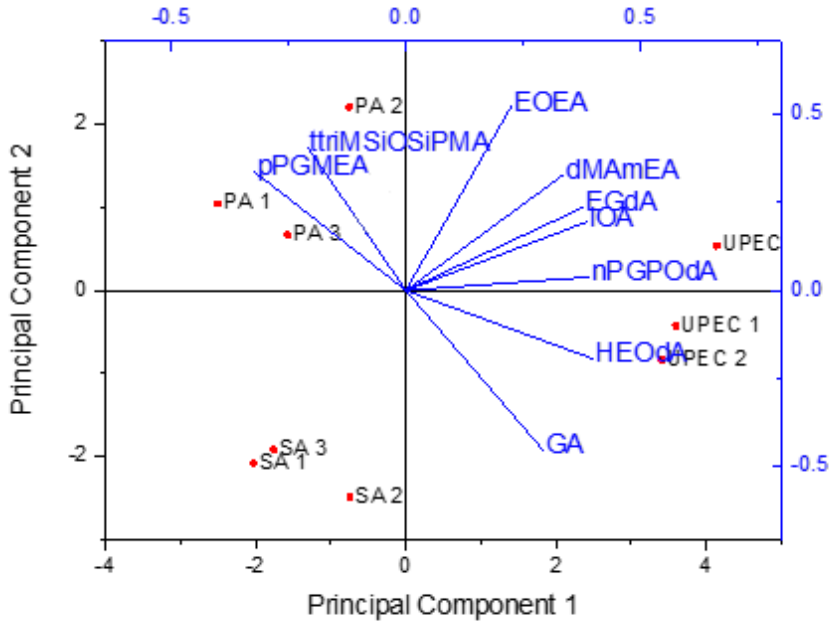


Figure 5.4. Biplot of principle component loadings for the nine selective materials laid over the principal component scores of the three bacteria species. PA = *P. aeruginosa*, SA = *S. aureus*, UPEC = Uropathogenic *E. coli*.

The five materials whose loadings were located in the upper right quadrant of the PCA score plot could be thought of as contributing (relatively) highly to both PC1 and PC2. HEOdA and GA contributed highly to PC1 but not to PC2. pPGMEA and ttriMSiOSiPMA contributed highly to PC2 but not to PC1.

The score plot showed that PC1 separated PA/SA from UPEC and that PC2 separated PA from SA. Therefore, in choosing materials with the greatest 'selectivity', polymers with high component loadings for each PC were examined. pPGMEA had a high loading in PC2 and a low loading in PC1; therefore, it differentially binds PA and SA/UPEC (PA had a high PC2 score and a low PC1 score). EOEA had a high loading in both PCs, so could differentially bind UPEC and PA/SA. Either HEOdA or GA could be selected for differential attachment of SA/UPEC to PA, since their loadings were high for PC1 and relatively low for PC2. GA required a multi-step synthesis before it could be available for polymerisation, hence HEOdA was selected. pPGMEA, HEOdA and EOEA possessed high differential attachment between the three species, which was corroborated by the biomass of each species on the three photocured spots (Figure 5.2). The biomass of each species were significantly different (no error bar overlap) to each other on pPGMEA and EOEA. A significant difference (no error bar overlap) in biomass existed between SA/UPEC and PA on HEOdA. The ability of these three materials to differentially bind (and therefore separate) the three bacteria species is presented in Table 5.1.

	pPGMEA	HEOdA	EOEA
P. aeruginosa	✓	*x*	✓
S. aureus	✓ (partially)	✓ (partially)	*x*
Uropathogenic *E. coli*	*x*	✓	✓

Table 5.1. Selective binding materials' species separation, based on the materials' component loadings (Figure 5.4). Ticks indicate high attachment and crosses indicate low attachment.

PCA was then performed on the normalised biomass of the three bacteria species on the three selected materials only (Table 5.1). It was found that PC1 and PC2 captured 81% and 18% of the variance respectively. Hence the first

two PCs were plotted against each other and 95% confidence ellipses created around the triplicate principle component scores for each species, using the same MATLAB script (Appendix I). The score plot and confidence ellipses are shown in Figure 5.5.

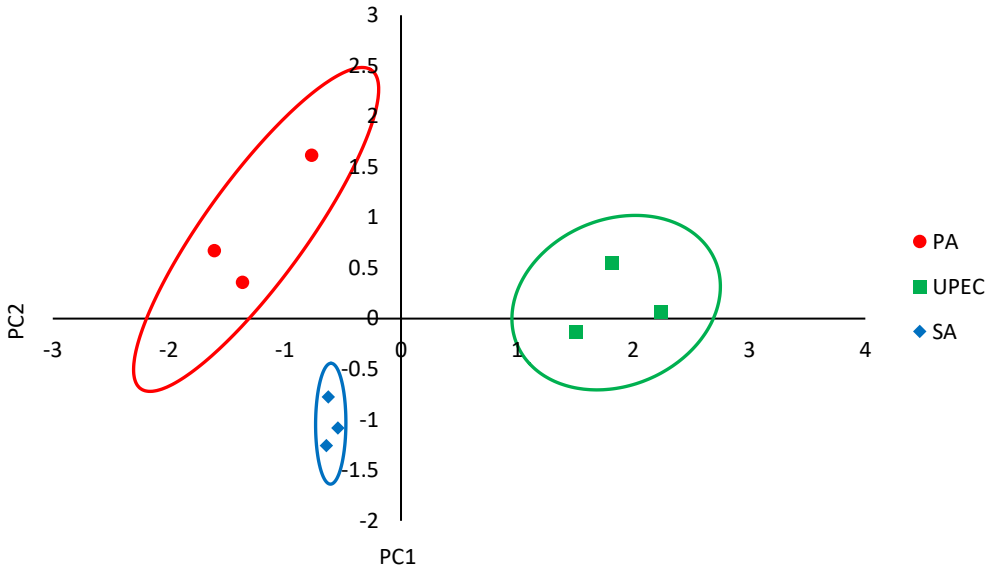


Figure 5.5. Score plot of PCs 1 and 2 for biomass of the three bacteria species on the three selected materials with differential bacterial attachment. 95% confidence ellipses are drawn around the triplicate data points. PA = *P. aeruginosa*, SA = *S. aureus*, UPEC = Uropathogenic *E. coli*.

As with the PCA score plot for the biomasses on the nine photopolymerised materials (Figure 5.3), the three bacteria species could be separated by PC1 and PC2. PA and SA were separated from UPEC by PC1. PA was also separated from SA by PC2. The 95% confidence ellipses showed clear separations of the PC scores for each species, indicating that the three materials could be used for differential attachment of the three species.

For differential sensing of bacterial attachment, LPG OFS coated in all three materials would be required. If only pPGMEA and HEOdA coated sensors were exposed to a culture of bacteria and a higher rate of change (of wavelength shift) was observed on pPGMEA than on HEOdA, it would be difficult to assess whether the culture contains PA or SA since the partial attachment of SA to HEOdA might be equivalent to the low attachment of PA to HEOdA. The EOEA

coated sensor would be required to allow separation PA and SA, based on their differential attachment to it (and the other two materials, in combination). Furthermore, if the bacteria culture was SA, it would attach to both the pPGMEA and HEOdA coated LPG OFS, making it difficult to differentiate the wavelength shifts.

5.4.4. GPC and ^{1}H NMR spectroscopy analysis of three selective binding materials

The three selected materials were scaled up using the CCT polymerisation method (section 2.2.1). After the polymers had been dried, the yield by weight was calculated. The molecular weights and polydispersity were determined using GPC. The monomer conversion was established by running each monomer, polymer crude mix and final polymer through ^{1}H NMR spectroscopy. The data are summarised in Table 5.2. ^{1}H NMR spectra are presented in Appendix K.

Polymer	Yield by weight	Molecular weight (g/mol ± % 0.95 CI)	Polydispersity (± % 0.95 CI)	Monomer conversion
pPGMEA	52%	9.226×10^{4} (± 16.964%)	2.464 (± 23.990%)	99%
HEOdA	69%	5.376×10^{6} (± 6.233%)	1.986 (± 8.815%)	82%
EOEA	64%	1.017×10^{5} (± 12.652%)	2.641 (± 17.893%)	90%

Table 5.2. Yield by weight, molecular weights, polydispersity and monomer conversion of the three materials with bacteria species selectivity. CI = confidence interval.

pPGMEA had the lowest yield by weight but the highest monomer conversion. HEOdA had the highest yield by weight but the lowest monomer conversion. HEOdA also had the lowest polydispersity, indicating lesser variation in polymer

chain length. HEOdA had the highest molecular weight. Polydispersity was below 3 and monomer conversion was above 80% for all the materials.

5.4.5. Coating thicknesses of the three materials on optical fibres

The three polymers were dissolved in DCM at 30% w/v. Insensitive lengths of optical fibre were dip coated firstly in the binary silane primer then in one of the polymer solutions. The weights of optical fibres before and after polymer coating were measured, as were the densities of the three polymers. The weight gain and polymer densities were used to calculate the average coating thickness of each material on optical fibres, using equation 4. Table 5.3 summarises these data.

Polymer	Density (g/mL)	Average weight gain (μg)	Average coating thickness (nm)
pPGMEA	1.55	9.1	499
HEOdA	1.91	12.7	565
EOEA	1.59	10.3	548

Table 5.3. Density of each selective material, the average weight gain of one hundred 3 cm lengths of coated optical fibres and the average coating thickness of each material on optical fibres, calculated using equation 4.

All coatings were in the range of 499-565 nm. HEOdA was the thickest coating, followed by EOEA and then pPGMEA. Polymers with higher densities appeared to give thicker coatings. The average coating thickness of EGDPEA:DEGMA on optical fibres was 511 nm, which was less than HEOdA and EOEA.

5.4.6. Calibration of LPG OFS in sodium chloride solutions

The four LPG OFS (uncoated and the three selective coatings) were exposed to sodium chloride solutions, ranging from 0 to 25% w/v in water, and transmission spectra collected. Spectra were processed and wavelength shift of attenuation bands plotted against sodium chloride concentration. Figure 5.6 is the processed spectra for the four LPG OFS in water.

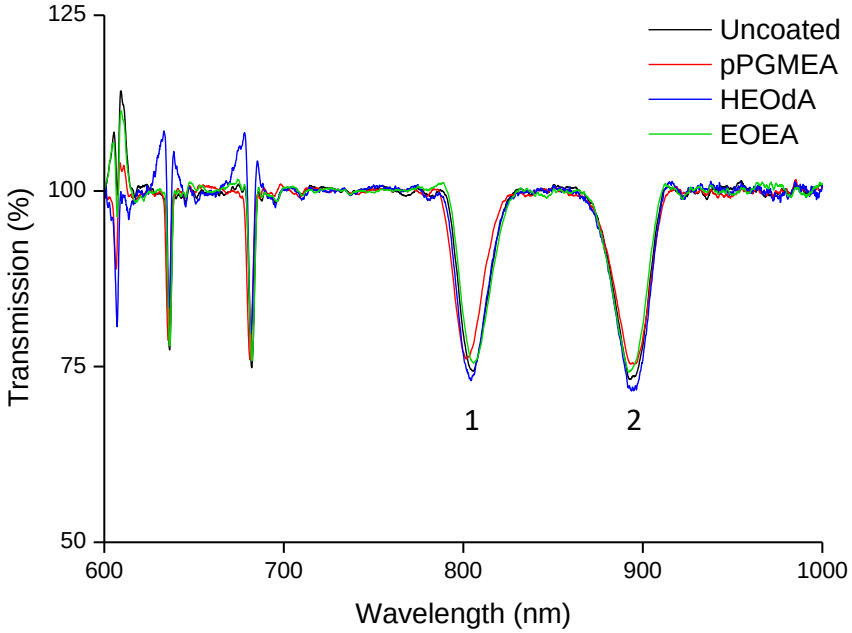


Figure 5.6. Processed transmission spectra from the four LPG OFS in water. Two attenuation bands were visible in the spectra, labelled '1' and '2'.

Two attenuation bands/peaks appeared in the optical spectrum for each sensor, representing core-cladding mode coupling at two different wavelengths [166,167]. For both peaks, the pPGMEA and HEOdA coating shifted the attenuations away from the uncoated peaks and away from the centre point between the attenuation bands. The EOEA coating caused the attenuation bands to shift back towards the centre point. None of the three coatings caused a shift greater than 5 nm from the uncoated LPG OFS.

Figure 5.7 shows the wavelength shifts of both attenuation peaks with increasing sodium chloride concentration, for all four LPG OFS.

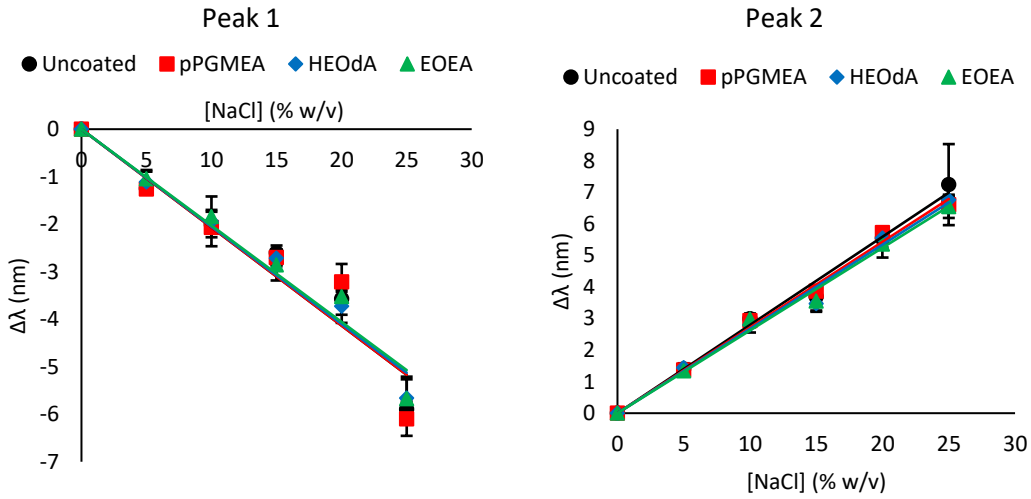


Figure 5.7. Wavelength shifts of both attenuation peaks from all four LPG OFS (uncoated and the three polymer coatings) in sodium chloride solutions of increasing concentration. Error bars are ± SD, N = 3.

Both peaks shifted linearly with an increase in [NaCl], with all R^2 values above 0.91, although peak 2 appeared to have better linearity. The two peaks for all sensors shifted in opposite directions with increasing sodium chloride concentration (and increasing refractive index). There was no difference in wavelength shift between any of the four LPG OFS surface modifications at any time point. Peak 2 from all four sensors had a greater rate of shift with increasing [NaCl]; an observation which was different from that made for the U and PC (EGDPEA:DEGMA) LPG OFS (Figure 4.4).

5.4.7. LPG OFS coated with selective binding materials in bacteria single cultures

5.4.7.1. Wavelength shifts for each selective material

Four LPG OFS (uncoated and the three selective coatings) were simultaneously exposed to single cultures of each species (PA, SA and UPEC) in RPMI-1640

medium and the wavelength shift of attenuation bands plotted against time of exposure at 6 hour intervals for 24 hours. Figure 5.8 are the wavelength shifts of peak 1 from each LPG OFS in the three bacteria species. Data for peak 2 is presented in Appendix L.

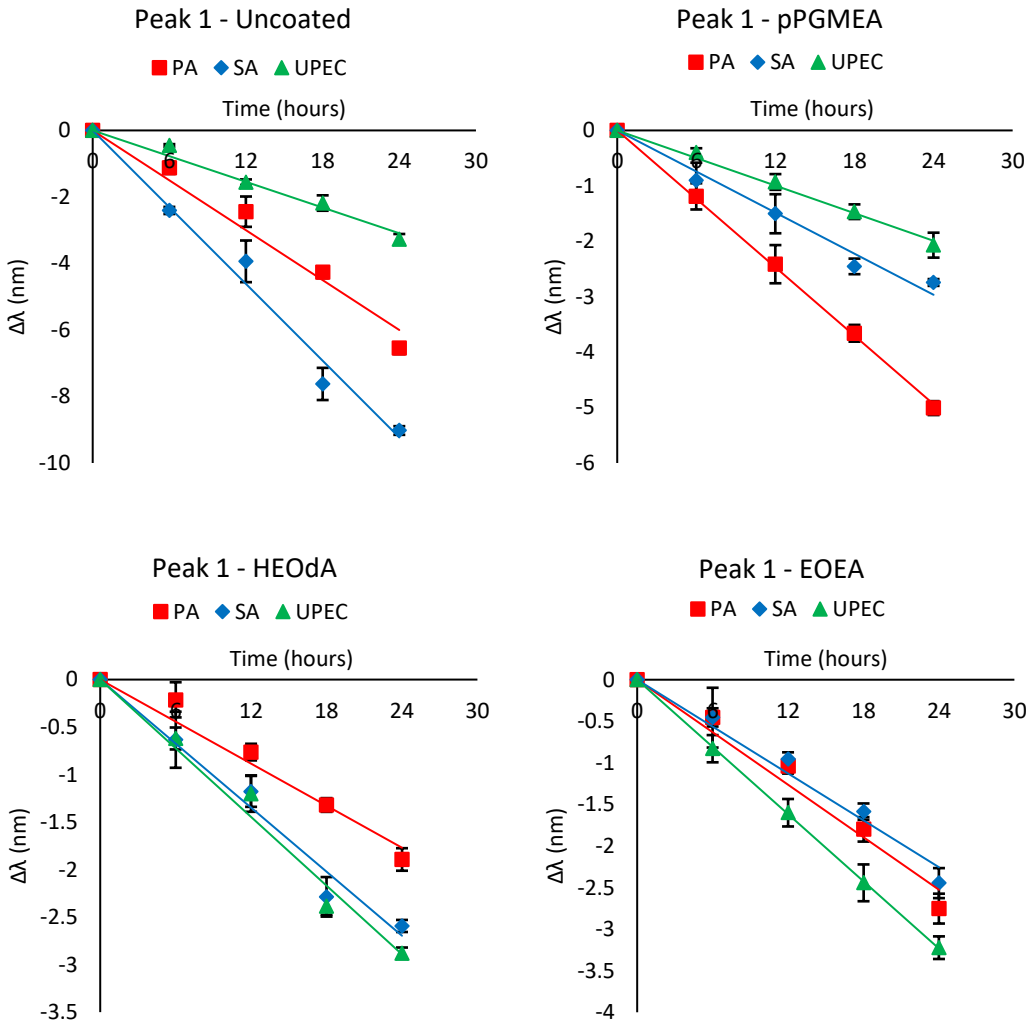


Figure 5.8. Wavelength shifts of peak 1 from each of the four modified LPG OFS immersed in single cultures of the three bacteria species in RPMI-1640 medium, for 24 hours. PA = *P. aeruginosa*, SA = *S. aureus*, UPEC = Uropathogenic *E. coli*. Error bars are ± SD, N = 3.

All attenuation peaks from each LPG OFS shifted linearly. Peaks 1 and 2 shifted in opposite directions, consistent with observations made with the calibration using sodium chloride. For the uncoated LPG OFS, SA gave the highest rate of change of wavelength shift, followed by PA and then UPEC. The wavelength

shifts were significantly different from each other (no error bar overlap) at all the time points after 0 hours.

For the pPGMEA coated LPG OFS, the wavelength shift was greatest in PA, followed by SA and UPEC. Significant differences were observed from 12 hours onwards (no error bar overlap). This was consistent with the biomass of these species on pPGMEA after 24 hours (Figure 5.2).

For the HEOdA coated LPG OFS, the highest wavelength shift was observed in UPEC, followed by SA and then PA. There was no difference between UPEC ad SA until 24 hours; the PA wavelength shift was significantly lower (no error bar overlap) than the other two species from 6 hours onwards. This was also consistent with the biomass of each species on HEOdA (Figure 5.2); SA had a higher mean biomass than UPEC (although not significant), which was significantly higher than the biomass of PA after 24 hours.

For the EOEA coated LPG OFS, the greatest wavelength shift occurred in UPEC, then PA and SA. The wavelength shift for UPEC was significantly higher (no error bar overlap) than the other two species from 12 hours onwards. There was no difference in wavelength shift between SA and PA. Although the biomass of PA/SA on EOEA were higher than UPEC (Figure 5.2), UPEC had the highest wavelength shift, which contradicts the result observed.

5.4.7.2. Wavelength shifts for each bacteria species

To compare the growth profiles of each bacteria on the different materials, the data presented in Figure 5.8 was replotted as the wavelength shifts for each bacteria species for peak 1 for the four surface modified LPG OFS (Figure 5.9). Data for peak 2 are displayed in Appendix L.

The highest attachment for PA was on the uncoated (silane primed only) LPG OFS. It also had significantly higher attachment to pPGMEA than the other two coatings (no error bar overlap) from 6 hours onwards. SA attachment was also highest on the uncoated LPG OFS. The wavelength shift from the three coated LPG OFS in SA culture medium were no different to each other. UPEC had

higher attachment on the uncoated, HEOdA coated and EOEA coated LPG OFS than the pPGMEA coated LPG OFS. There was no difference between these three LPG OFS, apart from at 24 hours, where the HEOdA coated LPG OFS displayed lower wavelength shift (no error bar overlap) than uncoated and EOEA. The pPGMEA coated LPG OFS was significantly lower than the other three (no error bar overlap) after 12 hours.

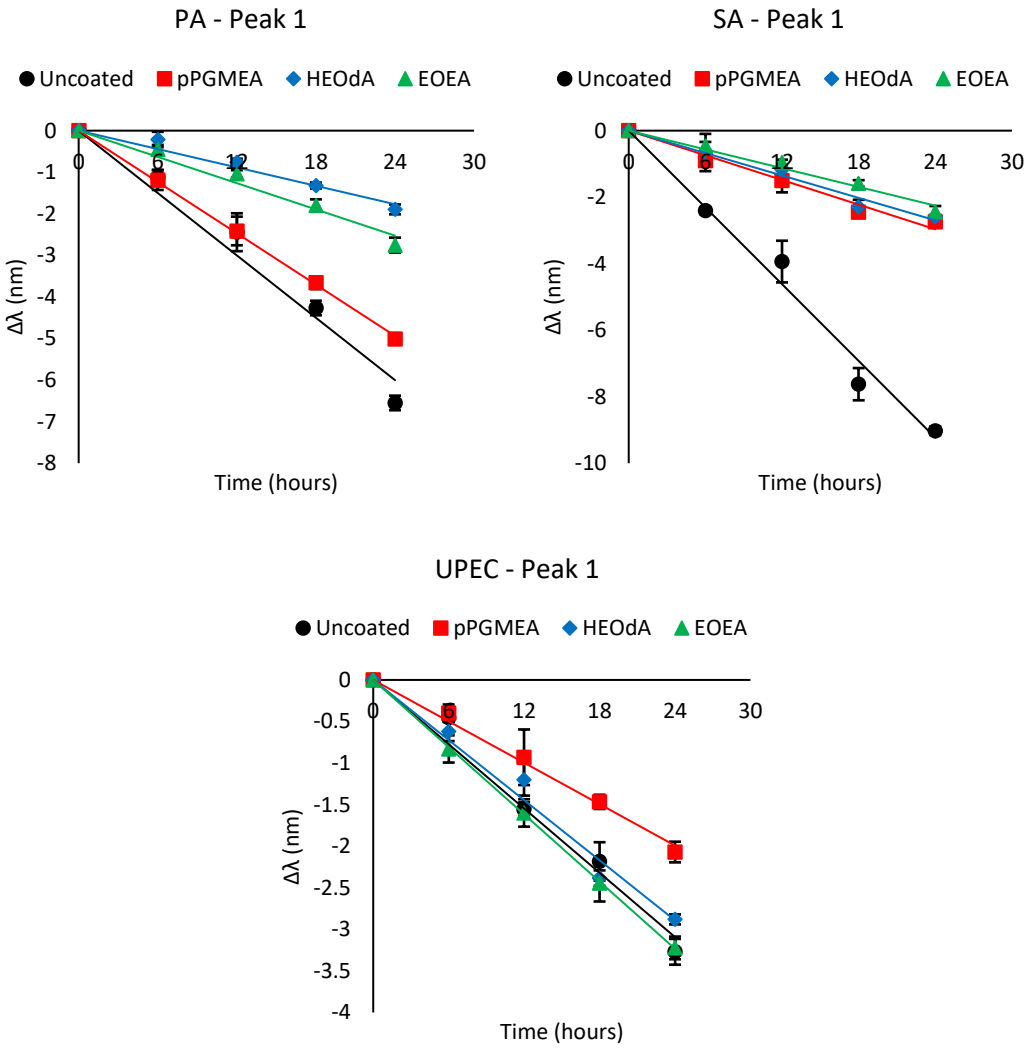


Figure 5.9. Wavelength shifts of peak 1 from the four modified LPG OFS exposed to single cultures of the three bacteria species in RPMI-1640 medium, for 24 hours. PA = *P. aeruginosa*, SA = *S. aureus*, UPEC = Uropathogenic *E. coli*. Error bars are ± SD, N = 3.

5.4.8. LPG OFS coated with selective binding materials in bacteria co-culture

5.4.8.1. Wavelength shifts in bacteria co-culture

Having demonstrated the differential biofilm formation of the three bacterial pathogens on the coated sensors in single cultures, the sensors were used to assess the biofilm formation within a mixed co-culture. LPG OFS with pPGMEA and EOEA coatings were immersed in a PA and UPEC co-culture (OD_{600} = 0.05 for each species, 50:50 volume), in RPMI-1640 medium, and the wavelength shifts of attenuation bands monitored over 24 hours. Figure 5.10 presents the wavelength shift of both attenuation peaks from both coated LPG OFS. SA was omitted from the co-culture, since it required staining with SYTO64, which would have stained all three species in a mixed biofilm, making them indistinguishable from each other. PA and UPEC expressed mCherry and GFP respectively, which allowed for differentiation of the two species using confocal microscopy.

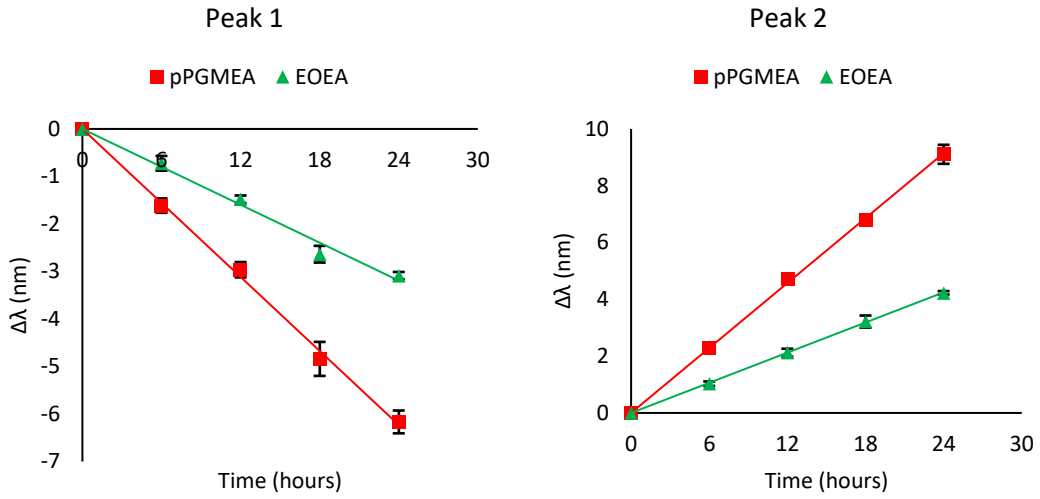


Figure 5.10. Wavelength shifts of both attenuation peaks from pPGMEA and EOEA coated LPG OFS exposed to a *P. aeruginosa* and Uropathogenic *E. coli* co-culture for 24 hours. Error bars are ± SD, N = 3.

Both peaks shifted linearly with increased time of immersion in bacteria co-culture medium; with $R^2 \geq 0.99$. Peaks also shifted in opposite directions, as observed in the calibration and the single culture study. The wavelength shifts

from the pPGMEA coated LPG OFS were significantly higher (no error bar overlap) than from the EOEA coated LPG OFS, at 6 hours and onwards.

5.4.8.2. Biomass of *P. aeruginosa* and Uropathogenic *E. coli* biofilms from co-culture media

Lengths of insensitive optical fibre, coated with pPGMEA or EOEA, were also exposed to the PA and UPEC co-culture in RPMI-1640 medium for 24 hours. *Z*-stack CLSM images were acquired at 6 hour intervals, using both mCherry and GFP channels (for PA and UPEC respectively). The biomass from each channel was quantified using COMSTAT, at each time point, after thresholding. Figure 5.11 shows the *z*-stack CLSM images and associated biomasses for both species on both coatings plotted against time.

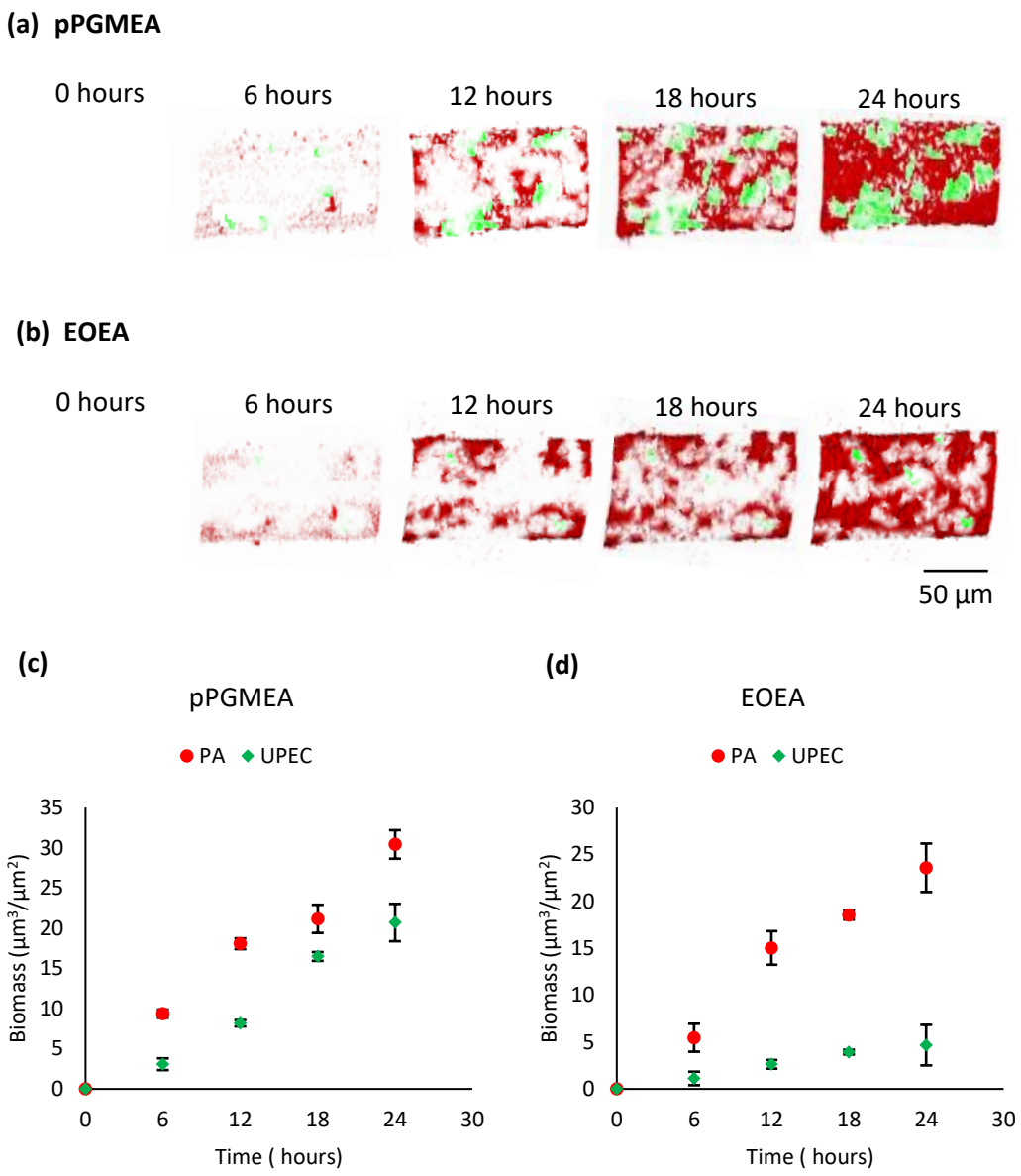


Figure 5.11. *Z*-stack CLSM images of PA and UPEC mixed biofilms, labelled with mCherry (red) and GFP (green) respectively, grown on **(a)** pPGMEA coated optical fibres and **(b)** EOEA coated optical fibres, from a 50:50 mixed co-culture. Images are shown at 6 hour intervals for 24 hours. The scale bar is 50 µm and is applicable to all images. **(c)** Quantified biomass of images in (a), using a COMSTAT threshold of 56 (PA, mCherry) and 60 (UPEC, GFP). Error bars are SD, n = 3. **(d)** Quantified biomass of images in (b), using a COMSTAT threshold of 56 (PA, mCherry) and 60 (UPEC, GFP). Error bars are SD, n = 3.

On pPGMEA, both bacteria species formed microcolonies in 6 hours, which matured over the next 18 hours. PA colonised more of the substratum than UPEC and more PA biofilm structures were observed at 24 hours. Each bacteria species occupied its own space(s) of the surface, with very little areas of

'overlap' of biofilms. On EOEA, PA also formed microcolonies at 6 hours, which matured progressively thereafter. However, UPEC had low attachment, with only small maturing biofilm structures observed at 24 hours. PA also colonised more of the substratum than UPEC and formed biofilms at a faster rate.

The PA biomass was higher than the UPEC biomass (no error bar overlap) on both coatings, at all time points after 0 hours. The biomass of both species were also higher on pPGMEA than on EOEA (no error bar overlap), at all time points after 0 hours, except for UPEC at 6 hours, which was not significantly higher on pPGMEA than EOEA.

5.4.8.3. Wavelength shift comparison between single and co-cultures

Figure 5.12 shows the wavelength shifts of both attenuation peaks for pPGMEA and EOEA coated LPG OFS immersed in PA and UPEC single and co-cultures in RPMI-1640 medium.

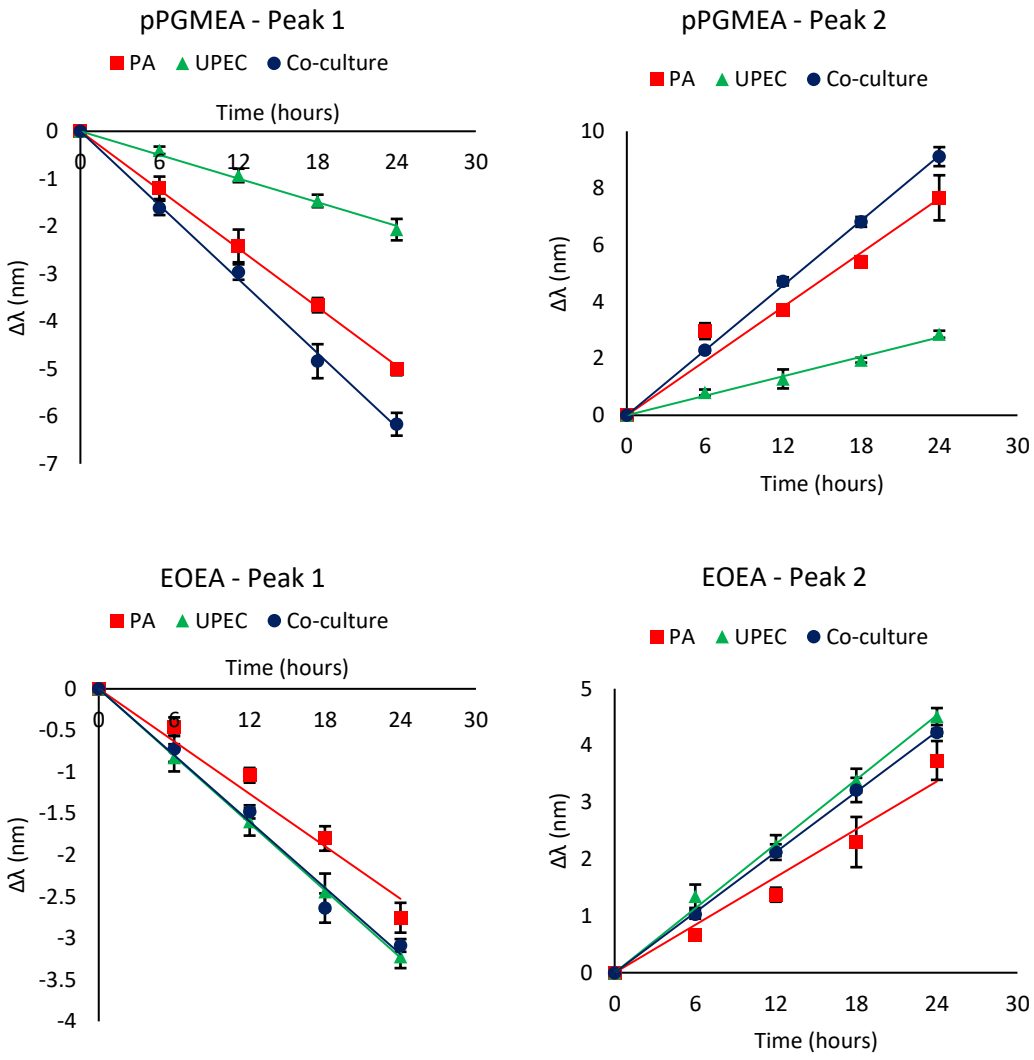


Figure 5.12. Comparison of wavelength shifts of both attenuation peaks, from pPGMEA and EOEA coated LPG OFS, for *P. aeruginosa* (PA) and Uropathogenic *E. coli* (UPEC) single cultures and the co-culture of the two species, in RPMI-1640 medium. Error bars are ± SD, N = 3.

For the pPGMEA coated LPG OFS, the co-culture caused the greatest wavelength shift over 24 hours, followed by the PA single culture and then the UPEC single culture. The wavelength shift for the co-culture was significantly higher than the PA wavelength shift (no error bar overlap) at 18 and 24 hours for peak 1, and 12, 18 and 24 hours for peak 2. The UPEC wavelength shift was significantly lower (no error bar overlap) than the other two at all time points after 0 hours. For the EOEA coated LPG OFS, there was no difference in wavelength shift between the co-culture and the UPEC single culture. The

wavelength shift for the PA single culture was significantly lesser (no error bar overlap) than those two, at all time points after 0 hours.

5.4.8.4. Relationship between wavelength shift and biomass ratios from co-cultures

The ratio of wavelength shift gradients between the two coated LPG OFS in single bacteria cultures were used to calculate the ratio of the two bacterial species in the co-culture, according to equation 7.

Wavelength shift ratio (pPGMEA:EOEA), Peak 1:	Wavelength shift ratio (pPGMEA:EOEA), Peak 2:
PA single culture = 1.91 (100% PA)	PA single culture = 2.29 (100% PA)
UPEC single culture = 0.62 (0% PA)	UPEC single culture = 0.58 (0% PA)
Co-culture = 2 (107% PA)	Co-culture = 2.11 (89% PA)

Table 5.4. Ratios of wavelength shift gradients (rates of change) between pPGMEA and EOEA coated LPG OFS in single and co-cultures of PA and UPEC, calculated using equation 7. Parentheses indicate the percentage of each species from the co-culture that caused the observed wavelength shifts.

Peak 1 could not be used for the correlation, since it gave a high ratio. Peak 2 showed the co-culture wavelength shift was predominantly caused by PA (89%). Peak 2 was selected for examination of the relationship between wavelength shift and biomass, since it provided the higher linearity (Figure 5.7) and had the higher wavelength shift over time of immersion in culture medium (Figure 5.12).

The growth rates determined from the biomass measurements at 24 hours (Figure 5.2) were also used to determine the percentage of each bacterial species in the co-culture according to equation 7. Results are shown in Table 5.5.

24 hour biomass ratio (pPGMEA:EOEA):
PA single culture = 0.89 (100% PA)
UPEC single culture = 0.12 (0% PA)
Co-culture = 0.68 (88% PA)

Table 5.5. Ratios of 24 hour biomass between pPGMEA and EOEA photopolymerised spots in single and co-cultures of PA and UPEC, calculated using equation 7. Parentheses indicate the percentage of each species in the co-culture biofilm.

A higher percentage of PA (88%) was also measured in the co-culture, determined from measurements of biomass. The bacteria species ratio corresponded closely with the ratio determined using the wavelength shift, with only a 1% difference (89% and 88%). Thus, two independent measurements of bacteria species measured the same percentage of two species in the co-culture, validating both methods.

5.5. Discussion

5.5.1. Nine materials identified from microarray data

The nine materials with species selectivity presented in Figure 5.1 were chemically diverse, with acrylates, methacrylates and diacrylates present. The pendant groups were also chemically varied; some materials had aliphatic chains in their structure, such as HEOdA, while others had ring structures, like GA. Sanni *et al*. [142] linked a value combining *c*Log*P* and the number of rotatable bonds (*n*RotB) of poly(meth)acrylate hydrocarbon pendant groups to reduced *P. aeruginosa* attachment. This may explain differing attachment rates of PA to the materials.

The selectivity may also be due to physiological differences between species. Gram-positive and Gram-negative differences between SA and the other two species may account for differing attachment rates. Gram-positive bacteria have a thick peptidoglycan cell wall, whereas gram-negative bacteria possess a thinner peptidoglycan cell wall sandwiched between an inner and outer membrane [274]. Previous studies on the hydrophilicity/hydrophobicity of different bacteria cell surfaces have shown that PA is hydrophobic and SA is hydrophilic [275,276]. These differences would have led to increased adhesion to materials with hydrophobic and hydrophilic pendant groups respectively.

5.5.2. Biomass of the three species on the selective materials

The differing rates of attachment between the three bacteria species resulted in different biomass on each material. The exact mechanisms by which the materials caused differential attachment are complex and still not fully understood. Steric effects and hydrophobic interactions [144] between bacteria cells and polymer pendant groups would have reduced or increased attachment respectively, resulting in lower or higher biomass [142]. Some of the materials clearly resisted attachment of some of the species, such as

pPGMEA for UPEC and HEOdA for PA. Others appeared to promote attachment, such as GA for SA.

All three species had the highest mean biomass on silane primed glass. The silanes are thought to introduce reactive silanols at the substrate surface [202], which may have promoted cell adhesion via hydrophobic interactions or hydrogen bonding with membrane moieties [35,36].

The biomass data in Figure 5.2 showed that no material completely prevented bacterial adhesion. In no case was there exceptionally high or low attachment to a material, resulting in a dataset with multiple dimensions. Therefore, PCA was used to reduce the dimensionality of the data, separate the species from their differential attachment to the nine materials, identify the fewest number of materials that could be used to separate the three species and select materials that could be used to identify each species.

5.5.3. PCA for identification of selective binding materials

PCA was used to find the vectors along which the largest variation in biomass existed from the differential attachment to the nine different polymers. The three bacteria species were successfully separated by their PC scores (Figure 5.3), based on PCs 1 and 2 that captured 60% and 26% of the variance respectively. PA and SA were separated by PC2, so any material which had a high or low loading for PC2 could be used to differentiate between the two species. pPGMEA was chosen as a selective material as it had a high loading for PC2. UPEC was separated from the other two species by PC1, hence materials with high or low loadings for PC1 allow for differentiation of UPEC from PA and SA. Hence EOEA and HEOdA was chosen, as they had high loadings for PC1. This lead to the material-species interactions presented in Table 5.1. The PC scores of each species' biomass to those three materials only (Figure 5.5) also showed the same separations of the three species across PCs 1 and 2, which captured 81% and 18% of the variance respectively.

The three materials can be used in combination for species selective sensing (using coated LPG OFS). Higher attachment (and therefore larger wavelength shifts) to pPGMEA and EOEA coated LPG OFS than HEOdA coated sensors would indicate the presence of PA. Similarly, higher wavelength shifts from pPGMEA and HEOdA coated LPG OFS would indicate SA attachment. Finally, higher wavelength shifts from HEOdA and EOEA coated LPG OFS would indicate UPEC attachment.

5.5.4. Synthesis of three polymers and coating of LPG OFS

To produce selective coatings for LPG OFS, the three selected polymers were scaled up. pPGMEA and EOEA took 24 hours to react. The monomer units had one reactive acrylate moiety that was activated by AIBN. The reaction rate was mediated by the cobalt catalyst (PhCobF) [193-195], allowing for control over the polydispersity. HEOdA, being a diacrylate, had two reactive moieties, allowing for an increased reaction rate. Hence the reaction was stopped after an hour, to prevent cross-linking. HEOdA also had to be precipitated in methanol, since it is a less polar molecule than the other two, due to the long aliphatic chain within the chemical structure. HEOdA had the highest molecular weight and lowest conversion of the three materials. The two reactive units meant the reaction happened quickly, with 'activated' acrylate units more numerous and therefore more likely to react. The fast reaction combined with early termination of the reaction lead to the lower polydispersity and higher molecular weight. HEOdA can hyperbranch during polymerisation, which may have caused the higher molecular weights observed. Hyperbranching could be assessed by using different standards for GPC analysis.

pPGMEA had the highest monomer conversion but the lowest yield by weight, with the opposite result observed for HEOdA. This was most likely caused by losses in transit, such as during the precipitation cycles and transfer to weighing vessels, rather than polymer losses during the reaction.

The coating thicknesses appeared to correlate with the polymer molecular weights and densities (Tables 5.2 and 5.3). Polymers with higher molecular weights/densities provided more viscous solutions in DCM, causing slower drainage of polymer solution into the polymer reservoir, causing greater polymer deposition on the primed optical fibre. The diacrylate polymer may also have allowed for greater hydrophobic interactions between C=C bonds (of the acrylate group) and the silanols from the primer [201,203]. The coatings did not affect the refractive index sensing capability of the LPG OFS, due to the evanescent wave extending beyond the coating thickness [262].

5.5.5. Calibration of LPG OFS in sodium chloride solutions

The calibration ensured that there was no difference in sensitivity to refractive index between the uncoated and three coated LPG OFS. Figure 5.6 shows two attenuation bands present in the optical spectra for all four LPG OFS in water. Referred to as dual resonance, this was caused by core-cladding mode coupling occurring at two different wavelengths, due to the grating being written at the PMTP [166,167].

When pPGMEA and HEOdA coatings were applied to LPG OFS, the two attenuation bands shifted further apart (from the uncoated attenuation bands). Applying a film of higher refractive index changed the effective index of cladding modes, governed by equation 1, causing core-cladding mode coupling to occur at wavelengths at a further distance apart [164]. However, the application of the EOEA coating caused the peaks to shift closer together (albeit by < 5 nm). The refractive index of EOEA may require measuring to examine why the negative shift was observed. However, this was more likely caused by external factors, such as mechanical strain, shifting the position of the peaks back towards the central position [153].

Both peaks shifted linearly with increasing sodium chloride concentration (Figure 5.7). A linear increase in sodium chloride concentration (and refractive

index) caused a linear change in the cladding mode effective index, in turn causing core-cladding mode coupling to occur linearly [163,164]. There was also no difference between wavelength shifts between the four LPG OFS. This suggests the coatings did not influence core-cladding mode coupling in sodium chloride. The change in cladding mode effective index (in sodium chloride solutions) occurred at the same rate for all four LPG OFS, despite the different starting positions of attenuation bands. Therefore, spectral differences between LPG OFS in bacteria culture medium would be due to differing bacterial attachment to sensor surfaces.

Peak 2 for all four sensors had a greater wavelength shift with increasing sodium chloride concentration and had greater linearity. This suggests that the turning point resonant wavelength was closer to the peak 2 than the peak 1 wavelength [167].

5.5.6. Selective material-coated LPG OFS in single bacteria culture media

The four LPG OFS were exposed to single cultures of each bacteria species, to determine if the differential attachment of bacteria to the three material coatings caused differential wavelength shifts, which would allow identification of pathogens from the spectral response.

For the uncoated (silane primer only) LPG OFS, SA caused a peak 1 wavelength shift of -9.02 nm, compared to -6.55 nm for PA and -3.27 nm for UPEC after 24 hours. This suggests that SA biofilms had a greater rate of change of refractive index, likely caused by increased attachment/biofilm formation compared to the other two species. The biomass of each species on the nine photopolymerised spots (Figure 5.2) indeed showed that SA biofilms had a higher mean biomass than the other two species after 24 hours, on primed glass substrates (29.31, 24.25 and 8.84 $\mu m^3/\mu m^2$, for SA, PA and UPEC respectively). PA formed biofilms of greater biomass than UPEC on silanised glass, hence caused greater wavelength shifts from the uncoated LPG OFS.

Silanised glass itself differentially attached the three species; higher biomasses caused greater wavelength shift increases (Figures 5.7 and 5.8).

For the pPGMEA coated LPG OFS, PA caused the highest wavelength shift (Figures 5.7 and 5.8), indicating greater attachment of PA to that sensor. The peak 1 wavelength shifts, after 24 hours, were -5.01, -2.74 and -2.07 nm, for PA, SA and UPEC respectively. This was corroborated by the biomass on photopolymerised pPGMEA (Figure 5.2), where PA had higher biomass than SA and UPEC after 24 hours (12.56, 7.88 and 0.71 $\mu m^3/\mu m^2$ respectively). The wavelength shift was significantly higher than for the other two species at 12 hours. Therefore, a pPGMEA coated LPG OFS could be used to selectively sense PA within 12 hours.

For the HEOdA coated LPG OFS, both SA and UPEC caused wavelength shifts of equal magnitude, until 24 hours, where the wavelength shifts were -2.88 and -2.59 nm, for UPEC and SA respectively. The biomasses of UPEC and SA on HEOdA (Figure 5.2) after 24 hours were 7.21 and 7.73 $\mu m^3/\mu m^2$ respectively. These were not statistically different to each other, hence the differing wavelength shift at 24 hours could be due to the UPEC biofilm having a higher refractive index than the SA biofilm, causing greater cladding mode effective index change. PA biofilm formation caused a smaller wavelength shift (-1.89 nm after 24 hours), due to its smaller biomass (Figure 5.2). This LPG OFS could be used to selectively sense SA and UPEC attachment, which coincides with Table 5.1, where HEOdA promotes adhesion of these two species. The wavelength shifts were separated from the PA wavelength shift in 6 hours. To separate the two species, the pPGMEA or EOEA coated LPG OFS could be used, which separated the wavelength shift caused by SA and UPEC in 12 hours.

For the EOEA coated LPG OFS, UPEC caused the greater wavelength shift after 24 hours (-3.22, -2.75 and -2.45 nm, for UPEC, PA and SA respectively), with a significantly higher wavelength shift occurring at 12 hours. However, the biomass of UPEC on EOEA was significantly lower than PA and SA (6.08, 14.16 and 8.61 $\mu m^3/\mu m^2$ respectively). This suggests that UPEC biofilms had higher

refractive index than the other two species, causing greater cladding mode effective index change, as observed on the HEOdA coated LPG OFS. Nevertheless, due to the differential wavelength shifts, an EOEA coated LPG OFS could be used to selectively sense UPEC within 12 hours.

The differing attachment profiles of each species to the three materials (Table 5.1) allows identification of an unknown species by matching its attachment profile to the three materials to the know controls. This can be done by comparing wavelength shifts from the three coated LPG OFS. If a culture of unknown bacteria species was presented, the three coated LPG OFS could all be immersed in the culture medium simultaneously and wavelength shift monitored. If higher wavelength shifts were observed on the pPGMEA and EOEA coated LPG OFS than on a HEOdA coating, PA would be the unknown microorganism. If higher wavelength shifts were observed on HEOdA and EOEA coated LPG OFS than on pPGMEA coatings, UPEC would be the unknown microorganism. Higher wavelength shifts on pPGMEA and HEOdA coated LPG OFS than on EOEA coatings would allow identification of SA. Significant differences between wavelength shifts appeared as early as 12 hours, hence species identification could be made within that time frame, offering a quicker, non-invasive method of pathogen identification than current protocols.

The three coated LPG OFS could be incorporated into ETTs and other medical devices, for *in situ* species identification. Using the PCA protocol highlighted would enable materials selective for other bacteria species to be identified, diversifying LPG OFS use and providing a useful clinical diagnostic tool. However, it has been shown that different strains and clinical isolates of one species interact differently with the same material [277]. Therefore, calibration measurements of wavelength shift are required for different strains, to build up a 'library' of spectral responses of coated LPG OFS, allowing for identification of species and strain.

LPG OFS with species selective coatings would also be a powerful research tool, allowing identification of unknown bacteria. Since LPG OFS and the selective

polymers are inexpensive to produce, they would provide a cheaper alternative to current research tools, such as Fourier-transform infrared spectroscopy (FT-IR) and 16S gene sequencing [278,279]. Furthermore, LPG OFS provide real time signal changes and easy comparison of wavelength shifts, removing the need for multi-step data analysis and complex mathematical interpretation of data.

5.5.7. Selective material-coated LPG OFS in bacteria co-cultures

Bacterial co-cultures are cultures of bacteria that contain more than one species. Studying co-cultures is necessary, as infections are often caused by more than one pathogen [272]. Furthermore, in research settings, multiple species are often studied simultaneously and in combination. Methods used to identify bacteria in mixed co-cultures include comparing pathogen-host interactions (via membrane-bound proteins) between species and using targets for specific bacterial ligands, such as lectins [182]. LPG OFS coated with selective materials could provide an inexpensive, faster alternative for studying co-cultures.

After a 24 hour incubation with the PA-UPEC co-culture a higher wavelength shift and thus a larger amount of biofilm was observed on the pPGMEA coated sensor compared with the EOEA coated sensor (Figure 5.10). The sum of the biomasses for each species, determined by confocal microscopy (Figure 5.11) corroborated this, with higher biomass totals on pPGMEA (51.11 $\mu m^3/\mu m^2$) than on EOEA (28.25 $\mu m^3/\mu m^2$). The wavelength shifts increased linearly with time on both sensors, indicating a linear change in mixed biofilm refractive index, as previously observed with single biofilms (section 5.4.7) and [170,171]. It may be useful to measure the refractive index of single and co-culture biofilms, to correlate refractive index to spectral shift.

On the pPGMEA coating, the co-culture caused a greater wavelength shift (after 12 hours) than the single cultures of PA or UPEC (Figure 5.12). This

indicated an increase to the mixed biofilm growth rate compared to single cultures of each species. The quantified biomass of mixed biofilms (Figure 5.11) indicated that PA formed biofilms at a faster rate than UPEC on pPGMEA. Furthermore, PA formed biofilms with higher biomasses on pPGMEA when in a co-culture than in a single culture (Figure 5.2). This suggests that UPEC acted as an antagonist, causing PA to progress through the biofilm life cycle quicker. It has previously been shown that PA formed biofilms more readily than *E. coli* in a 50:50 mixed culture, suggesting that *E. coli* antagonised PA [280]. UPEC also formed biofilms of higher biomass on pPGMEA in a co-culture than in a single culture. This also suggests that UPEC was stressed or antagonised by PA. Both PA and UPEC have been shown to form biofilms at a higher rate on silicone substrates when in a co-culture (50:50 ratio of species), compared to single cultures of each [281], corroborating the observations in Figures 5.10, 5.11 and 5.12; both species formed biofilms more rapidly in a co-culture, causing a greater rate of change of wavelength shift.

On EOEA coated LPG OFS, there were no differences in wavelength shifts between the co-culture and the UPEC single culture. This suggests that UPEC formed biofilms at a greater rate in a single culture than in a co-culture. This was also observed when comparing biomass in single and co- cultures (Figures 5.2 and 5.11), where UPEC biomass was higher on EOEA in single cultures than in co-cultures. This could be due to the production of indole by *E. coli*, which is thought to inhibit PA quorum-related competition factors, allowing *E. coli* to outcompete PA, increasing its survivability and lowering biofilm formation [282]. PA in a single culture caused smaller wavelength shifts than in a co-culture (Figure 5.12). The biomass of PA on EOEA in a co-culture (Figure 5.11) was higher than in a single culture (Figure 5.2), suggesting that the wavelength shift on EOEA coated LPG OGS from the co-culture incubation was predominantly caused by PA biofilm formation. PA has previously been observed forming biofilms faster in a 50:50 mixed culture with *E. coli* [281].

The CLSM images of mixed biofilms (Figure 5.11) showed that PA colonised more of the optical fibre surface and formed biofilms at a faster rate than UPEC,

on both coatings. This was previously observed in studies comparing biofilm formation of PA and *E. coli* from a co-culture [280]. It is thought that UPEC stressed/antagonised PA, causing it to rapidly attach and form biofilms. UPEC occupied less of the surface and so was likely able to survive as planktonic cells for longer than PA, particularly when EOEA was investigated. This has also been observed and was thought to be caused by the production of indole by *E. coli* [282]. On both coatings, there was very little 'overlap' of biofilms and each species appeared to occupy their own distinct spaces on the surface. This suggests that there may have been some competition between the species for space. PA attached more quickly and formed biofilms, restricting the amount of space available for UPEC biofilm formation. This has also been previously observed by Culotti *et al*. [283], albeit with the opposite observation, with PA occupying distinct spaces on an acrylic substrate predominantly occupied by an *E. coli* biofilm. This was thought to be due to competition for nutrients between the species, with *E. coli* becoming stressed quicker than PA, colonising the surface and preventing PA from accessing the areas that were colonised.

A correlation was established between the pPGMEA:EOEA wavelength shift ratio for co-cultures, using peak 2, and for biomass of each species in the co-culture. The PA-UPEC co-culture biofilm was found to be composed of 88-89% PA (Tables 5.4 and 5.5). This further illustrates that PA attached and formed biofilms more readily than UPEC. The two coated LPG OFS could be used in combination to identify species from mixed cultures, in 24 hours. For example, if the ratio of wavelength shifts, for peak, 2 is also 2.11 (Table 5.4), an assumption can be made that PA dominates the biofilms, by an 88:12 ratio. The wavelength shift and biomass ratios could also be established for other species in a mixed co-culture, for further coated LPG OFS (after single culture calibrations). If a correlation is observed, the coated LPGs could also identify species in a mixed culture and by how much each species makes up the total biomass.

pPGMEA and EOEA coated LPG OFS accurately determined the ratio of PA and UPEC in a mixed co-culture. This provides many advantages in healthcare and

research; an infection caused by the two pathogens could be rapidly diagnosed, allowing antibiotics specific for PA and UPEC to be administered. In research, LPG OFS could be used to identify and quantify PA and UPEC speedily, removing the need for expensive analytical tools and complex data interpretation. LPG OFS also provides a powerful method of investigating complex multi-species environments, such as the gut microbiome [271].

The pPGMEA and EOEA coated sensors could also be incorporated into ETTs and other medical devices for confirmation and identification of multiple VAP-causing pathogens. The relationship between wavelength shift and co-culture biomass could also be established, as in chapter 4. This would allow biomass quantification on device surfaces, irrespective of species.

5.6. Conclusions

This study combined LPG OFS with materials that differentially bound three bacteria species to selectively sense those species, in single and co-cultures. Nine materials with differential attachment were identified from data acquired from a polymer microarray incubation with PA, SA and UPEC, which possessed chemically diverse pendant groups, such as hydrophobic ring structures and long aliphatic chains. Incubation of silanised glass slides containing photopolymerised spots of these nine materials in single cultures of PA, SA and UPEC showed that the biomass of each species varied significantly on each spot and between spots. No material had extremely high or zero attachment of any bacteria species.

PCA allowed the three bacteria species to be separated based on their differential attachment to the nine materials, with separations by PCs 1 and 2, which captured 60% and 26% of the variance respectively. Matching the component loadings of the nine materials with the PC scores of the bacteria species allowed the contribution of each material to the two PCs to be observed, in turn allowing three materials to be chosen which could separate the three species. These three materials (pPGMEA, HEOdA and EOEA) could be used in combination to allow identification of each of the three bacteria, based on their differential attachment to them, which was further confirmed by PCA of the biomass of the three bacteria species to those three materials only.

The three materials were polymerised on a larger scale and used to coat three LPG OFS. Polymers with higher molecular weights and densities were found to give the thickest coatings, possible due to their increased viscosity and therefore slower polymer drainage from the substrate during dip coating. Exposure of the three coated LPG OFS simultaneously to single cultures of PA, SA and UPEC in RPMI-1640 for 24 hours gave differential wavelength shift profiles for each bacteria species on each coated sensor. This allowed identification of each species from the wavelength shift profiles, within 12 hours. The three coated LPG OFS could be used in combination to identify

unknown single cultures of the three species, providing the initial calibration with the three species is carried out.

Exposure of the pPGMEA and EOEA coated LPG OFS to a PA-UPEC co-culture also gave differential wavelength shifts, which were used to quantify the amount of PA and UPEC within a co-culture biofilm in 24 hours, providing sensors were first calibrated from single culture experiments. This allowed comparison of biofilm growth rates of each species between single and co-cultures, offering insightful information on their interaction. PA formed biofilms more quickly on both substrates than UPEC, suggesting that PA may be more sensitive to the environment and condition changes. On pPGMEA, both bacteria species formed biofilms at a faster rate in co-cultures than in single cultures, whereas on EOEA, UPEC formed biofilms more rapidly in a single culture than in a co-culture. On EOEA, as on pPGMEA, PA formed biofilms quicker in a co-culture than in a single culture. However, further research is needed into the behaviour of bacteria in single and co-cultures, as well as interstrain differences, which would be applicable to healthcare settings.

Overall, the coated LPG OFS could be used in combination for the identification of unknown bacteria species and to quantify the amount of each species in a mixed co-culture. This offers exciting opportunities for healthcare and research.

6. Summary and future work

6.1. Summary

Bacterial attachment and subsequent biofilm formation on ETT surfaces can result in the development of VAP, which causes significant mortality and morbidity among mechanically ventilated patients. The overuse of broad spectrum antibiotics for VAP may facilitate the spread of antimicrobial resistance, hence emphasis now lies on infection prevention, by modifying ETT surfaces to resist bacterial adhesion. Current ETT modifications include silver hydrogel coatings and polyurethane-cuffed ETTs, neither of which have been shown to effectively reduce VAP incidence or mortality. Furthermore, the silver hydrogel coated ETT imposes significantly higher costs to healthcare services. Since bacteria-surface interactions during cell attachment are poorly understood, the high throughput microarray screening process employed by Hook *et al*. [186] allowed for hundreds of potentially attachment-resistant materials to be screened simultaneously. Several 'hit' materials were discovered, with the best performing material, *in vitro* and *in vivo*, scaled up for ETT coating in chapter 3. This material was a novel polymer, ethylene glycol dicyclopentenyl ether acrylate – *co* – diethylene glycol methyl ether methacrylate (EGDPEA:DEGMA).

EGDPEA:DEGMA coatings, combined with a binary silane primer, reduced *P. aeruginosa* biomass and mean biofilm thickness by 95% and 96% respectively, on ETT device tubes, in RPMI-1640 medium, *in vitro*. On device cuffs in RPMI-1640 medium, and on tubes and cuffs in ASM G and ASM N, biomass and mean thickness were reduced by 100%. Effectively reducing biofilm growth would result in a reduced VAP risk. Both EGDPEA:DEGMA and the silane primer are safe for use in humans and have been CE-marked as coatings for silicone urinary catheters, hence the route to market for a coated ETT would be considerably shorter than a new device modification. EGDPEA:DEGMA offers an inexpensive anti-attachment modification for ETTs.

There were differing rates of bacterial attachment between device tubes and cuffs and between uncoated and coated substrates. Therefore, chemical and physical differences between these substrates were examined using ToF-SIMS and optical profiling in chapter 3. ToF-SIMS allowed the presence of the acrylate and methacrylate to be noted on coated substrates, as well as significantly higher ion intensity for the phthalate ion on device cuffs. This indicates that the phthalate plasticiser, DEHP, was present on cuffs, which may have had a bactericidal effect, resulting in reduced biomass/mean thickness on cuffs. Optical profiling showed a higher surface roughness on cuffs than on tubes, with a reduction in surface roughness upon polymer (and primer) coating. However, a correlation between surface roughness and bacterial adhesion was not established, hence the chemical profile of ETT surfaces outweighed the effect of surface roughness during bacterial attachment.

There is currently no method of monitoring bacterial attachment to ETT surfaces in real time. Removal of the device for inspection has been shown to cause tracheal wall damage and facilitate VAP development. In chapter 4, LPG OFS were newly and successfully used to monitor *P. aeruginosa* attachment to ETTs in real time, with high sensitivity. A developing biofilm (cells and EPS) on sensor surfaces caused a linear change in local refractive index, linearly changing the cladding mode effective index, resulting in linear wavelength shifts of the attenuation bands. The rate of change of wavelength shift was indicative of bacterial attachment, with lesser wavelength shifts observed on silane primed and EGDPEA:DEGMA coated LPG OFS, where less attachment occurred. Incorporating the LPG OFS into the lumen of ETTs and onto ETT cuffs allowed the real time, label-free monitoring of biofilm formation on uncoated device surfaces *in vitro*. An exponential function was applied to the inverse biomass versus wavelength shift plots, in RPMI-1640, ASM G and ASM N, allowing the biomass of *P. aeruginosa* biofilms to be quantified from the wavelength shift alone in each medium. Hence, the LPG OFS could be used as sensing instrumentation for ETT tubes, allowing for the real time, *in situ*

monitoring of biofilm formation to device surfaces and the potential for interception of ETT-centred infection.

Current methods of pathogenic bacteria identification is a time consuming process and faster, non-invasive methods are required. Correct bacteria species identification would result in the reduction of broad spectrum antibiotic use, helping to curb the spread of antimicrobial resistance. Identification of bacteria from unknown cultures would also provide a powerful research tool. In chapter 5, LPG OFS, coated with three materials that possessed species selectivity, were successfully used in combination to identify each of three pathogenic bacteria species (*P. aeruginosa* (PA), *S. aureus* (SA) and Uropathogenic *E. coli* (UPEC)) from single cultures. The wavelength shifts of attenuation bands from each coated LPG OFS were different between species. Using the differential wavelength shifts allowed for species identification from the spectral response in 12 hours, providing a novel, rapid, label-free and non-invasive tool for identifying the three bacteria species.

LPG OFS, coated with pPGMEA and EOEA, were also used in combination to quantify the amount of PA and UPEC from a mixed co-culture of the two bacteria species, providing a calibration of coated LPG OFS in single cultures was first conducted. The ratio of the wavelength shift gradients of the two coated LPG OFS in the co-culture indicated an 88:12 split for PA:UPEC in a mixed biofilm. The two coated LPG OFS also allowed differences in biofilm formation of each bacteria species between single and co-cultures to be investigated.

The coated LPG OFS used in this thesis allow for accurate, non-invasive and label-free bacteria identification from single and co-cultures, in 12 and 24 hours respectively. Quantification of species in a mixed co-culture could also be achieved in 24 hours. This offers faster alternatives to current methods. However, the interaction between different clinical isolates of each species and the selective materials are required to develop a robust species identification tool. The LPG OFS can be incorporated into ETTs and other medical devices for identification of VAP-causing pathogens, in real time and *in situ*.

6.2. Recommendations for future work

Although EGDPEA:DEGMA was successfully synthesised, the conversion of EGDPEA was only 57% and the feed ratio was 1.3:1, when a 3:1 feed ratio was expected. These results were thought to be caused by residual oxygen in the reaction mixture. Hence, optimisation of polymerisation protocols is required, to minimise oxygen presence. Optimisation of coating mechanical properties could be achieved by studying the interaction of the silane primer with PVC and the polymer with the silanes, via water contact angle (WCA) measurements.

The *in vivo* effectiveness of EGDPEA:DEGMA coatings on PVC ETTs would need to be established prior to human trials, by implanting uncoated and coated ETT sections into mice, inoculating them with fluorescently-labelled bacteria and comparing the fluorescence between uncoated and coated substrates. If successful, an entire ETT can be coated, after silane priming, and the *in situ* effectiveness tested. This could involve intubating pigs with the modified ETTs, inoculating them with VAP-causing pathogens, then withdrawing the device after a set time and analysing bacterial coverage on them. Comparing the coated ETT with an uncoated counterpart would allow the *in situ* assessment of EGDPEA:DEGMA to be made.

Since the safety of the materials involved have already been established, the coated ETT can then be trialled in humans, using similar methods employed for the silver hydrogel coated ETT; half of the test subjects would be intubated using normal PVC ETTs and the other half with the EGDPEA:DEGMA coated ETT. VAP rates and mortality could be assessed over the trial period and the effectiveness of the coated ETT noted. If successful, medical device approval and CE marking can be applied for through the Medicines and Healthcare products Regulatory Agency (MHRA) and the device licensed for use in clinical settings.

The *in vivo* response of the LPG OFS has not been examined, so an *in vivo* model would need to be designed and performed. The sensitive region of the LPG OFS could be implanted subcutaneously into mice, with the ends of the optical fibre

rolled up and kept compact, so to not disturb the natural movement of the animal. Anaesthetising the animal and recording transmission spectra at certain time points would give rise to the wavelength shift profiles shown in chapter 4. The sensor response in the presence and absence of inoculated pathogens could be monitored, to confirm whether the LPG OFS responds to bacterial adhesion *in vivo* in the same way it does *in vitro*.

The LPG OFS instrumented ETT could also be trialled *in vivo*, using the live porcine tracheal model. Intubated pigs could be inoculated and the spectral response from the LPG OFS instrumentation noted. The exponential function plotted in chapter 4 could then be tested to see if biomass on ETTs can be quantified from the wavelength shift *in vivo*. The exponential function could also be established for other bacteria species, by repeating the experiments in chapter 4 using other pathogenic bacteria. The wavelength shifts and the biomass on ETTs could be quantified and the mathematical function between them noted. A 'library' of wavelength shift-biomass formulae could be generated, allowing for quantification of biomass of multiple species' biofilms on ETT surfaces.

It would be useful to image and quantify the biomass of single culture biofilms grown on optical fibres coated with the three selective materials from chapter 5 over 24 hours. This would allow the relationship between wavelength shift and biomass to be established for the three coatings. This would have the added benefit of biomass quantification, as well as species identification, both as a stand-alone tool or as an instrument incorporated into a medical device.

WCA measurements could be made on bacterial cells and the selective materials to gain a better understanding of bacterial attachment to materials with certain pendant groups. WCA would allow a correlation (if any) to be observed between hydrophilicity/hydrophobicity of materials/bacteria and attachment. This would allow the rational design of materials with bacteria species selectivity or anti-attachment properties.

More materials with differential bacterial attachment could be identified and used to design LPG OFS systems that can identify more bacterial species from unknown single cultures, or quantify the amount of bacteria from a mixed co-culture containing species other than *P. aeruginosa* and Uropathogenic *E. coli*, as well as mixed co-cultures containing more than two species. Furthermore, the differences in wavelength shift caused by different strains of the same bacteria species could be investigated, allowing a calibration for multiple clinical strains, in the hope of developing a diagnostic tool.

7. Appendices

7.1. Appendix A. Procedure of processing optical spectra and calculating wavelength shift in OriginPro 8.6.

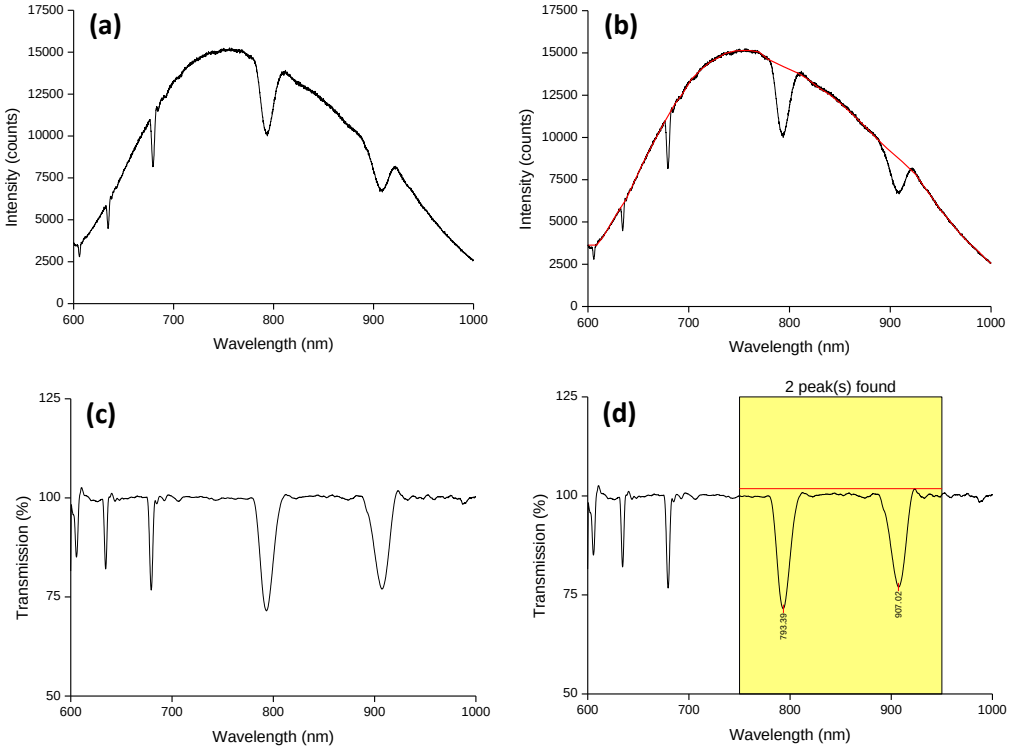


Figure 7.1. (a) Transmission spectra, imported from SpectraSuite. **(b)** A baseline is drawn over the optical spectra (red line), omitting the attenuation peaks. **(c)** Processed spectra, resulting from dividing spectra (a) by baseline (b). Note the change in the *y*-axis from intensity to transmission. **(d)** Peak finder used to find the wavelengths (*x*) at which the minimum transmission (*y*) value is located (peak apex – maximum transmission loss from 100%).

7.2. Appendix B. Method of producing Artificial Sputum Medium (ASM).

Reagents:

NaCl @ 3.03 g/L

Stock concentrations:

Chemical	Formula	Molarity of stock (M)	Volume of stock (mL)	Moles required for stock (M)	Amount of chemical for stock (g)
Disodium Hydrogen Phosphate Anhydrous	Na_2HPO_4	0.125	40	0.005	0.710
Monosodium Phosphate Anhydrous	NaH_2PO_4	0.130	40	0.005	0.624
Potassium Nitrate	KNO_3	0.035	40	0.035	0.141
Potassium Sulphate	K_2SO_4	0.027	40	0.001	0.189
Ammonium Chloride	NH_4Cl	0.228	40	0.009	0.488
Potassium Chloride	KCl	0.153	40	0.006	0.456
3-(N-morpholino) propanesulfonic acid (MOPS)	$C_7H_{15}NO_4S$	1	40	0.040	8.370

Prepare stock concentrations by dissolving the correct amount in 30 mL of deionised water and then adjust volume to 40 mL. Filter sterilise the solution with a 0.22 µm syringe filter. 10 mL of each stock is required per litre of ASM.

Amino acid supplements:

Amino acid	Molarity for 100x stock (mM)	Moles needed for stock (mn)	Amount of amino acid for stock (g per 40 mL)
Aspartame^	82.7	3.308	0.440
Threonine	107.2	4.288	0.511
Serine	144.6	5.784	0.608
Glutamic acid^	154.9	6.196	0.912
Proline	166.0	6.640	0.764
Glycine	120.3	4.812	0.361
Alanine	178.0	7.120	0.627
Cysteine*	16.0	0.640	0.078
Valine	111.7	4.468	0.523
Methionine	63.3	2.532	0.378
Isoleucine#	112.1	4.468	0.588
Leucine	160.9	6.436	0.844
Tyrosine^	80.2	3.208	0.581
Phenylalanine	53.0	2.120	0.350
Ornithine-HCl	67.6	2.704	0.456
Lysine	212.8	8.512	1.244
Histidine	51.9	2.076	0.322
Tryptophan*^	1.3	0.052	0.011
Arginine	30.6	1.224	0.213

Prepare the 100x stock solutions by dissolving the correct amount in 30 mL of deionised water and then adjust volume to 40 mL.

*Cysteine and Tryptophan are at such small quantities that a 1000x stock is prepared by dissolving the correct amount in deionised water. A 100x stock is then prepared by mixing 4 mL of the 1000x stock with 36 mL deionised water as before.

^Aspartame should be dissolved in 0.5 M NaOH, not water. Glutamic acid should be dissolved in 1 M HCl, not water. Tyrosine should be dissolved in 1 M NaOH, not water. Tryptophan should be dissolved in 0.2 M NaOH, not water. Volume adjustment should also be made using 0.2 M NaOH.

#Isoleucine requires being heated to 50°C for 30 minutes to dissolve.

Filter sterilise the solution with a 0.22 µm syringe filter. 10 mL of each stock is required per litre of ASM.

Additional supplements:

Chemical	Formula	Molarity of stock (M)	Volume of stock (mL)	Moles required for stock (M)	Amount of chemical for stock (g)
Calcium Chloride	$CaCl_2$	0.175	40	0.007	0.780
Magnesium Chloride	$MgCl_2$	0.061	40	0.002	0.230
Glucose*	$C_6H_{12}O_6$	0.300	40	0.012	2.160
L-Lactic Acid^	$C_3H_6O_3$	0.930	40	0.037	3.350
Iron (II) Sulphate Heptahydrate#	$FeSO_4.7H_2O$	0.036	40	0.00144	0.400

Prepare the 100x stock solutions by dissolving the correct amount in 30 mL deionised water and then adjust the volume to 40 mL.

*Omit glucose for ASM N.

^L-Lactic Acid is purchased as a solution with a density gradient of 1.209 g/ML. For a 40 mL stock this equates to 2.77 mL of L-Lactic Acid and 37.23 mL deionised water. To prepare this mix 2.77 mL of lactic acid with 30 mL deionised water. pH the solution to 7 with 5 M NaOH and then make up to 40 mL.

Because the amount of Iron (II) Sulphate Heptahydrate is too low to accurately weigh, a 10000x stock is prepared and then 400 µL mixed with 39.6 mL of deionised water to make a 100x stock.

#Filter sterilise the solution with a 0.22 µm syringe filter. 10 mL of each stock is required per litre of ASM.

7.3. Appendix C. ^{1}H NMR spectra of EGDPEA:DEGMA.

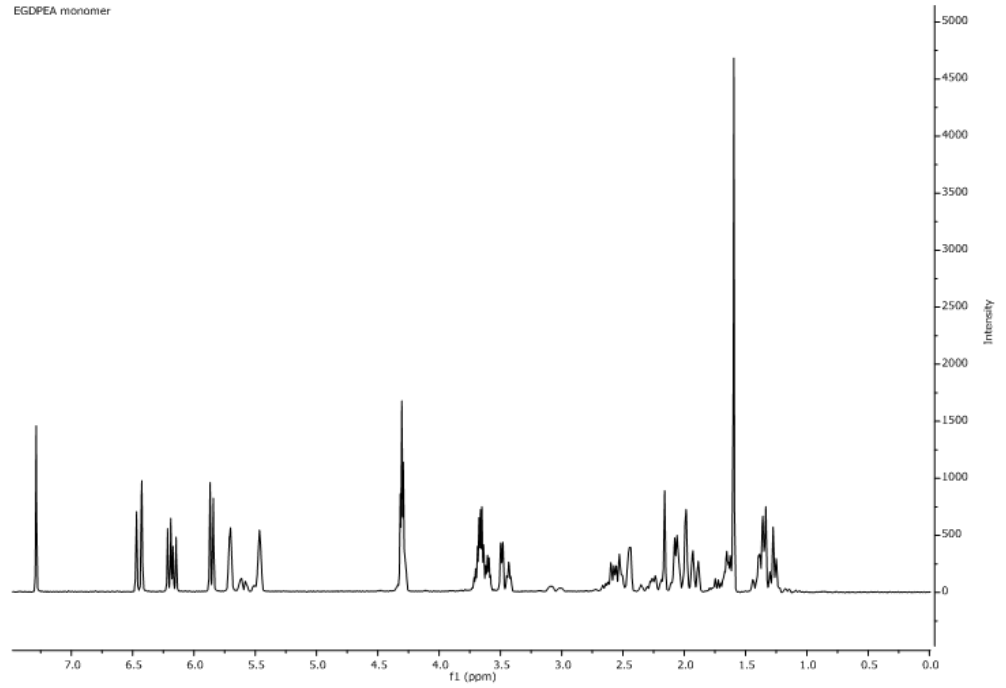


Figure 7.2. ^{1}H NMR spectrum of EGDPEA monomer, obtained at a spectrometer frequency of 400.3 MHz.

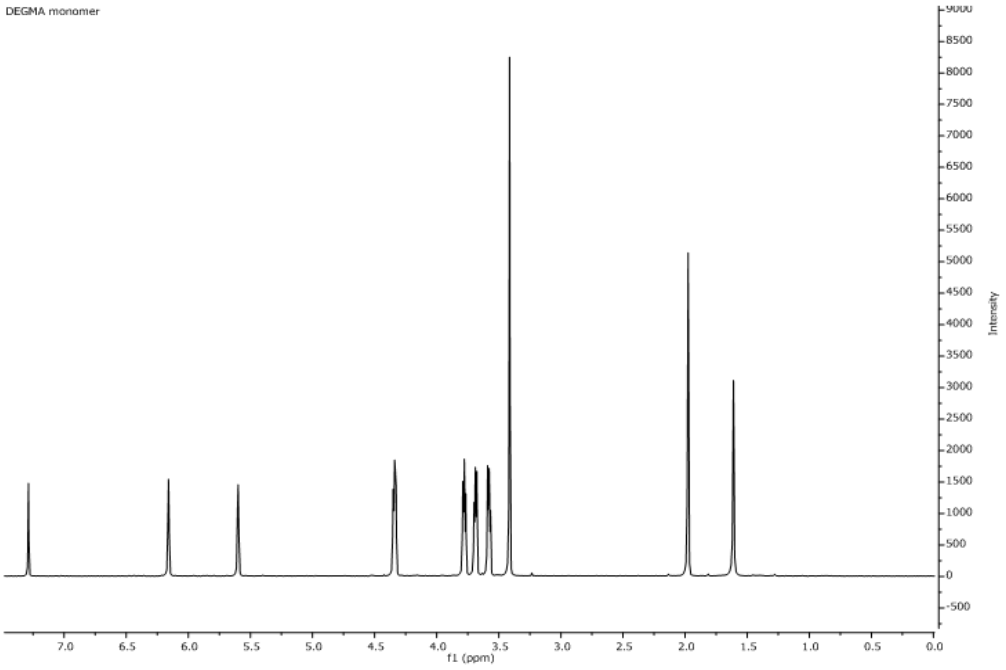


Figure 7.3. ^{1}H NMR spectrum of DEGMA monomer, obtained at a spectrometer frequency of 400.3 MHz.

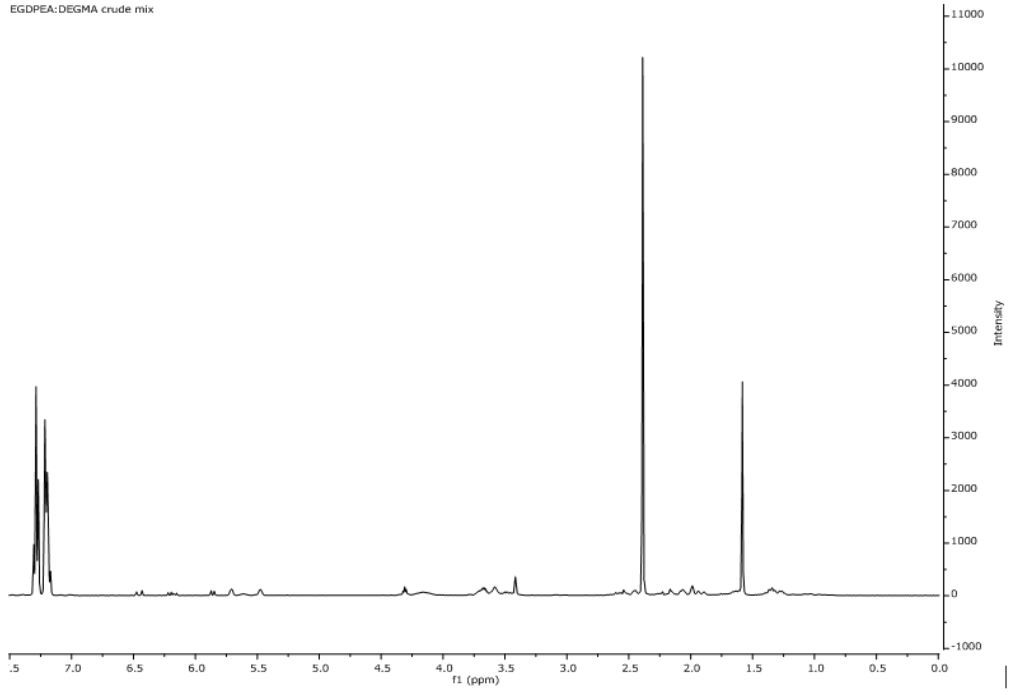


Figure 7.4. ^{1}H NMR spectrum of EGDPEA:DEGMA crude mix (before precipitation), obtained at a spectrometer frequency of 400.3 MHz.

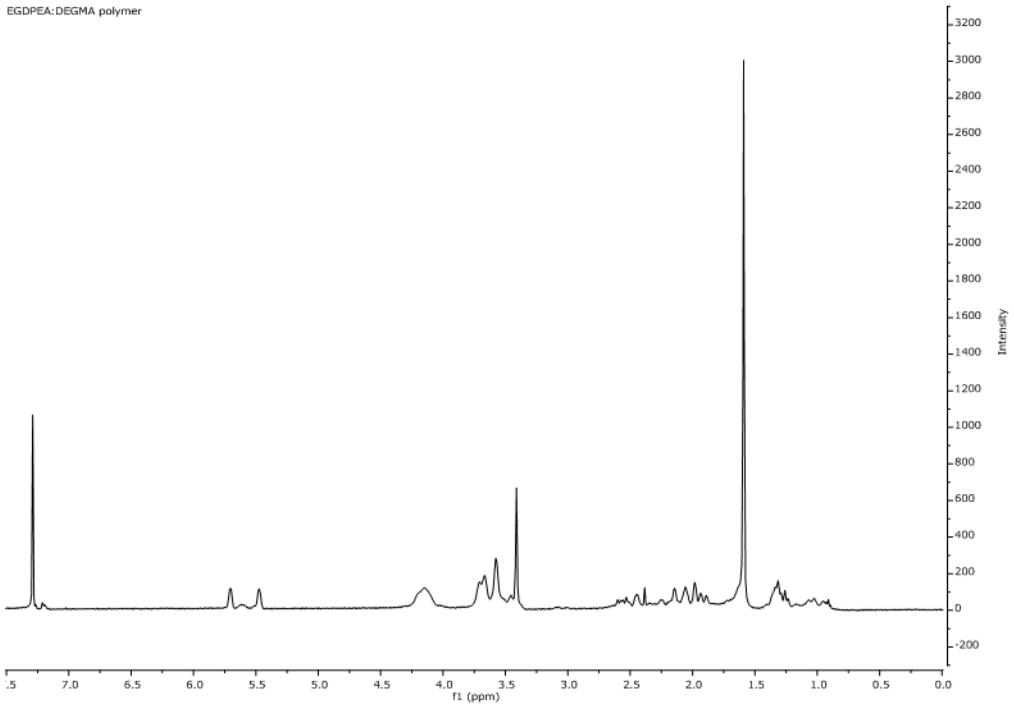


Figure 7.5. ^{1}H NMR spectrum of EGDPEA:DEGMA polymer (after precipitation), obtained at a spectrometer frequency of 400.3 MHz.

7.4. Appendix D. Negative mass spectra of U, C, PC and P tubes and cuffs, from ToF-SIMS. Ion intensity maps of acrylate, methacrylate, silicate and phthalate anions obtained from ToF-SIMS.

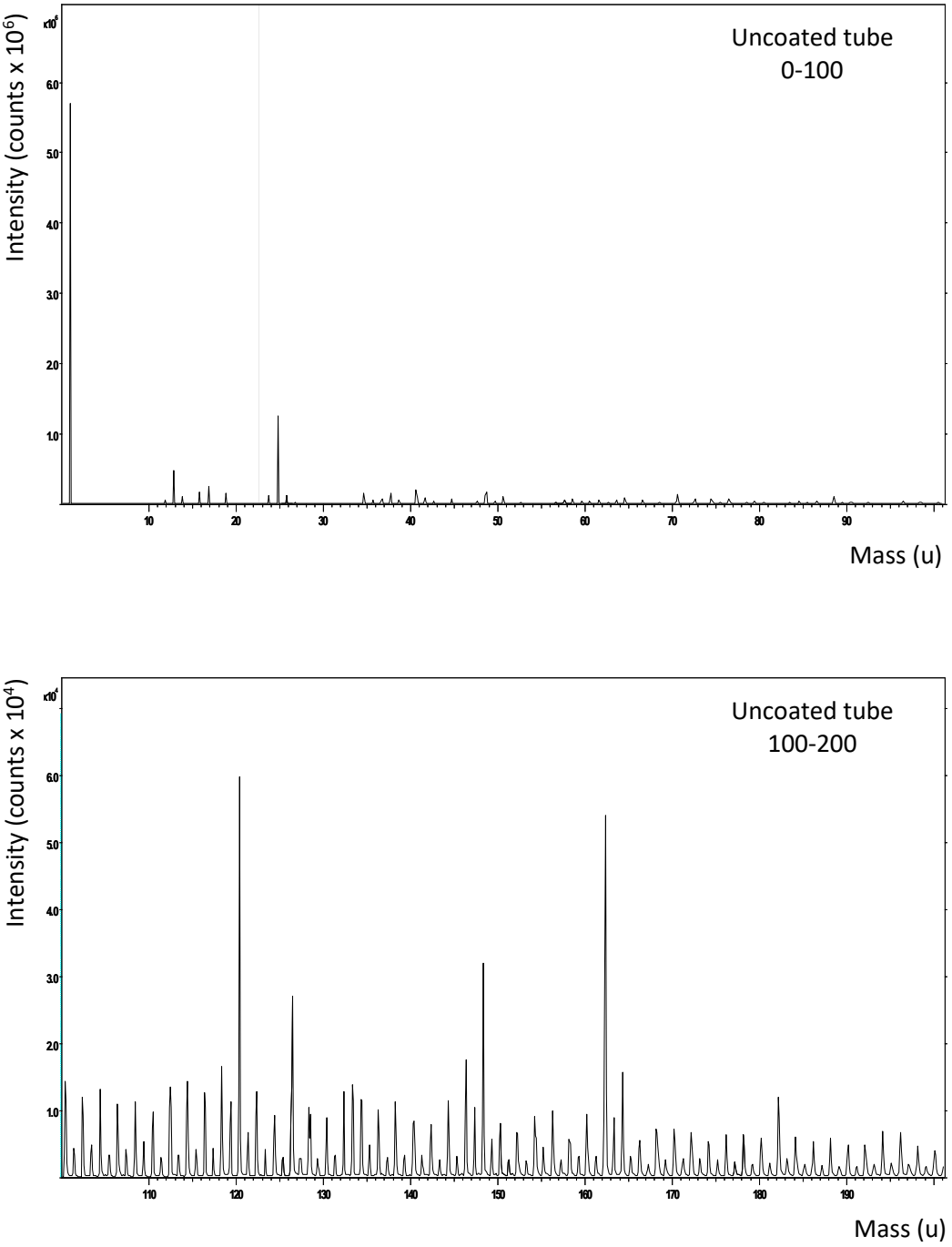


Figure 7.6. Negative mass spectra of uncoated ETT tubes, obtained from ToF-SIMS. A mass range of 0-200 is shown, presented as 2 x 100 mass range spectra.

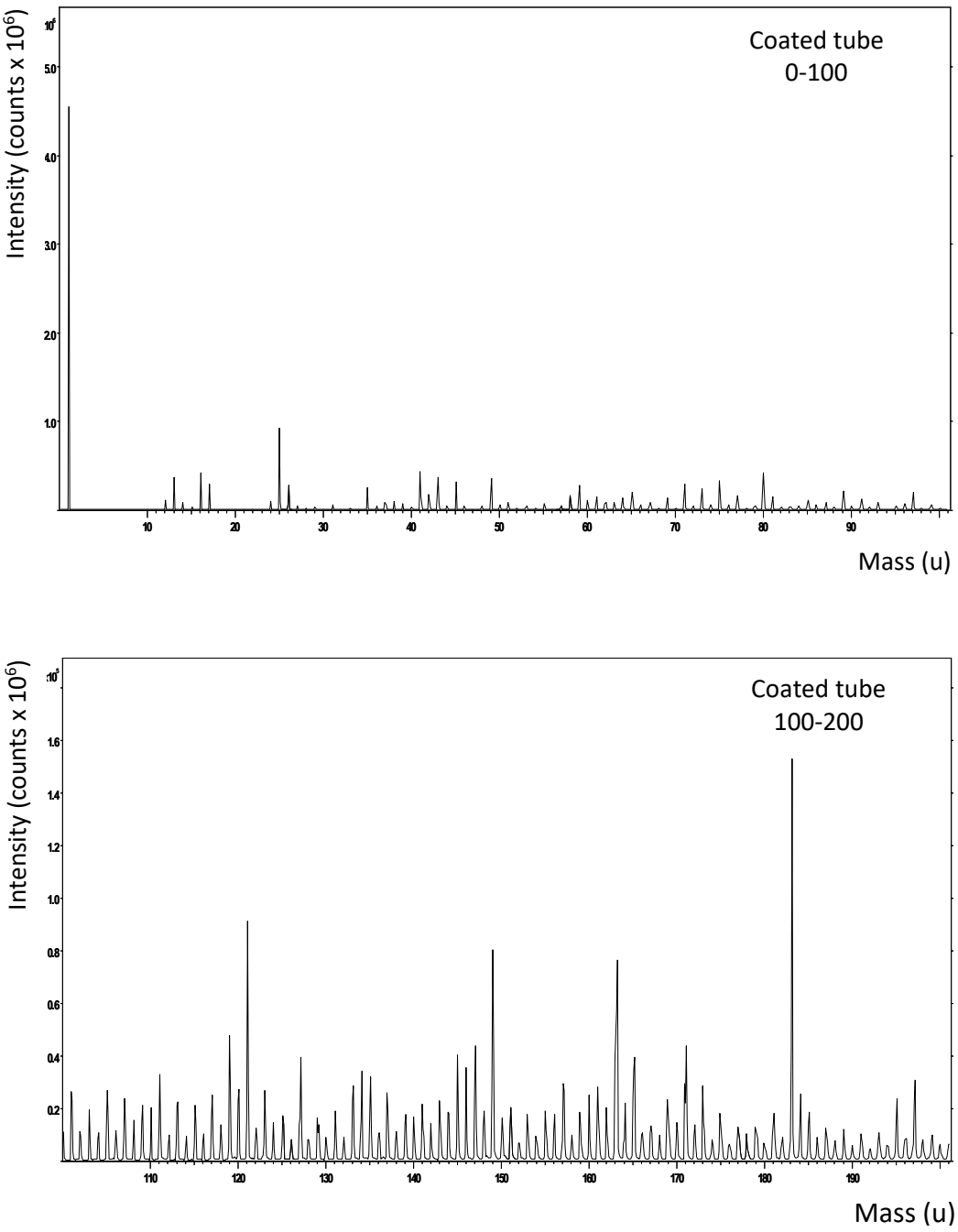


Figure 7.7. Negative mass spectra of coated ETT tubes, obtained from ToF-SIMS. A mass range of 0-200 is shown, presented as 2 x 100 mass range spectra.

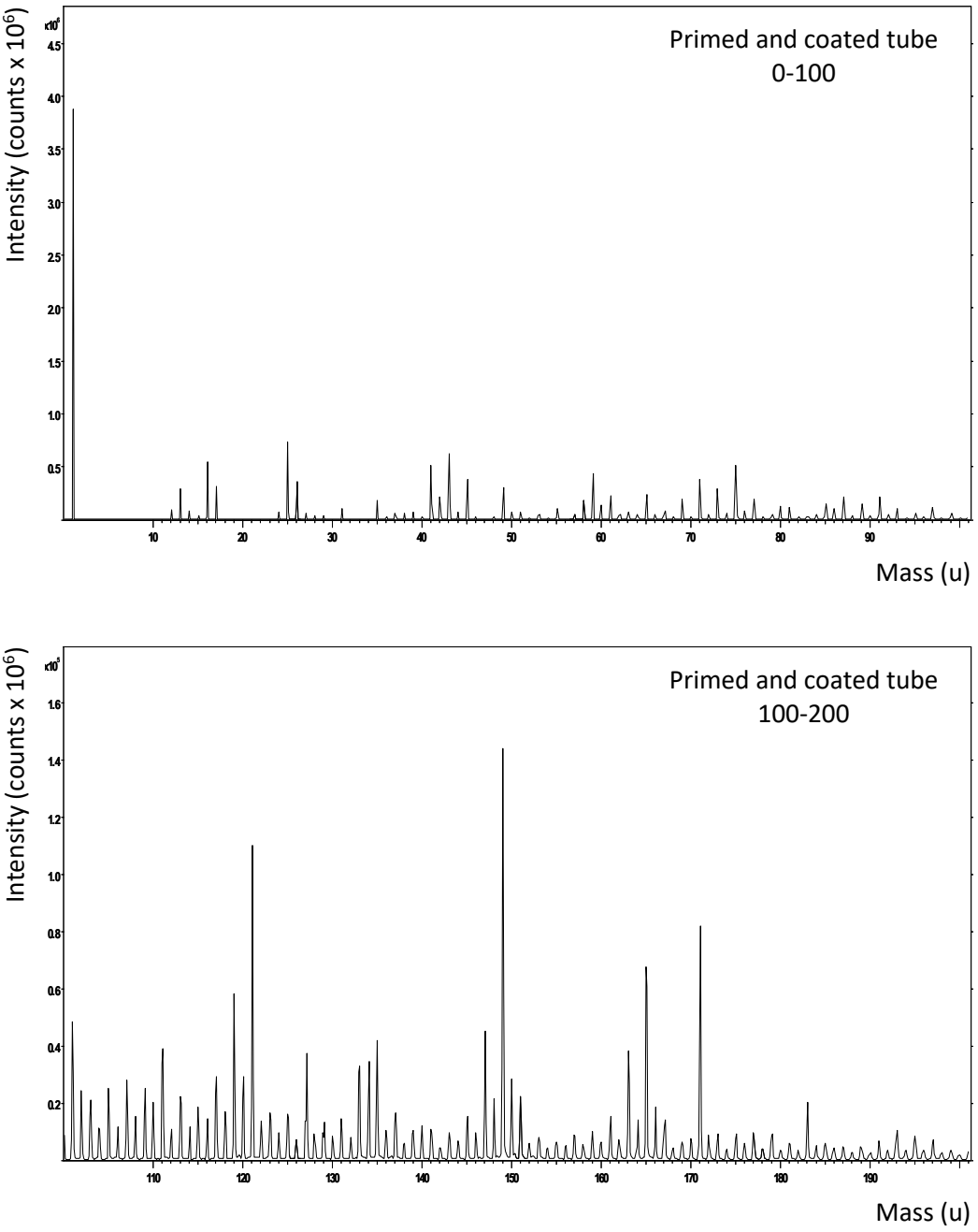


Figure 7.8. Negative mass spectra of primed and coated ETT tubes, obtained from ToF-SIMS. A mass range of 0-200 is shown, presented as 2 x 100 mass range spectra.

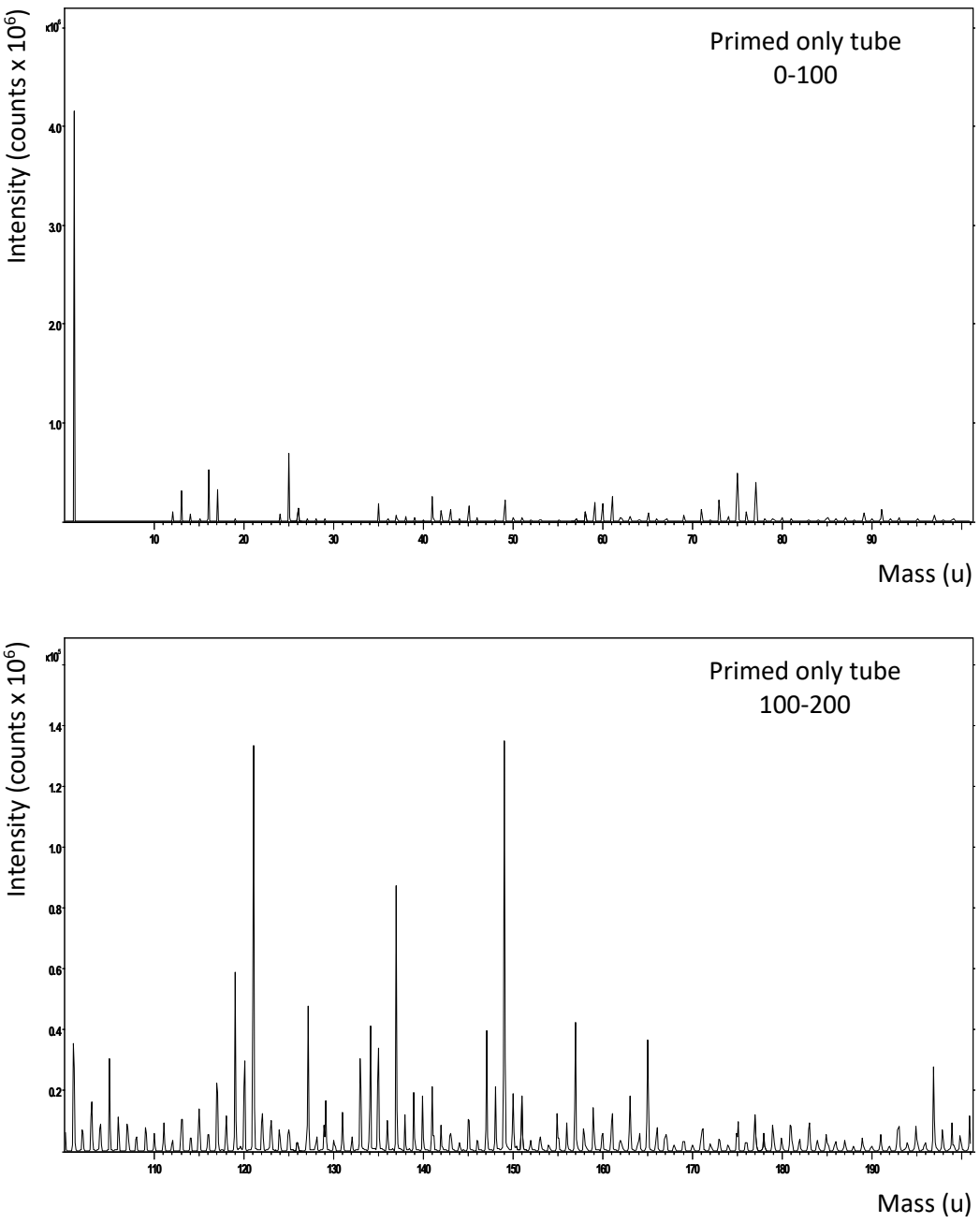


Figure 7.9. Negative mass spectra of primed only ETT tubes, obtained from ToF-SIMS. A mass range of 0-200 is shown, presented as 2 x 100 mass range spectra.

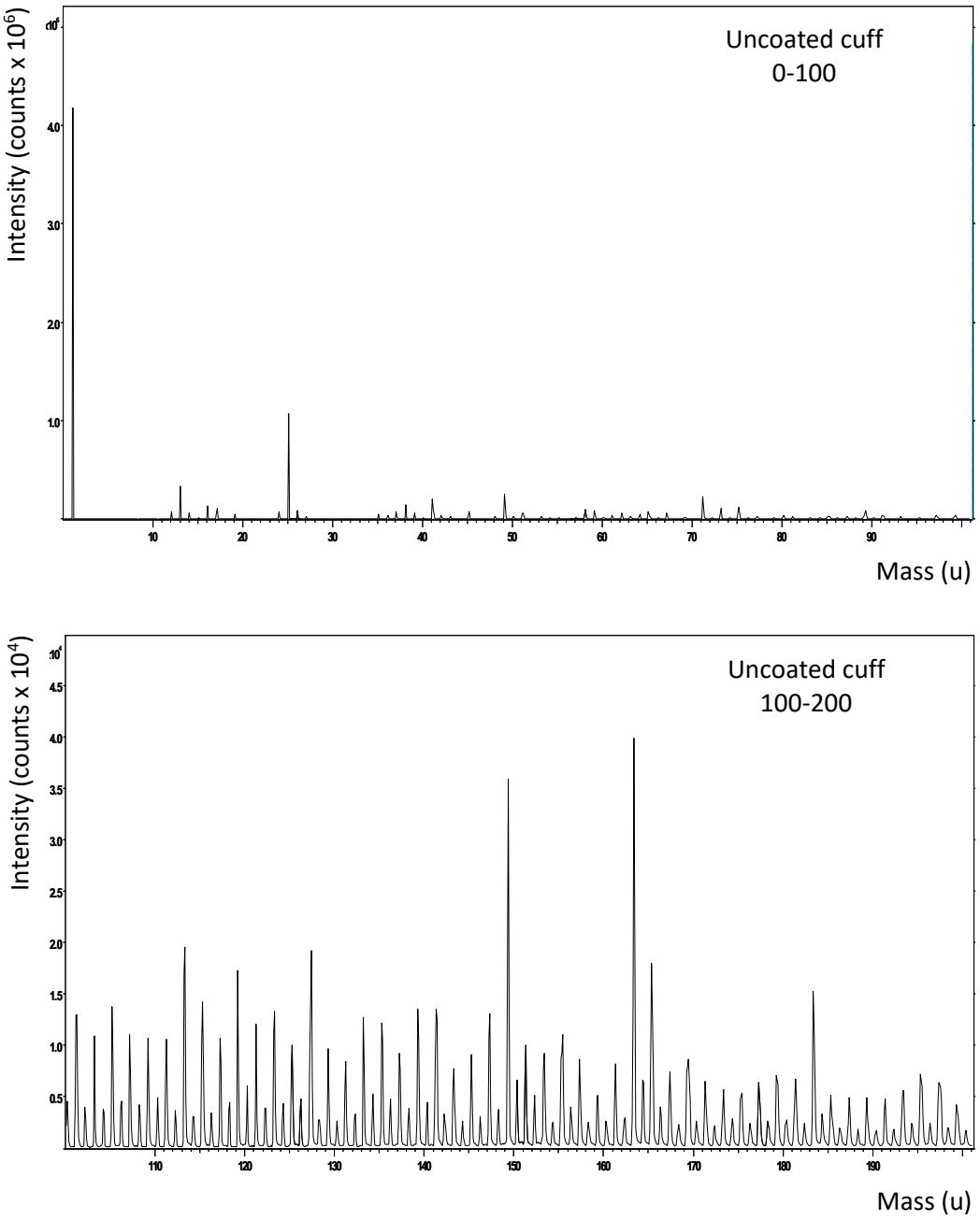


Figure 7.10. Negative mass spectra of uncoated ETT cuffs, obtained from ToF-SIMS. A mass range of 0-200 is shown, presented as 2 x 100 mass range spectra.

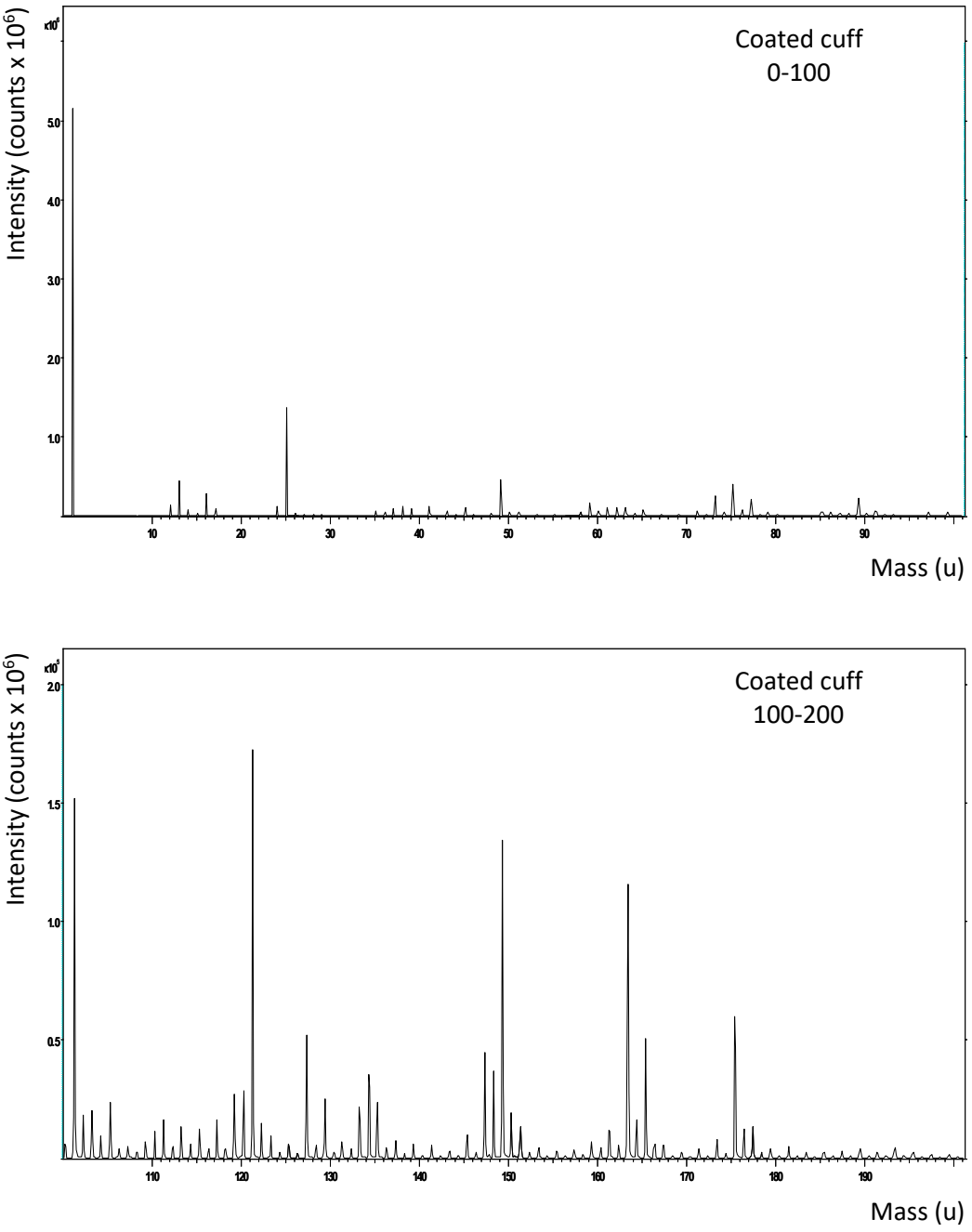


Figure 7.11. Negative mass spectra of coated ETT cuffs, obtained from ToF-SIMS. A mass range of 0-200 is shown, presented as 2 x 100 mass range spectra.

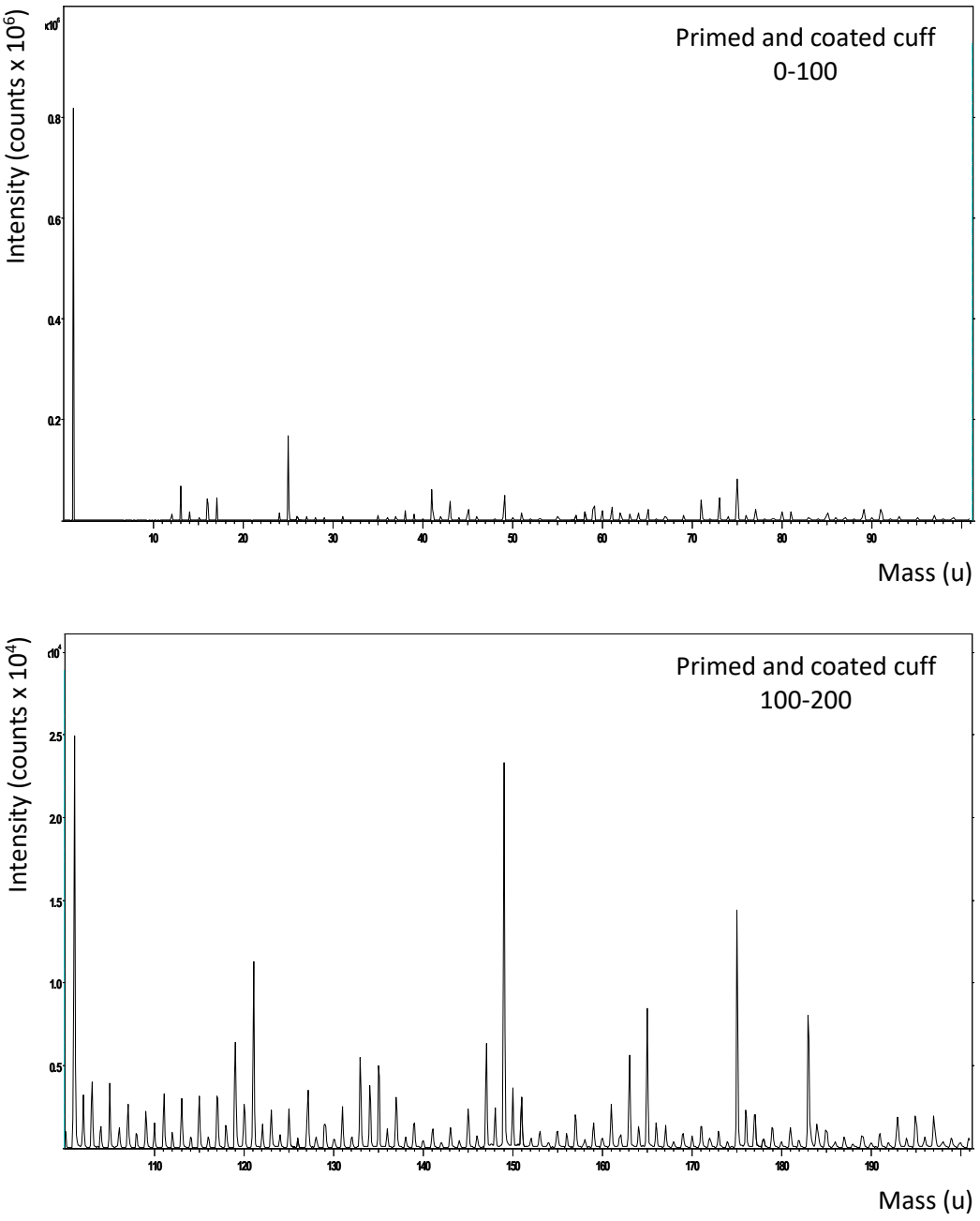


Figure 7.12. Negative mass spectra of primed and coated ETT cuffs, obtained from ToF-SIMS. A mass range of 0-200 is shown, presented as 2 x 100 mass range spectra.

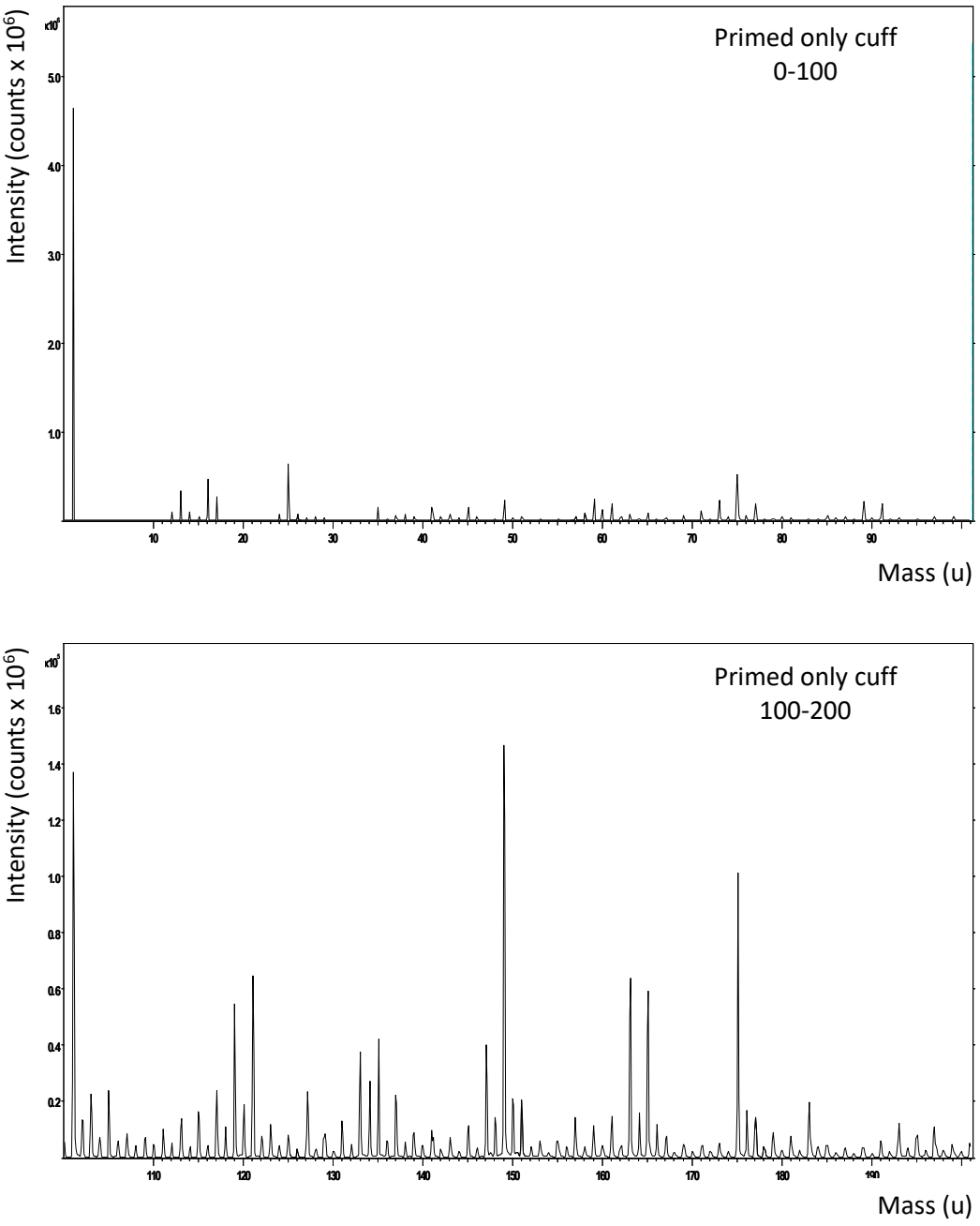
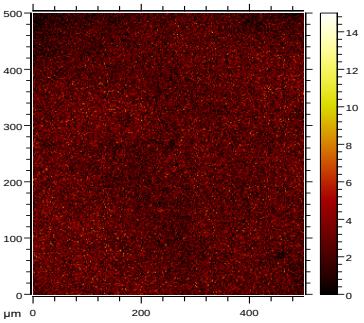


Figure 7.13. Negative mass spectra of primed only ETT cuffs, obtained from ToF-SIMS. A mass range of 0-200 is shown, presented as 2 x 100 mass range spectra.

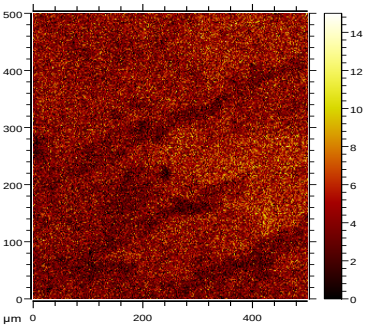
Ion intensity maps.

Acrylate ($C_3H_3O_2^-$) on device tubes:

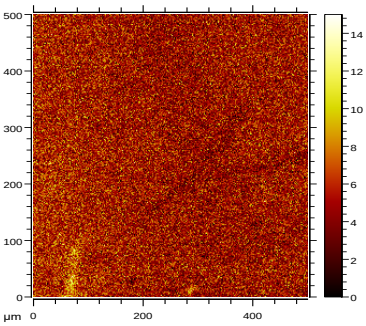
Uncoated



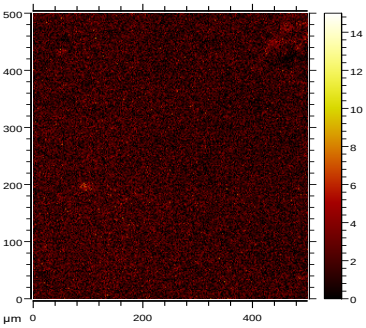
Coated



Primed and coated

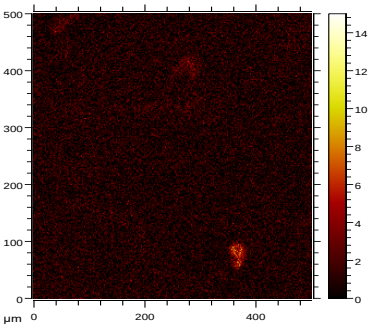


Primed only

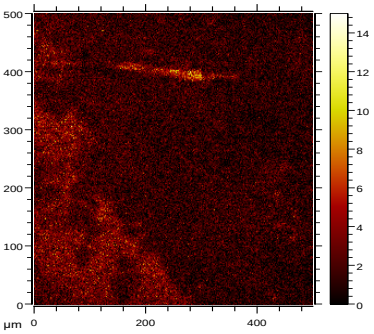


Acrylate ($C_3H_3O_2^-$) on device cuffs:

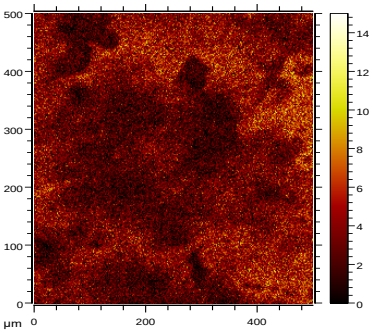
Uncoated



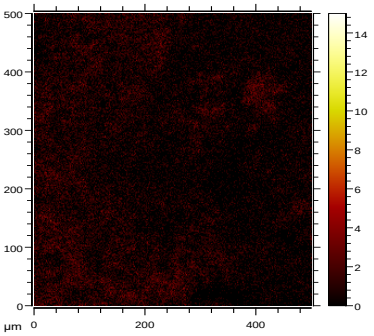
Coated



Primed and coated

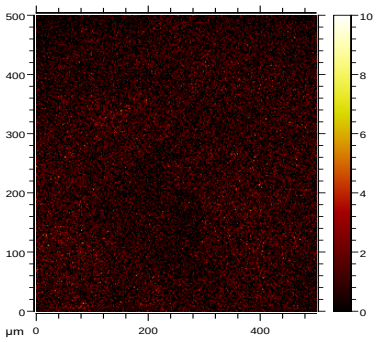


Primed only

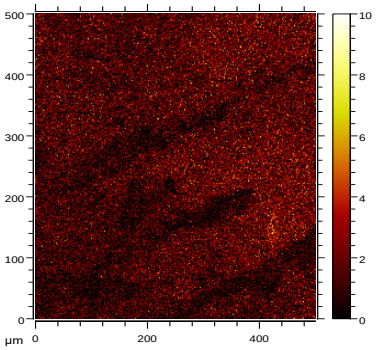


Methacrylate ($C_4H_5O_2^-$) on device tubes:

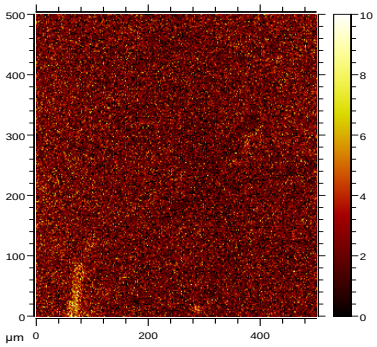
Uncoated



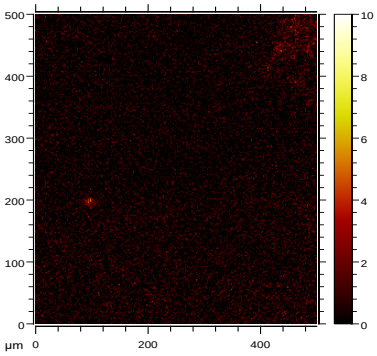
Coated



Primed and coated

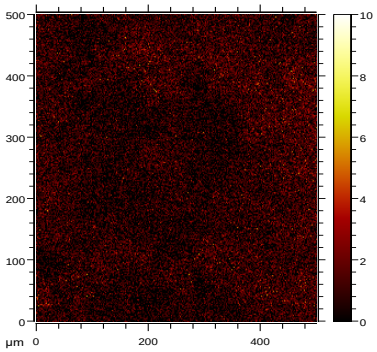


Primed only

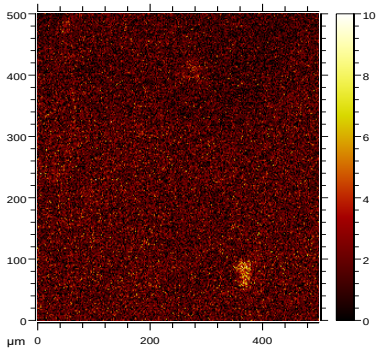


Methacrylate ($C_4H_5O_2^-$) on device cuffs:

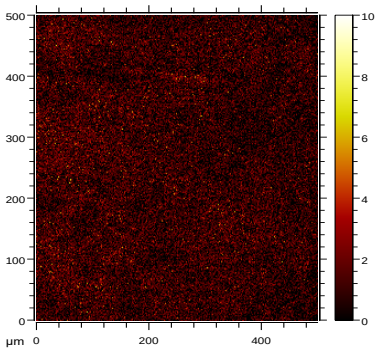
Uncoated



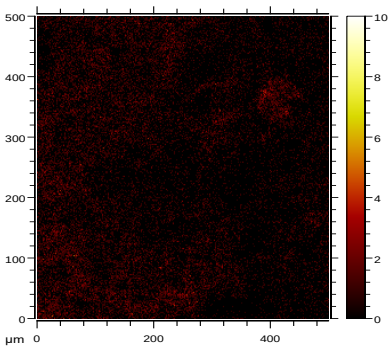
Coated



Primed and coated

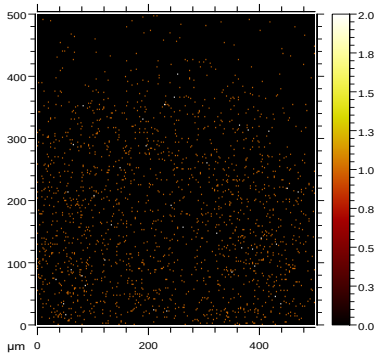


Primed only

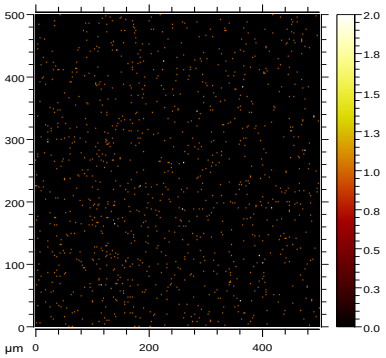


Silicate (SiO_4^{4-}) on device tubes:

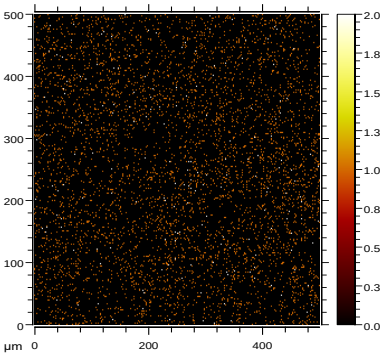
Uncoated



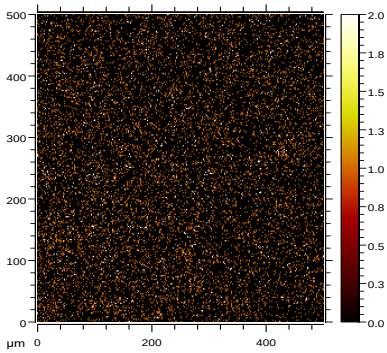
Coated



Primed and coated

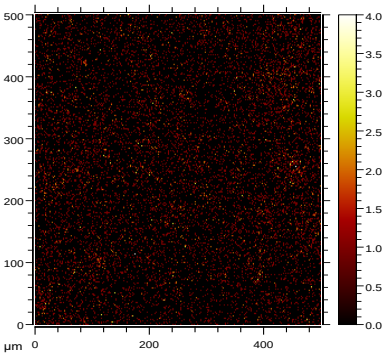


Primed only

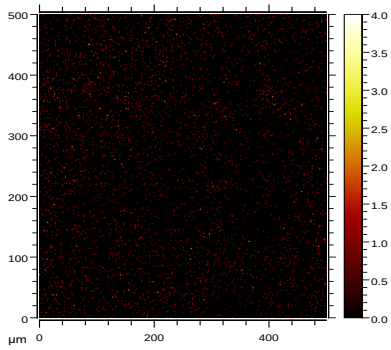


Silicate (SiO_4^{4-}) on device cuffs:

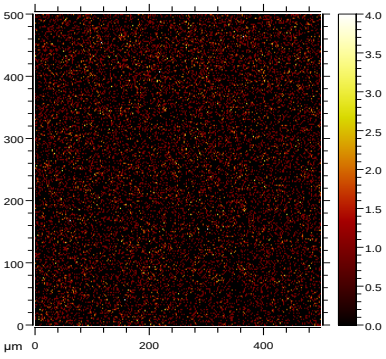
Uncoated



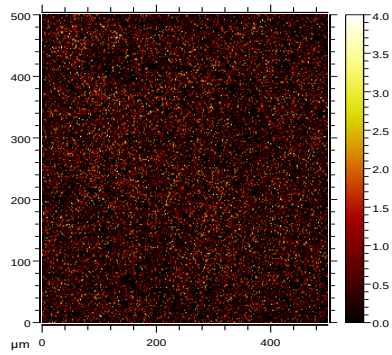
Coated



Primed and coated

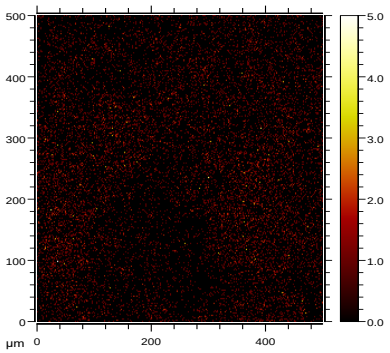


Primed only

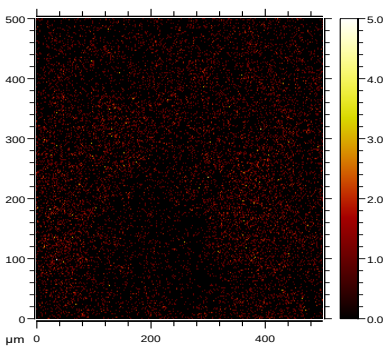


Phthalate ($C_8H_4O_4^{2-}$) on device tubes:

Uncoated

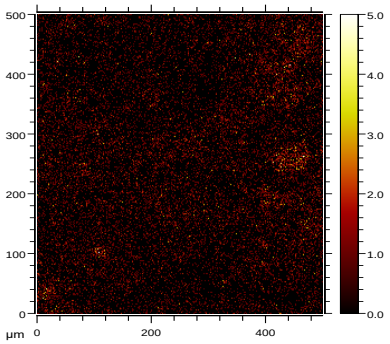


Primed only

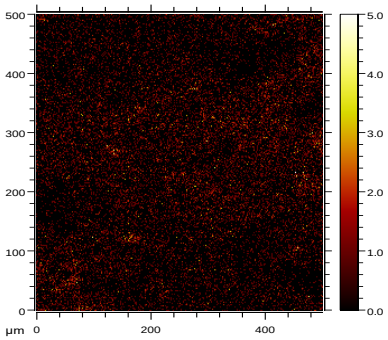


Phthalate ($C_8H_4O_4^{2-}$) on device cuffs:

Uncoated



Primed only



7.5. Appendix E. 2D CLSM images of *P. aeruginosa* (PA01-N, mCherry) biofilms on ETT tubes and cuffs at 24, 48 and 72 hours.

RPMI-1640

Tube:

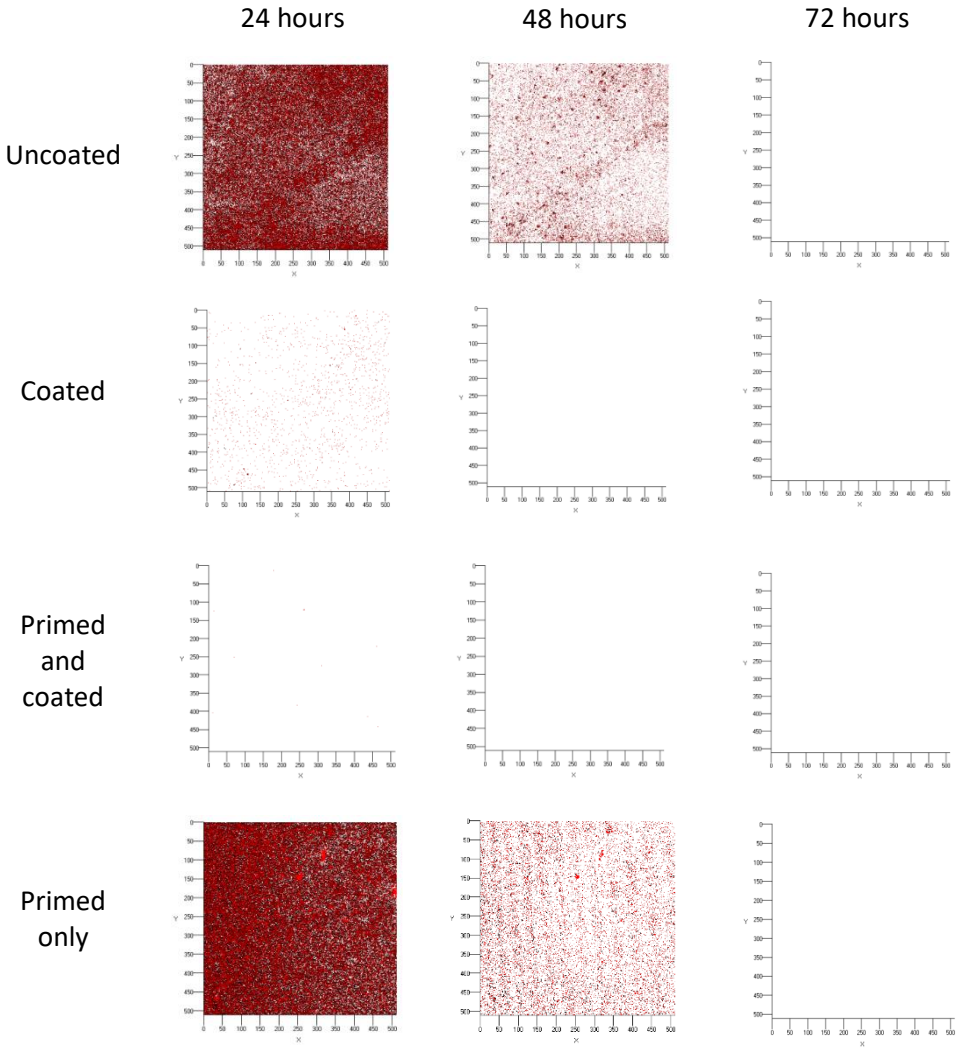


Figure 7.14. 2D CLSM images of *P. aeruginosa* biofilms, labelled with mCherry, on uncoated, polymer coated, primed and coated and primed only ETT tubes, at 24, 48 and 72 hours, in RPMI-1640 medium. Scale bars are 500 µm x 500 µm.

RPMI-1640

Cuff:

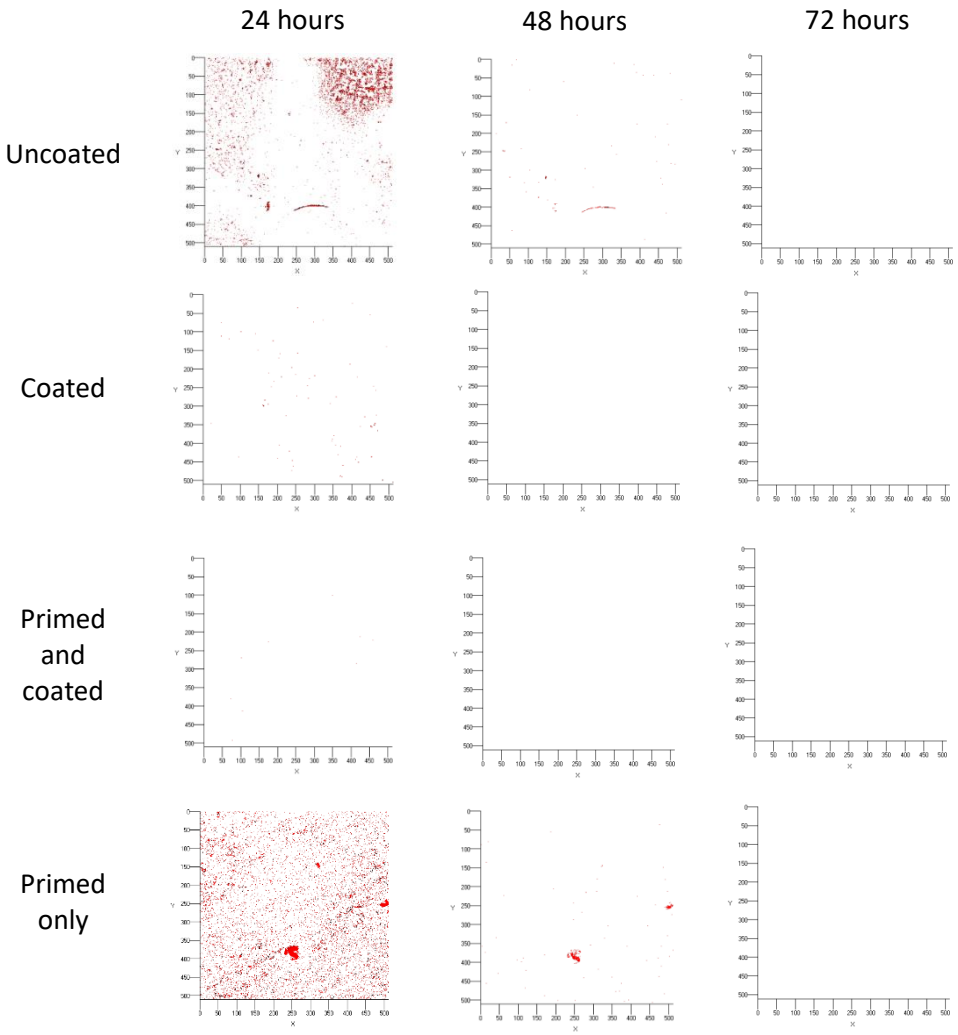


Figure 7.15. 2D CLSM images of *P. aeruginosa* biofilms, labelled with mCherry, on uncoated, polymer coated, primed and coated and primed only ETT cuffs, at 24, 48 and 72 hours, in RPMI-1640 medium. Scale bars are 500 µm x 500 µm.

ASM G

Tube:

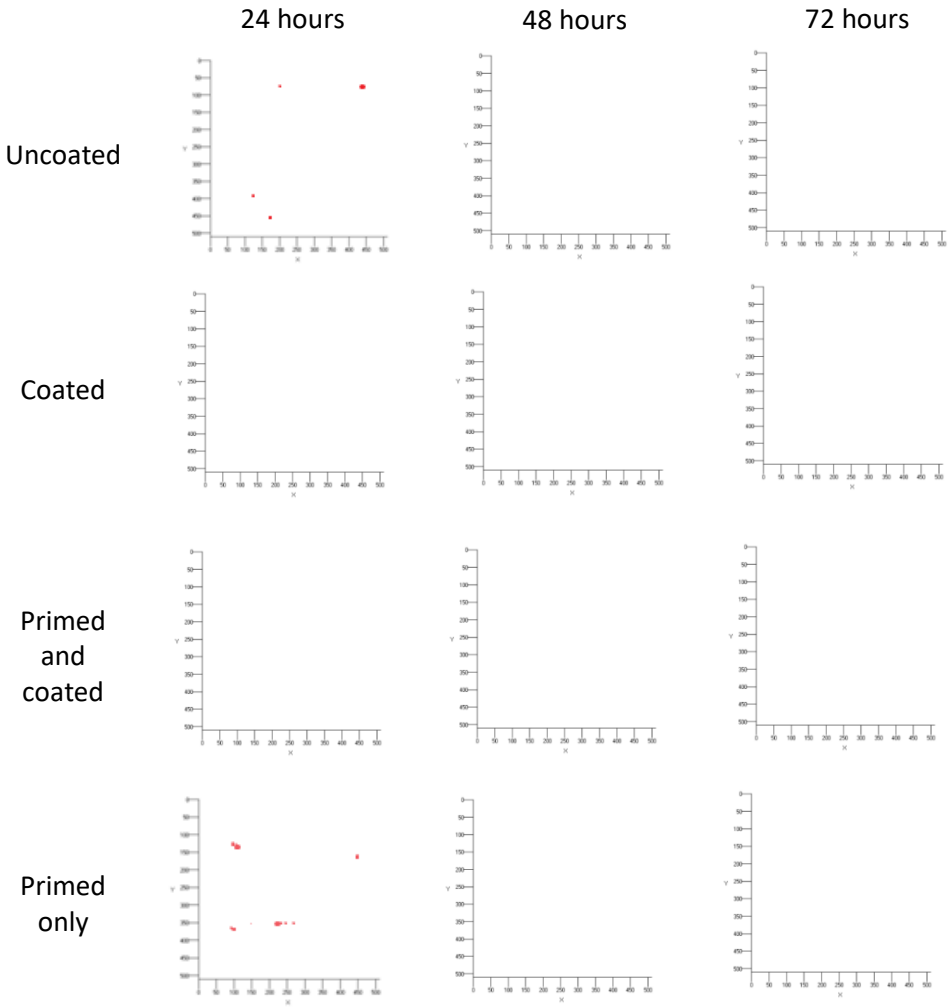


Figure 7.16. 2D CLSM images of *P. aeruginosa* biofilms, labelled with mCherry, on uncoated, polymer coated, primed and coated and primed only ETT tubes, at 24, 48 and 72 hours, in ASM G. Scale bars are 500 µm x 500 µm.

ASM G

Cuff:

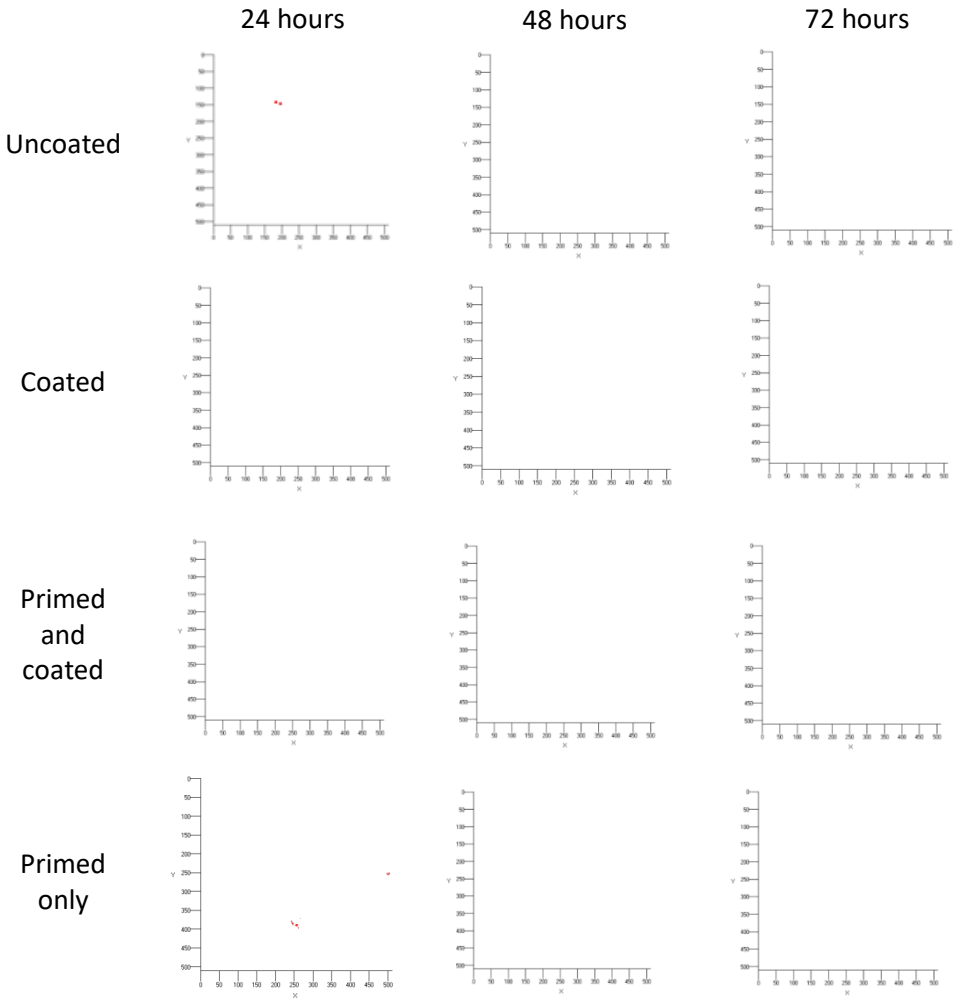


Figure 7.17. 2D CLSM images of *P. aeruginosa* biofilms, labelled with mCherry, on uncoated, polymer coated, primed and coated and primed only ETT cuffs, at 24, 48 and 72 hours, in ASM G. Scale bars are 500 µm x 500 µm.

ASM N

Tube:

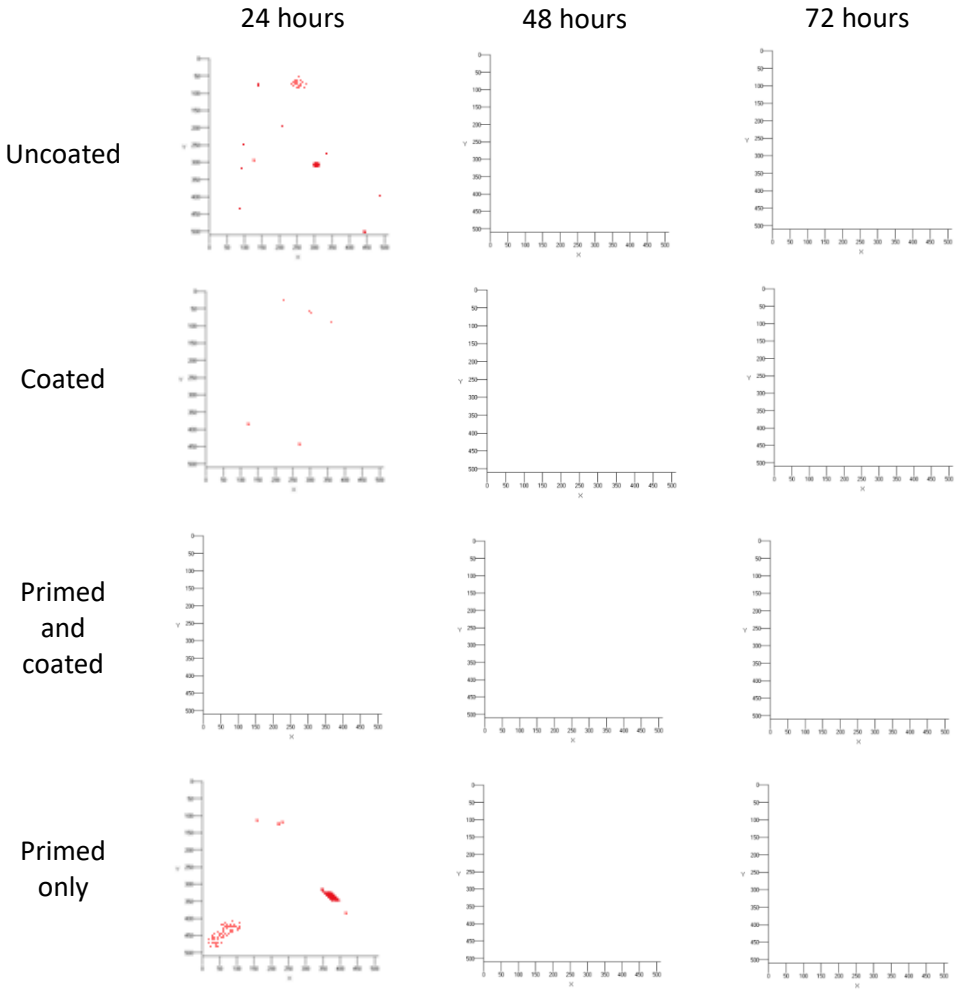


Figure 7.18. 2D CLSM images of *P. aeruginosa* biofilms, labelled with mCherry, on uncoated, polymer coated, primed and coated and primed only ETT tubes, at 24, 48 and 72 hours, in ASM N. Scale bars are 500 µm x 500 µm.

ASM N

Cuff:

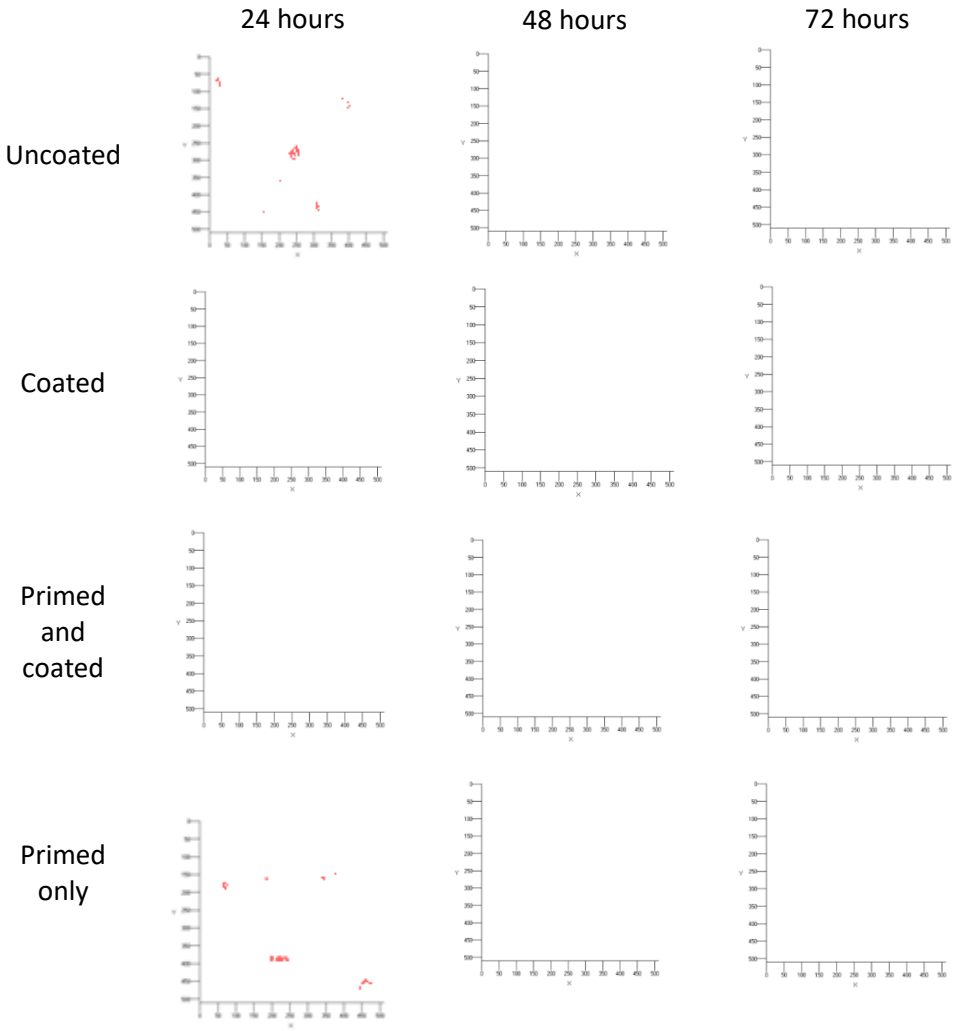


Figure 7.19. 2D CLSM images of *P. aeruginosa* biofilms, labelled with mCherry, on uncoated, polymer coated, primed and coated and primed only ETT cuffs, at 24, 48 and 72 hours, in ASM N. Scale bars are 500 µm x 500 µm.

7.6. Appendix F. Exponential relationship between the inverse biomass of *P. aeruginosa* biofilms and the wavelength shift of peak 2, from LPG OFS in the PTFE well and LPG OFS-ETT systems, in all three culture media.

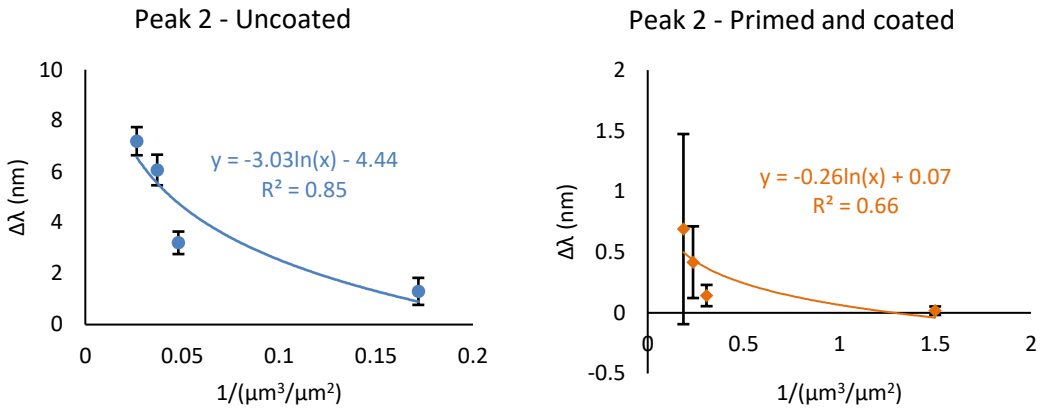


Figure 7.20. Exponential relationship between the inverse biomass of *P. aeruginosa* biofilms on U and PC LPG OFS and the wavelength shift of peak 2 from U and PC LPG OFS exposed to *P. aeruginosa* culture medium in RPMI-1640, for 24 hours. Error bars are ± SD of wavelength shift, N = 8. Line equations and R^2 are also displayed.

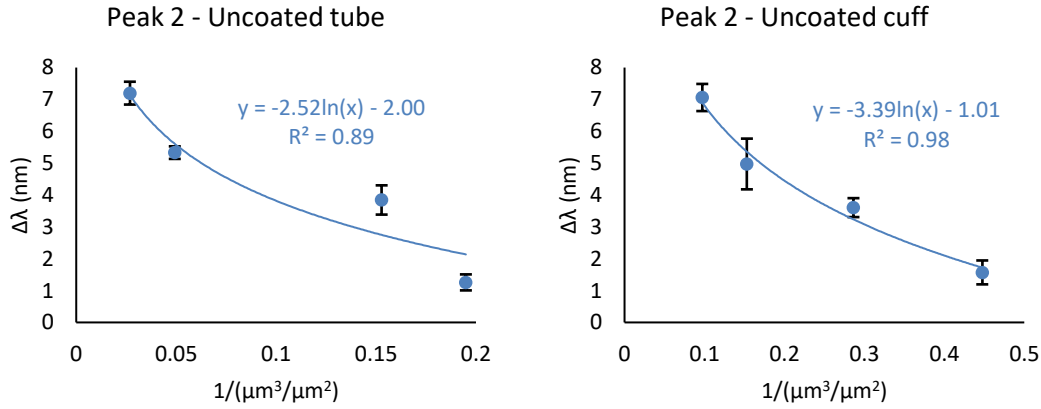


Figure 7.21. Exponential relationship between the inverse biomass of *P. aeruginosa* biofilms on U ETT tubes and cuffs and the wavelength shift of peak 2 from U LPG OFS-ETT systems exposed to *P. aeruginosa* culture medium in RPMI-1640, for 24 hours. Error bars are ± SD of wavelength shift, N = 3. Line equations and R^2 are also displayed.

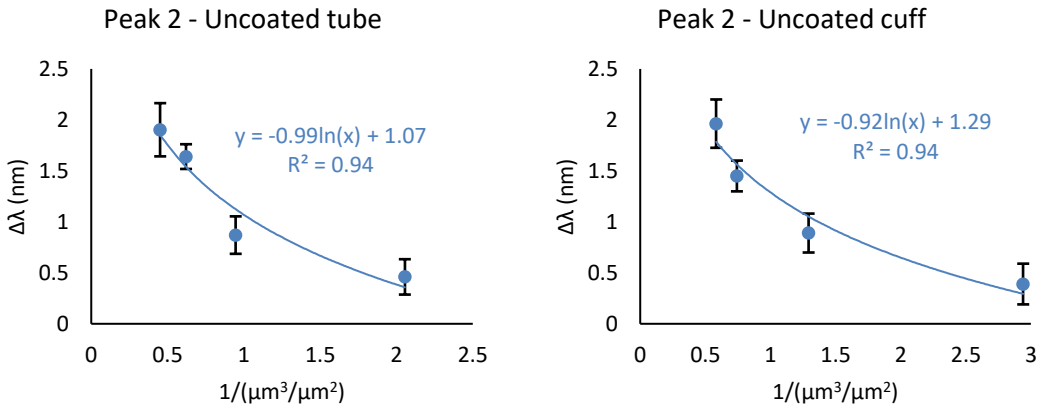


Figure 7.22. Exponential relationship between the inverse biomass of *P. aeruginosa* biofilms on U ETT tubes and cuffs and the wavelength shift of peak 2 from U LPG OFS-ETT systems exposed to *P. aeruginosa* culture medium in ASM G, for 24 hours. Error bars are ± SD of wavelength shift, N = 3. Line equations and R^2 are also displayed.

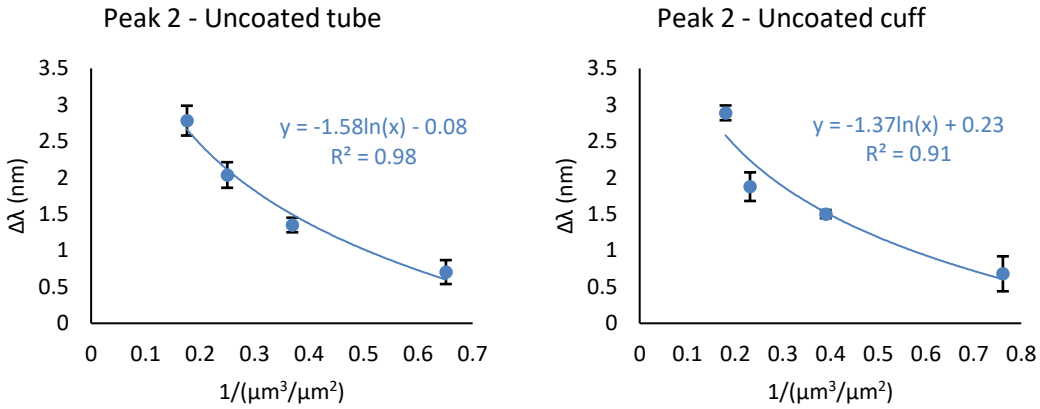
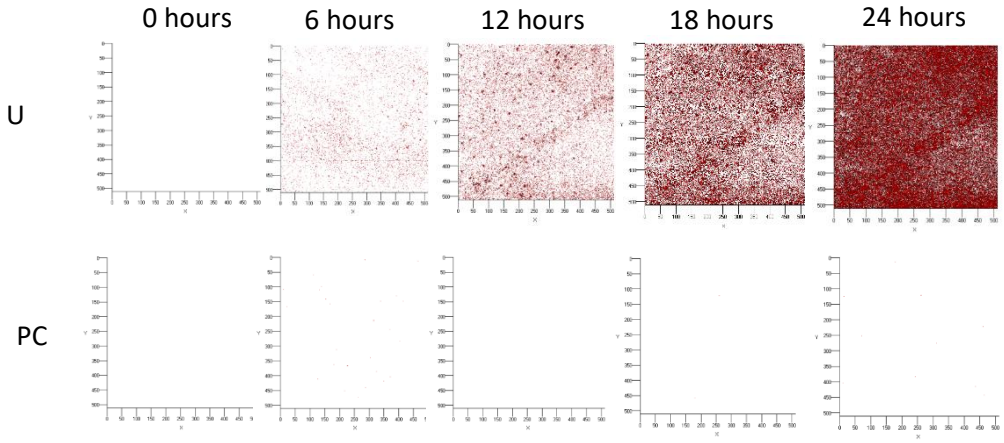


Figure 7.23. Exponential relationship between the inverse biomass of *P. aeruginosa* biofilms on U ETT tubes and cuffs and the wavelength shift of peak 2 from U LPG OFS-ETT systems exposed to *P. aeruginosa* culture medium in ASM N, for 24 hours. Error bars are ± SD of wavelength shift, N = 3. Line equations and R^2 are also displayed.

7.7. Appendix G. 2D CLSM images of *P. aeruginosa* (PA01-N) biofilms, labelled with mCherry, grown on U and PC ETT tubes and cuffs, in RPMI-1640, ASM G and ASM N.

RPMI-1640

Tube:



Cuff:

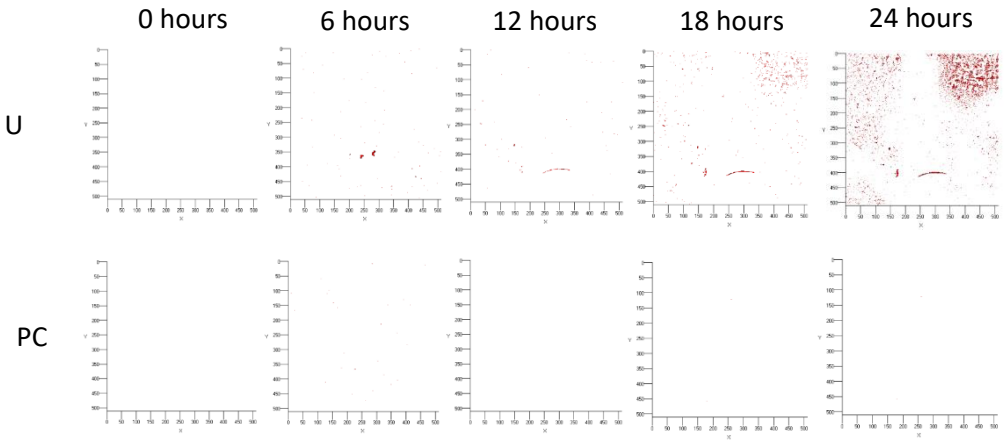
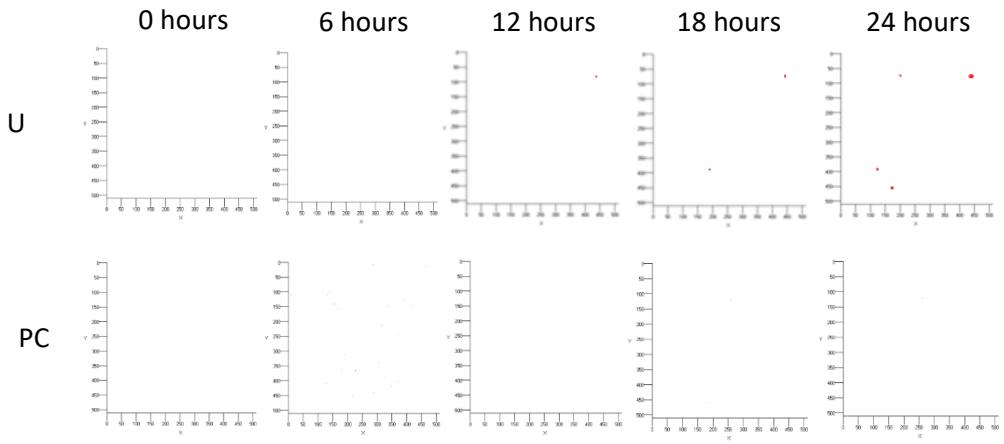


Figure 7.24. 2D CLSM images of *P. aeruginosa* (PA01-N) biofilms, labelled with mCherry, on U and PC ETT tubes and cuffs in RPMI-1640 medium, taken at 6 hour intervals for 24 hours. Scale bars are 500 µm x 500 µm.

ASM G

Tube:



Cuff:

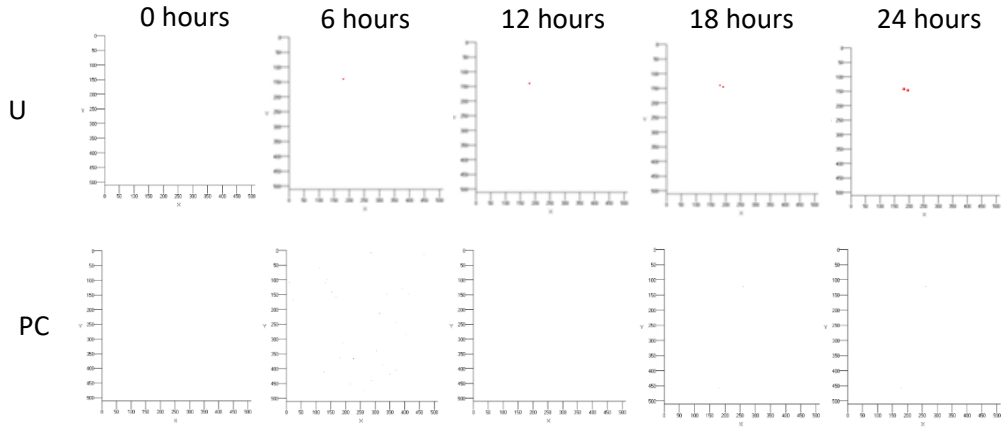
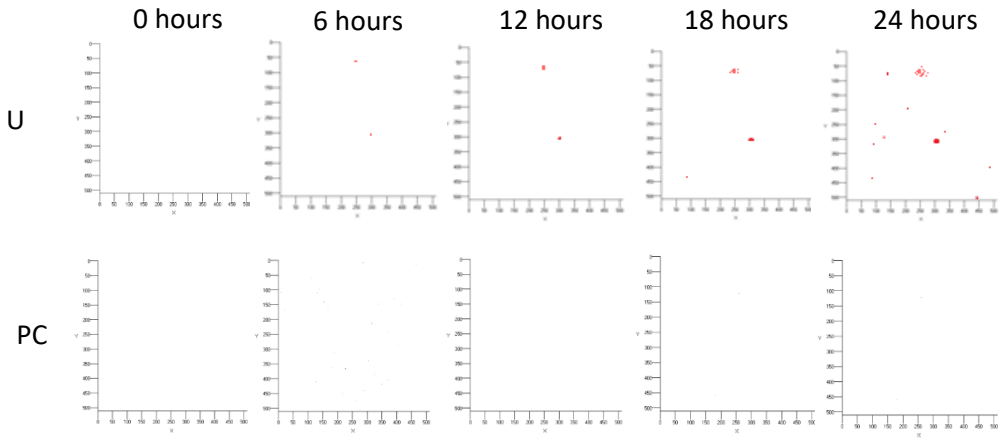


Figure 7.25. 2D CLSM images of *P. aeruginosa* (PA01-N) biofilms, labelled with mCherry, on U and PC ETT tubes and cuffs in ASM G, taken at 6 hour intervals for 24 hours. Scale bars are 500 µm x 500 µm.

ASM N

Tube:



Cuff:

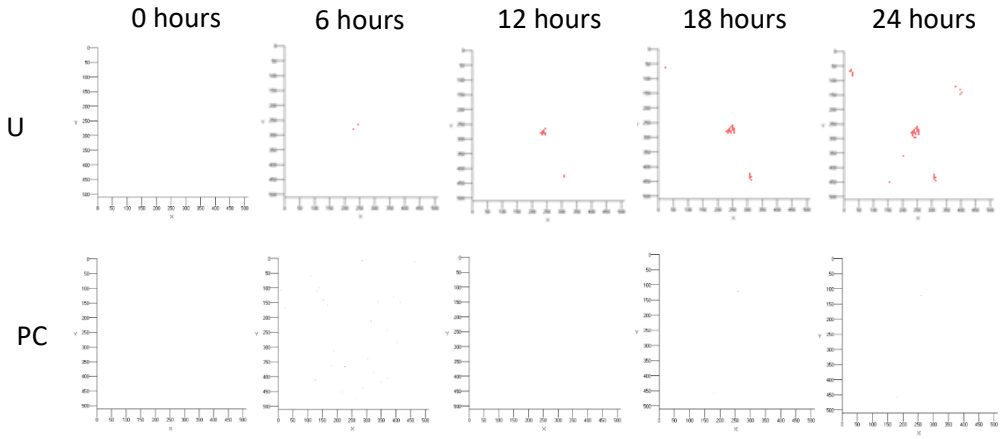


Figure 7.26. 2D CLSM images of *P. aeruginosa* (PA01-N) biofilms, labelled with mCherry, on U and PC ETT tubes and cuffs in ASM N, taken at 6 hour intervals for 24 hours. Scale bars are 500 µm x 500 µm.

7.8. Appendix H. Wavelength shifts of peak 2 for U and PC LPG OFS-ETT systems in RPMI-1640, ASM G and ASM N.

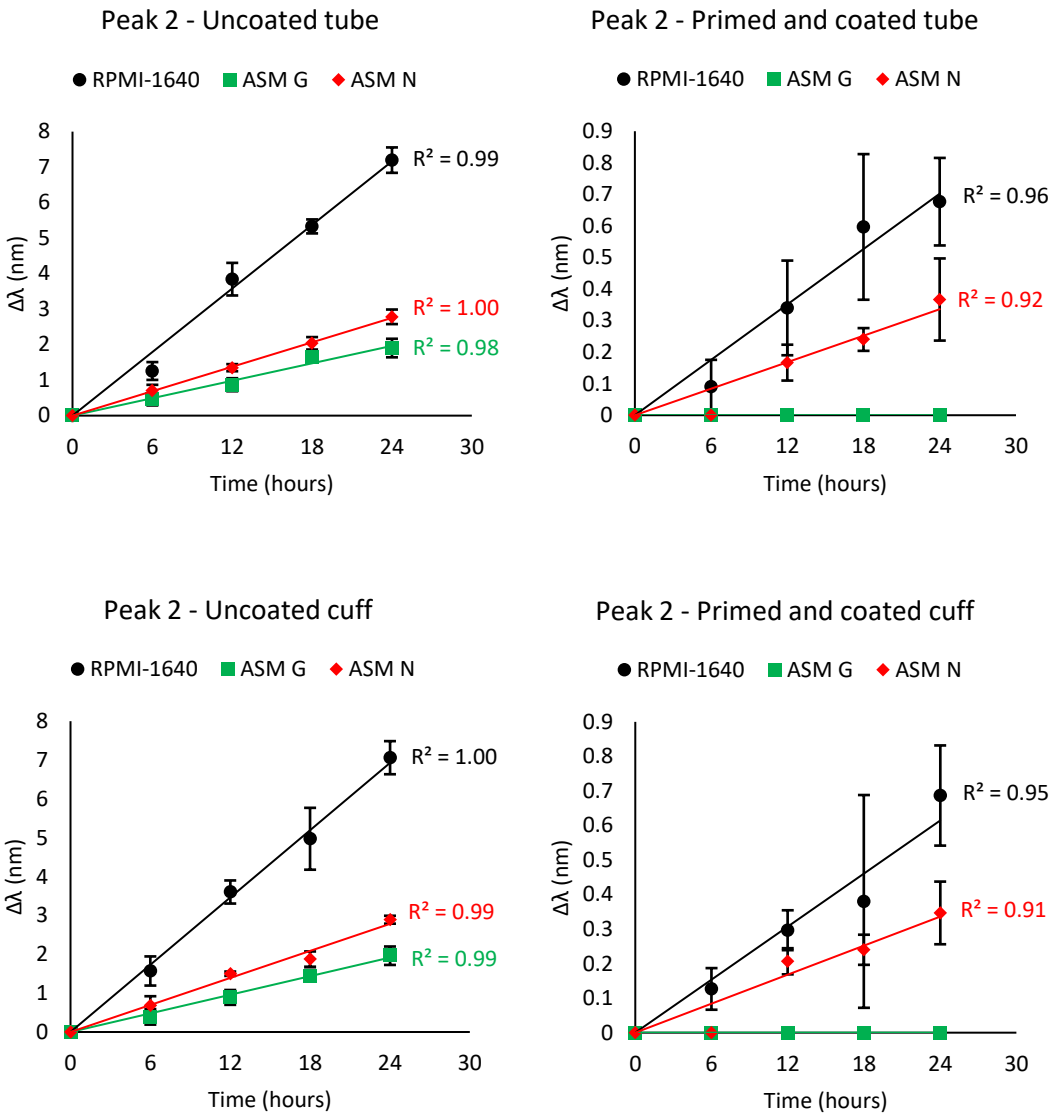


Figure 7.27. Wavelength shift profiles of attenuation peak 2 from U and PC LPG OFS-ETT systems exposed to *P. aeruginosa* culture in RPMI-1640, ASM G and ASM N. R^2 are displayed in labels of corresponding colours. Error bars are ± SD, N = 3.

7.9. Appendix I. MATLAB 2016a script used to determine 95% confidence ellipses for triplicate repeats of *P. aeruginosa*, *S. aureus* and Uropathogenic *E. coli* biomass on the nine photocured selective materials in the principle component score plot.

```
%% Use to generate PCA confidence ellipses
% By Andrew Hook 2016
% Requires set of XY coordinates as data1 double array, all replicates
% grouped together
% Outputs Output array with XY coordinates of ellipses, staggered every two
% columns
% Will run error_ellipse script

replicates = 3;
Loops = size(data1,1)/replicates;

for m=1:Loops
   clearvars -except data1 Output Loops m
   data(1:replicates,1:2) = data1((m-1)*replicates+1:(m-1)*replicates+replicates,1:2);
   error_ellipse
   r_ellipse(:,1)=r_ellipse(:,1) + X0;
   r_ellipse(:,2)=r_ellipse(:,2) + Y0;
   Output(1:100,1+(m-1)*2)=r_ellipse(1:100,1);
   Output(1:100,2+(m-1)*2)=r_ellipse(1:100,2);
end
close all
clearvars -except data1 Output
```

"data1" represents the principal component 1 and 2 scores, in triplicate, for the biomass of the three bacteria species on the nine photocured spots.

7.10. Appendix J. 2D CLSM images of *P. aeruginosa*, *S. aureus* and Uropathogenic *E. coli* on the nine photopolymerised materials with bacteria species selectivity.

Pseudomonas aeruginosa

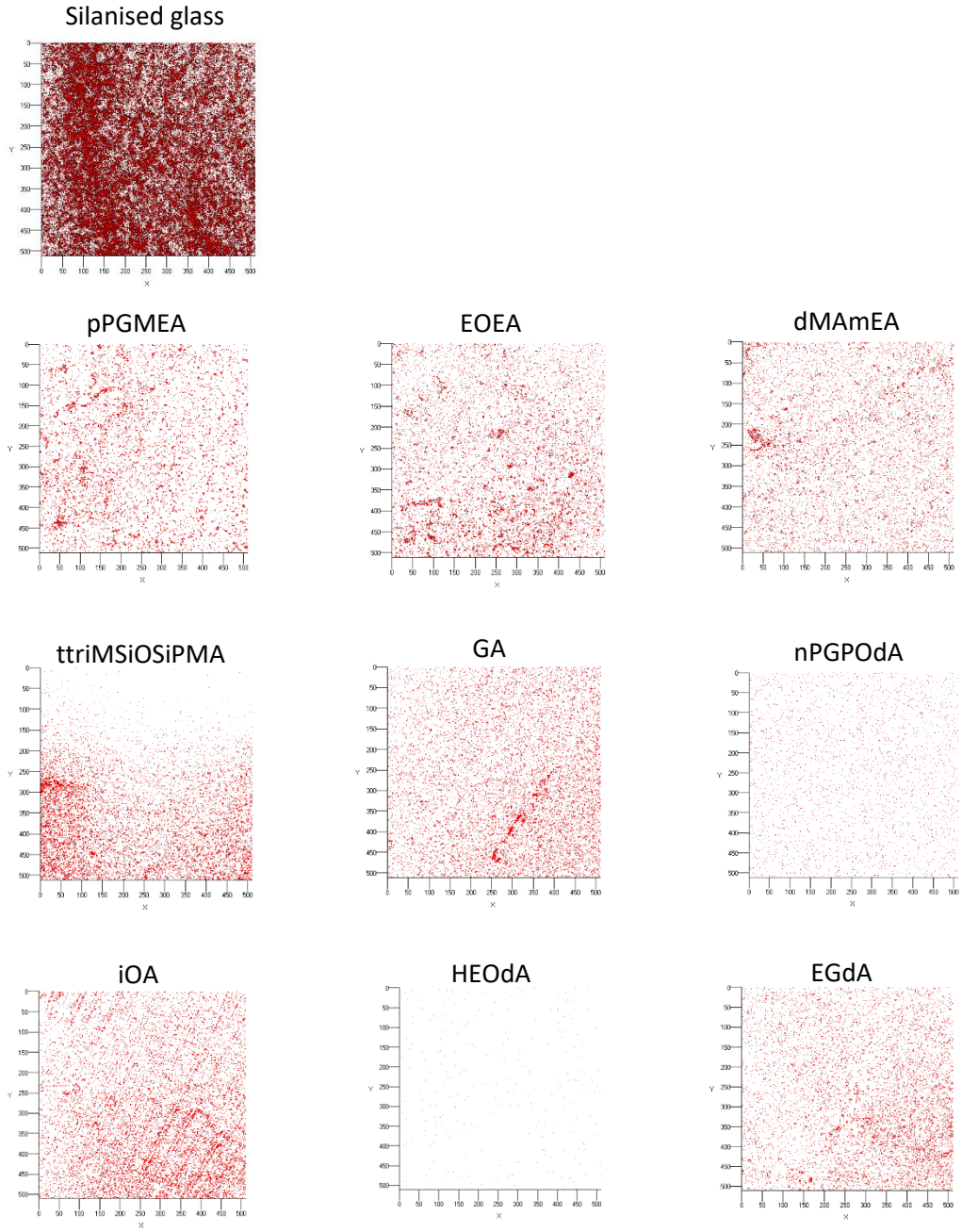


Figure 7.28. 2D CLSM images of *P. aeruginosa* biofilms, labelled with mCherry, on the nine photocured polymer spots, after a 24 hour incubation. The red areas represent biofilm. Scale bars are 500 µm x 500 µm.

Staphylococcus aureus

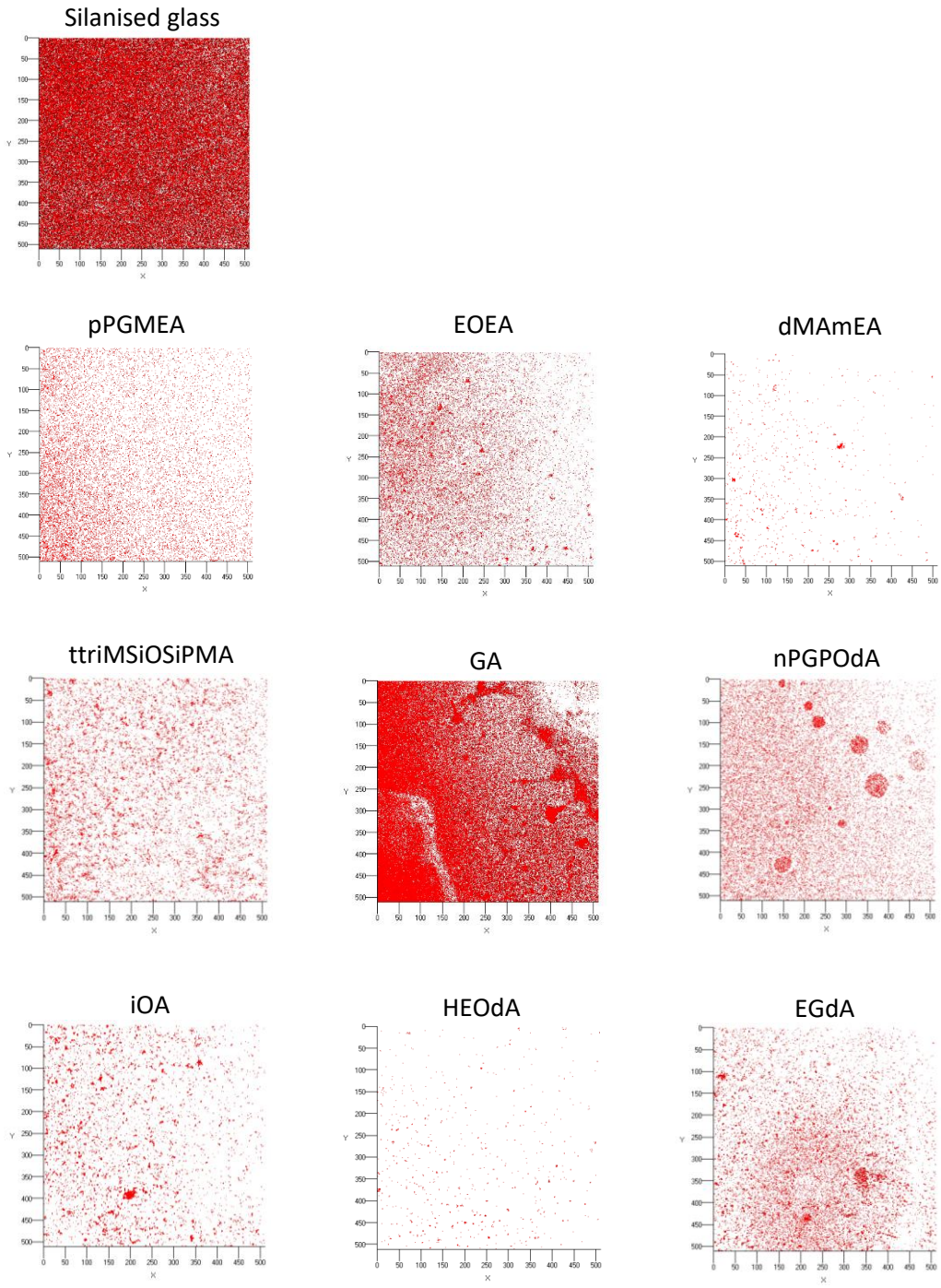


Figure 7.29. 2D CLSM images of *S. aureus* biofilms, stained with SYTO64, on the nine photocured polymer spots, after a 24 hour incubation. The red areas represent biofilm. Scale bars are 500 µm x 500 µm.

Uropathogenic *Escherichia coli*

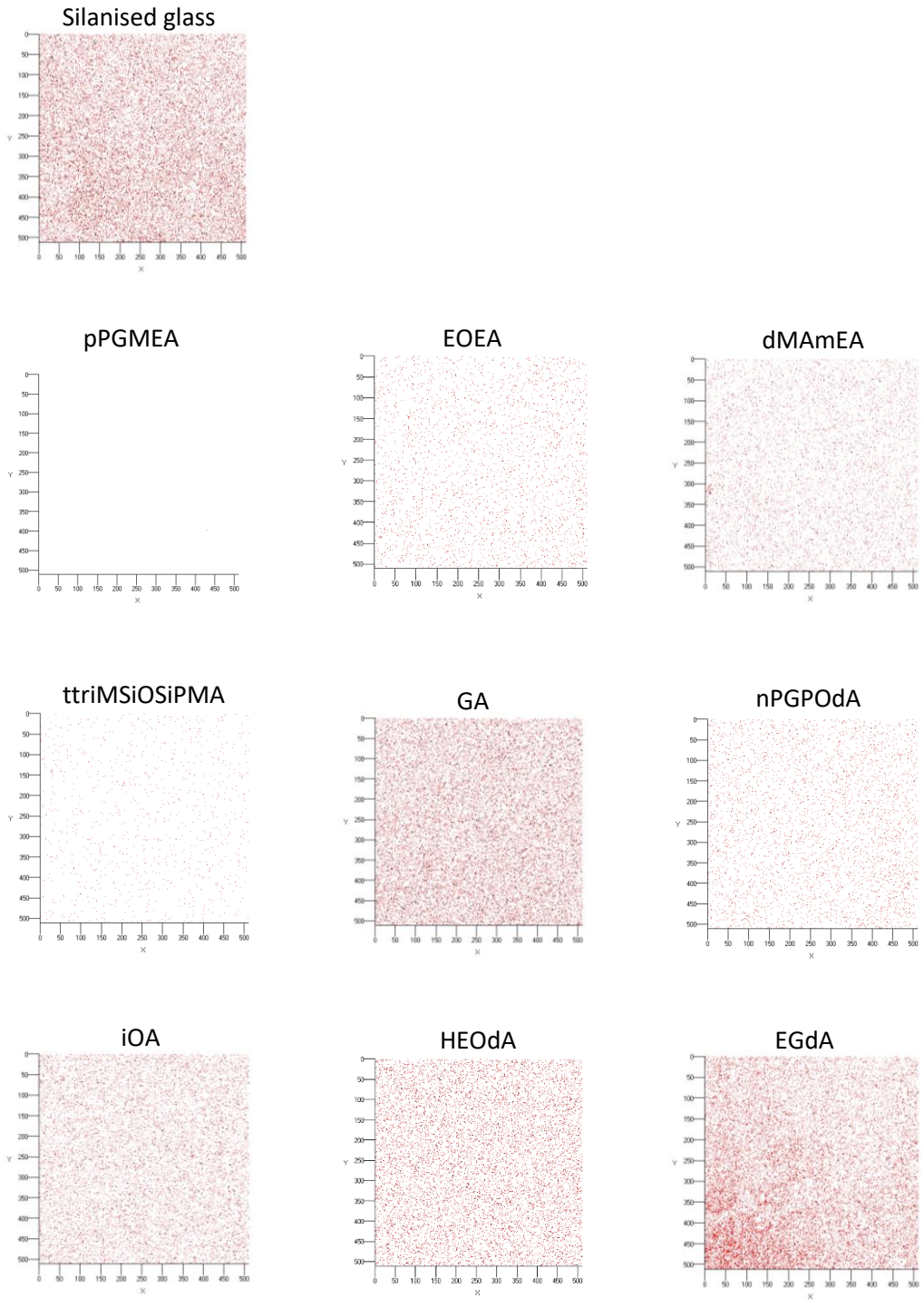


Figure 7.30. 2D CLSM images of Uropathogenic *E. coli* biofilms, labelled with Green Fluorescent Protein (GFP) on the nine photocured polymer spots, after a 24 hour incubation. The red areas represent biofilm. Scale bars are 500 µm x 500 µm.

7.11. Appendix K. ^{1}H NMR spectra of the three materials with bacteria species selectivity.

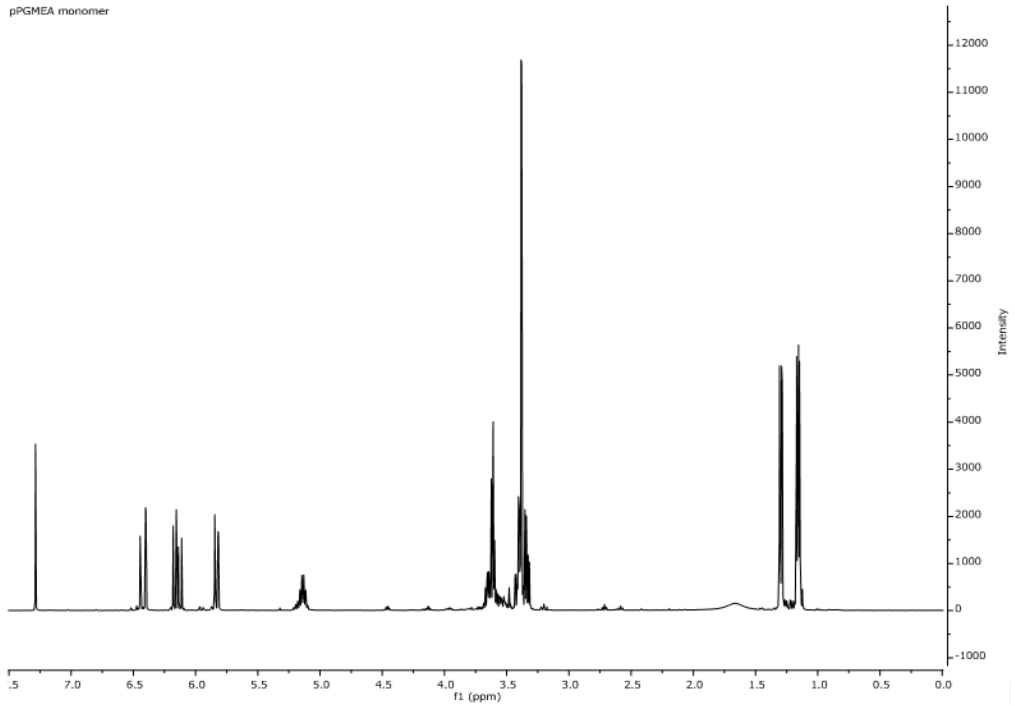


Figure 7.31. ^{1}H NMR spectrum of pPGMEA monomer, obtained at a spectrometer frequency of 400.3 MHz.

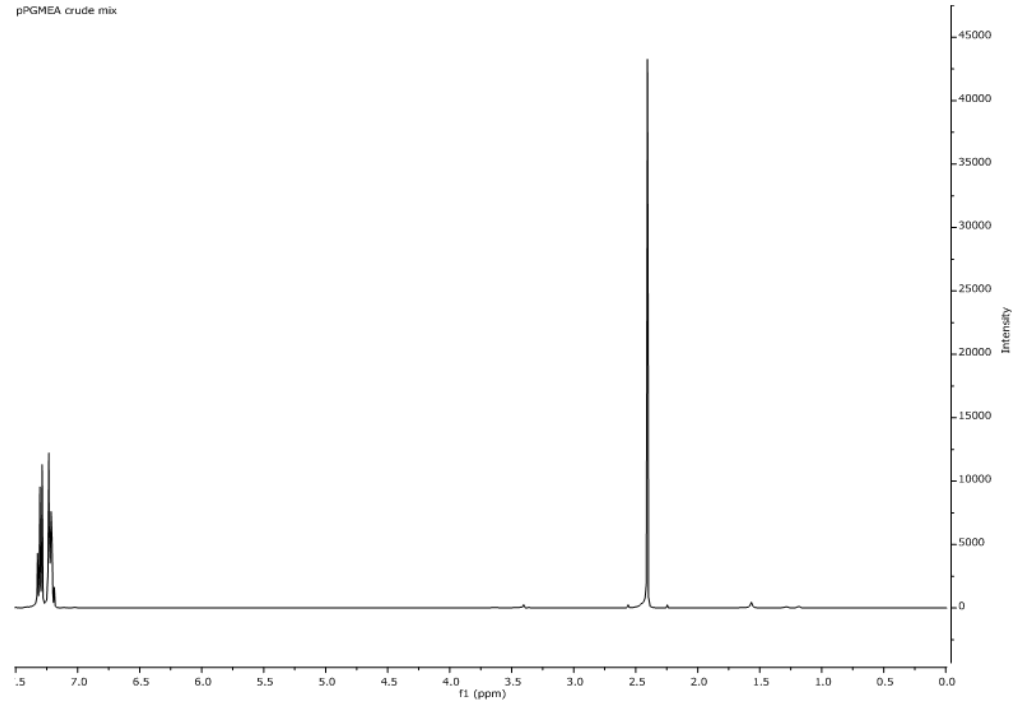


Figure 7.32. ^{1}H NMR spectrum of pPGMEA crude mix (before precipitation), obtained at a spectrometer frequency of 400.3 MHz.

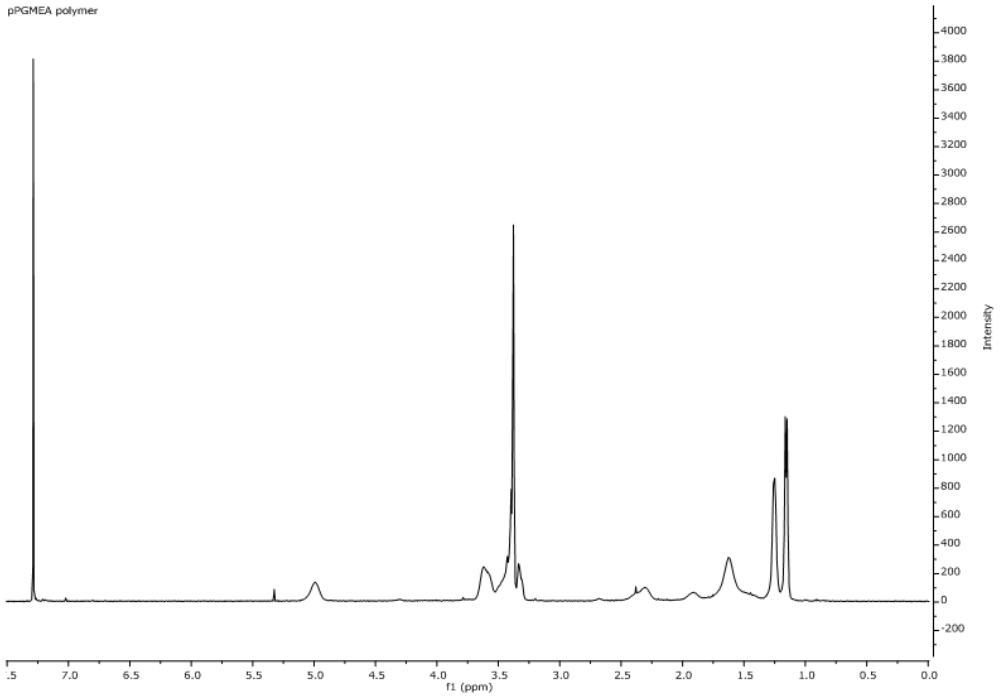


Figure 7.33. ^{1}H NMR spectrum of pPGMEA polymer (after precipitation), obtained at a spectrometer frequency of 400.3 MHz.

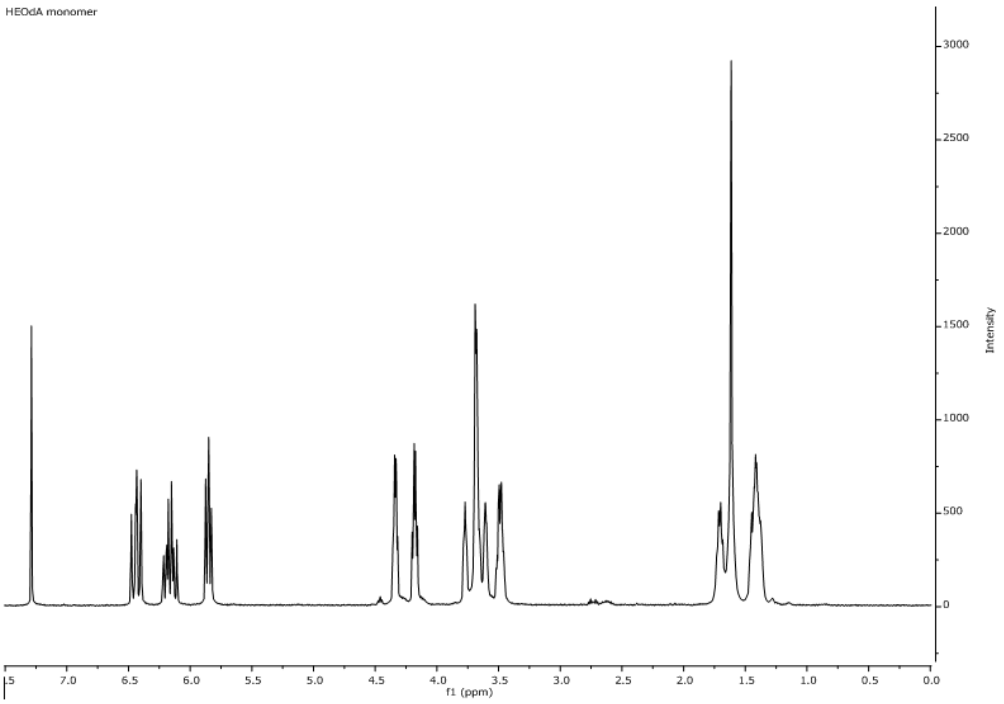


Figure 7.34. ^{1}H NMR spectrum of HEOdA monomer, obtained at a spectrometer frequency of 400.3 MHz.

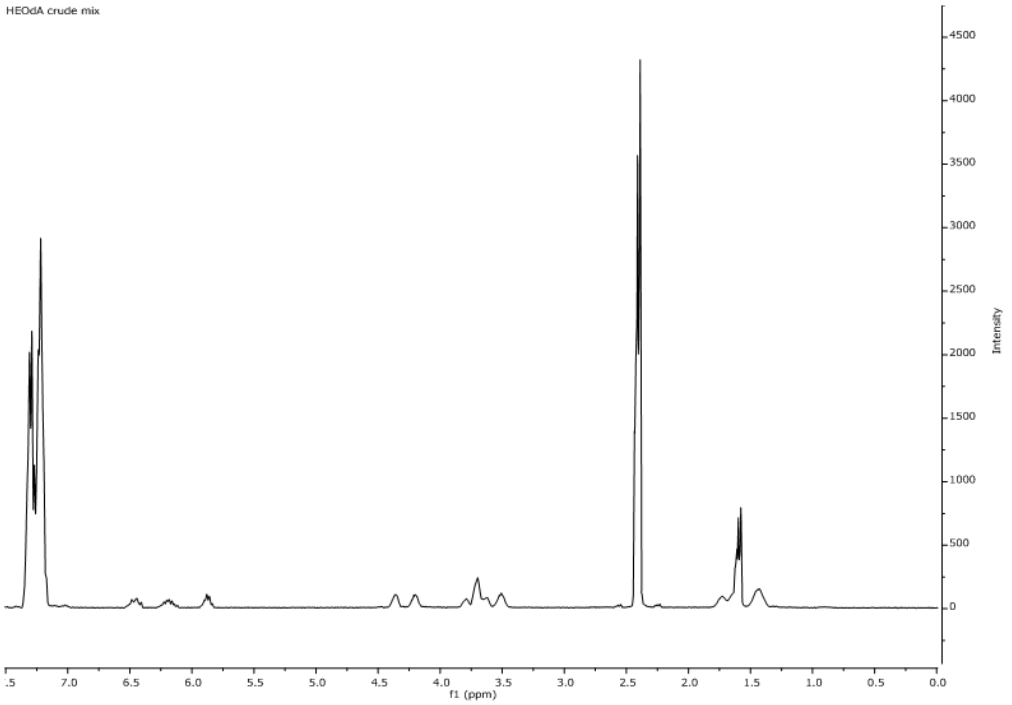


Figure 7.35. ^{1}H NMR spectrum of HEOdA crude mix (before precipitation), obtained at a spectrometer frequency of 400.3 MHz.

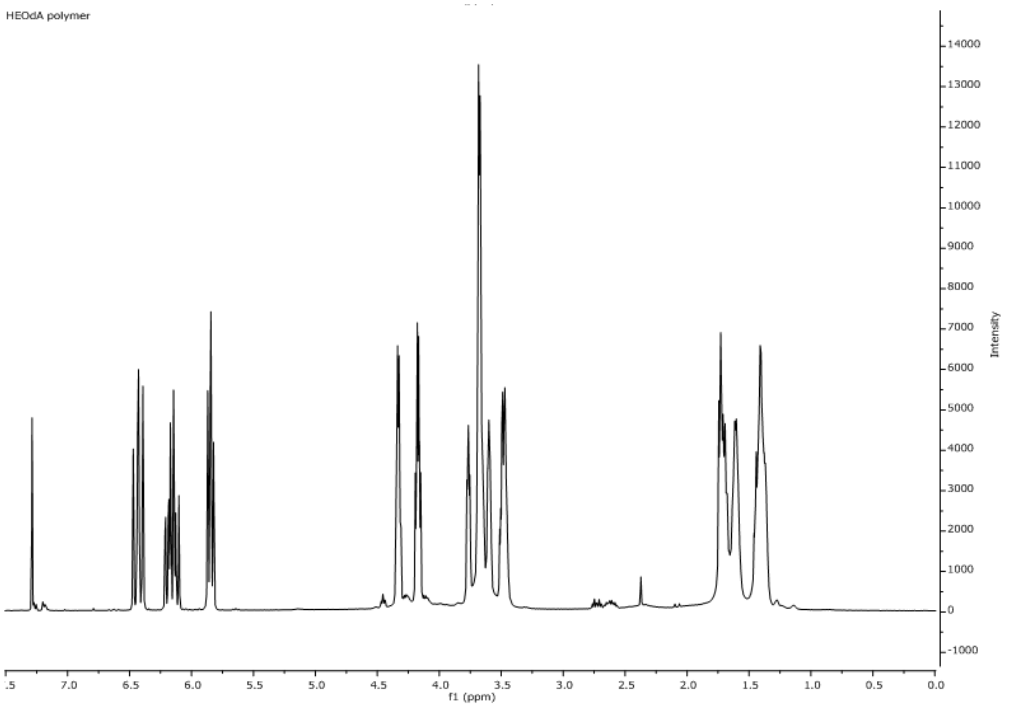


Figure 7.36. ^{1}H NMR spectrum of HEOdA polymer (after precipitation), obtained at a spectrometer frequency of 400.3 MHz.

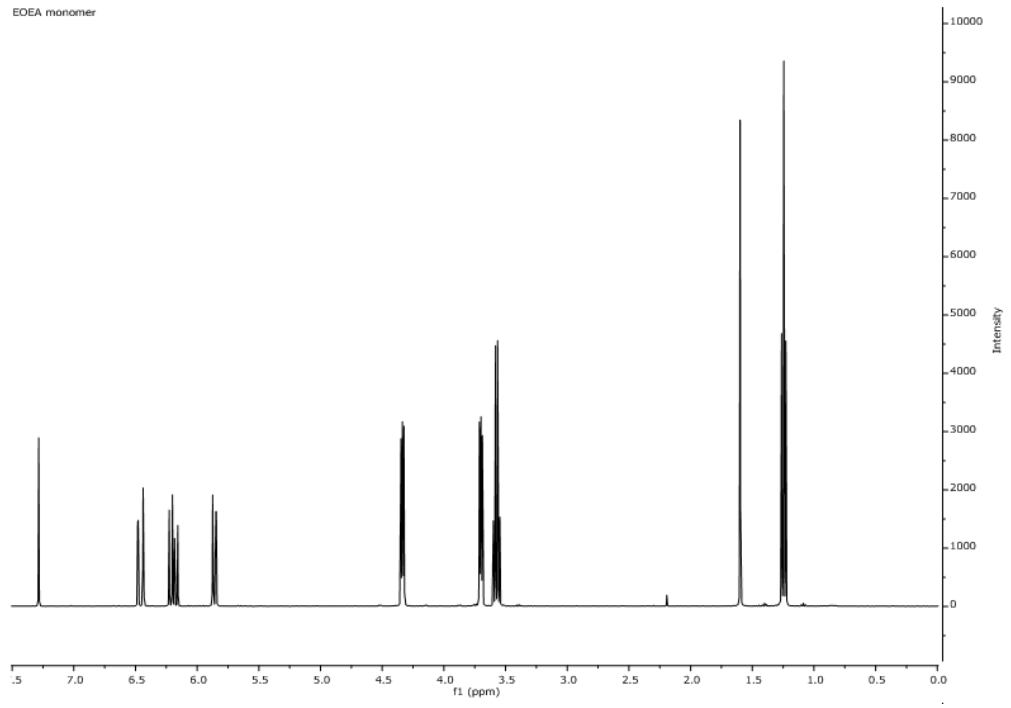


Figure 7.37. ^{1}H NMR spectrum of EOEA monomer, obtained at a spectrometer frequency of 400.3 MHz.

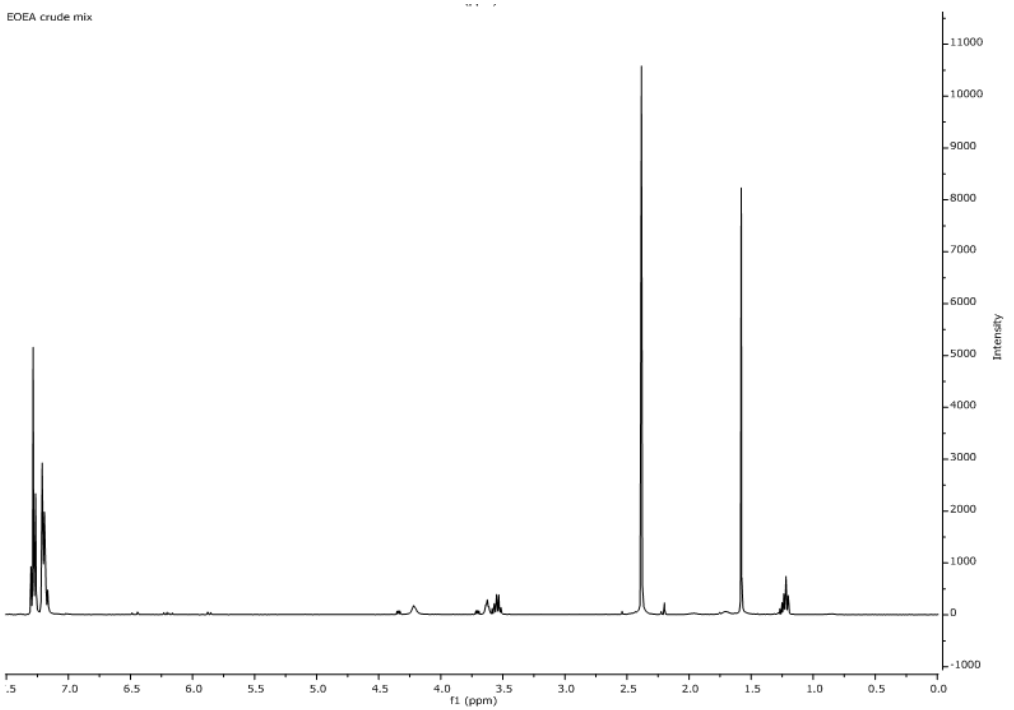


Figure 7.38. ^{1}H NMR spectrum of EOEA crude mix (before precipitation), obtained at a spectrometer frequency of 400.3 MHz.

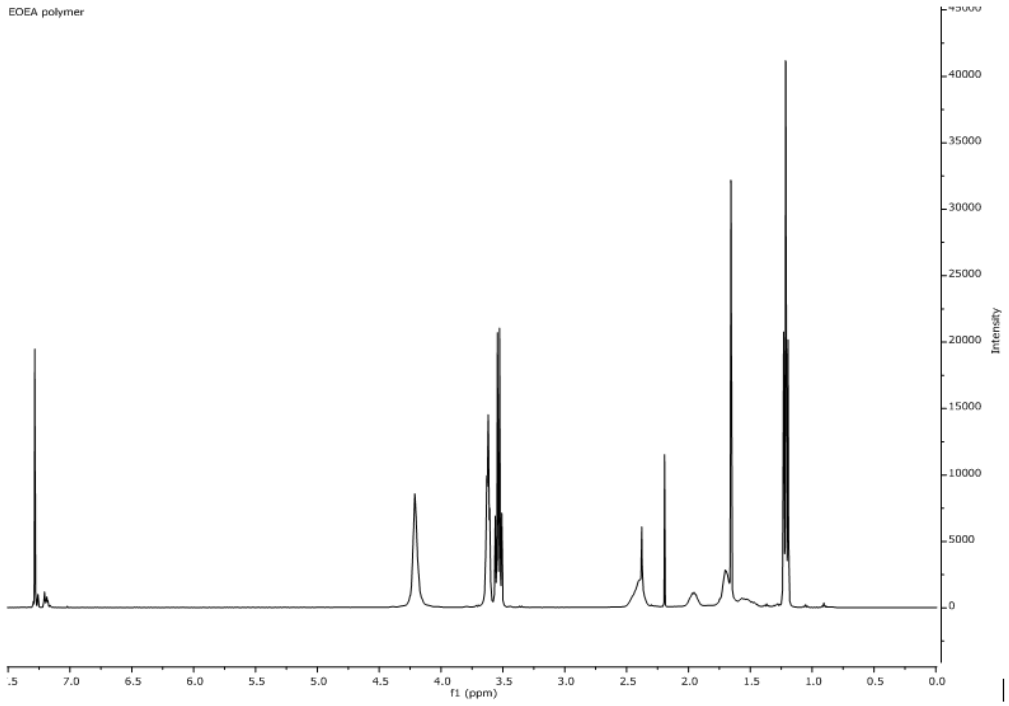


Figure 7.39. ^{1}H NMR spectrum of EOEA polymer (after precipitation), obtained at a spectrometer frequency of 400.3 MHz.

7.12. Appendix L. Wavelength shifts of peak 2 from LPG OFS coated with the three selective binding materials exposed to single cultures of the three bacteria species in RPMI-1640 medium.

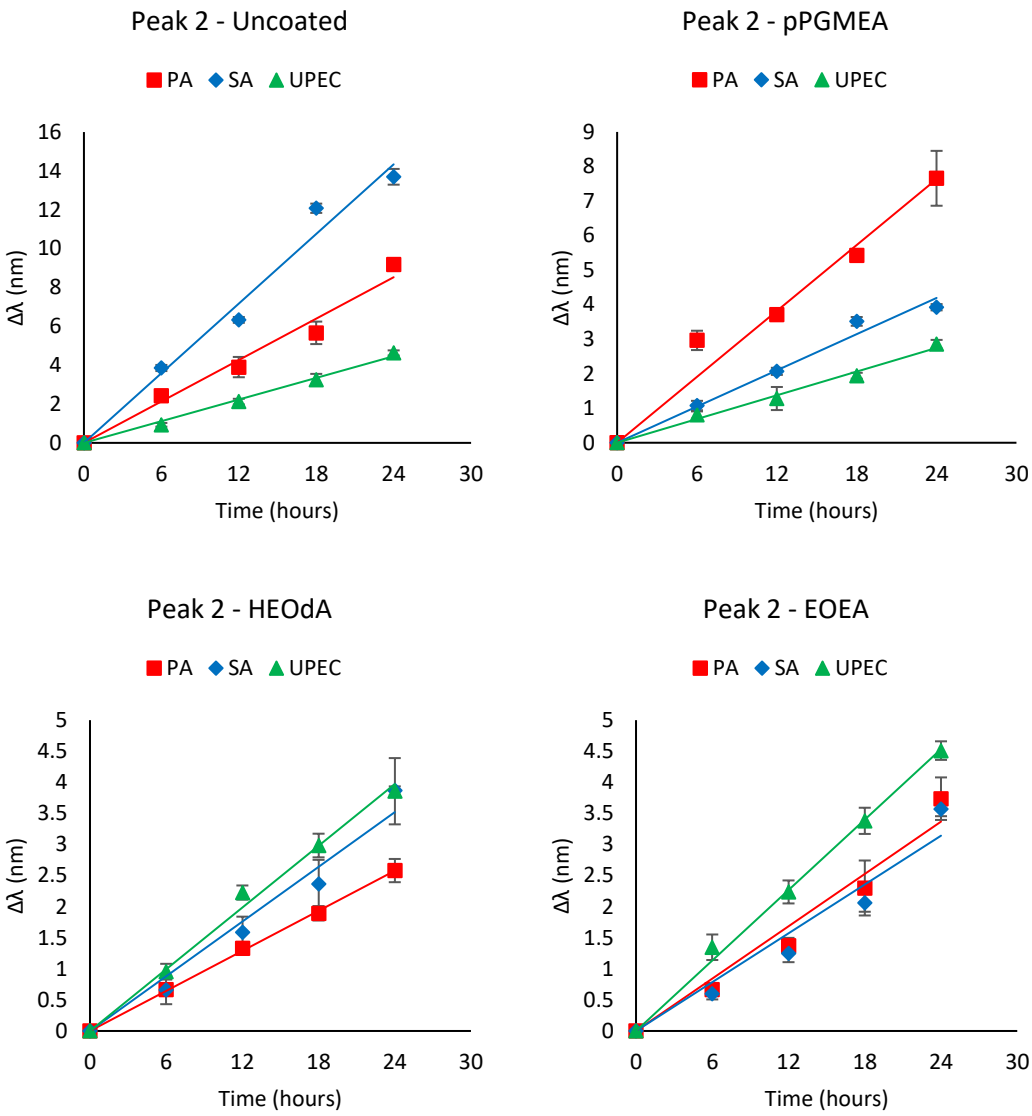


Figure 7.40. Wavelength shifts of peak 2 from each of the four modified LPG OFS immersed in single cultures of the three bacteria species in RPMI-1640 medium for 24 hours. PA = *P. aeruginosa*, SA = *S. aureus*, UPEC = Uropathogenic *E. coli*. Error bars are ± SD, N = 3.

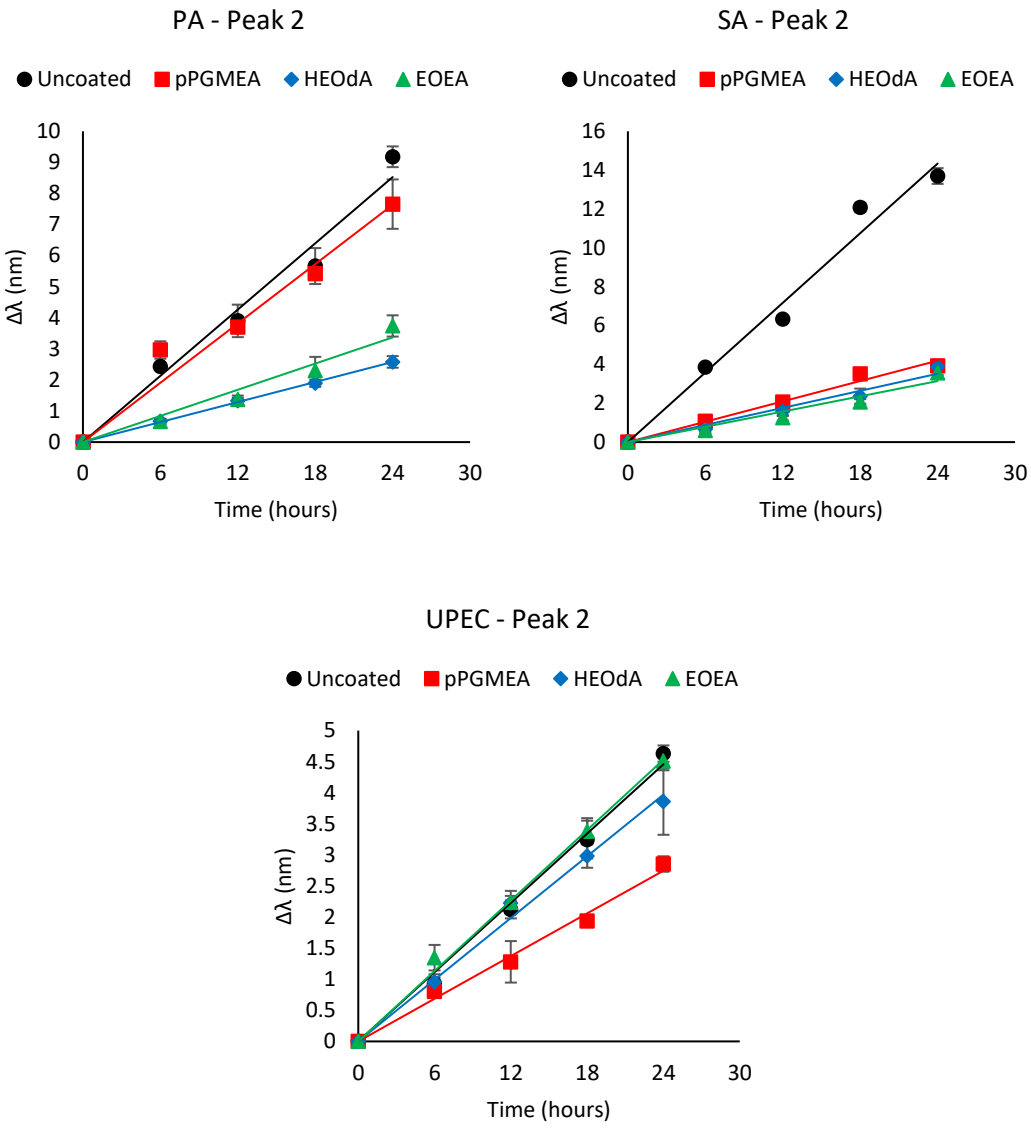


Figure 7.41. Wavelength shifts of peak 2 from the four modified LPG OFS exposed to single cultures of the three bacteria species in RPMI-1640 medium for 24 hours. PA = *P. aeruginosa*, SA = *S. aureus*, UPEC = Uropathogenic *E. coli*. Error bars are ± SD, N = 3.

8. References

1. Koenig SM and Truwit JD. Ventilator-Associated Pneumonia: Diagnosis, Treatment, and Prevention. *Clin Microbiol Rev* **19**, 637-657 (2006).
2. Kalanuria AA, Zai W and Mirski M. Ventilator-associated pneumonia in the ICU. *Crit Care* **18**, 208 (2014).
3. Chastre J, Fagon JY. Ventilator-associated pneumonia. *Am J Respir Crit Care Med* **165**, 867-903 (2002).
4. Yu FTS and Shizhuo Y. Fibre Optic Sensors. *Marcel Decker Inc.*, New York (2002).
5. Fair RJ and Tor Y. Antibiotics and Bacterial Resistance in the 21st Century. *Perspect Medicin Chem* **6**, 25-64 (2014).
6. Margolis GS. Paramedic: Airway Management. *Jones and Bartlett*, Sudbury (2004).
7. Hasan A. Understanding Mechanical Ventilation – A Practical Handbook. *Springer*, London (2010).
8. Freeman BS and Berger JS. Anesthesiology Core Review. *McGraw Hill Education*, Washington DC (2014).
9. Beebe RWO and Funk DL. Fundamentals of Emergency Care Volume 1. *Delmar*, Albany (2001).
10. Fonseca L, Vieira FN and Azzolin KO. Factors associated to the length of time on mechanical ventilation in the postoperative period of cardiac surgery. *Rev Gaucha Enferm* **35**, 67-72 (2014).
11. Masoudifar M, Aghadavoudi O and Nasrollahi L. Correlation between timing of tracheostomy and duration of mechanical ventilation in patients with potentially normal lungs admitted to intensive care unit. *Adv Biomed Res* **1**, 25 (2012).
12. Blot SI, Rello J and Koulenti D. The value of polyurethane-cuffed endotracheal tubes to reduce microaspiration and intubation-related pneumonia: a systematic review of laboratory and clinical studies. *Crit Care* **20,** 203 (2016).
13. Haas CF, Eakin RM Konkle MA and Blank R. Endotracheal Tubes: Old and New. *Respiratory Care* **59**, 933-955 (2014).
14. Douroumis D. Hot-Melt Extrusion Pharmaceutical Applications. *Wiley*, Kent (2012).
15. Rosato DV. Extruding Plastics: A practical processing handbook. *Springer*, Chatham (2013).
16. Morton WJ, Muller CT, Goodwin N, Wilkes AR and Hall JE. Investigation of phthalate release from tracheal tubes. *Anaesthesia* **68**, 377-381 (2013).
17. Spiegel JE. Endotracheal Tube Cuffs: Design and Function. *Anesthesiology News, McMahon Publishing* (2010).
18. Costerton JW, Lewandowski Z, Caldwell DE, Korber DR and Lappin-Scott HM. Microbial biofilms. *Annu Rev Microbiol* **49**, 711-745 (1995).
19. Donlan RM. Biofilms: Microbial Life on Surfaces. *Emerg Infect Dis* **8**, 881-890 (2002).

20. Mah TF, Pitts B, Pellock B, Walker GC, Stewart PS *et al*. A genetic basis for Pseudomonas aeruginosa biofilm antibiotic resistance. *Nature* **426**, 306-310 (2003).
21. Costerton JW, Geesey GG and Cheng KJ. How bacteria stick. *Sci Am* **238**, 86–95 (1978).
22. Orgad O, Oren Y, Walker SL and Herzberg M. The role of alginate in Pseudomonas aeruginosa EPS adherence, viscoelastic properties and cell attachment. *Biofouling* **27**, 787-798 (2011).
23. Rasamiravaka T, Labtani Q, Duez P and El Jaziri M. The Formation of Biofilms by *Pseudomonas aeruginosa*: A Review of the Natural and Synthetic Compounds Interfering with Control Mechanisms. *Biomed Research International* **2015**, 1-17 (2015).
24. Archer NK, Mazaitis MJ, Costerton JW, Leid JG, Powers ME *et al*. *Staphylococcus aureus* biofilms; Properties, regulation and roles in human disease. *Virulence* **2**, 445-459 (2011).
25. Davies CE, Hill KE, Wilson MJ, Stephens P, Hill CM *et al*. Use of 16S ribosomal DNA PCR and denaturing gradient gel electrophoresis for analysis of the microfloras of healing and nonhealing chronic venous leg ulcers. *J Clin Microbiol* **42**, 3549–3557 (2004).
26. Bjarnsholt T. The role of bacterial biofilms in chronic infections. *APMIS Suppl* **136**, 1-51 (2013).
27. Sanders R. Discovery opens door to attacking biofilms that cause chronic infections. *UC Berkeley News* (2012).
28. Talsma SS. Biofilms on medical devices. *Home Healthc Nurse* **25**, 589-594 (2007).
29. Percival SL, Suleman L, Vuotto C and Donelli G. Healthcare-associated infections, medical devices and biofilms: risk, tolerance and control. *J Med Microbiol* **64**, 323-334 (2015).
30. Esposito S, Purello SM, Bonnet E, Novelli A, Tripodi *et al*. Central venous catheter-related biofilm infections: An up-to-date focus on meticillin-resistant *Staphylococcus aureus*. **1**, 71-78 (2013).
31. De Souza PR, De Andrade D, Cabral DB and Watanabe E. Endotracheal tube biofilm and ventilator-associated pneumonia with mechanical ventilation. *Microsc Res Tech* **77**, 305-312 (2014).
32. Hoiby N, Bjarnsholt T Givskov M, Molin S and Ciofu. Antibiotic resistance of bacterial biofilms. *Int J Antimicrob Agent* **35**, 322-332 (2010).
33. Stewart PS. Mechanisms of antibiotic resistance in bacterial biofilms. *Int J Med Microbiol* **292**, 107-13 (2002).
34. Sauer K, Camper AK, Ehrlich GD, Costerton JW and Davies DG. *Pseudomonas aeruginosa* displays multiple phenotypes during development as a biofilm. *J Bacteriol* **184**, 1140-1154 (2002).
35. Donelli G, De Paoli P, Fadda G, Marone P, Nicoletti G *et al*. A Multicenter Study on Central Venous Cather-Associated Infections in Italy. *Journal of Chemotherapy* **13**, 251-262 (2013).
36. Bruinsma GM, van der Mei HC and Busscher HJ. Bacterial adhesion to surface hydrophilic and hydrophobic contact lenses. *Biomaterials* **22**, 3217-3224 (2001).

37. Klemm P and Schembri MA. Bacterial adhesins: function and structure. *Int J Med Microbiol* **290**, 27-35 (2000).
38. Keizer DW, Slupsky CM, Kalisiak M, Campbell AP, Crump MP *et al.* Structure of a Pilin Monomer from *Pseudomonas aeruginosa*. Implications for the assembly of pili. *Journal of biological chemistry* **276**, 24186-24193 (2001).
39. Proft T and Baker N. Pili in Gram-negative and Gram-positive bacteria – structure, assembly and their role in disease. *Cell Mol Life Sci* **66**, 613-635 (2009).
40. Mulvey MA. Adhesion and entry of uropathogenic *Escherichia coli*. *Cellular Microbiology* **4**, 257-271 (2002).
41. Kaplan JB. Biofilm dispersion. *J Dent Res* **89**, 205-218 (2010).
42. Oliveira M, Nunes SF, Carneiro C, Bexiga R, Bernardo F *et al.* Time course of biofilm formation by Staphylococcus aureus and Staphylococcus epidermidis mastitis isolates. *Vet Microbiol* **124**, 187-191 (2007).
43. Balcazar JL, Subirats J and Borrego CM. The role of biofilms as environmental reservoirs of antibiotic resistance. *Front Microbiol* **6**, 1216 (2015).
44. Nosanchuk JD, Lin J, Hunter RP and Aminov RI. Low-dose antibiotics: current status and outlook for the future. *Front Microbiol* **5**, 478 (2014).
45. Rutherford ST and Bassler BL. Bacterial Quorum Sensing: Its role in Virulence and Possibilities for Its Control. *Cold Spring Harb Perspect Med* **2**, 1-25 (2012).
46. Skindersoe ME, Alhede M, Phipps R, Yang L, Jensen PO *et al*. Effects of Antibiotics on Quorum Sensing in *Pseudomonas aeruginosa*. *Antimicrob Agents Chemother* **52**, 3648-3663 (2008).
47. Daehnel K, Harris R, Maddera L and Silverman P. Fluorescence assays for F-pili and their application. *Microbiology* **151**, 3541-3548 (2005).
48. Lee J and Zhang L. The hierarchy quorum sensing network in *Pseudomonas aeruginosa*. *Protein Cell* **6**, 26-41 (2015).
49. Ren CL, Konstan MW, Yegin A, Rasouliyan L, Trzaskoma B *et al*. Multiple antibiotic resistant Pseudomonas aeruginosa and lung infection decline in patients with cystic fibrosis. *J Cyst Fibros* **11**, 293-299 (2012).
50. Smith DJ, Ramsay KA, Yerkovich ST, Reid DW, Wainwright CE *et al*. Pseudomonas aeruginosa antibiotic resistance in Australian cystic fibrosis centres. *Respirology* **21**, 329-337 (2016).
51. Liu R, Zhu J, Yu Z, Joshi D, Zhang H *et al*. Molecular analysis of long-term biofilm formation on PVC and cast iron surfaces in drinking water distribution system. *J Environ Sci (China)* **26**, 865-874 (2014).
52. Sottile FD, Marrie TJ, Prough DS, Hobgood CD, Gower DJ *et al.* Nosocomial pulmonary infection: possible etiologic significance of bacterial adhesion to endotracheal tubes. *Crit Care Med* **14**, 265-270 (1986).
53. Inglis TJ, Millar MR, Jones JG and Robinson DA. Tracheal tube biofilm as a source of bacterial colonization of the lung. *J Clin Microbiol* **27**, 2014-2018 (1989).
54. Bauer TT, Torres A, Ferrer R, Heyer CM, Schultze-Werninghaus G *et al.* Biofilm formation in endotracheal tubes. Association between pneumonia and the persistence of pathogens, *Monaldi Arch Chest Dis* **57,** 84-87 (2002).

55. Hamilton VA and Grap MJ. The role of the endotracheal tube cuff in microaspiration. *Heart Lung* **41** (2012).
56. Koerner RJ. Contribution of endotracheal tubes in the pathogenesis of ventilator-associated pneumonia. *Journal of Hospital Infection* **2**, 83-89 (1997).
57. Gil-Perotin S, Ramirez P, Marti V, Sahuquillo JM, Gonzalez E *et al*. Implications of endotracheal tube biofilm in ventilator-associated pneumonia response: a state of concept. *Crit Care* **16**, 1-8 (2012).
58. Afshari A, Pagani L and Harbarth S. Year in review 2011: Critical Care – infection. *Crit Care* **16**, 242-247 (2012).
59. Mangram AJ, Sohn J, Zhou N, Hollingworth AK, Ali-Osman FR *et al*. Trauma-associated pneumonia: time to redefine ventilator-associated pneumonia in trauma patients. *The American Journal of Surgery* **210**, 1056-1062 (2015).
60. Weinstein RA, Bonten MJM, Kollef MH and Hall JB. Risk Factors for Ventilator-Associated Pneumonia: From Epidemiology to Patient Management. *Clinical Infectious Diseases* **38**, 1141-1149 (2004).
61. Cook DJ, Walter SD, Cook RJ, Griffith LE, Guyatt GH *et al*. Incidence of and risk factors for ventilator-associated pneumonia in critically ill patients. *Ann Intern Med* **129**, 433-440 (1998).
62. Beck-Sague CM, Sinkowitz RL, Chinn RY, Vargo J, Kaler W *et al*. Risk factors for ventilator-associated pneumonia in surgical intensive-care-unit patients. *Infect Control Hosp Epidemiol* **17**, 374-376 (1994).
63. Elastrous S, Boujdaria R and Merghili S. Incidence and risk factors of ventilator –associated pneumonia: a one-year prospective study. *Clin Intensive Care* **7**, 276-281 (1996).
64. American Thoracic Society, Infectious Diseases Society of America. Guidelines for the management of adults with hospital-acquired, ventilator-associated, and healthcare-associated pneumonia. *Am J Respir Crit Care Med* **171**,388–416 (2005).
65. Harrison D. Number of mechanically ventilated patients during 2012. *Intensive Care National Audit and Research Centre (ICNARC),* London, (Copyright ICNARC 2014).
66. Heredia-Rodriguez M, Pelaez MT, Fierro I, Gomez-Sanchez E, Gomez-Pesquera E *et al*. Impact of ventilator-associated pneumonia on mortality and epidemiological features of patients with secondary peritonitis. *Ann Intensive Care* **6**, 24 (2016).
67. Baker AM, Meredith JW and Haponik EF. Pneumonia in intubated trauma patients. Microbiology and outcomes. *Am J Respir Crit Care Med* **153**, 343-349 (1996).
68. Craig CP and Connelly S. Effect of intensive care unit nosocomial pneumonia on duration of stay and mortality. *Am J Infect Control* **12**, 233-238 (1984).
69. Papazian L, Bregeon F, Thirion X, Gregoire R, Saux P *et al*. Effects of ventilator-associated pneumonia on mortality and morbidity. *Am J Respir Crit Care Med* **154**, 91-97 (1996).
70. Khilnani GC and Jain N. Ventilator-Associated Pneumonia: Changing microbiology and implications. *Indian J Crit Care Med* **17**, 331-332 (2013).

71. Park DR. The microbiology of ventilator-associated pneumonia. *Respir Care* **50**, 742-763 (2005).
72. Vincent JL, Bihari DJ, Suter PM, Bruining HA, White J *et al*. The prevalence of nosocomial infection in intensive care units in Europe. *JAMA* **274,** 639-644 (1995).
73. Rea-Neto A, Youssef NCM, Tuche F, Brunkhorst F, Ranieri VM *et al*. Diagnosis of ventilator-associated pneumonia: a systematic review of the literature. *Crit Care* **12**, R56 (2008).
74. Chastre J, Viau F, Brun P, Pierre J, Dauge MC *et al*. Prospective evaluation of the protected specimen brush for the diagnosis of pulmonary infections in ventilated patients. *Am Rev Respir Dis* **130**, 924-929 (1984).
75. Fabregas N, Ewig S, Torres A, El-Ebiary M, Ramirez J *et al*. Clinical diagnosis of ventilator associated pneumonia revisited: comparative validation using immediate post-mortem lung biopsies. *Thorax* **54**, 867-873 (1999).
76. Miller PR, Johnson JC, Karchmer T, Hoth JJ, Meredith JW *et* al. National nosocomial infection surveillance system: from benchmark to bedside in trauma patients. *J Trauma* **60**, 98-103 (2006).
77. Pugin J, Auckenthaler R, Mili N, Janssens JP, Lew PD *et al*. Diagnosis of ventilator-associated pneumonia by bacteriologic analysis of bronchoscopic and nonbronchoscopic "blind" bronchoalveolar lavage fluid. *Am Rev Respir Dis* **143**, 1121-1129 (1991).
78. Swoboda SM, Dixon T and Lipsett PA: Can the clinical pulmonary infection score impact ICU antibiotic days? *Surg infect (Larchmt)* **7,** 331-339 (2006).
79. Torres A, Ewig S, Lode H and Carlet J. Defining, treating and preventing hospital acquired pneumonia: European perspective. *Intensive Care Med* **35,** 9-29 (2009).
80. Dimopoulos G, Poulakou G, Pneumatikos IA, Armaganidis A, Kollef MH *et al*. Short-versus long-duration antibiotic regimens for ventilator-associated pneumonia: a systematic review and meta-analysis. *Chest* **144,** 1759-1767 (2013).
81. Masterton RG. Antibiotic de-escalation. *Crit Care Clin* **27,** 149-162 (2011).
82. Munoz-Price LS and Weinstein RA. Acinetobacter Infection. *N Engl J Med* **358,** 1271-1281 (2008).
83. Ragle BE, Karginov VA and Wardenburg JB. Prevention and Treatment of *Staphylococcus aureus* Pneumonia with a β-Cyclodextrin Derivative. *Amtimicrob Agents Chemother* **54**, 298-304 (2010).
84. Chastre J, Wolff M, Fagon JY, Chevret S, Thomas F *et al.* Comparison of 8 vs 15 days of antibiotic therapy for ventilator-associated pneumonia in adults: a randomized trial. *JAMA* **290,** 2588-2598 (2003).
85. Martin-Loeches I, Deja M, Koulenti D, Dimopoulos G, Marsh B *et al*. Potentially resistant microorganisms in intubated patients with hospital-acquired pneumonia: the interaction of ecology, shock and risk factors. *Intensive Care Med* **39,** 672-681 (2013).
86. Lipsitch M, Bergstrom CT and Levin BR. The epidemiology of antibiotic resistance in hospitals. Paradoxes and prescriptions. *PNAS* **97**, 1938-1943 (1999).

87. Kollef MH, Hamilton CW and Ernst FR. Economic impact of ventilator-associated pneumonia in a large cohort study. *Infect Control Hosp Epidemiol* **33**, 250-256 (2012).
88. Amin A. Clinical and Economic Consequences of Ventilator-Associated Pneumonia. *Clin Infect Dis* **49**, 36-43 (2009).
89. Wagh H and Acharya D. Ventilator-Associated Pneumonia – an Overview. *BJMP* **2**, 16-19 (2009).
90. Zolfaghari PS and Wyncoll DLA. The tracheal tube: gateway to ventilator-associated pneumonia. *Crit Care* **15**, 310 (2011).
91. Pneumatikos IA, Dragoumanis CK and Bouros DE. Ventilator-associated Pneumonia or Endotracheal Tube-associated Pneumonia? An Approach to the Pathogenesis and Preventive Strategies Emphasizing the Importance of Endotracheal Tube. *Anesthesiology* **110**, 673-690 (2009).
92. Mietto C, Foley K, Salerno L, Oleksak J, Pinciroli R *et al*. Removal of endotracheal tube obstruction with a secretion clearance device. *Resp Care* **59**, 122-126 (2014).
93. Thorens JB, Kaelin RM, Joillet P and Chevrolet JC. Influence of the quality of nursing on the duration of weaning from mechanical ventilation in patients with chronic obstructive pulmonary disease. *Crit Care Med* **23**, 1807-1815 (1995).
94. Torres A, Serra-Batlles J, Ros E, Piera C, de la Bellacasa JP *et al*. Pulmonary aspiration of gastric contents in patients receiving mechanical ventilation: the effect of body position. *Ann Intern Med* **116**, 540-543 (1992).
95. Drakulovic MB, Torres A, Bauer TT, Nicolas JM, Nogue S *et al*. Supine body position as a risk factor for nosocomial pneumonia in mechanically ventilated patients: a randomised trial. *Lancet* **354**, 1581-1588 (1999).
96. Bonten MJM, Gaillard CA, van der Geest S, van Tiel FH, Beysens AJ *et al*. The role of intragastric acidity and stress ulcus prophylaxis on colonization and infection in mechanically ventilated ICU patients. A stratified, randomized, double-blind study of sucralfate versus antacids. *Am J Respir Crit Care Med* **52**, 1825-1834 (1995).
97. Cook D, Guyatt G, Marshall J, Leasa D, Fuller H *et al*. A comparison of sucralfate and ranitidine for the prevention of upper gastrointestinal bleeding in patients requiring mechanical ventilation. *N Eng J Med* **338**, 791-797 (1998).
98. Bergmans DCJJ, Bonten MJM, Gaillard CA, Paling JC, van der Geest S *et al*. Prevention of Ventilator-associated Pneumonia by Oral Decontamination, A Prospective, Randomized, Double-blind, Placebo-controlled study. *Am J Resp Crit Care Med* **164**, 383-388 (2001).
99. Pugin J, Auckenthaler R, Lew DP and Suter PM. Oropharyngeal decontamination decreases incidence of ventilator-associated pneumonia: a randomized, placebo-controlled, double-blind clinical trial. *JAMA* **265**, 2704-2710 (1991).
100. Abele-Horn M, Dauber A, Bauernfeind A, Russwurm W, Seyfarth-Metzger I *et al*. Decrease in nosocomial pneumonia in ventilated patients by selective oropharyngeal decontamination (SOD). *Intensive Care Medicine* **23**, 187-195 (1997).

101. DeRiso AJII, Ladowski JS, Dillon TA, Justice JW and Peterson AC. Chlorhexidine Gluconate 0.12% Oral Rinse Reduces the Incidence of Total Nosocomial Respiratory Infection and Nonprophylactic Systemic Antibiotic Use in Patients Undergoing Heart Surgery. *Chest* **109**, 1556-1561 (1996).
102. Valles J, Peredo R, Burgueno MJ, Rodrigues de Freitas AP, Millan S *et al*. Efficacy of single-dose antibiotic against early-onset pneumonia in comatose patients who are ventilated. *Chest* **143**, 1219-1225 (2013).
103. Keyt, H, Faverio P and Restrepo MI. Prevention of ventilator-associated pneumonia in the intensive care unit: A review of the clinically relevant recent advancements. *Indian J Med Res* **139**, 814-821 (2014).
104. Francolini I and Donelli G. Prevention and control of biofilm-based medical-device-related infections. *Pathogens and Disease* **59**, 227-238 (2010).
105. Poelaert J, Depuydt P, De Wolf A, Van de Velde S, Herck I *et al*. Polyurethane cuffed endotracheal tubes to prevent early postoperative pneumonia after cardiac surgery: a pilot study. *J Thorac Cardiovasc Surg* **135**, 771-776 (2008).
106. Suhas P, Kundra P and Cherian A. Polyurethane cuffed versus conventional endotracheal tubes: Effect on ventilator-associated pneumonia rates and length of Intensive Care Unit stay. *Indian J Anaesth* **60**, 163-167 (2016).
107. Miller MA, Arndt JL, Konkle MA, Chenoweth CE, Iwashyna TJ *et al*. A Polyurethane Cuffed Endotracheal Tube (PUC-ETT) is Associated with Decreased Rates of Ventilator-Associated Pneumonia. *J Crit Care* **26**, 280-286 (2011).
108. Clement JL and Jarrett PS. Antibacterial Silver. *Met Based Drugs* **1**, 467-482 (1994).
109. Wakshlak RBK, Pedahzur R and Avnir D. Antibacterial activity of silver-killed bacteria: the “zombies” effect. *Sci Rep* **5** (2013).
110. Swathy JR, Udhaya Sankar M, Chaudhary A, Aigal S and Pradeep T. Antimicrobial silver: An unprecedented anion effect. *Sci Rep* **4** (2014).
111. Kollef MH, Afessa B, Anzueto A, Veremakis C, Kerr KM *et al*. Silver-coated endotracheal tubes and incidence of ventilator-associated pneumonia: the NASCENT randomized trial. *JAMA* **300**, 805-813 (2008).
112. Li X, Yuan Q, Wang L, Du L and Deng L. Silver-coated endotracheal tube versus non-coated endotracheal tube for preventing ventilator-associated pneumonia among adults: a systematic review of randomized controlled trials. *J Evid Bassed Med* **5**, 25-30 (2012).
113. Saini H, Chhibber S and Harjai K. Antimicrobial and antifouling efficacy of urinary catheters impregnated with a combination of macrolide and fluoroquinolone antibiotics against *Pseudomonas aeruginosa*. *Biofouling* **32**, 511-522 (2016).
114. Shapur NK, Duvdevani M, Friedman M, Zaks B, Gati I *et al*. Sustained release varnish containing chlorhexidine for prevention of biofilm formation on urinary catheter surface: in vitro study. *J Endourol* **26**, 26-31 (2012).

115. Fisher LE, Hook AL, Ashraf W, Yousef A, Barrett DA *et al*. Biomaterial modification of urinary catheters with antimicrobials to give long-term broadspectrum antibiofilm activity. *Journal of Controlled Release* **202**, 57-64 (2015).
116. Hornyak I, Madacsi E, Kalugyer P, Vacz G Horvathy *et al*. Increased Release Time of Antibiotics from Bone Allografts through a Novel Biodegradable Coating. *Biomed Research International* **2014**, 1-8 (2014).
117. Davidoff SN, Sevy JO, Brooks BD, Grainger DW and Brooks AE. Evaluating antibiotic release profiles as a function of polymer coating formulation. *Biomed Sci Instrum* **47**, 46-51 (2011).
118. Tiwari A. Handbook of Antimicrobial Coatings. *Elsevier*, Amsterdam (2018).
119. Bakhshi H, Yeganeh H, Mehdipour-Ataei S, Shokrgozar MA, Yari A *et al*. Synthesis and characterization of antibacterial polyurethane coatings from quaternary ammonium salts functionalized soybean oil based polyols. *Mater Sci Eng C* **33**, 153-164 (2013).
120. Lalani R and Liu L. Electrospun Zwitterionic Poly(Sulfobetaine Methacrylate) for Nonadherent, Superabsorbent, and Antimicrobial Wound Dressing Applications. *Biomacromolecules* **13**, 1853-1863 (2012).
121. Lee WF and Tsai CC. Synthesis and solubility of the poly(sulfobetaine)s and the corresponding cationic polymers: 1. Synthesis and characterization of sulfobetaines and the corresponding cationic monomers by nuclear magnetic resonance spectra. *Polymer* **35**, 2210-2217 (1994).
122. Smith RS, Zhang Z, Bouchard M, Li J, Lapp HS *et al*. Vascular catheters with a nonleaching poly-sulfobetaine surface modification reduce thrombus formation and microbial attachment. *Sci Transl Medi* **4**, 132-153 (2012).
123. Bauer U and Federle W. The insect-trapping rim of Nepenthes pitchers. *Plant Signal Behav* **4**, 1019-1023 (2009).
124. Leslie DC, Waterhouse A, Berthet JB, Valentin TM, Watters Al *et al*. A bioinspired omniphobic surface coating on medical devices prevents thrombosis and biofouling. *Nature Biotechnology* **32**, 1134-1140 (2014).
125. Hammouda B. Solvation Characteristics of a Model Water-Soluble Polymer. *Journal of Polymer Science. Part B: Polymer Physics* **44**, 3195-3199 (2006).
126. Harris LG, Tosatti S, Wieland M, Textor M and Richards RG. Staphylococcus aureus adhesion to titanium oxide surfaces coated with non-functionalized and peptide-functionalized poly(L-lysine)-grafted-poly(ethylene glycol) copolymers. *Biomaterials* **25**, 4135-4148 (2004).
127. Kingshott P, Wei J, Bagge-Ravn D, Gadegaard N and Gram L. Covalent Attachment pf Poly(ethylene glycol) to Surfaces, Critical for Reducing Bacterial Adhesion. *Langmuir* **19**, 6912-6921 (2003).
128. Du J, Bandara HM, Du P, Huang H, Hoang K *et al*. Improved Biofilm Antimicrobial Activity of Polyethylene Glycol Conjugated Tobramycin Compared to Tobramycin in Pseudomonas aeruginosa Biofilms. *Mol Pharm* **12**, 1544-1553 (2015).

129. Roosjen A, Norde W, van der Mei HC and Busscher HJ. The Use of Positively Charged or Low Surface Free Energy Coatings versus Polymer Brushes in Controlling Biofilm Formation. *Progr Colloid Polym Sci* **132**, 138-144 (2006).
130. Harris JM. Poly(ethyleneglycol) Chemistry: Biotechnical and Biomedical Applications. *Plenum Press*, New York (1992).
131. Gombotz WR, Guanghui W, Horbett TA and Hoffman AS. Protein adsorption to poly(ethylene oxide) surfaces. *Journal of Biomedical Materials Research* **25**, 1547-1562 (1991).
132. McPherson T, Kidane A, Szleifer I and Park K. Prevention of Protein Adsorption by Tethered Poly(ethylene oxide) Layers: Experiments and Single-Chain Mean-Field Analysis. *Langmuir* **14**, 176-186 (1998).
133. Costa L, gad AM and Camino G. Thermal and Thermooxidative Degradation of Poly(ethylene oxide)-Metal Salt Complexes. *Macromolecules* **25**, 5512-5518 (1992).
134. Ivanova EP, Hasan J, Webb HK, Gervinskas G, Juodkazis S *et al*. Bactericidal activity of black silicon. *Nature Communications* **4** (2013).
135. Reddy ST, Chung KK, McDaniel CJ, Darouiche RO, Landman J *et al*. Micropatterned Surfaces for Reducing the Risk of Catheter-Associated Urinary Tract Infection: An *In Vitro* Study on the Effect of Sharklet Micropatterned Surfaces to Inhibit Bacterial Colonization and Migration of Uropathogenic *Escherichia coli. J Endourol* **25**, 1547-1552 (2011).
136. Diaz C, Cortizo MC, Schilardi PL, Gomez de Saravia SG and Lorenzo de Mele MAF. Influence of the Nano-micro structure of the surface on bacterial adhesion. *Mat Res* **10**, 11-14 (2007).
137. Govindarajan R, Duraiyan J, Kaliyappan K and Palanisamy M. Microarray and its applications. *J Pharm Bioallied Sci* **4**, 310-312 (2012).
138. Vaishampayan P, Osman S, Andersen G and Venkateswaran K. High-density 16S microarray and clone library-based microbial community composition of the Phoenix spacecraft assembly clean room. *Astrobiology* **10**, 499-508 (2010).
139. Anderson DG, Levenberg S and Langer R. Nanoliter-scale synthesis of arrayed biomaterials and application to human embryonic stem cells. *Nature Biotechnology* **22**, 863-866 (2004).
140. Khan F, Smith JO, Kanczler JM, Tare RS, Oreffo ROC et al. Discovery and Evaluation of a Functional Ternary Polymer Blend for Bone Repair: Translation from a Microarray to a Clinical Model. *Adv Functional Mater* **23**, 2850-2862 (213).
141. Hook AL, Chang CY, Yang J, Luckett J, Cockayne A *et al*. Combinatorial discovery of polymers resistant to bacterial attachment. *Nature Biotechnology* **30**, 868-875 (2012).
142. Sanni O, Chang CY, Anderson DG, Langer R, Davies MC *et al*. Bacterial Attachment to Polymeric Materials Correlates with Molecular Flexibility and Hydrophilicity. *Adv Healthc Mater* **4**, 695-701 (2015).
143. Stratton TR, Applegate BM and Youngblood JP. Effect of steric hindrance on the properties of antibacterial and biocompatible copolymers. *Biomacromolecules* **12**, 50-56 (2011).

144. Hsu L, Fang J, Borca-Tasciuc D, Worobo R and Moraru CI. The effect of micro- and nanoscale topography on the adhesion of bacterial cells to solid surfaces. *Appl Environ Microbiol* **79**, 2703-2712 (2013).
145. Adlington K, Nguyen NT, Eaves E, Yang J, Chang CY *et al*. Application of Targeted Molecular and Material Property Optimization to Bacterial Attachment-Resistant (Meth)acrylate Polymers. *Biomacromolecules* **17**, 2830-2838 (2016).
146. Honeybourne D, Costello JC and Barham C. Tracheal damage after endotracheal intubation: comparison of two types of endotracheal tubes. *Thorax* **37**, 500-502 (1982).
147. Pal BP. Fundamentals of Fibre Optics in Telecommunication and Sensor Systems. *New Age International Publishers*, New Delhi (1992).
148. Guo Z. Progress in Optical Fibres Research. *Nova Science Publishers*, New York (2007).
149. Wang P, Brambilla G, Ding M, Semenova Y, Wu Q *et al*. Investigation of single-mode–multimode–single-mode and single-mode–tapered-multimode–single-mode fiber structures and their application for refractive index sensing. *JOSA B* **28**, 1180-1186 (2011).
150. Yu FTS and Shizhuo Y. Fibre Optic Sensors. *Marcel Decker Inc.*, New York (2002).
151. Fidanboylu K and Efendioglu HS. Fibre Optic Sensors and their applications. 5th International Advanced Technologies Symposium (IATS'09), May 13-15, 2009, Karabuk, Turkey. Keynote Address, 1-6 (2009).
152. Tracey PM. Intrinsic Fiber-Optic Sensors. *IEEE Transactions on Industry Applications* **27**, 96-98 (1991).
153. Berthold JW. Historical Review of Microbend Fiber Optic Sensors. *Journal of Lightwave Technology* **13**, 1193-1199 (1995).
154. Udd E, Schulz W, Seim J, Corones J, and Laylor HM, Fiber Optic Sensors for Infrastructure Applications. *Oregon Department of Transportation*, Washington DC (1998).
155. Connelly MC. Fiber Sensors. *Elsevier*, Limerick (2005).
156. Zaynetdinov M, See EM, Geist B, Ciovati G, Robinson HD *et al*. A Fiber Bragg Grating Temperature Sensor for 2-400 K. *IEEE Sensors Journal* **15**, 1908-1912 (2014).
157. Irigoyen M, Sanchez-Martin JA, Bernabeu E and Zamora A. Tapered optical fiber sensor for chemical pollutants detection is seawater. *Measurement Science and Technology* **28** (2017).
158. Casas JR and Cruz JS. Fiber Optic Sensors for Bridge Monitoring. *Journal of Bridge Engineering* **8**, 362-373 (2003).
159. James SW and Tatam RP. Optical fibre long-period grating sensors: characteristics and applications. *Meas Sci Technol* **14**, 49-61 (2003).
160. Gouveia CAJ, Baptista JM and Jorge PAS. Refractometric Optical Fiber Platforms for Label Free Sensing. Current Developments in Optical Fibre Technology. *InTech*, Madeira (2013).
161. Bhatia V and Vengsarkar AM. Optical fiber long-period grating sensors. *Optics Letters* **21**, 692-694 (1996).

162. Saez-Rodriguez D, Cruz JL, Johnson I, Webb DJ, Large MCJ *et al*. Water Diffusion Into UV Inscripted Long Period Grating in Microstructured Polymer Fibre. *IEEE Sensors Journal* **10**, 1169-1173 (2010).
163. Marques L, Hernandez FU, James SW, Morgan SP, Clark M *et al*. Highly sensitive optical fibre long period grating biosensor anchored with silica core gold shell nanoparticles. *Biosensors and Bioelectronics* **75**, 222-231 (2016).
164. Erdogan T. Cladding-mode resonances in short- and long-period fiber grating filters. *Journal of the Optical Society of America A* **14**, 1760-1773 (1997).
165. James SW, Topliss SM and Tatam RP. Properties of Length-Apodized Phase-Shifted LPGs Operating at the Phase Matching Turning Point. *Journal of Lightwave Technology* **30**, 2203-2209 (2012).
166. Cheung SC, Topliss SM, James SW and Tatam RP. Response of fibre optic long period gratings operating near the phase matching turning point to the deposition of nanostructured coatings. *Journal of the Optical Society of America. B Optical Physics* **25**, 897-902 (2008).
167. Chen H and Gu Z. Filtering characteristics of film-coated long-period fiber gratings operating at the phase-matching turning point. *Optik – International Journal for Light and Electron Optics* **125**, 6003-6009 (2014).
168. Hromadka J, Tokay B, James SW, Tatam RP and Korposh S. Optical fibre long period grating gas sensor modified with metal organic framework thin films. *Sensors and Actuators B: Chemical* **221**, 891-899 (2015).
169. Korposh S, Lee SW, James SW and Tatam RP. Refractive index sensitivity of fibre-optic long period gratings coated with SiO_2 nanoparticle mesoporous thin films. *Meas Sci Technol* **22**, 1-10 (2011).
170. Smietana M, Bock WJ, Mikulic P, Ng A, Chinnappan R *et al*. Detection of bacteria using bacteriophages as recognition elements immobilized on long-period fiber gratings. *Optics Express* **19**, 7971-7978 (2011).
171. Tripathi SM, Bock WJ, Mikulic P, Chinnippan R, Ng A et al. (2012) Long period grating based biosensor for the detection of *Escherichia coli* bacteria. *Biosensors and Bioelectronics* **35**, 308-312 (2012).
172. Srey S, Jahid IK and Ha SD. Biofilm formation in food industries: A food safety concern. *Food Control* **31**, 572-585 (2013).
173. Callow ME and Callow JA. Marine biofouling: a sticky problem. *Biologist* **49**, 1-5 (2004).
174. Caliendo AM, Gilbert DN, Ginocchio CC, Hanson KE, May L *et al*. Better Tests, Better Care: Improved Diagnostics for Infectious Diseases. *Clin Infect Dis* **57**, 139-170 (2013).
175. Loesche WJ and Grossman NS. Periodontal Disease as a Specific. Albeit Chronic, Infection: Diagnosis and Treatment. *Clin Microbiol Rev* **14**, 727-752 (2001).
176. Jarlier V, Nicolas MH, Fournier G and Philippon A. Extended Broad-Spectrum Beta-Lactamases Conferring Transferable Resistance to Newer Beta-Lactam agents in Enterobacteriaceae: Hospital Prevalence and Susceptibility Patterns. *Reviews of Infectious Diseases* **10**, 867-878 (1988).

177. Kaye KS, Cosgrove S, Harris A, Eliopoulos GM and Carmeli Y. Risk Factors for Emergence of Resistance to Broad-Spectrum Cephalosporins among *Enterobacter* spp. *Antimicrob Agents Chemother* **45**, 2628-2630 (2001).
178. World Health Organisation, Antimicrobial resistance fact sheet, September 2016.
179. Public Health England, Health matters: antimicrobial resistance, December 2015.
180. Worthington RJ and Melander C. Comnination Approaches to Combat Multi-Drug Resistant Bacteria. *Trends Biotechnol* **31**, 177-184 (2013).
181. McBride ME and Girard KF. A selective method for the isolation of Listeria monocytogenes from mixed bacterial populations. *Translational Research* **55**, 153-157 (1960).
182. Richards SJ, Otten L and Gibson MI. Glycosylated gold nanoparticle libraries for label-free multiplexed lectin biosensing. *J Mater Chem B* **4**, 3046-3053 (2016).
183. Sharon N. Bacterial lectins, cell-cell recognition and infectious disease. *FEBS Lett* **217**, 145-157 (1987).
184. Magennis EP, Fernandez-Trillo F, Sui C, Spain SG, Bradshaw DJ *et al*. Bacteria-instructed synthesis of polymers for self-selective microbial binding and labelling. *Nature Materials* **13**, 748-755 (2014).
185. Pernagallo S, Wu M, Gallagher MP and Bradley M. Colonising new frontiers – microarrays reveal biofilm modulating polymers. *J Mater Chem* **21**, 96-101 (2011).
186. Hook AL, Anderson DG, Langer R, Williams P, Davies MC *et al*. High throughput methods applied in biomaterial development and discovery. *Biomaterials* **31**, 187-198 (2010).
187. Inzana TJ. The application of nanoparticle optical fibre sensors in the diagnosis of bacterial infections. *J Bacteriol Parasitol* **4**, 200-208 (2013).
188. Debuigne A, Poli R, Jerome C, Jerome R and Detrembleur C. Overview of cobalt-mediated polymerization: Roots, state of the art and future prospects. *Progress in Polymer Science* **34**, 211-239 (2009).
189. Gridnev AA and Ittel SD. Catalytic Chain Transfer in Free-Radical Polymerizations. *Chem Rev* **101**, 3611-3659 (2001).
190. Billmeyer FW. Textbook of Polymer Science, 3rd Edition. *Wiley Interscience*, New York (1984).
191. Nurumbetov G, Engelis N, Godfrey J, Hand R, Anastasaki A *et al*. Methacrylic block copolymers by sulfur free RAFT (SF RAFT) free radical emulsion polymerisation. *Polymer Chemistry* **8**, 1084-1094 (2017).
192. Soeriyadi AH, Li GZ, Slavin S, Jones MW, Amos CM *et al*. Synthesis and modification of thermoresponsive poly(oligo(ethylene glycol)methacrylate) via catalytic chain transfer polymerization and thiol-ene Michael addition. *Polym Chem* **2**, 815-822 (2011).
193. Semsarzadeh MA and Amiri S. Controlled free radical polymerization of vinyl acetate with cobalt acetoacetonate. *J Chem Sci* **124**, 521-527, (2012).
194. Wayland BB, Poszmik G and Mukerjee SL. Living Radical Polymerization of Acrylates by Organocobalt Porphyrin Complexes. *J Am Chem Soc* **116**, 7943-7944 (1994).

195. Debuigne A, Caille JR and Jerome R. Highly Efficient Cobalt-Mediated Radical Polymerization of Vinyl Acetate. *Angew Chem Ed Engl* **44**, 1101-1104 (2005).
196. Allan LEN, Perry MR and Shaver MP. Organometallic mediated radical polymerization. *Progress in Polymer Science* **37**, 127-156 (2012).
197. Bryaskova R, Detrembleur C, Debuigne A and Jerome R. Cobalt-Mediated Radical Polymerisation (CMRP) of Vinyl Acetate Initiated by Redox Systems: Toward the Scale-UP of CMRP. *Macromolecules* **39**, 8263-8268 (2006).
198. Mouquinho AI, Petrova KT, Barros MT and Sotomayor JC. New Polymer Networks for PDLC Films Application. *InTech*, Rijeka (2012).
199. Kurdikar DL and Peppas NA. Method of Determination of Initiator Efficiency: Application to UV Polymerizations Using 2,2-Dimethoxy-2-phenylacetophenone. *Macromolecules* **27**, 733-738 (1994).
200. Ates S, Aydogan B, Torun L and Yagci Y. Synthesis and characterization of triptycene type cross-linker and its use in photoinduced curing applications. *Polymer* **51**, 825-831 (2010).
201. Bascom WD. Structure of Silane Adhesion Promoter Films on Glass and Metal Surfaces. *Macromolecules* **5**, 792-798 (1972).
202. Plueddemann EP. Silane adhesion promoter in coatings. *Progress in Organic Coatings* **11**, 297-308 (1983).
203. Mittal KL. Silanes and Other Coupling Agents, Volume 4. *Taylor and Francis Group*, Boca Raton (2007).
204. Fearn S. An Introduction to Time-of-Flight Secondary Ion Mass Spectrometry (ToF-SIMS) and its Application to Materials Science. *Morgan & Claypool*, San Rafael (2015).
205. Vickerman JC and Briggs D. ToF-SIMS: Materials Analysis by Mass Spectrometry, 2nd Edition. *IM Publications LLP*, Chichester (2013).
206. Spool AM. The Practice of TOF-SIMS. *Momentum Press*, Opa-Locka (2016).
207. Inoue M and Murase A. Reduction of matrix effects in TOF-SIMS analysis by metal-assisted SIMS (MetA-SIMS). *Surface and Interface Analysis* **37**, 1111-1114 (2005).
208. Hofmann JP, Rohnke M and Weckhuysen BM. Recent advances in secondary ion mass spectrometry of solid acid catalysts: large zeolite crystals under bombardment. *Phys Chem Phys* **16**, 5465-5474 (2014).
209. Bertrand P and Weng LT. Time-of-Flight Secondary Ion Mass Spectrometry (ToF-SIMS). *Mikrochim Acta* **13**, 167-182 (1996).
210. Brison J, Muramoto S and Castner DG. ToF-SIMS Depth Profiling of Organic Films: A Comparison between Single Beam and Dual-beam analysis. *J Phys Chem C Nanometer Interfaces* **114**, 5565-5573 (2010).
211. Lee CH, Mong HY and Lin WC. Noninterferometric wide-field optical profilometry with nanometer depth resolution. *Optics Letters* **27**, 1773-1775 (2002).
212. NanoScience Instruments, "How a Profilometer Works", (http://www.nanoscience.com/technology/optical-profiler-technology/how-profilometer-works/), accessed 30 August 2017.

213. Zeta Instruments. Zeta-20 Optical Profiler Operation Manual. Copyright Zeta Instruments, Inc. (2012).
214. Bosseboeuf A and Petitgrand S. Characterization of the static and dynamic behaviour of M(O)EMS by optical techniques: status and trends. *J Micromech Microeng* **13**, 23-33 (2003).
215. Paddock SW. Confocal Microscopy – Methods and Protocols. *Humana Press*, Totowa (1999).
216. Pawley JB. Handbook of Biological Confocal Microscopy. *Plenum Press*, New York (1990).
217. Fellers TJ and Davidson MW. Introduction to Confocal Microscopy. Olympus Microscopy Resource Centre (http://www.olympusmicro.com/primer/techniques/confocal/confocalintro.html), accessed 27 August 2017.
218. Gustafsson MGL, Betzig E, Hess HF, Patterson GH, Lippincott-Schwartz *et al*. Introduction to Superresolution Microscopy. Carl Zeiss Microscopy Online Campus (http://zeiss-campus.magnet.fsu.edu/print/superresolution/introduction-print.html), accessed 27 August 2017.
219. Prasad V, Semwogerere D and Weeks ER. Confocal microscopy of colloids. *J Phys: Cond Mat* **19**, 1-25 (2007).
220. Wilson T. Resolution and optical sectioning in the confocal microscope. *Journal of Microscopy* **244**, 113-121 (2011).
221. Holloway BW. Genetic recombination in Pseudomonas aeruginosa. *J Gen Microbiol* **13**, 572-581 (1955).
222. Hinterdorfer P and van Oijen A. Handbook of Single-Molecule Biophysics. *Springer*, New York (2009).
223. Molecular Probes Inc. Fact Sheet. SYTO® Red Fluorescent Nucleic Acid Stains. Revised January 2001.
224. Chalfie M and Kain SR. Green Fluorescent Protein – Properties, Applications and Protocols. *Wiley Interscience*, Hoboken (2006).
225. Heydorn A, Nielsen AT, Hentzer M, Sternberg C, Givskov M *et al*. Quantification of biofilm structures by the novel computer program COMSTAT. *Microbiology* **146**, 2395-2407 (2000).
226. Malacara D and Thompson BJ. Handbook of Optical Engineering. *Marcel Dekker*, New York (2001).
227. Neumann W. Fundamentals of Dispersive Optical Spectrometer Systems. *SPIE Press*, Bellingham (2014).
228. Tyler BJ, Hook AL, Pelster A, Williams P, Alexander MR *et al*. Development and characterization of a stable adhesive bond between a poly(dimethylsiloxane) catheter material and a bacterial biofilm resistant acrylate polymer coating. *Biointerfaces* **12** (2017).
229. Skyberg JA, Siek KE, Doetkott C and Nolan LK. Biofilm formation by avian Escherichia coli in relation to media, source and phylogeny. *J Appl Microbiol* **102**, 548-554 (2007).

230. Kirchner S, Fothergill JL, Wright EA, James CE, Mowat E *et al*. Use of Artificial Sputum Medium to Test Antibiotic Efficacy Against *Pseudomonas aeruginosa* in Conditions More Relevant to the Cystic Fibrosis Lung. *J Vis Exp* **64**, 3857-3864 (2012).
231. Tabachnik NF, Blackburn P and Cerami A. Biochemical and Rheological Characterization pf Sputum Mucins from a Patient with Cystic Fibrosis. *J Biol Chem* **256**, 7161-7165 (1981).
232. Frederick CB and Reynolds CH. Modelling the reactivity of acrylic acid and acrylate anion with biological nucleophiles. *Toxicol Lett* **47**, 241-247 (1989).
233. Hradil J, Kralova E and Benes MJ. Methacrylate anion exchangers with enhanced affinity for nitrates. *Reactive and Functional Polymers* **33**, 263-273 (1997).
234. Freeman T. Environmental Geology. *Wiley and Sons*, Missouri (2004).
235. Lauw SJL, Lee JHQ, Tessensohn ME, Leong WQ and Webster RD. The electrochemical reduction of di-(2-ethylhexyl) phthalate (DEHP) in acetonitrile. *J Electroanalyt Chem* **794**, 103-111 (2017).
236. Palmer KL, Mashburn LM, Singh PK and Whiteley M. Cystic Fibrosis Sputum Supports Growth and Cues Key Aspects of *Pseudomonas aeruginosa* Physiology. *J Bacteriol* **187**, 5267-5277 (2005).
237. Morishima Y, Lim HS, Nozakura S and Sturtevant JL. Effect of monomer sequence distribution in 2-vinylnaphthalene-maleic acid copolymers on energy migration and eximer formation in aqueous solution. *Macromolecules* **22**, 1148-1154 (1989).
238. Hesse P. Radical Polymerisation Kinetics in Aqueous Solution and in Systems with Secondary and Tertiary Radicals Studied by Novel Pulsed-Laser Techniques. *Cuvillier Verlag*, Gottingen (2008).
239. Yimsiri P and Mackley MR. Spin and dip coating of light-emitting polymer solutions: Matching experiment with modelling. *Chemical Engineering Science* **61**, 3496-3505 (2006).
240. Hwang J, Shoji N, Endo A and Daiguji H. Effect of Withdrawal Speed on Film Thickness and Hexagonal Pore-Array Dimensions of SBA-15 Mesoporous Silica Thin Film. *Langmuir* **30**, 15550-15559 (2014).
241. Spangler LL, Torkelson JM and Royal JS. Influence of solvent and molecular weight on thickness and surface topography of spin-coated polymer films. *Polymer Engineering and Science* **30**, 644-653 (1995).
242. Sadhir RK and Sanjana ZN. Plasma deposited thin films suitable as moisture sensors. *J Mater Sci* **26**, 4261-4267 (1991).
243. Kane SR, Ashby PD and Pruitt LA. ATR-FTIR as a thickness measurement technique for hydrated polymer-on-polymer coatings. *J Biomed Mater Res* **91B**, 613-620 (2009).
244. Fung C, Naughton S, Turnbull L, Tingpej P, Rose B *et al*. Gene expression of *Pseudomonas aeruginosa* in a mucin-containing synthetic growth medium mimicking cystic fibrosis lung sputum. *J Med Microbiol* **59**, 1089-1100 (2010).
245. Bowden GH and Li YH. Nutritional influences on biofilm development. *Adv Dent Res* **11**, 81-99 (1997).

246. Shehata TE and Marr AG. Effect of Nutrient Concentration on the Growth of *Escherichia coli*. *J Bacteriol* **107**, 210-216 (1971).
247. Brennan AL, Gyi KM, Wood DM, Johnson J, Holliman R *et al*. Airway glucose concentrations and effect on growth of respiratory pathogens in cystic fibrosis. *Journal of Cystic Fibrosis* **6**, 101-109 (2007).
248. Van Sambeek L, Cowley ES, Newman DK and Kato R. Sputum Glucose and Glycemic Control in Cystic Fibrosis-Related Diabetes: A Cross-Sectional Study. *PLoS One* **10** (2015).
249. Mulcahy LR, Isabella VM and Lewis K. Pseudomonas aeruginosa biofilms in disease. *Microb Ecol* **68**, 1-12 (2014).
250. Garrett TR, Bhakoo M and Zhang Z. Bacterial adhesion and biofilms on surfaces. *Progress in Natural Science* **18**, 1049-1056 (2008).
251. Latini G, De Felice C, Del Vecchio A, Barducci A, Ferri M *et al*. Di-(2-ethylhexyl) phthalate leakage and color changes in endotracheal tubes after application in high-risk newborns. *Neonatology* **95**, 317-323 (2009).
252. Habib MR and Karim MR. Antimicrobial and Cytotoxic Activity of Di-(2-ethylhexyl) Phthalate and Anhydrosophoradiol-3-acetate Isolated from *Calotropis gigantean* (Linn.) Flower. *Mycobiology* **37**, 31-36 (2009).
253. Abbassy MA, Masoud SA and Nassar AMK. *In Vitro* Antibacterial Activity And Phytochemical Analysis Of *Abrus Precatorius* Linn. *Egy J Plant Pro Res* **4**, 1-14 (2016).
254. Villaneuva ME, Salinas A, Gonzalez JA, Teves S and Copello GJ. Dual antibacterial effect of immobilized quaternary ammonium and aliphatic groups on PVC. *New J Chem* **39**, 9200-9206 (2015).
255. Kramer PA, Banker GS, Nadkarni PD and Kildsig DO. Effect of Surface Roughness and Coating Solvent on Film Adhesion to Tablets. *J Pharm Sci* **64**, 1554-1557 (1975).
256. Wunderink RG and Rello J. Ventilator-Associated Pneumonia. *Springer*, New York (2001).
257. Wolf AV. Aqueous Solutions and Body Fluids. Their Concentrative Properties and Conversion Tables. *Hoeber*, New York (1966).
258. http://shodhganga.inflibnet.ac.in/bitstream/10603/1966/7/07_chapter%202.pdf, accessed 3 December 2017.
259. Paul PH and Kychakoff G. Fiber-optic evanescent field absorption sensor. *Appl Phys Lett* **51**, 12 (1987).
260. Nugroho RWN, Odelius K, Hoglund A and Albertsson AC. The nature of polymer grafts and substrate shape on the surface degradation of poly(L-lactide). *Journal of Applied Polymer Science* **132**, 1-11 (2015).
261. Allara DL, Baca A and Pryde CA. Distortions of Band Shapes in External Reflection Infrared Spectra of Thin Polymer Films on Metal Substrates. *Macromolecules* **11**, 1215-1220 (1978).
262. Luo A, Gao K, Liu F, Qu R and Fang Z. Evanescent-field coupling based on long period grating and tapered fiber. *Optics Communications* **240**, 69-73 (2004).
263. Tsuda H and Urabe K (2009) Characterization of Long-period Grating Refractive Index Sensors and Their Applications. *Sensors* **9**, 4559-4571 (2009).

264. Ding JF, Zhang AP, Shao LY, Yan JH and He S. Fiber-taper seeded long-period grating pair as a highly sensitive refractive-index sensor. *IEEE Photonics Technology Letters* **17**, 1247-1249 (2005).
265. Tian Y, Wang W, Wu N, Zou X and Wang X. Tapered Optical Fiber Sensor for Label-Free Detection of Biomolecules. *Sensors* **11**, 3780-3790 (2011).
266. Bakke R, Kommedal R and Kalvenes S. Quantification of biofilm accumulation by an optical approach. *J Microbiol Methods* **1**, 13-26 (2001).
267. Limoli DH, Jones CJ and Wozniak DJ. Bacterial Extracellular Polysaccharides in Biofilm Formation and Function. *Microbiol Spectr* **3** (2015).
268. Voberkova S Hermanova S, Hrubanova K and Krzyzanek V. Biofilm formation and extracellular polymeric substances (EPS) production by Bacillus subtilis depending on nutritional conditions in the presence of polyester film. *Folia Microbiol (Praha)* **61**, 91-100 (2016).
269. Henkel Adhesives, Medical Device Adhesives (http://na.henkel-adhesives.com/medical-device-adhesives-17800.htm), accessed 27 September 2017.
270. Kim DW, Zhang Y, Cooper KL and Wang A. In-fiber reflection mode interferometer based on a long-period grating for external refractive-index measurement. *Appl Opt* **44**, 5368-5373 (2005).
271. Shreiner AB, Kao, JY and Young VB. The gut microbiome in health and in disease. *Curr Opin Gastroenterol* **31**, 69-75 (2015).
272. Evans AS and Feldman HA. Bacterial Infections of Humans: Epidemiology and Control. *Springer*, New York (1982).
273. Ringner M. What is principal component analysis? *Nature Biotechnology* **26**, 303-304 (2008).
274. Brown L, Wolf JM, Prados-Rosales R and Casadevall A. Through the wall: extracellular vesicles in Gram-positive bacteria, mycobacteria and fungi. *Nat Rev Microbiol* **13**, 620-630 (2015).
275. Gallardo-Moreno AM, Navarro-Perez ML, Vadillo-Rodriguez V, Bruque JM and Gonzalez-Martin ML. Insights into bacterial contact angles: difficulties in defining hydrophobicity and surface Gibbs energy. *Colloids Surf B Biointerfaces* **88**, 373-380 (2011).
276. Allison DG, Brown MR, Evans DE and Gilbert P. Surface hydrophobicity and dispersal of Pseudomonas aeruginosa from biofilms. *FEMS Microbiol Lett* **59**, 101-104 (1990).
277. Goulter RM, Gentle IR and Dykes GA. Issues in determining factors influencing bacterial attachment: a review using the attachment of *Escherichia coli* to abiotic surfaces as an example. *Lett Appl Microbiol* **49**, 1-7 (2009).
278. Schawe R, Fetzer I, Tonniges A, Hartig C, Geyer W *et al*. Evaluation of FT-IT spectroscopy as a tool to quantify bacteria in binary mixed cultures. *J Microbiol Methods* **86**, 182-187 (2011).
279. Janda JM, Abbott SL. 16S rRNA Gene Sequencing for Bacterial Identification in the Diagnostic Laboratory: Pusles, Perils and Pitfalls. *J Clin Microbiol* **45**, 2761-2754 (2007).

280. Kuznetsova MV, Maslennikova IL, Karpunina TI, Nesterova LY and Demakov VA. Interactions of Pseudomonas aeruginosa in predominant biofilm or planktonic forms of existence in mixed cultures with Escherichia coli in vitro. *Can J Microbiol* **59**, 604-610 (2013).
281. Cerqueira L, Oliveira JA, Nicolau A, Azevedo NF and Vieira MJ. Biofilm formation with mixed cultures of Pseudomonas aeruginosa/Escherichia coli on silicone using artificial urine to mimic urinary catheters. *Biofouling* **29**, 829-840 (2013).
282. Chu W, Zere TR, Weber MM, Wood TK, Whiteley M *et al*. Indole Production Promotes *Escherichia coli* Mized-Culture Growth with *Pseudomonas aeruginosa* by Inhibiting Quorum signalling. *Appl Environ Microbiol* **78**, 411-419 (2012).
283. Culotti A and Packman AI. *Pseudomonas aeruginosa* Promotes *Escherichia coli* Biofilm Formation in Nutrient-Limited Medium. *PloS One* **9** (2014).